Spring 5-8-2015

Springtime Melt Onset on Arctic Sea Ice from Satellite Observations and Related Atmospheric Conditions

Angela C. Bliss
University of Nebraska - Lincoln, angela.bliss@oregonstate.edu

SPRINGTIME MELT ONSET ON ARCTIC SEA ICE FROM SATELLITE OBSERVATIONS AND RELATED ATMOSPHERIC CONDITIONS

by

Angela C. Bliss

A DISSERTATION

Presented to the Faculty of

The Graduate College at the University of Nebraska

In Partial Fulfillment of Requirements

For the Degree of Doctor of Philosophy

Major: Earth and Atmospheric Sciences

(Meteorology/Climatology)

Under the Supervision of Professor Mark R. Anderson

Lincoln, Nebraska

May, 2015

SPRINGTIME MELT ONSET ON ARCTIC SEA ICE FROM SATELLITE OBSERVATIONS AND RELATED ATMOSPHERIC CONDITIONS

Angela C. Bliss, Ph.D.
University of Nebraska, 2015
Advisor: Mark R. Anderson

The timing of snowmelt onset (MO) on Arctic sea ice derived from passive microwave satellite data is examined by determining the melting area (in km^2) on a daily basis for the spring and summer melt season months over the 1979 – 2012 data record. The date of MO on Arctic sea ice has important implications for the amount of total solar energy absorbed by the ice-ocean system in a given year. Increasingly early mean MO dates have been recorded over the 34-year data record. Statistically significant trends indicate that MO is occurring 6.6 days $decade^{-1}$ earlier in the year over all Arctic sea ice extent. Larger trends exist in sub-regions of the Arctic Ocean including the Barents, Kara, Laptev, East Siberian, Chukchi, and Beaufort Seas and in the Central Arctic region. The Bering Sea is the only sub-region of the Arctic that has a positive trend in mean MO date indicating that melting is occurring later in the year. Temporal and spatial variability in melting events are examined in the time series of daily MO areas via the identification of several types of melting events. These melting events are characterized based on the magnitude of area melted and duration of the event. Daily maps of MO during melting events are compared with the atmospheric conditions from reanalysis data to investigate the nature of spatial variability in melting area. The occurrence of transient cyclones tends to produce large, contiguous areas of melting on sea ice located in the warm sector of the cyclone. By contrast, high pressure and attendant clear sky conditions tend to produce sporadic, discontinuous areas of melting area. Interannual variability in daily

MO area is assessed using an annual accumulation of daily MO area for each melt season. Trends in mean MO dates are evident in the annual accumulations, however, regional variability is high and outlier events can occur. This work illustrates the need for a better understanding of the synoptic weather conditions leading to specific patterns in MO area to improve the predictability of early season Arctic sea ice response to a changing climate.

ACKNOWLEDGEMENTS

I would like to acknowledge my advisor Dr. Mark Anderson for helping me to develop this research over the last five years and providing guidance to me whenever I found myself obsessing about the details. I would also like to thank my committee members Dr. Steve Hu, Dr. Robert Oglesby, and Dr. Song Feng for their work in supporting and reviewing this work, greatly improving it in the process.

I also acknowledge NASA [grant: NNX08AP34A] and NOAA [grant: NA08AR4310677] for providing the funding necessary to complete this research.

TABLE OF CONTENTS

LIST OF FIGURES

LIST OF TABLES

CHAPTER 1 – INTRODUCTION

Arctic sea ice is a sensitive indicator of climate change that has seen remarkable changes over the last several decades. Due to the large size and inhospitable conditions in the Arctic region, consistent in situ observations of sea ice characteristics are relatively hard to come by. Therefore, one of the best tools to study changes in sea ice are remotely sensed observations via satellite. A mostly consistent record of sea ice from passive microwave sensors begins in late 1978 and continues through present day.

At first glance, melting on Arctic sea ice appears straightforward. When melting atop the sea ice first begins, the surface albedo of bare ice and any snow cover overlying the sea ice is reduced, leading to more melt. The positive feedback loop that occurs causes melt ponds to form on the ice surface, leads open up in the ice pack, and eventually the ice can melt away completely. However, sea ice is coupled to both atmospheric conditions and ocean circulation and direct correlations between the onset of melting in the spring and the late summer sea ice extent minima have not been found.

Trends in early melt onset (MO) have been documented on the sea ice over the last several decades; however, existing studies of MO reduce the usefulness of the data by averaging the data spatially and temporally. While this technique provides a useful summary for climate studies, the spatial and temporal patterns in the data within a given year are lost. This work is aimed at investigating those shorter time scale variations in the timing of MO in the spring and the related spatial patterns in MO in response to synoptic scale atmospheric conditions at the surface. In particular, the weather patterns

causing surface air temperatures to warm to the freezing point and induce MO are investigated to relate the atmospheric conditions with distinct spatial patterns in MO.

This study is designed to examine temporal and spatial patterns in the onset of melting on Arctic sea ice on a daily basis during the melt season for years 1979 – 2012. The dataset provides annual maps of the day from the first of year on which MO was detected on Arctic sea ice. This work provides summary statistics for the record of MO dates and reports statistically significant decadal trends in the onset of melting for the Arctic as a whole and for sub-regions within the Arctic.

To examine patterns in MO on a daily basis, the area of melting (in km^2) is calculated from the MO date maps for each year. Time series of the daily MO area reveal distinct melting events that are described and characterized based on the magnitude of area melted, the duration of the melting event, and the timing of when the event occurs during the melt season. Several case studies representing various melting event types identified in the daily time series of MO area are examined in detail to determine the spatial patterns in MO that occur. Further, mean sea level pressures, temperatures, and surface winds are used to summarize the weather conditions present at the time of MO.

Finally, interannual variability in the timing of daily MO areas is examined by summing the daily MO areas through each melt season producing an accumulation of MO area. Comparisons of annual MO area accumulations reveal regional and interannual variability in melting area and a shift in melt onset timing over the data record. The ultimate goal of this work is to begin identifying the surface weather patterns at the onset of melting that are driving observed trends in MO. Linking MO patterns with

atmospheric conditions could improve our understanding of changes in the increasingly sensitive Arctic sea ice and improve predictability of MO timing in the future.

CHAPTER 2 – SCIENTIFIC BACKGROUND
ARCTIC SEA ICE CHANGE AND MELT ONSET

2.1 Sea ice change over the satellite record

A largely consistent record of sea ice has been created using passive microwave satellite observations beginning in late 1978 through present day. These data were collected at a 25 km x 25 km resolution first by NASA's Scanning Multichannel Microwave Radiometer (SMMR) sensor onboard the Nimbus-7 platform during the years 1979 – 1987 and subsequently the Defense Meteorological Satellite Program's series of Special Sensor Microwave Imager (SSM/I) and Sounder (SSMIS) sensors onboard the F8, F11, F13, and F17 platforms from 1988 – present. Throughout this data record, one aspect of sea ice change that has received the most attention is the annual minima of sea ice extent, which occurs during September, following the summer melt season. Record-low annual sea ice extents have been recorded numerous times during the last decade, most recently on 13 September, 2012 when an extent minimum of 3.4×10^6 km^2 was reached [*Parkinson and Comiso*, 2013], exceeding the previous record set on 14 September, 2007 (Figure 2.1) by 0.2×10^6 km^2 [*Comiso et al.,* 2008]. The reductions in sea ice extent allow for increased absorption of heat flux by the ocean which increases atmospheric temperatures, leading to a delay in the timing of freeze up in the fall and winter. The delay in fall freeze-up delays the closing off of ocean heat-flux in the fall and winter months leading to increased warming and reduced sea ice growth during the winter.

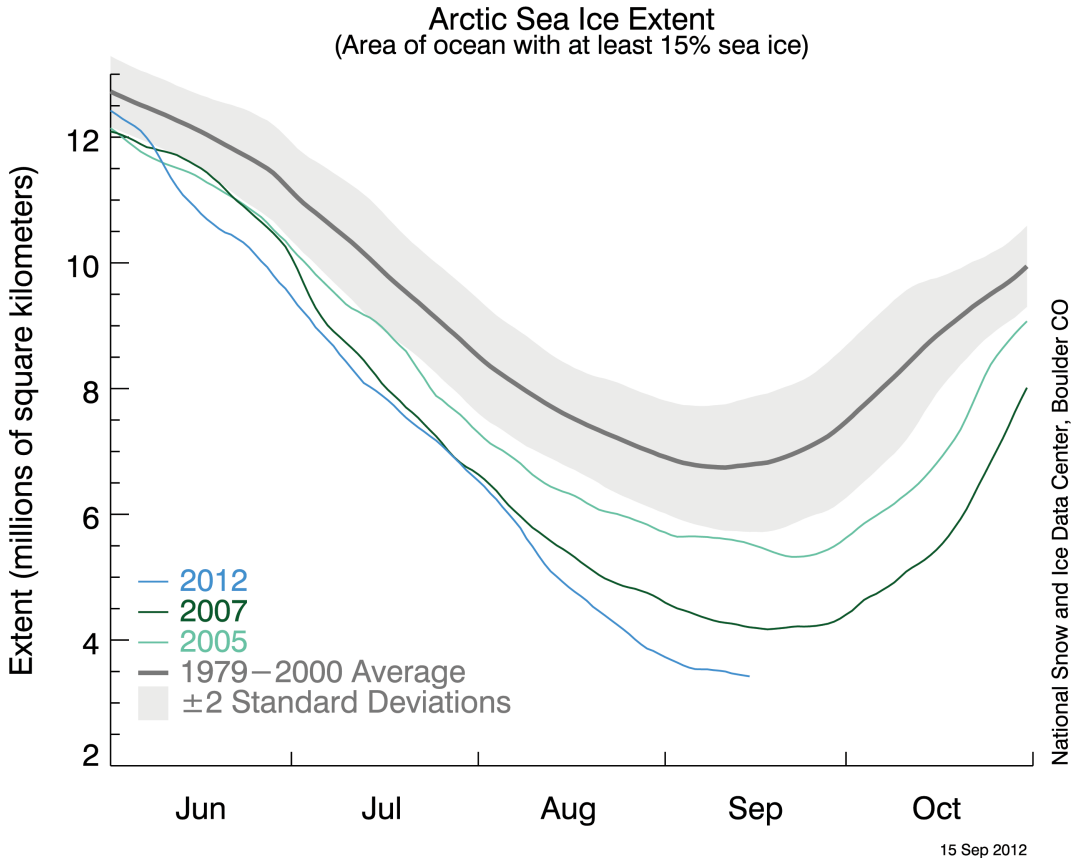

Figure 2.1 Extent of Arctic sea ice (in millions of km^2) for record-breaking ice minima years 2012, 2007, and 2005 versus the 1979 – 2000 average sea ice extent [From *NSIDC* 2012].

The reductions in sea ice areal extent observed are consistent with overall reductions in Arctic sea ice volume. Sea ice is becoming increasingly young and thin [*Maslanik et al.*, 2007, 2011; *Kwok et al.*, 2009; *Comiso* 2012] which makes it more susceptible to melting throughout the spring and summer months when air temperatures warm and the amount of solar radiation in the polar region increases [*Ngheim et al.*, 2007; *Lindsay et al.*, 2009]. Unsurprisingly, following the 2007 record-low sea ice extent minima, the January 2008 multiyear ice extent (Figure 2.2d) was also extremely low [*Comiso* 2012]. The thicker, multiyear sea ice that does exist in recent years is primarily

concentrated on the North American side of the Arctic, north of the Canadian Arctic Archipelago (Figure 2.2). At the same time, the proportion of thin first-year ice, which has not survived through a melt season, is increasing. This thinner sea ice is more readily melted and transported by ocean currents and surface winds [*Stroeve et al.*, 2011; *Comiso* 2012]. Divergence as the sea ice is transported by winds and currents tends to spread out the sea ice, reducing the ice concentration and increasing the proportion of dark, open ocean, allowing for easier melting of the remaining sea ice [*Stroeve et al*., 2011]. The atmospheric conditions during the melt season and in preceding years influence the amount of sea ice able to survive the melt season.

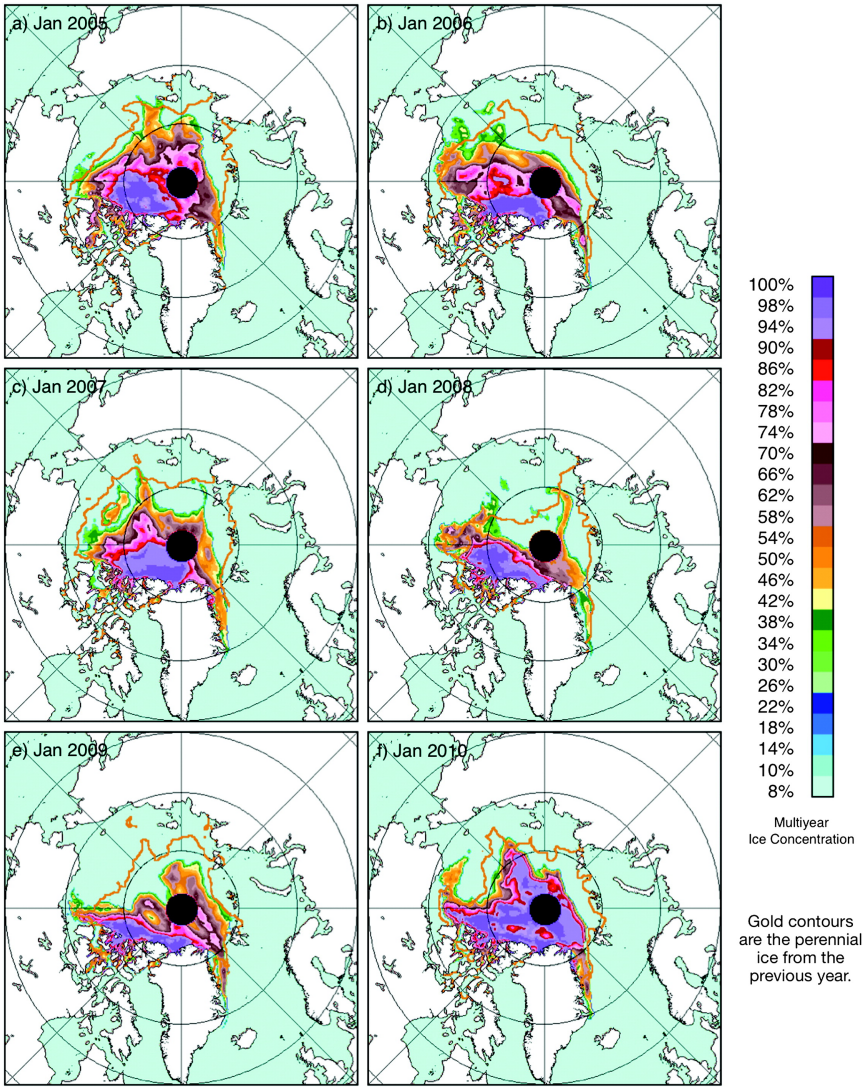

Figure 2.2 January multiyear ice concentration for years 2005 – 2010 [from *Comiso* 2012].

2.2 Sensitivity of sea ice to atmospheric conditions

At the regional scale, it has been shown that the annual low sea ice extent, which typically occurs in September, is influenced by several preconditioning factors that force a thinner sea ice pack at the beginning of the melt season. Further, atmospheric forcing through the spring and summer can increase melt and transport of the weakened, thin sea

ice through the melt season [*Rigor and Wallace*, 2004; *Maslanik et al.* 2007; *Deser and Teng*, 2008; *Ogi et al*., 2008]. These preconditioning factors can include the extensive loss of multiyear sea ice in previous years [*Ngheim et al*., 2007], overall thinning of the multiyear ice cover [*Kwok et al*., 2009], changes in winter sea ice motion and concentration [*Rigor et al*., 2002; *Deser and Teng*, 2008], and warmer temperatures hindering growth of sea ice extent and thickness in winter months [*Comiso et al*., 2008]. Reduced ice volume at the beginning of the melt season results in a greater potential for extremely low sea ice extent, even following an average melt season in terms of volume melted.

Summer weather conditions can compound the effects from preconditioning, producing record low sea ice extent minima such as occurred September 2007 [*Comiso et al*., 2008] and September 2012 [*Simmonds and Rudeva*, 2012; *Parkinson and Comiso*, 2013]. Compounding summer circulation influences can include: enhanced warm air advection via southerly surface winds, the wind-driven transport of ice northward away from the coastlines, and increased export of sea ice out of the Arctic completely [*Zhang et al*., 2000; *Comiso et al*., 2008; *Ogi et al*., 2008; *Lindsay et al*., 2009]. In fact, slight displacements in the relative location of surface low or high pressure systems can greatly change the local ice transport and influence local sea ice extent on a day-to-day basis [*Maslanik et al*., 2007]. Although these conditions can produce extremely low sea ice extents, *Tietsche et al*. [2011] show that the sea ice recovers quickly, on the order of two years time, following an anomalous event due to the quick exchange of excess heat flux in the Arctic. However, this point is argued in the literature as it is likely that the record sea ice extent minima in 2007 and in following years has increased heat in the ice-ocean

system such that it will be difficult for sea ice to grow enough during winter to be able to survive a summer melt season [*Comiso* 2012].

Research shows that declining sea ice thickness [*Nghiem et al.,* 2007; *Kwok et al.,* 2009] leaves the ice cover more susceptible to melt forcing conditions such as anomalous winds advecting sea ice away from the coast and increased ice transport out of the Arctic [*Ogi and Wallace,* 2007; *Comiso et al.,* 2008; *Lindsay et al.,* 2009]. Preconditioning of the ice cover (e.g. reduction in overall sea ice volume and loss of multiyear ice, increased proportion of thin, seasonal ice, etc.) [*Comiso et al.,* 2008] leaves the sea ice more vulnerable to episodic melting events during the summer such as occurred during "The Great Arctic Cyclone of August 2012," coined by *Simmonds and Rudeva* [2012].

2.3 The ice-albedo feedback loop

The surface albedo of sea ice changes throughout the year depending on the conditions of the ice surface. Fresh snow has a relatively high albedo of 0.846 [*Perovich et al.,* 2007] and typically falls on the sea ice through mid-May [*Curry et al.,* 1995]. As the snow cover ages, the albedo is reduced, nearing 0.8075 as the snow begins melting [*Perovich et al.,* 2007]. As the snow cover continues to melt and ponds form on the ice and leads open up, albedo quickly drops to and roughly stabilizes to a minimum albedo around 0.458 before freeze-up begins in August [*Perovich et al.,* 2007].

The albedo changes on the sea ice surface that occur when melt begins allow for increased absorption of solar radiation, which then increases the amount of melting that occurs in the ice-ocean system [*Curry et al*., 1995]. *Curry et al.* [1995] describe the mechanisms surrounding the ice-albedo feedback mechanism (Figure 2.3). Based on the conceptual diagram of the ice-albedo feedback mechanism, melting on the ice surface

and the formation of melt ponds and leads decreases the surface albedo of the sea ice (Figure 2.3). The decrease in surface albedo leads to an increase in surface temperatures, which then has a negative impact on snow cover, sea ice extent, and sea ice thickness. The result is a positive feedback loop in which melting leads to more heat in the ice-ocean system and continued decline in sea ice.

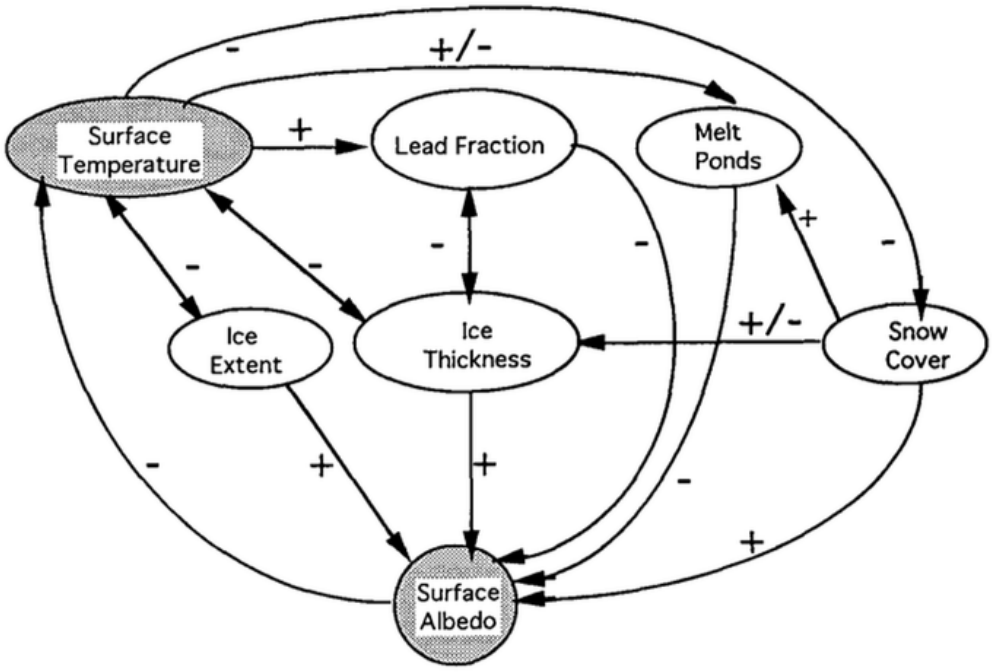

Figure 2.3 The ice-albedo feedback mechanism. Arrows indicate the direction of interaction. Positive (+) relationships result in an increase in both quantities. Negative (−) relationships result in the opposite response in quantity 2 when quantity 1 changes. Uncertain relationships or relationships that vary seasonally are indicated with a ± [from *Curry et al.,* 1995].

2.4 Passive microwave observations of sea ice melt

Several algorithms exist to determine the date of MO on Arctic sea ice from passive microwave satellite observations [e.g. *Smith*, 1998; *Drobot and Anderson*, 2001a; *Belchansky et al*., 2004; *Markus et al.*, 2009] and also from active microwave satellite

observations [e.g. *Winebrenner et al*., 1994; *Forster et al*., 2001; *Kwok et al*., 2003]. However, MO dates from passive microwave observations are largely consistent for a longer time period (1979 – present) than active microwave products.

The passive microwave methods identify the point in time at which liquid water becomes present in the snow cover on sea ice or in the absence of snow cover on the ice surface due to the higher emissivity of liquid water in the microwave portion of the electromagnetic spectrum [*Drobot and Anderson*, 2001a]. The day on which MO occurs is closely associated with near-freezing air temperatures, thus the onset of melting is a sensitive indicator of the near-surface atmospheric conditions. Due to the close relationship between melting and air temperatures the timing of MO can give information directly related to the larger scale weather conditions present giving rise to the surface air temperatures at the time of melt [*Anderson,* 1987].

Variations in the onset of melting through the satellite record can indicate differences occurring in spring weather systems [*Anderson and Drobot,* 2001; *Wang et al.,* 2011; *Stroeve et al.,* 2014]. In addition to inter-annual variability, there is high regional variability in the onset of melting in the Arctic [*Anderson,* 1987; *Belchansky et al.* 2004; *Stroeve et al.,* 2014]. Sub-regions within the Arctic have highly variable MO timing that is largely independent of the MO timing of other regions during a given year [*Anderson,* 1987]. This is likely due to variations in local atmospheric conditions and differences in geography for locations across the Arctic. For example, a region with open water (versus land or ice-locked area) upwind of the region of interest can influence the timing of melting due to the availability of ocean heat flux in ice-free ocean regions [*Anderson,* 1987; *Drobot and Anderson,* 2001b].

2.5 Implications of melt onset timing

Observations indicate the melt season is lengthening through changes in timing of the onset of melt in the spring and also by delaying the timing of freeze-up in the fall [*Belchansky et al*., 2004; *Stroeve et al.*, 2006, 2014; *Markus et al.*, 2009]. *Markus et al.* [2009] reports an increase in melt season length of 20 days for the Arctic between 1979 and 2007 due to earlier MO in the spring and later freeze-up in autumn. However, *Perovich et al.* [2007] has shown that an earlier date of MO on Arctic sea ice has a greater impact on the overall absorption of solar radiation in the ice-ocean system. Despite this larger influence of early MO on the surface energy budget in the Arctic, no direct correlation between the date of MO and September sea ice extent minima has been found [*Wang et al*., 2011]. Regardless, the date of MO in the Arctic signals the beginning of the melt season, and begins ice-albedo feedbacks, which continue to propagate through the remainder of the melt season [*Stroeve et al*., 2006; *Markus et al*., 2009].

The albedo reduction of the snow cover atop sea ice associated with the onset of melt, during the spring and early summer when the sun angle is higher, increases the absorption of solar radiation [*Perovich and Polashenski,* 2012]. Following an initial reduction in snow albedo, melt ponds form and seasonal ice melts completely allowing more radiation to be absorbed. Increasing absorption leads to delays in freeze-up and the continued thinning of the ice volume, compounding the loss of sea ice.

The date on which melting atop sea ice begins in the spring is, therefore, extremely important. The combination of higher incident solar radiation and reduced sea ice concentrations, resulting from melting in the ice pack, maximizes the effects of the

snow-ice albedo feedback [*Curry et al.,* 1995; *Perovich and Polashenski,* 2012; *Stroeve et al.,* 2014]. Since solar radiation in the Arctic gradually tapers off through the summer months following the solstice, *Perovich et al.* [2007] has shown that the timing of freeze-up in the fall does not impact the next year's ice conditions to the same extreme that early melt onset can influence the annual low September sea ice extent for the current year [*Perovich et al.,* 2007, *Stroeve et al.,* 2014]. The curves shown in Figure 2.4 indicate the increase in cumulative heat input into the ice-ocean system for each day that the length of the melt season is lengthened by changing the MO (black curve) or freeze-up date (white curve). The steeper slope of the MO curve indicates a larger net impact on heat input for a single day's increase in melt season length when earlier MO occurs versus a delay in the freeze-up date (Figure 2.4).

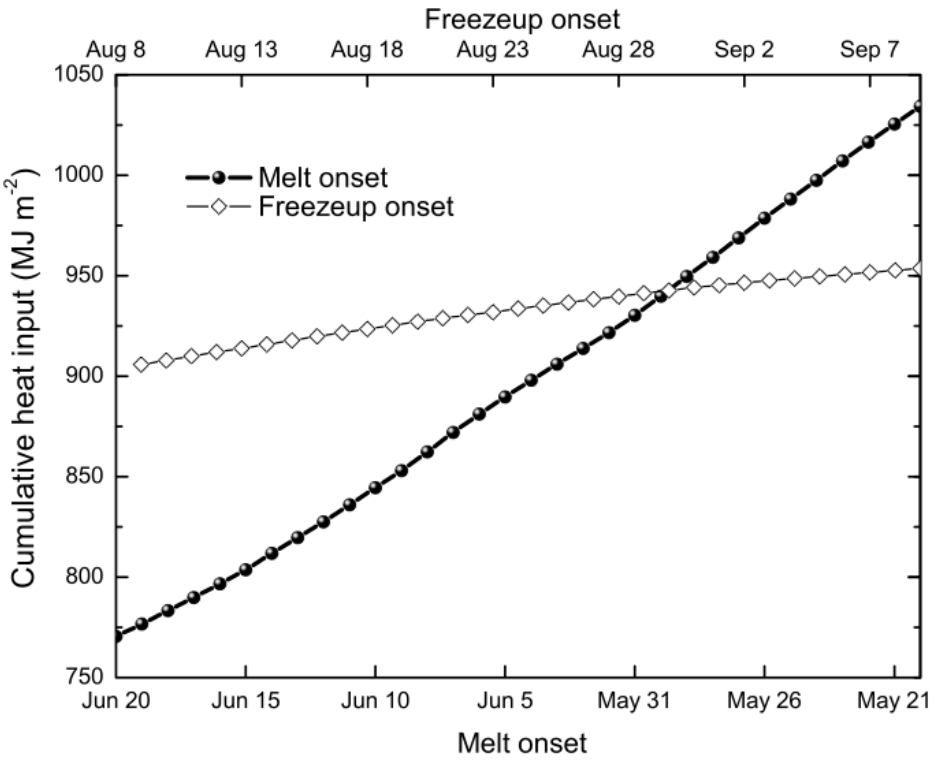

Figure 2.4 Effect of melt onset and fall freeze-up dates on the total solar energy absorbed by the ice-ocean system. The melt onset curve is relative to a constant 15 August freeze-up date and the freeze-up onset curve is relative to a constant 1 June melt onset date [from *Perovich et al.,* 2007].

While it is understood that weather conditions play a significant role in inducing the onset of melting on the sea ice cover by increasing air temperatures to the freezing point, little work has been done to examine the various patterns in synoptic scale weather events that cause the high variability in MO timing regionally and interannually. Given the several day time scale at which synoptic systems impact the sea ice surface in a given region, this type of analysis needs to be done on a day-by-day basis. Arctic sea ice is varying rapidly and is a sensitive indicator of climate change and the satellite record of melt onset timing can be used to further examine the drastic reductions in Arctic sea ice

seen over the last several decades and eventually improve predictability of summer sea ice conditions.

CHAPTER 3 – DATA AND METHODOLOGY

3.1 Melt onset dates from the Advanced Horizontal Range Algorithm

3.1.1 The AHRA

MO dates used in this study come from the Snow Melt Onset Over Arctic Sea Ice from SMMR and SSM/I-SSMIS Brightness Temperatures, Version 3 (V3) data set that is available for download from the National Snow and Ice Data Center (NSIDC) [*Anderson et al*., 2014]. The MO dates are calculated using the advanced horizontal range algorithm (AHRA) developed by *Drobot and Anderson* [2001a]. The data are available at a 25 km x 25 km resolution gridded array and are formatted using NSIDC's polar stereographic 304 x 448 pixel Northern Hemisphere grid [*NSIDC,* 2014]. The data are formatted as an annual view of the day of year (DOY) on which MO occurred at each grid pixel location. The newest version of the data (V3) have been reprocessed from the passive microwave brightness temperatures (Tbs) to improve the consistency of the data processing and extend the record of annual MO dates to cover the years 1979 – 2012 [*Bliss and Anderson*, 2014].

The AHRA utilizes horizontally polarized, daily average Tbs from the 19 (18 for SMMR) and 37GHz channels to determine the date of MO on Arctic sea ice and snow cover [Drobot and Anderson, 2001a]. Tbs were obtained from the SMMR sensor on board the NASA Nimbus-7 satellite platform and the series of SSM/I and the SSMIS from the Defense Meteorological Satellite Program's (DMSP) F8, F11, F13, and F17 platforms beginning in late 1978 through present day. The Tb data are inconsistent in that SMMR Tbs were only collected every second day, while SSM/I and SSMIS Tbs are

available daily (Table 3.1). Prior to the calculation of MO dates, the Tbs from different sensors are intercalibrated through time using linear regression coefficients determined from sensor overlap areas using DMSP F8 as the baseline sensor [*Jezek et al.,* 1991; *Abdalati et al.*, 1995; *Stroeve et al.*, 1998; *W. Meier Pers. Comm*., 2011].

Table 3.1 Temporal Coverage of Passive Microwave Sensors

Platform	Sensor	Start Date	End Date	Temporal Resolution
NASA Nimbus-7	SMMR	1979	20 Aug 1987	Every second day
DMSP F8	SSM/I	1988	1991	Daily
DMSP F11	SSM/I	1992	1995	Daily
DMSP F13	SSM/I	1996	2007	Daily
DMSP F17	SSMIS	2008	2012	Daily

The onset of melting in the spring occurs when the transition point between cold, wintertime conditions when sea ice is covered by dry snow, and when the sea ice and overlying snow pack become wet due to diurnal temperature swings or transient weather events that cause the air temperatures to rise above 273° K [*Livingstone et al*., 1987]. During this transition period that occurs at MO, the air temperatures can continue to fluctuate above and below the freezing point and daily average air temperatures can still be below 273° K [*Livingstone et al*., 1987]. The AHRA method identifies the increase in Tbs that occur when liquid water is introduced in the snowpack atop the sea ice and increases the emissivity of the surface in the passive microwave channels [*Kunzi et al*., 1982; *Livingstone et al*., 1987; *Drobot and Anderson*, 2001a].

To determine the date of MO for a given year, the AHRA tracks the difference between the 19 (18 GHz for SMMR Tbs) and 37 GHz horizontally polarized Tbs at a given point (the horizontal range or HR) on a daily basis [*Drobot and Anderson*, 2001a]. If the HR for the day is > 4.0 K it is assumed that wintertime conditions exist at the point and no MO is detected. If the HR for the day is < −10.0 K then liquid water is likely

present in the snowpack, causing a greater increase in the 37 GHz channel relative to the 18/19 GHz channel, and the date is recorded as the day of melt onset. Once a MO date is assigned at a pixel, the algorithm ignores the pixel for the remainder of the year.

If the HR falls between −10.0 K and 4.0 K, the 10 days prior and 9 days following the date in question are tested. In this stage of the algorithm, two values are calculated: (1) the minimum HR from the 10 days prior is subtracted from the maximum HR for the 10 days prior and (2) the minimum HR from the 9 days following is subtracted from the maximum HR in the 9 days following. The difference between min and max HR before and after the date being tested, are compared. If the difference between Tbs during the periods prior to and following the day in question is > 7.5 K a melt onset date is assigned. If this value is < 7.5 K no melt date is determined and the algorithm continues to the next day. During the testing stage of the algorithm, a difference (> 7.5 K) between the values prior to and following the date indicates a change in the time series of daily Tbs, thus the AHRA determines that MO has occurred. A MO date is calculated once per year at each pixel. The use of the time series window surrounding the day makes the AHRA insensitive to spurious Tbs and weather interference [*Drobot and Anderson*, 2001a].

3.1.2 Masking in the melt onset date data set

For the newest version of the data set (V3) used in this work, some changes to the processing were made in addition to updating the record of annual MO dates through the 2012 melt season [*Anderson et al.,* 2014]. The previous version of the data set (version 2) was masked in such a way that a MO date was calculated only at those locations where a MO date could be calculated for every year in the 20-year period 1979 – 1998 [*Drobot*

2000]. This climatology mask was static and determined the pixels for which a melt date was calculated every year. The new data set (V3) no longer uses a static mask; instead, the MO dates are calculated for locations determined to be sea ice covered at the beginning of each melt season. The melt dates in a given year are calculated for pixel locations where sea ice concentration is 50% on one or both of the first 2 days with Tb data in March. The sea ice concentration data used for the mask are Goddard merged sea ice concentrations available as part of the NOAA/NSIDC Arctic Sea Ice Climate Data Record [*Meier et al.*, 2013]. The Goddard merged sea ice concentrations are based on an algorithm that utilizes a combination of sea ice concentrations from the Bootstrap and NASA Team sea ice concentration algorithms. The beginning of March is used to represent full sea ice extent, since early March roughly corresponds to the annual maximum Arctic sea ice extent (e.g. *Parkinson and Comiso* [2013]). The first 2 days of data in March are used to account for days on which sea ice concentrations may be missing. Tbs were collected every second day during SMMR (1979 – 1987) years (Table 3.1); therefore, the sea ice concentrations used to create the ice mask for the MO dates data set may include 2 days during the period 1–5 March in each year.

Since the sea ice mask is no longer static, the sea ice locations (especially along the ice edge) that experience MO throughout the melt season fluctuate from year to year. Additionally, differences in the orbit path and swath width between the SMMR and SSM/I-SSMIS sensors, result in diameter changes of the data gap surrounding the North Pole (known as the pole hole). The version 2 climatology mask eliminated the differences between pole hole diameter that occur throughout the data record; however, the reduction in diameter increases the amount of sea ice area for which MO is calculated,

thus, increasing useable MO data for analyses over smaller temporal subsets of the data record. Version 2 of the data set included a 2-pixel buffer that eliminated coastal sea ice locations where possible uncertainties in the Tbs from land–ocean spillover can occur. Newer versions of the Tb data have now corrected for this spillover uncertainty [*Cavalieri et al.*, 1999]; therefore, the buffer is no longer used for V3.

3.2 Melt onset date methodology and sea ice regions

All statistics reported in this work are calculated only for pixel locations where a MO date exists in all 34 years of the data record. The sea ice locations (indicated by color) in Figure 3.1 show the MO date climatology mask used in the calculation of statistics. Pixel locations in white do not have a MO date for one or more years and are excluded. Statistics are calculated for all of the Arctic sea ice cover (hereafter called the Arctic Region) and for smaller sub-regions that divide the Arctic into common geographic regions (Figure 3.1). Boundaries between sub-regions are indicated by differing colors in Figure 3.1. The regional boundaries used here are the same as used by *Meier et al.* [2007] except that sea ice locations in the Baltic Sea are included in the V3 data set. These regional boundaries are also similar to those of other works including *Parkinson et al.* [1999] and *Markus et al.* [2009] except that the region mask used here divides regions within the Arctic Ocean into smaller seas. The sea ice areas that remain following the application of the climatology mask for each region (in km^2) are presented in Table 3.2. The area for the Arctic Region is the area sum of all 15 sub-regions shown in Figure 3.1.

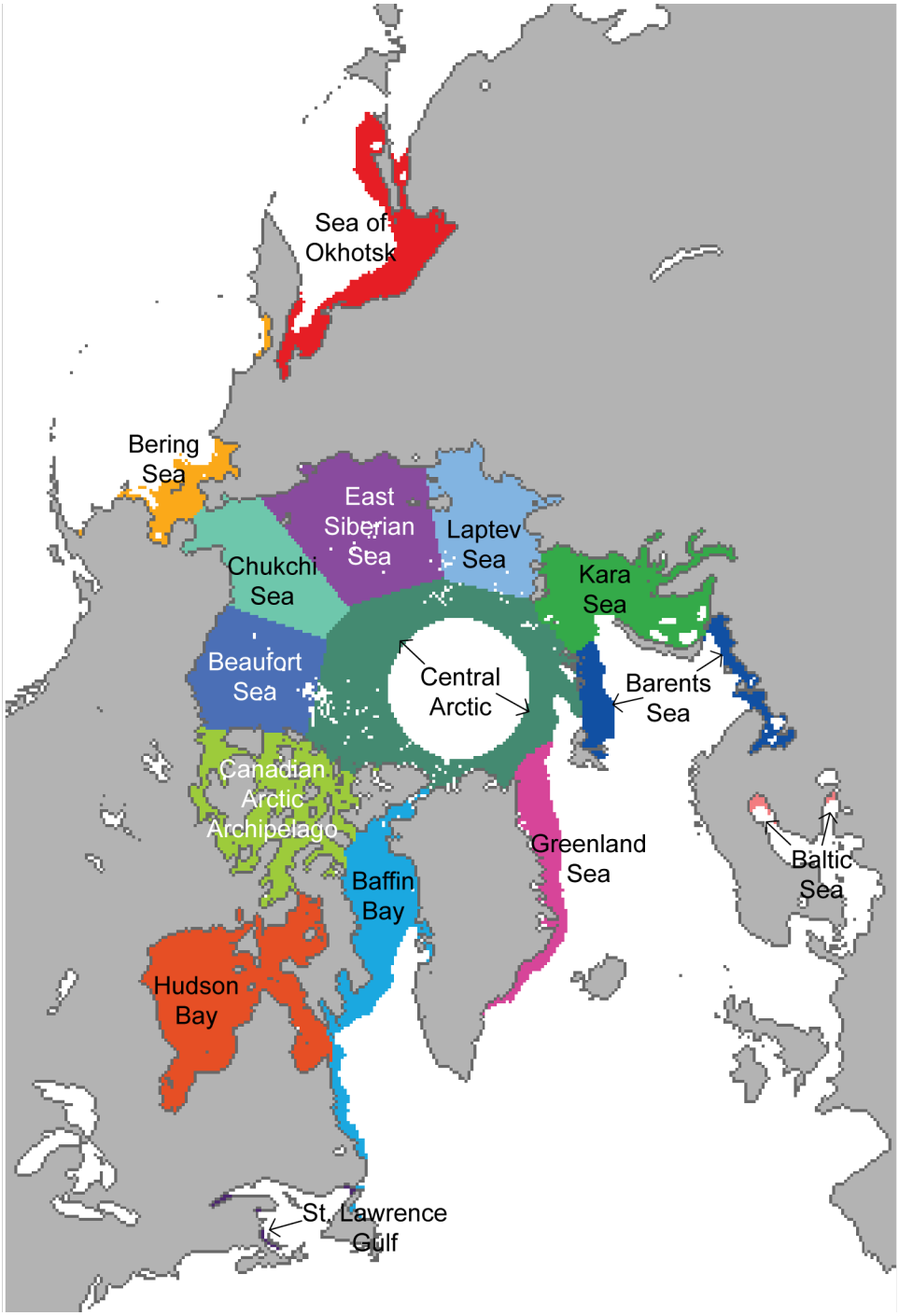

Figure 3.1 Map illustrating region boundaries and sea ice locations used in the analysis of annual MO area accumulations. All sea ice locations represented here are included in statistics and figures for the Arctic Region.

Table 3.2 Arctic Region Areas

Region	Area (10^5 km^2)
Arctic Region	110.0
Arctic Ocean Region	87.5
Barents Sea	3.5
Kara Sea	8.3
Laptev Sea	8.4
East Siberian Sea	12.6
Chukchi Sea	8.2
Beaufort Sea	9.0
Canadian Archipelago	7.4
Central Arctic	17.9
Baffin Bay	8.2
Greenland Sea	4.0
Bering Sea	2.7
Sea of Okhotsk	6.3
Hudson Bay	13.3
Baltic Sea	0.2
St. Lawrence Gulf	0.1

For this work, the MO dates for the 1979 – 2012 study period are examined for three different regional groupings: (1) the Arctic Region, (2) the Arctic Ocean region, and (3) the larger sub-regions of the Arctic indicated below (Table 3.3). The Arctic Region consists of all sea ice locations remaining following the application of the climatology mask shown in Figure 3.1 (i.e. all sea ice locations shown in Figure 3.1 and sub-regions listed in Table 3.3). The Arctic Ocean region consists of the collection of Arctic sub-regions including: the Barents, Kara, Laptev, East Siberian, Chukchi, Beaufort, and Greenland Seas; the Canadian Arctic Archipelago; the Central Arctic region; and Baffin Bay (Table 3.3, Figure 3.2). The Arctic Ocean Region consists of the larger, centrally located sub-regions with relatively high variability in MO timing and excludes sub-regions farther south where MO timing is typically early and less variable than the land-locked sub-regions of the north [*Bliss and Anderson*, 2014]. All regional analyses in the

following chapters will focus on the sub-regions where enough grid points remain for a more robust analysis. The Baltic Sea and St. Lawrence Gulf regions are very small, representing 0.2 x 10^5 km^2 and 0.1 x 10^5 km^2 respectively (Table 3.2). The Baltic Sea and St. Lawrence Gulf regions are included in calculations for the Arctic Region for the sake of completeness; however, they will not be discussed in any detail in the following chapters (Table 3.3).

Table 3.3 Listing of Arctic Sub-regions Included in the Arctic Region, Arctic Ocean Region, and Regional Analyses

Sub-Region	Arctic Region	Arctic Ocean Region	Regional Analysis
Barents Sea	X	X	X
Kara Sea	X	X	X
Laptev Sea	X	X	X
East Siberian Sea	X	X	X
Chukchi Sea	X	X	X
Beaufort Sea	X	X	X
Canadian Arctic Archipelago	X	X	X
Central Arctic	X	X	X
Baffin Bay	X	X	X
Greenland Sea	X	X	X
Bering Sea	X		X
Sea of Okhotsk	X		X
Hudson Bay	X		X
Baltic Sea	X		
St. Lawrence Gulf	X		

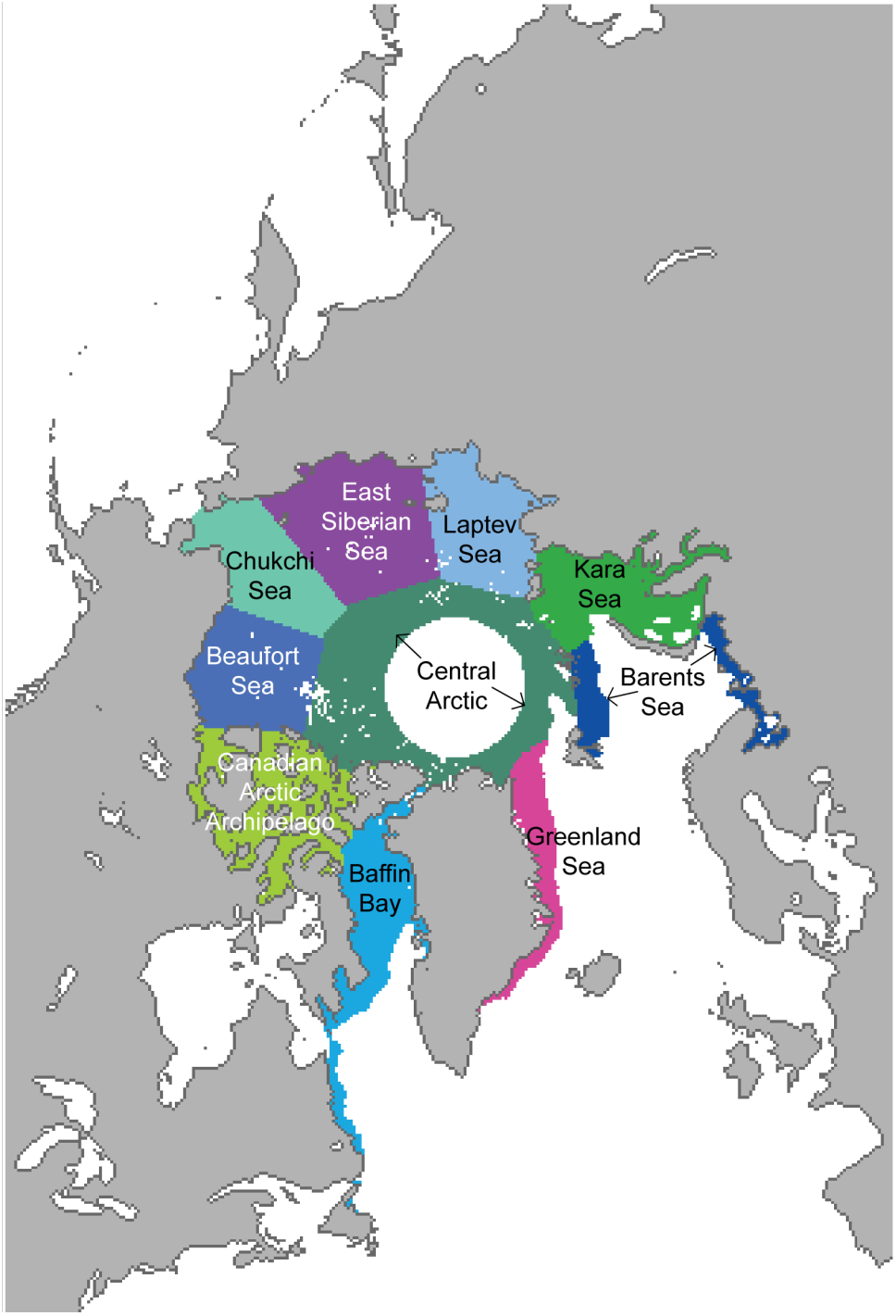

Figure 3.2 Arctic Ocean sub-regions.

For this work, the annual MO date maps from the V3 data set are partitioned into a daily area of MO based on the climatology mask shown in Figure 3.1. Daily MO area

time series for each year in the data record are generated by scaling the sum of pixel point locations experiencing MO on each day of the melt season by the grid resolution of the MO date data (25 km x 25 km). This calculation results in a time series describing the temporal patterns in the area (in km^2) of sea ice for each melt season (discussed in Chapter 5). The spatial variability in MO area on a daily basis is examined by mapping the pixel locations experiencing MO on a day-by-day basis (discussed in Chapter 6). Finally, the interannual variability in MO area is addressed by accumulating daily MO areas through each melt season for regional comparison in Chapter 7.

3.3 Atmospheric data

The influence of atmospheric conditions leading to MO for the Arctic Ocean sub-regions is assessed by comparing the spatial patterns in daily MO areas (Chapter 6) with near-surface data from reanalysis products. Synoptic scale weather patterns are assessed over the Arctic Ocean sub-regions when large daily areas of MO occur since the timing of MO is closely related to the point in time when air temperatures reach the freezing point. Cyclonic activity has the potential to raise air temperatures via advection of warmer air and trapping of longwave energy by cloud cover; thus, three daily mean parameters are used to characterize the near-surface atmosphere at the time of an increase in MO area on a day-by-day basis including: mean sea level pressures (MSLP), 925 hPa air temperatures, and 10 m wind vector magnitudes. Reanalysis products used include data from the NASA Modern-Era Retrospective analysis for Research and Applications (MERRA) project [*Reinecker et al.*, 2011], NCEP – DOE Reanalysis II (R2) project [*Kanamitsu et al.,* 2002], and the NCEP/NCAR Reanalysis Project (R1) [*Kalnay et al.,* 1996].

Surface energy budgets over the ice-covered polar-regions in the reanalysis products are plagued by problems related to overly simplistic physical parameterizations of sea ice albedo, cloud radiative properties, and the surface energy budgets over permanent land ice in the model [*Cullather and Bosilovich*, 2012]. The 2 m air temperatures in reanalysis data are strongly influenced by the modeled surface energy budget problems in polar regions; therefore, it is preferred to use 925 hPa air temperatures over sea ice locations to help reduce surface-based issues in reanalysis fields [*Serreze et al.,* 2003]. 925 hPa air temperatures are low enough to be representative of the near-surface conditions and anomalies at the 925 hPa level correlate well with surface temperature anomalies [*Serreze and Barrett*, 2008]. Note that because the 925 hPa level is at height above the surface, mean daily 925 hPa temperatures are expected to vary from actual surface temperatures and are not considered an exact representation of the temperatures at the surface when MO is occurring. As such, daily mean 925 hPa air temperatures need not reach 273 ºK for MO to occur on the sea ice surface.

The 925 hPa air temperatures and MSLPs used in this analysis are from the NASA MERRA IAU 3d assimilated state on pressure product and are available for download from the NASA Goddard Earth Sciences Data and Information Services Center (GES DISC) and the Global Modeling and Assimilation Office (GMAO) [*GES DISC*, 2015]. These MERRA data are available for the 1979 – 2012 record of MO dates and have a 1.25º x 1.25º horizontal resolution. Daily averaged 925 hPa air temperature and MSLP fields are used in the analysis of MO area. It is important to note that the MERRA data on pressure levels are not extrapolated downward below the height of topography.

Therefore the 925 hPa air temperature data from MERRA are not continuous fields and missing data occurs where land topography intersects the 925 hPa pressure level. However, missing data due to topography is restricted to areas over land only, and the MERRA 925 hPa air temperatures are continuous over ocean and sea ice locations.

Daily mean 10 m wind vector magnitudes are calculated from U and V wind vectors from the NCEP-DOE Reanalysis 2 Daily Averages product. The U and V wind data are available for download from the NOAA-ESRL Physical Sciences Division [*ESR-PSD*, 2015]. The data are currently available for 1979 – 2014 and are at a 2.5º x 2.5º horizontal resolution. These data, although at a coarser resolution than the NASA MERRA products, were chosen because the NASA MERRA product lacks a 10 m wind parameter. Therefore, in order to use a reanalysis parameter that corresponds with the standard level for surface wind observations a concession has been made in this case for reduced spatial resolution in the R2 data. In the special case where a long-duration melting event occurs (described in Chapter 6), composites of surface data from the NCEP/NCAR Reanalysis Project (R1) were obtained from the NOAA-ESRL Physical Sciences Division [*Kalnay et al.,* 1996; *ESR-PSD*, 2014]. These data include MSLP composites and anomalies, surface 2 m air temperature composites and anomalies, and surface wind vector magnitudes. The R1 data have a longer temporal coverage (1948 – present) and the same 2.5º x 2.5º horizontal resolution as the R2 data.

The atmospheric data from the various reanalysis parameters are used to describe the general synoptic conditions at times when melting is indicated in the daily MO areas presented in this work. The effects of relatively high and low pressures and the resultant wind directions on 925 hPa air temperatures over Arctic sub-regions are expected to

influence the temporal and spatial patterns in melting area that are present over the 1979 – 2012 data record.

CHAPTER 4 – CLIMATOLOGY OF MELT ONSET DATES 1979 – 2012: STATISTICS AND TRENDS

4.1 Annual melt onset dates

Annual maps of MO dates for the Arctic from the Snow Melt Onset Over Arctic Sea Ice (V3) dataset [*Anderson et al.*, 2014] summarize the timing of MO for each melt season during the 1979 – 2012 data record (Figure 4.1). The melt date at each pixel location represents the day from the first of the year (DOY) on which melting first began for the given year. Generally, the MO dates occur earlier in the year (warm colors) in the peripheral regions of the sea ice cover at lower latitudes where air temperatures are also generally warmer (Figure 4.1). The latest MO dates (cool colors) occur close to the North Pole (surrounding the 'pole hole') and in the northern reaches of the Canadian Arctic Archipelago where sea ice is generally thicker, multiyear ice (Figure 2.2). Considerable year-to-year variability in the timing of MO occurs regionally. This regional variability in MO dates is related to variability in the atmospheric conditions, as well as changes in the sea ice extent from year to year.

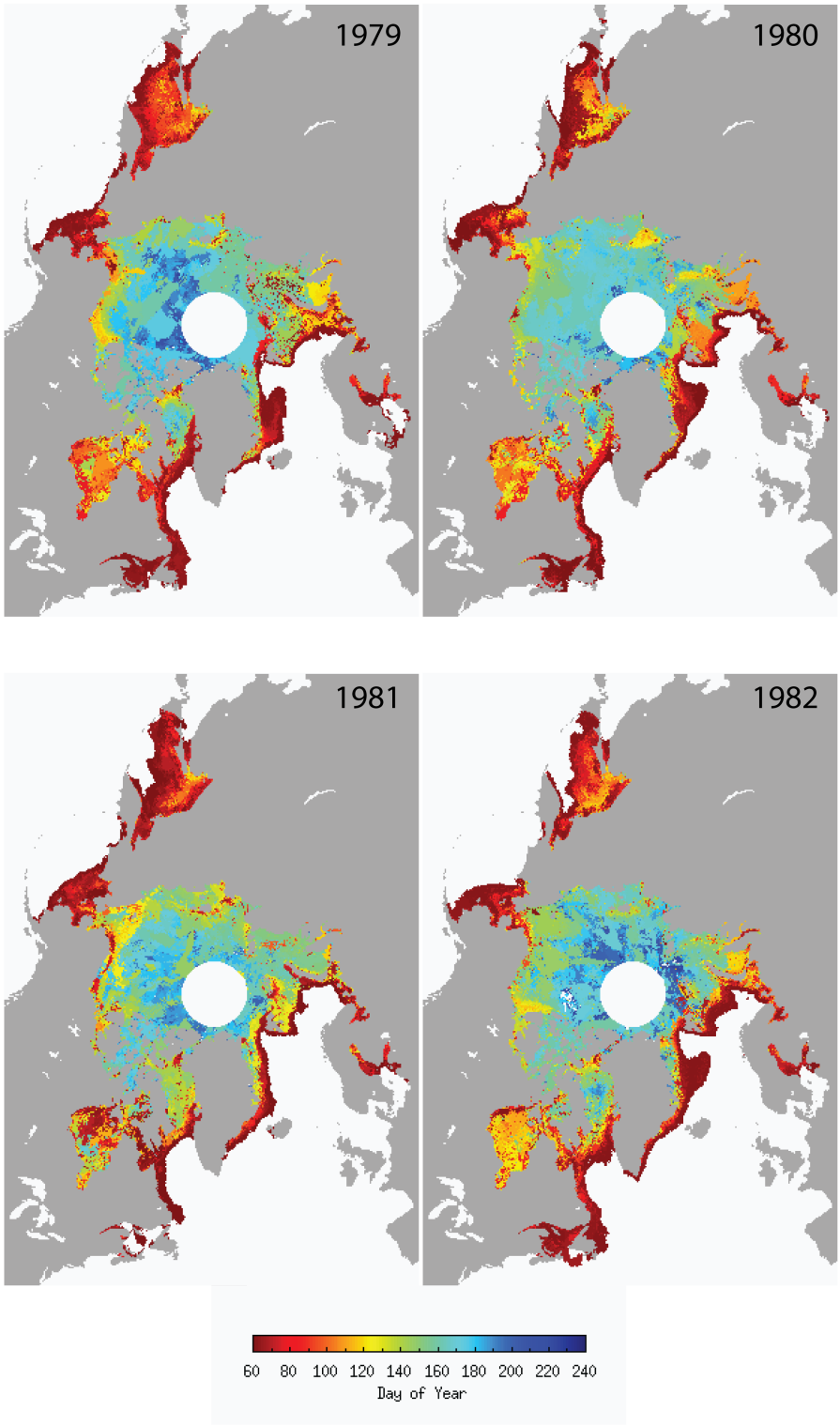

Figure 4.1 Annual melt onset date maps for 1979 – 2012 (maps available from *Anderson et al.,* 2014).

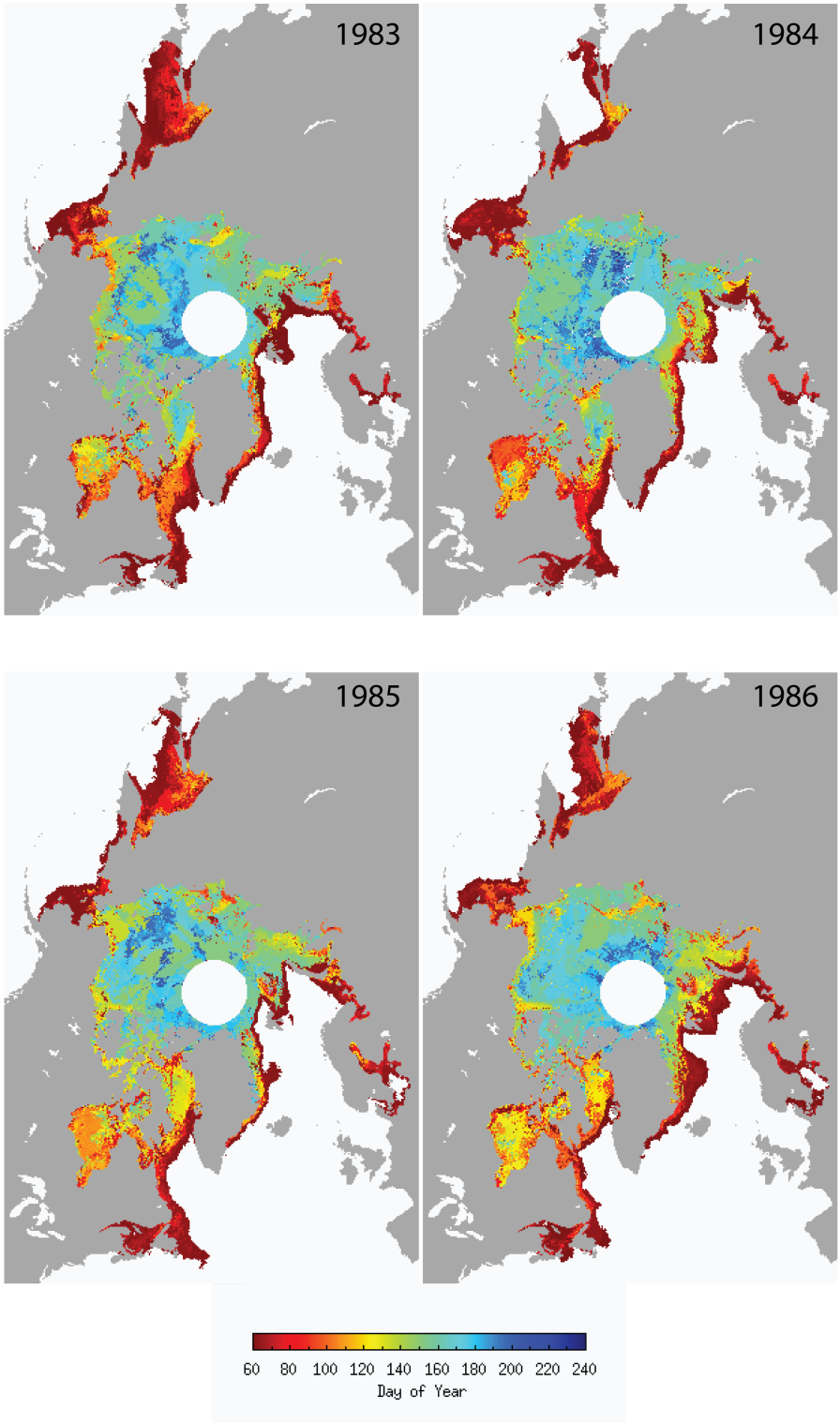

Figure 4.1 Continued.

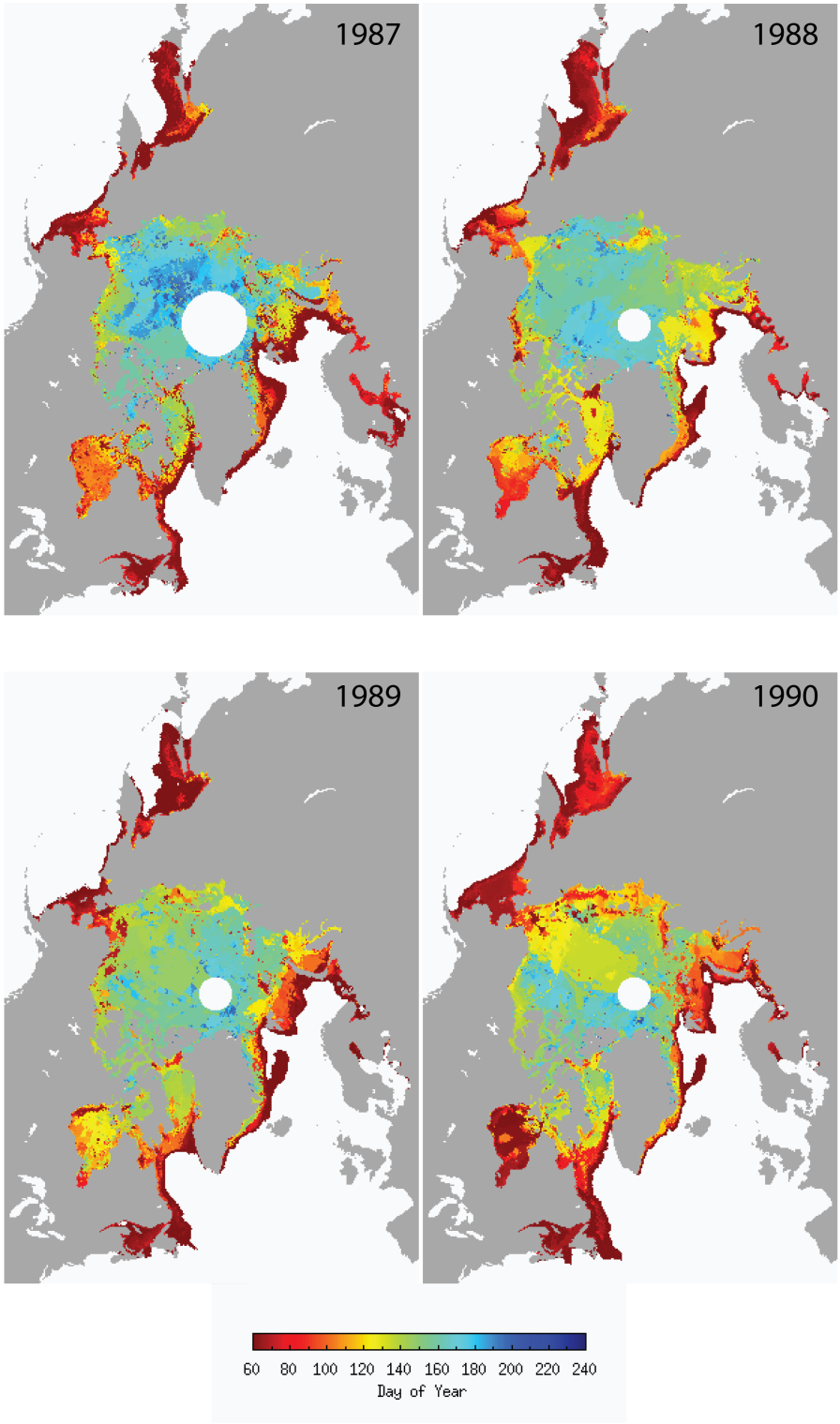

Figure 4.1 Continued.

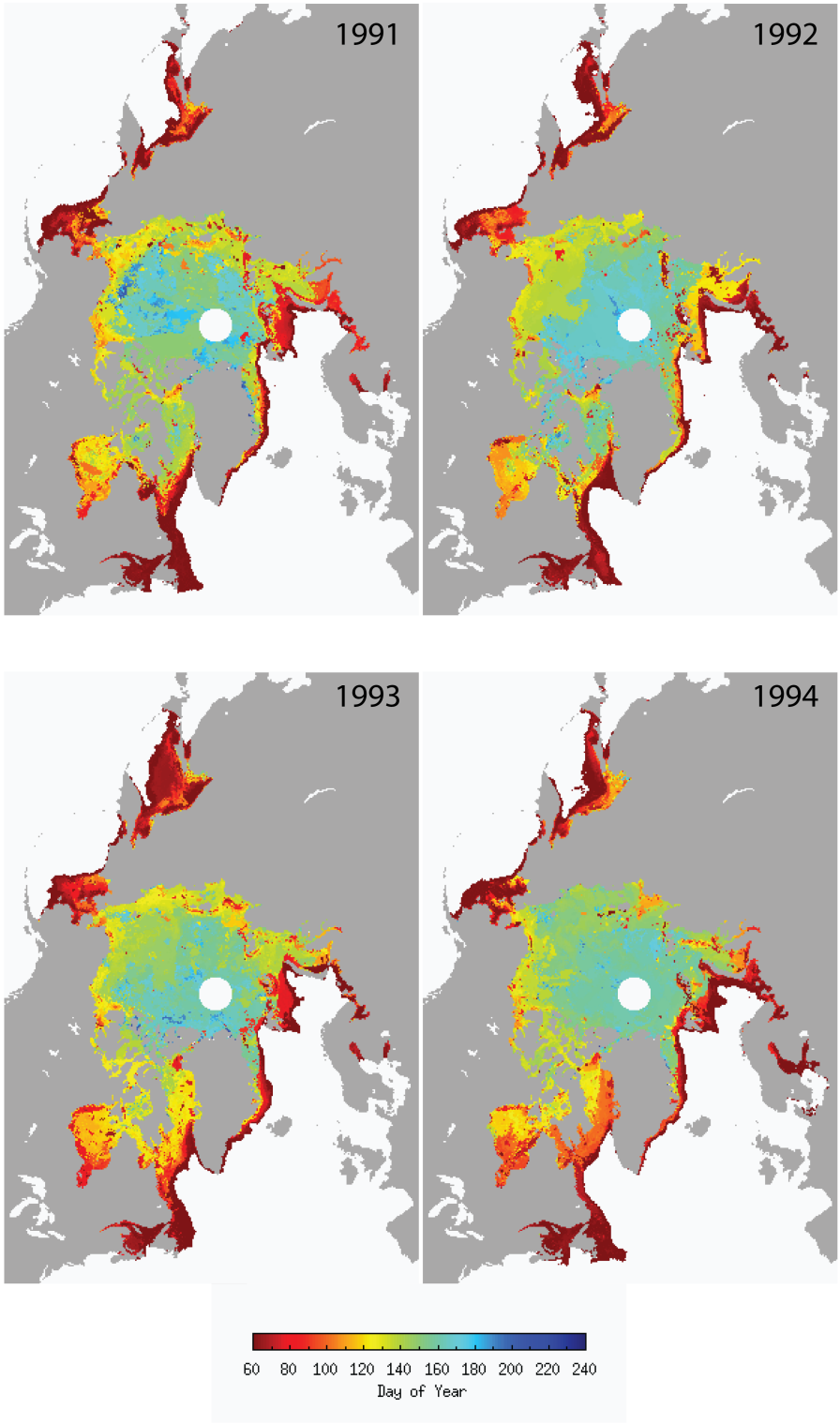

Figure 4.1 Continued.

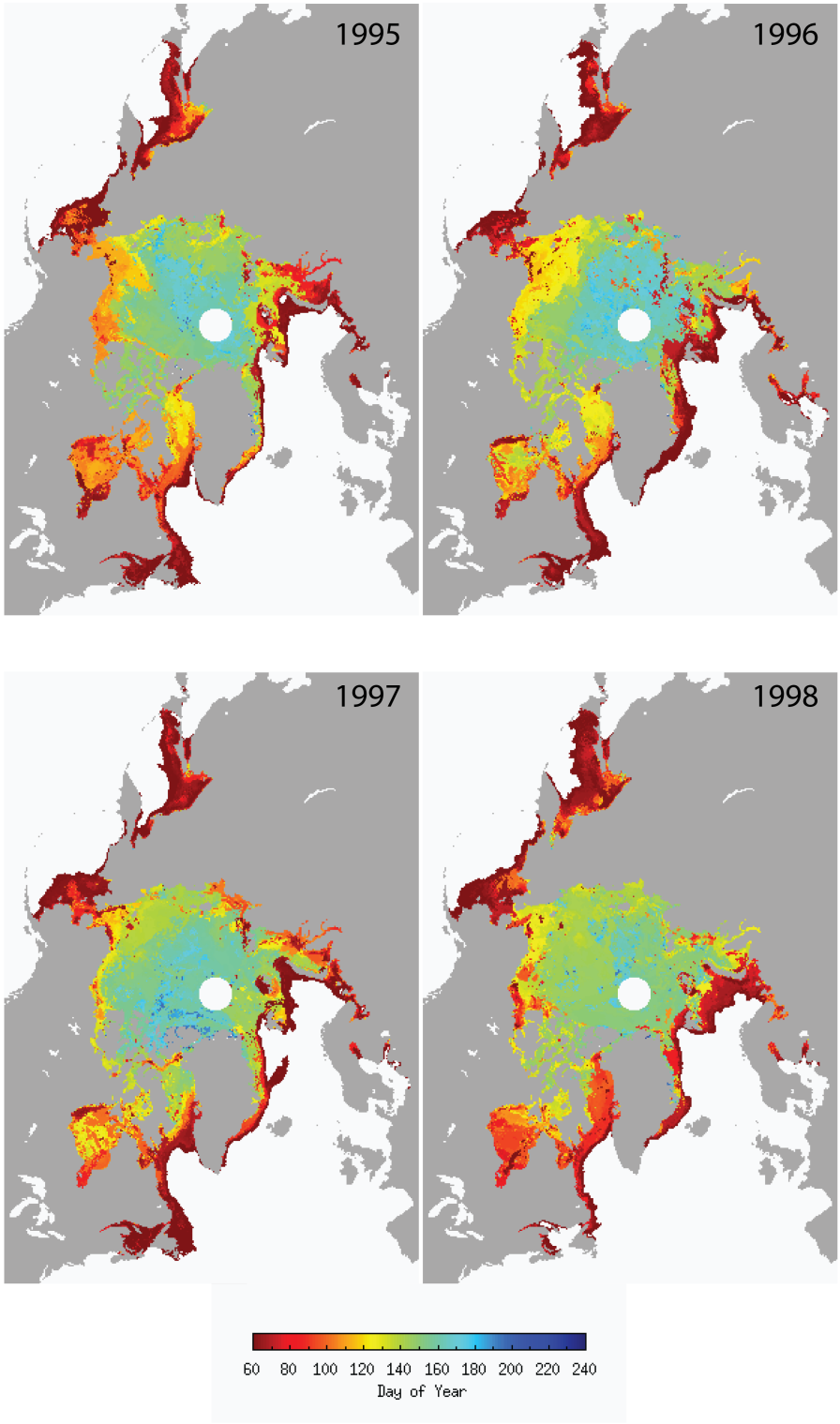

Figure 4.1 Continued.

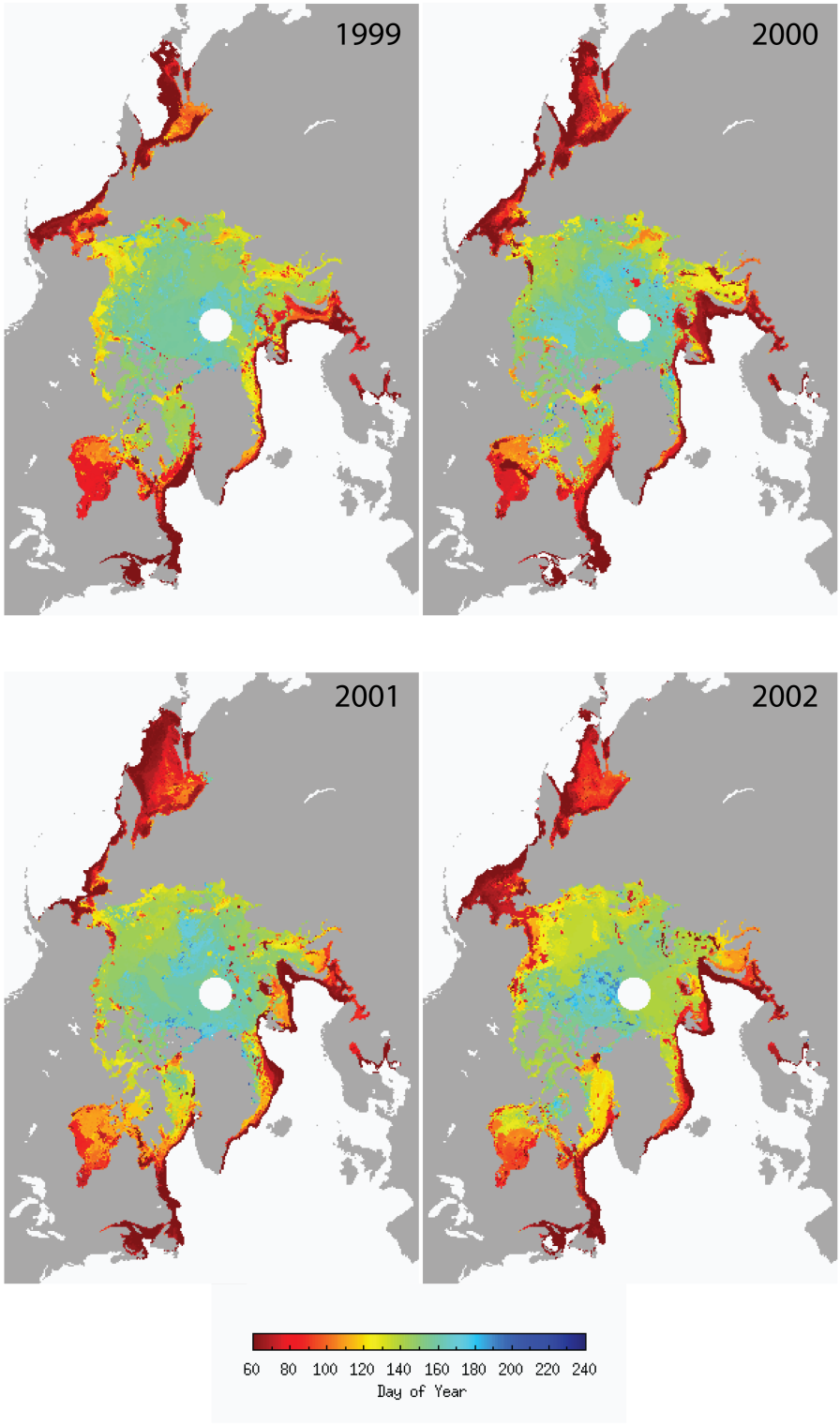

Figure 4.1 Continued.

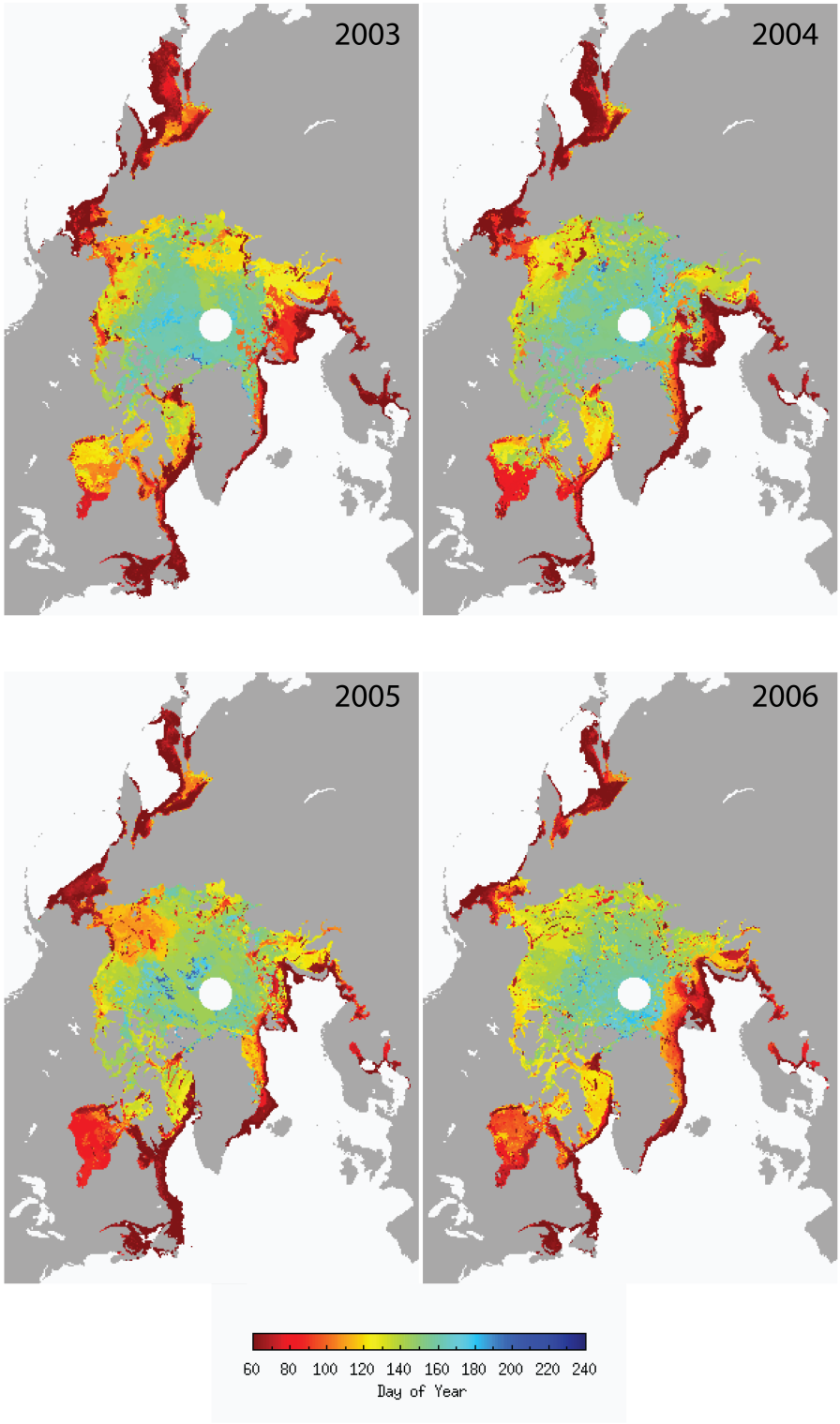

Figure 4.1 Continued.

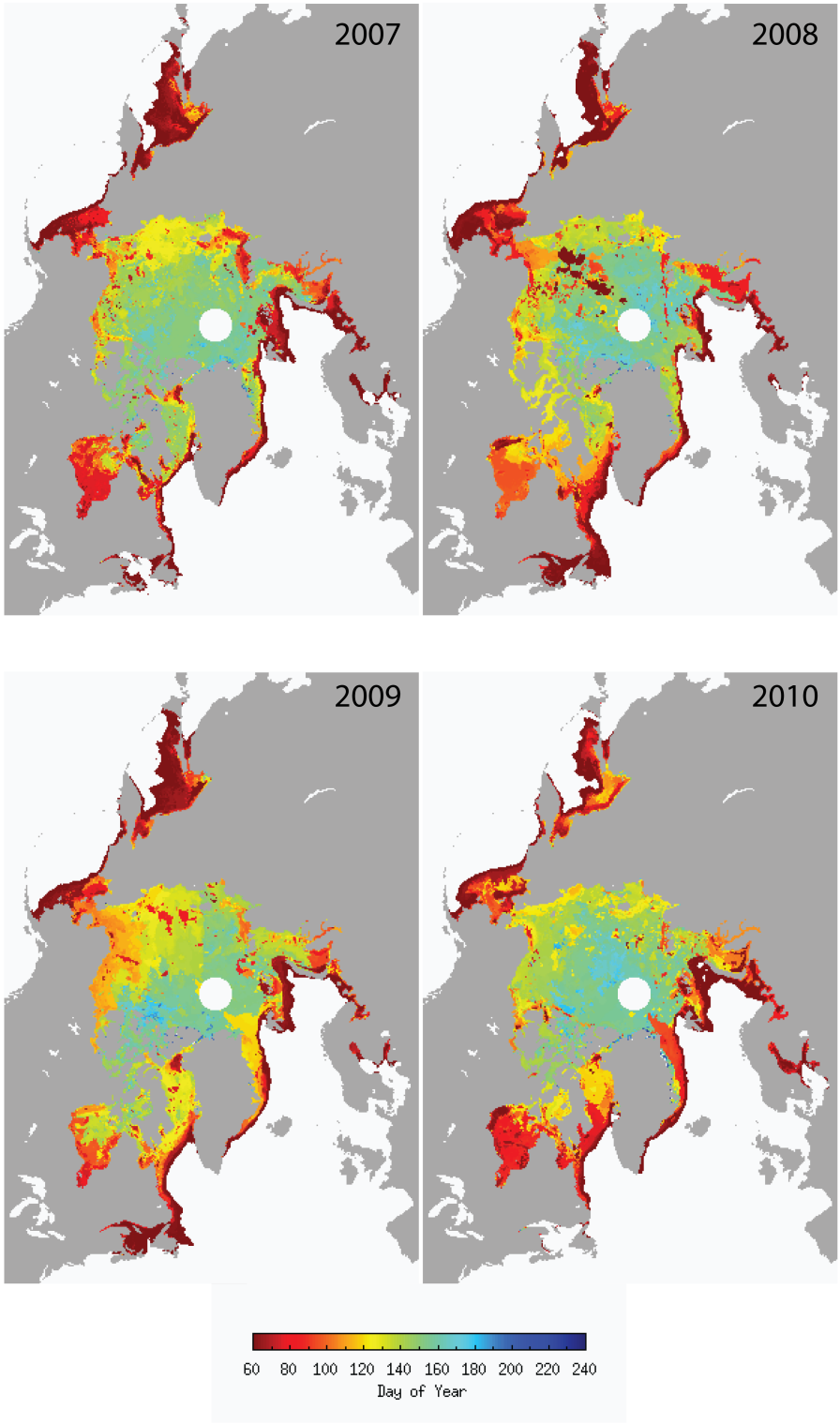

Figure 4.1 Continued.

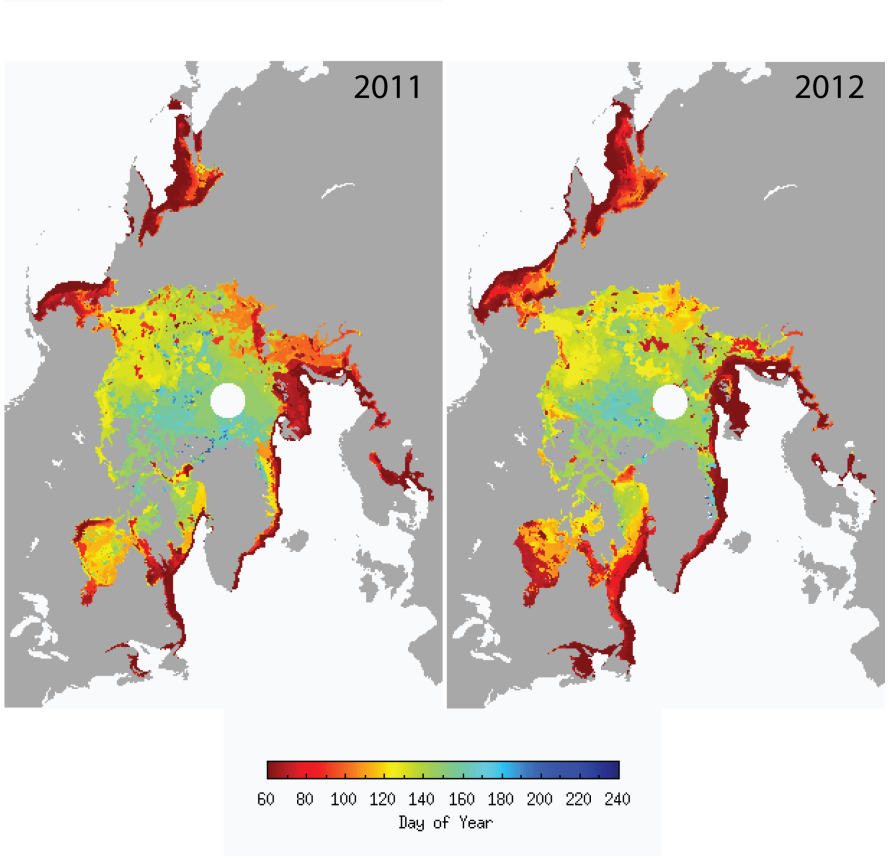

Figure 4.1 Continued.

Note that annual maps of MO dates (Figure 4.1) have a varying sea ice edge. Since MO dates are calculated over the sea ice extent at the beginning of the melt season (March), the area over which MO can be calculated fluctuates from year to year [*Anderson et al.,* 2014]. However, all statistics reported hereafter are calculated only over pixel point locations where a MO date exists for all 34-years in the record.

4.2 General melt onset date statistics

Mean MO dates for the Arctic Region during the 34-year data record vary greatly but systematically across the extent of sea ice cover (Figure 4.2). The mean date of MO for the Arctic Region is 13 May (132.5 DOY) with a standard deviation of ± 7.3 days

(Table 4.1). In general, the mean MO dates occur earliest at sea ice locations along the periphery of the sea ice edge and in the southernmost locations such as the Sea of Okhotsk, Bering Sea, Hudson Bay, Gulf of St. Lawrence, Greenland Sea, Baltic Sea, and Barents Sea (Table 4.1, Figure 4.2). For the Arctic Ocean sub-regions (Figure 3.2), the mean MO date is 22 May (141.9 DOY), 9 days later than the mean MO date for the whole Arctic Region (Table 4.1). Additionally, the mean earliest and mean latest MO date for the Arctic Ocean sub-regions occur later in the year than for the Arctic Region (Table 4.1). This difference between Arctic Region and Arctic Ocean sub-region means indicates a general latitudinal dependence on the timing of MO. By eliminating, the southerly, peripheral sub-regions from the analysis, the sub-regions at the highest latitudes (in the Arctic Ocean) tend to experience MO at a date later in the year. Further, the mean standard deviation of the Arctic Ocean is slightly larger than that of the Arctic Region (Table 4.1), indicating that the MO dates in the Arctic Ocean sub-regions are more variable than those locations at lower latitudes; however, the standard deviation of MO dates can be large in portions of these early-melting regions. Regions with larger standard deviations in mean MO date have larger variability in MO timing from year to year (Figure 4.3).

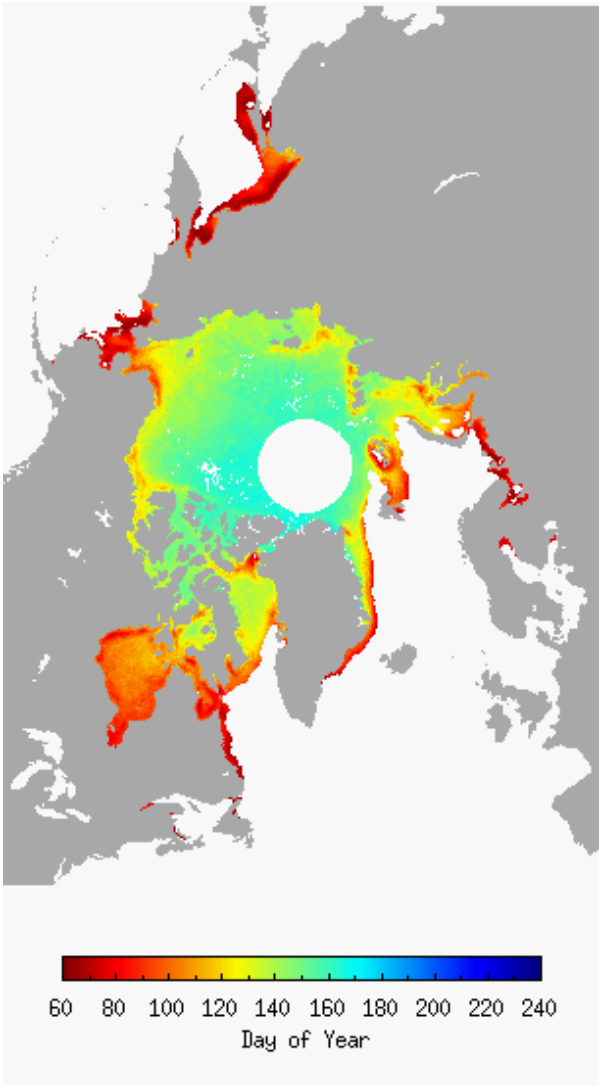

Figure 4.2 Mean melt onset dates for the 1979 – 2012 record (from *Anderson et al*. 2014).

Table 4.1 Mean Regional Melt Onset Date Statistics for 1979–2012

	Mean MO date (DOY)	Mean standard deviation (days)	Mean earliest MO (DOY)	Mean latest MO (DOY)	Mean range (days)
Arctic Region	13 May (132.5)	7.3	121.0	146.5	25.5
Arctic Ocean	22 May (141.9)	8.7	128.0	158.5	30.4
Barents Sea	4 April (93.9)	12.2	69.5	121.8	52.2
Kara Sea	11 May (130.5)	12.8	98.4	152.4	54.0
Laptev Sea	25 May (144.9)	11.7	115.9	167.1	51.2
East Siberian Sea	31 May (150.1)	14.5	127.4	174.8	47.4
Chukchi Sea	17 May (136.3)	12.7	112.6	160.6	48.0
Beaufort Sea	28 May (148.0)	9.9	130.1	165.3	35.2
Canadian Archipelago	29 May (149.0)	7.7	135.9	168.2	32.2
Central Arctic	10 June (160.9)	9.5	143.8	181.5	37.7
Sea of Okhotsk	22 March (80.8)	5.3	70.9	93.3	22.4
Bering Sea	21 March (79.9)	7.2	69.8	95.7	25.9
Hudson Bay	17 April (106.6)	8.6	89.2	125.0	35.8
Baffin Bay	1 May (120.6)	10.0	102.5	137.7	35.2
Greenland Sea	29 April (118.9)	11.1	96.3	135.0	38.7
Baltic Sea	20 March (78.8)	10.4	63.0	99.4	36.4
St. Lawrence Gulf	15 March (73.2)	6.4	62.1	91.6	29.4

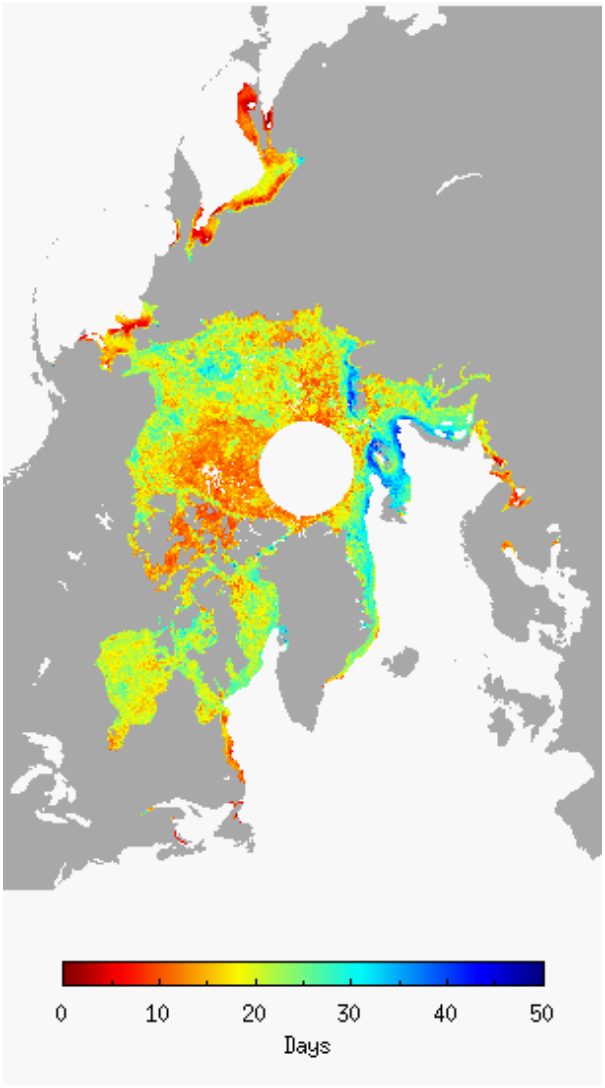

Figure 4.3 Standard deviation of melt onset dates for the 1979 – 2012 record (from *Anderson et al.* 2014).

The earliest MO dates during 1979 – 2012 occur at the beginning of the melt season, in early March, for most of the peripheral regions of the sea ice area (Figure 4.4). For portions of the Central Arctic, Canadian Archipelago, and the northern portion of the Beaufort Sea, the earliest MO dates do not occur until mid-late May. The earliest MO dates in other locations of the Arctic Ocean occur in late March and early April (warm colors in Figure 4.4). The latest MO dates in the record for much of the sea ice regions

within the Arctic Ocean occur during August, while the coastal regions of the Arctic Ocean typically have the latest MO dates near the end of May through June (Figure 4.5). Two distinct areas of the sea ice cover appear to have a small range (warm colors in Figure 4.6), (1) in the peripheral sea ice regions (including the Sea of Okhotsk, the Bering Sea, the Labrador Sea (in the Baffin Bay region), and the southern Barents Sea) and (2) the North American side of the Arctic including parts of the Central Arctic, the northern Beaufort Sea, and the Canadian Archipelago regions. The variability in MO dates described by both ranges and standard deviations for these locations is small; however, the timing of MO is distinctly different. In the southern, peripheral regions, where the sea ice is primarily composed of seasonal, first year ice, air temperatures warm to the melting point earlier in the year and early MO dates are observed. Conversely, sea ice in the Central Arctic is typically thicker, more compact, multiyear ice. Furthermore, air temperatures would warm later in the year than farther south, leading to the later mean MO dates observed.

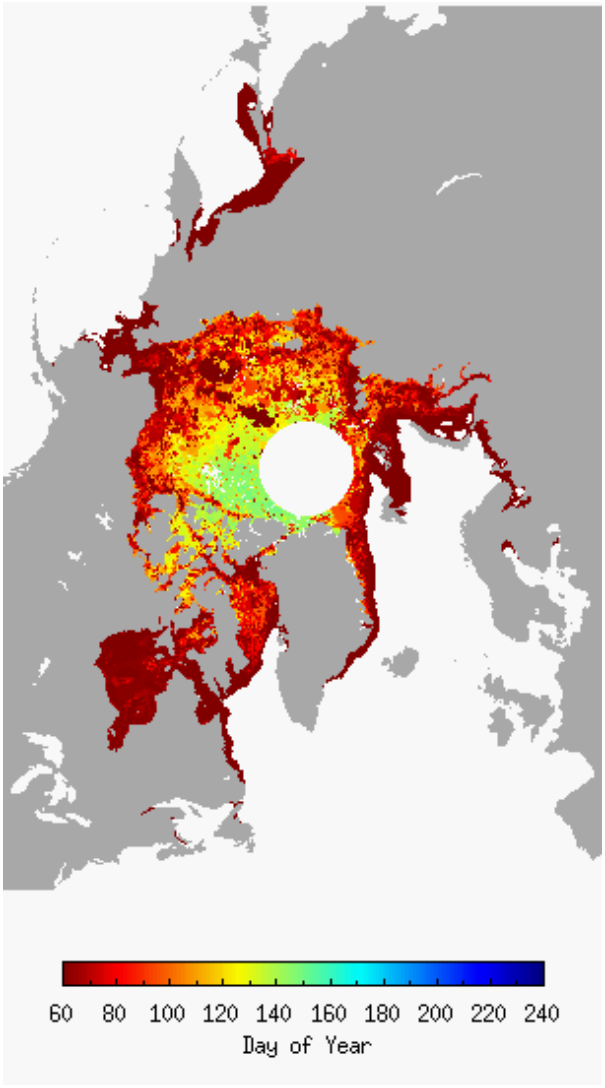

Figure 4.4 Earliest melt onset dates for the 1979 – 2012 record (from *Anderson et al.* 2014).

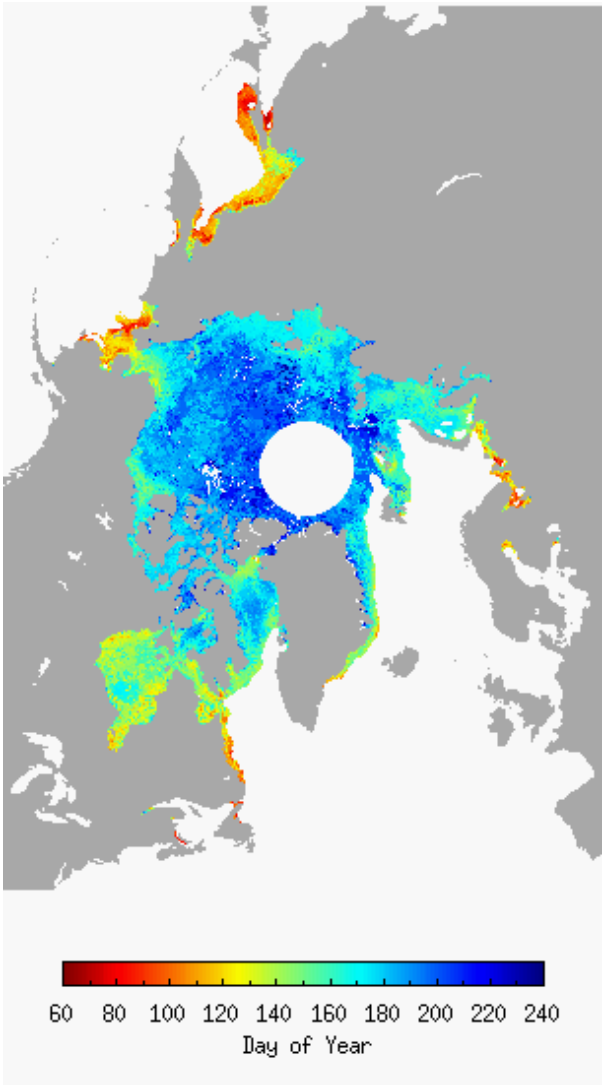

Figure 4.5 Latest melt onset dates for the 1979 – 2012 record (from *Anderson et al.* 2014).

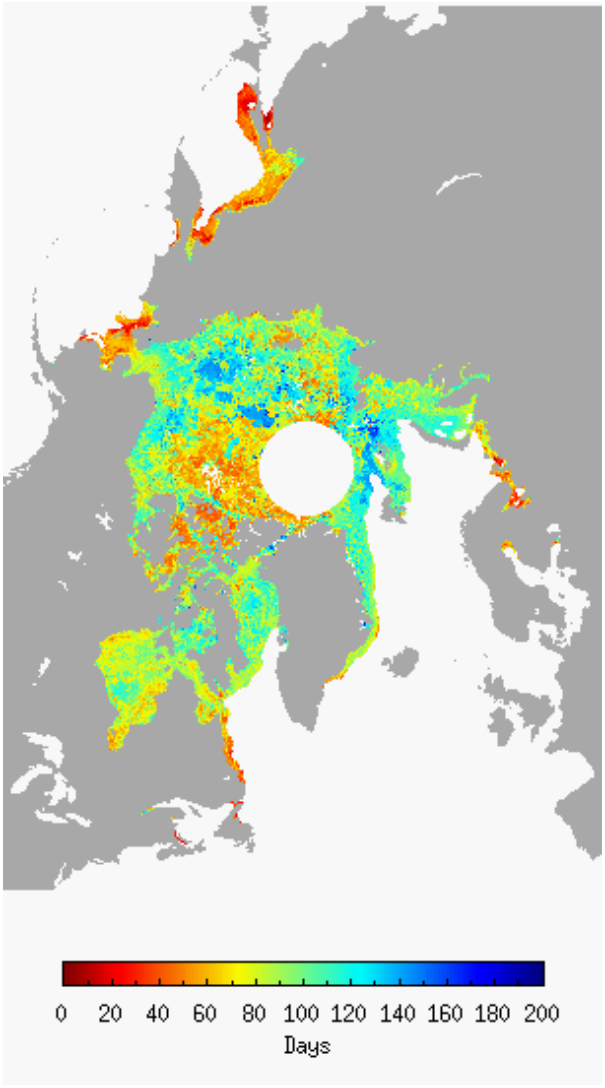

Figure 4.6 Range of melt onset dates for the 1979 – 2012 record (from *Anderson et al*. 2014).

The St. Lawrence Gulf and Baltic Sea regions have the earliest mean MO dates, occurring 15 March (73.2 DOY) and 20 March (78.8 DOY), respectively, although both areas are small (0.1 x 10^5 and 0.2 x 10^5 km^2) (Table 3.2). Other regions with relatively early mean MO dates (Table 4.1) are the Bering Sea, 21 March (79.9 DOY); the Sea of Okhotsk, 22 March (80.8 DOY); and the Barents Sea, 4 April (93.9 DOY). However, it is important to note that the early-melting sea ice in the Barents Sea is located in the

southern, coastal portion of the region, while the sea ice in the northern half of the Barents, adjacent to the Central Arctic region, melts at a later date (Figure 4.2). The other peripheral and southern regions including: Hudson Bay, Baffin Bay, and the Greenland Sea have a mean MO date which occurs in the latter half of April. The remaining regions are located within the Arctic Ocean and have mean MO dates that range from 11 May (130.5 DOY) in the Kara Sea to 10 June (160.9 DOY) in the Central Arctic region (Table 4.1).

4.3 Trends in melt onset

Decadal trends in MO are determined by applying a least squares linear regression fit line to the time series of annual mean MO dates for the Arctic Region and all sub-regions. Trends in the time series of annual mean MO dates indicate that MO is occurring earlier in the year for the majority of Arctic sea ice over the 1979 – 2012 data record (Figure 4.7). For the Arctic Region, a statistically significant trend (99% confidence level) of -6.6 days decade^{-1} exists, indicating that MO is occurring earlier in the year in recent years when compared to the years at the beginning of the data record. Statistically significant negative trends also exist for sub-regions of the Arctic Ocean including: the Barents, Kara, Laptev, East Siberian, Chukchi, and Beaufort Seas, and the Canadian Archipelago and the Central Arctic region (99% confidence level) (Figure 4.7). These trends range from -4.6 days decade^{-1} in the Canadian Archipelago to -11.8 days decade^{-1} in the East Siberian Sea. R^2 values vary, but are strongest for the Arctic Region and the Central Arctic where the R^2 value is at least 0.76 (Figure 4.7). Statistically significant trends also exist in the Bering Sea and Baffin Bay although at a 95% confidence level with weak R^2 values (Figure 4.7). Southerly, peripheral regions of the

sea ice where the mean MO dates occur earliest, as described in Section 4.2, tend to have very weak R^2 relationships and insignificant trends. Despite weak relationships, the trend is negative for nearly all of the peripheral regions (Figure 4.7).

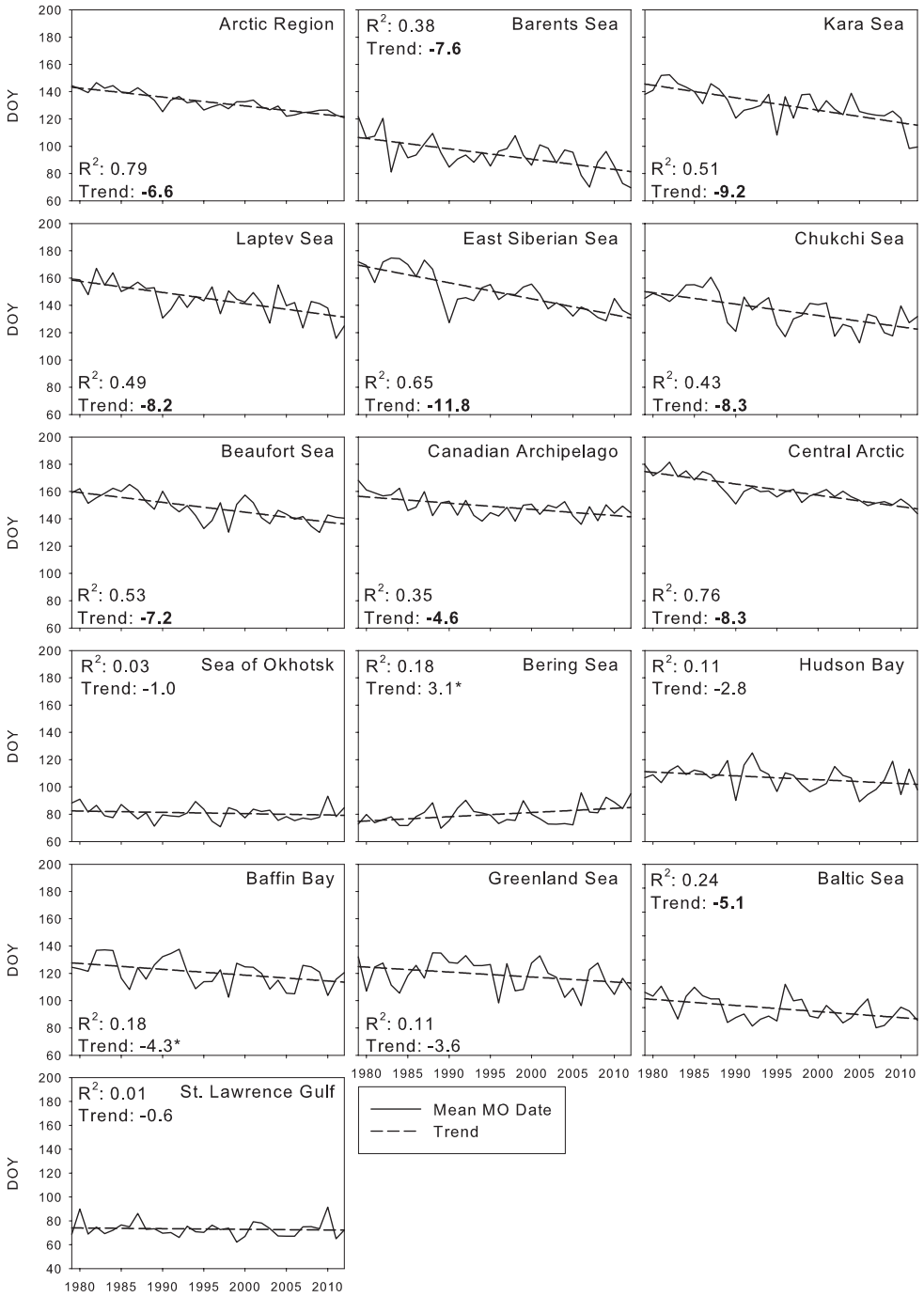

Figure 4.7 Time series of annual mean MO date and least squares linear regression trend (days decade^{-1}) for the Arctic Region and sub-regions. Bold trends are statistically significant at the 99% confidence level. An * indicates statically significant trends at the 95% confidence level.

An interesting finding to note is the statistically significant (95% confidence level) positive trend occurring in the Bering Sea. The Bering Sea is the only region of sea ice that shows a trend towards later MO dates through the data record. Although the relationship is weak (R^2 of 0.18) and the area of sea ice in the region is small (2.7×10^5 km^2), this region is showing an anomalous change in MO that is different from all other regions. Calculations for these trends and statistics are normalized to locations where MO dates exist in all years of the data record; however, the ice edge in this data set changes from year to year with the extent of sea ice at the beginning of March. Therefore it is interesting to note that the sea ice cover is actually more extensive in the Bering Sea in recent years than in the earliest years of the data record as noted by the positive yearly trend in sea ice extent described by *Cavalieri and Parkinson* [2012]. The sea ice extent trend is apparent and complementary to the positive trend in V3 MO dates. For an example of this, see Figure 4.1, where Bering Sea ice extent (using the 50% concentration threshold) is larger in 2012 than in 1979.

4.4 Comparison of statistics and trends with other works

The MO dates presented here are similar to the "early melt onset" dates determined by *Markus et al.* [2009] although differences in melt dates reported by both works are expected due to differences in data processing. Table 4.2 provides a comparison of trends in the mean MO dates presented here and early melt onset trends reported by *Stroeve et al.* [2014], an update to the *Markus et al.* [2009] melt season length analysis. In general, the direction of trends towards earlier MO is in agreement for most regions (except for the Sea of Okhotsk). However, for some regions including the Arctic Region, the Laptev, East Siberian, and Chukchi Seas, the magnitudes of the trends

are different by 5 days decade^{-1} or larger (Table 4.2). The greatest magnitude difference in trends occurs for the East Siberian Sea where a 10 day decade^{-1} difference between trends is observed, however, the *Stroeve et al.* [2014] trend is not statistically significant. Similar statistically significant trends do exist for the Barents and Kara Seas and Baffin Bay where the difference in trends is ≤ 4 days decade^{-1}. Another comparison can be made with the MO trend for the Canadian Arctic Archipelago determined by *Howell et al.* [2009], which reported a statistically significant trend of -3.1 days decade^{-1}. The early melt onset trend for the Canadian Arctic Archipelago determined by *Stroeve et al.* [2014] is -1.0 days decade^{-1} (not statistically significant), while the trend for the V3 mean MO dates reported here is -4.6 days decade^{-1} (99% confidence level).

Table 4.2 Comparison of Trends[a] in V3 Mean MO Date with Other Reported Trends (in days decade^{-1})

	Mean MO Date Trend (1979 – 2012)	Stroeve et al., 2014 Early Melt Onset Trend (1979 – 2013)	Howell et al., 2009 Melt Onset Trend (1979 – 2008)
Arctic Region	**-6.6**	**-1.9**	--
Barents Sea	**-7.6**	**-7.1**	--
Kara Sea	**-9.2**	**-5.2**	--
Laptev Sea	**-8.2**	-2.8*	--
East Siberian Sea	**-11.8**	-1.8	--
Chukchi Sea	**-8.3**	-1.6	--
Beaufort Sea	**-7.2**	-2.4*	--
Canadian Archipelago	**-4.6**	-1.0	-3.1*
Central Arctic	**-8.3**	**-2.5**	--
Sea of Okhotsk	-1.0	1.9	--
Bering Sea	3.1*	1.4	--
Hudson Bay	-2.8	-3.3*	--
Baffin Bay	-4.3*	-3.3*	--
Greenland Sea	-3.6	**-5.5**	--
Baltic Sea	**-5.1**	--	--
St. Lawrence Gulf	-0.6	--	--

[a]*Bold indicates statistical significance at the 99% confidence level. An * indicates statistical significance at the 95% confidence level.*

The mean MO dates for many of the sub-regions within the Arctic Ocean (Table 4.1) are comparable to mean early melt onset dates for 1979 – 2012 reported by *Stroeve et al.* [2014]. In general, the mean MO dates from this work occur earlier in the year than those reported by *Stroeve et al.* [2014] with the exception of the Central Arctic region. The mean MO dates for the East Siberian, Chukchi, and Beaufort Seas and the Canadian Arctic Archipelago and Central Arctic vary from the *Stroeve et al.* [2014] means by 6.5 days in the Chukchi Sea to as little as 0.6 days in the Central Arctic region. In peripheral sea ice regions, the differences between mean MO dates from this work and *Stroeve et al.* [2014] early melt onset dates increase to as much as 30.6 days for the Barents Sea region. Given differences in the melt onset algorithms and data processing used here and in the *Markus et al.* [2009] method, particularly with respect to how the sea ice boundary is determined using sea ice concentrations in each method, it is expected that the greatest differences in MO statistics will occur in marginal ice zones.

Each method for determining MO dates can result in a different value due to differences in the algorithms and data processing steps used to produce the melt dates. For example, both the AHRA method used here and the *Markus et al.* [2009] method attempt to remove noise in the Tb data that could give erroneous melt dates. The AHRA method utilizes a 10-day time series window (described in Chapter 3) to remove spurious Tbs, likely the result of weather effects, which could indicate a MO date that is too early in the season. The *Markus et al.* [2009] method determines if a calculated melt onset date is valid by comparing the 8 surrounding pixels to test for spatial homogeneity. Further, sea ice concentrations are used differently to determine the extent of sea ice in each method. The AHRA method relies on a 50% sea ice concentration threshold at the

beginning of the melt season in March, while the *Markus et al.* [2009] method considers pixels with concentrations greater than 80% for fewer than 5 days during the year to be ice-free. The differences in the ice edge in each method as a result of these differing thresholds likely contribute considerably to differences in the statistics for marginal ice zones when calculated over a set regional boundary. Despite these differences, various methods for determining MO dates show a significant trend towards increasingly early MO for the majority of Arctic sea ice, in agreement with the works of others (e.g. *Stroeve et al.,* 2006, 2014; *Markus et al.,* 2009).

MO dates can vary widely from year to year in Arctic sub-regions depending on when the daily maximum air temperatures in different regions reach the melting point. Although, on average, there is latitudinal dependence on timing of MO, springtime weather conditions and temperature anomalies are important for explaining the year to year variability in MO timing for much of the sea ice within the Arctic Ocean [*Anderson and Drobot*, 2001; *Belchansky et al.,* 2004; *Markus et al.,* 2009; *Wang et al.,* 2011]. Springtime weather conditions, including cyclonic activity, can have an influence on the air temperatures and the surface energy budget of the sea ice through the trapping of longwave heat when conditions are cloudy or through increased incoming shortwave radiation when conditions are cloud free and the sun rises in spring.

CHAPTER 5 – DAILY MELT ONSET AREA

5.1 Daily time series of melt onset area

Annual MO dates for the snow cover atop Arctic sea ice can be examined on a daily basis by partitioning the annual MO date maps (Figure 4.1) for each year in the data record into an amount of sea ice area experiencing MO each day. The time series of daily MO area is calculated for each day of the melt season after 1 March (DOY 60). For each day, the number of grid point locations with a MO date assigned is multiplied by the grid resolution (25 km x 25 km), producing a value for the area of sea ice experiencing MO for that date. To ensure that the daily MO areas are directly comparable from year to year, MO area is only calculated over grid points where a MO date exists for all 34 years of the record (identified in Figure 3.1 by colored pixels). Therefore, all pixels with fewer than 34 years of annual MO dates (identified in Figure 3.1 by white pixels) are excluded from this analysis. The total area of sea ice coverage (km^2) for the Arctic and all sub-regions following the exclusion of pixels that are missing a MO date for one or more years are presented in Table 3.2.

The passive microwave data used to generate the MO dates used here have different temporal coverage. Data from the SMMR sensor for years 1979 – 1987 were collected every second day, while SSM/I and SMMIS data collected since 1988 are collected daily (Table 3.1); thus, a 3-day running mean is applied to each time series to make the daily MO areas before 1988 more comparable to daily SSM/I and SSMIS data since 1988. The running mean can slightly smooth the daily MO area curves and can shift

the apex of a peak in the curve (a local maximum MO day) ± 1 day; however, note that even after the application of the 3-day running mean, the time series curves for the SMMR years 1979 – 1987 (e.g. Figure 5.1) have a more jagged appearance than for other years. Although the curves for the SMMR years appear differently, the general shape of the curves indicate the timing and magnitude of any peaks in MO area in a similar manner as for the other years in the record.

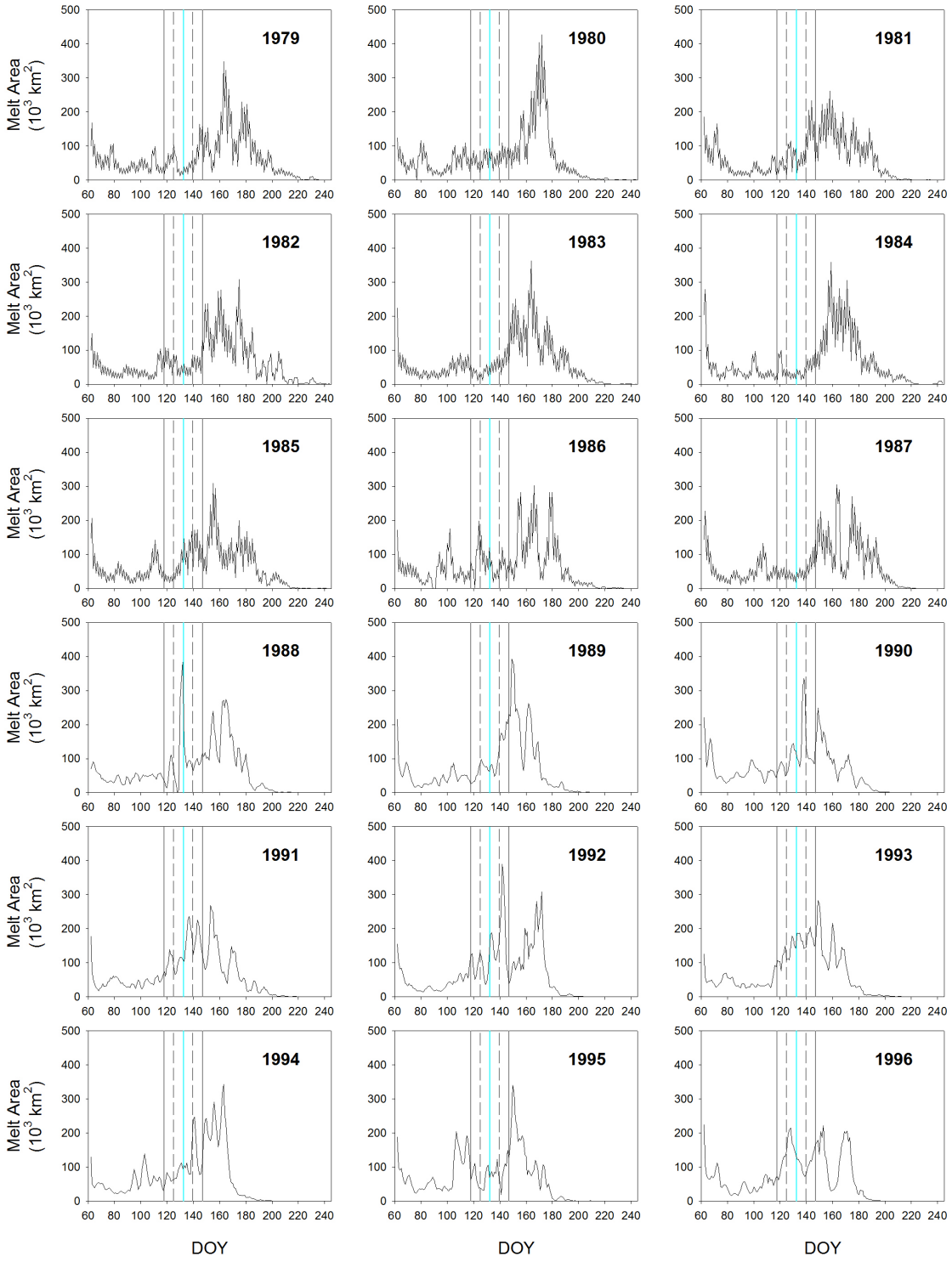

Figure 5.1 Arctic Region time series of daily MO area (1979 – 2012). The cyan line indicates the mean MO date, while the dashed and solid black lines indicate ± 1 and ± 2 standard deviations from the mean respectively.

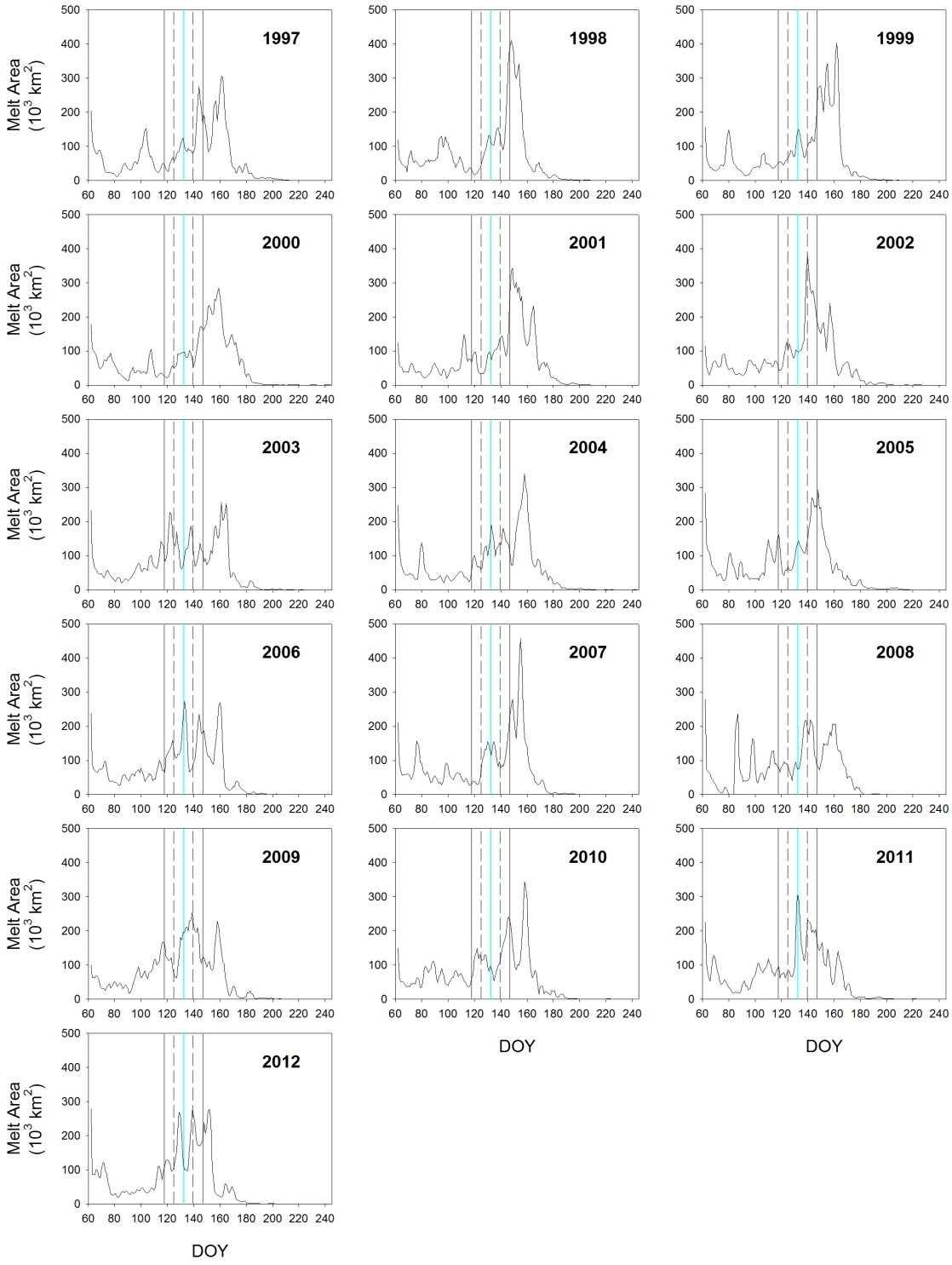

Figure 5.1 Arctic Region (Continued).

The time series of daily MO area for each year indicate the amount of spatial area experiencing MO for each day throughout the melt season. Peaks in the daily MO area time series for the Arctic Region (Figure 5.1) tend to indicate that the largest amounts of melting area occur between 10 May (DOY 130) and 29 June (DOY 180); however, there are also numerous peaks in MO area that can occur near the beginning of the melt season (e.g. near 1 March (DOY 60) and 21 March (DOY 80) in 1999, 2000, 2004, and 2007). The specific timing of peaks in the daily MO area for the Arctic Region are variable from year to year and the daily MO area time series can be used to identify periods of melting on the sea ice or periods of time when melting is suppressed.

Since the daily MO area time series for the Arctic Region describe the timing of MO area for all sea ice cover in the Arctic (Figure 5.1), much of the variation over smaller spatial scales within the Arctic is masked by the grouping of all Arctic sub-regions together. The most highly variable MO dates occur in sub-regions within the Arctic Ocean including the Kara, Laptev, East Siberian, and Chukchi Seas (see Chapter 4.2). Mean MO dates in these regions range from 11 May (DOY 130.5) in the Kara Sea to 31 May (DOY 150.1) in the East Siberian Sea (Table 4.1). The largest mean range in MO dates (54 days) occurs in the Kara Sea (Table 4.1). The Kara Sea mean MO range indicates that the mean MO date varies by nearly 8 weeks over the 34-year record, making the Kara Sea the most highly variable sub-region of the Arctic. As a result of comparatively little variation in regions outside of the central regions of Arctic sea ice extent (Table 4.1) and/or smaller areas of sea ice in peripheral regions such as the St. Lawrence Gulf and the Baltic Sea (Table 3.2, Figure 3.1) the daily MO area analysis is

focused on the more highly variable sub-regions located in and nearest to the Arctic Ocean (Figure 3.2).

Eliminating the peripheral sea ice regions that are located outside of the Arctic Ocean primarily impacts the amount of daily MO area that occurs earliest in the year (Figure 5.2). The peripheral seas are located at lower latitudes where MO tends to occur earlier in the year (Figure 4.2); thus, eliminating the peripheral seas from the time series of daily MO area plots, does not change the patterns in the 3-day averaged time series for the bulk of the melt season after ~ 10 April (DOY 100). Therefore, focusing the following analysis only on the Arctic Ocean sub-regions is reasonable considering that the timing of daily MO area for the majority of the melt season is not being skewed by region choice.

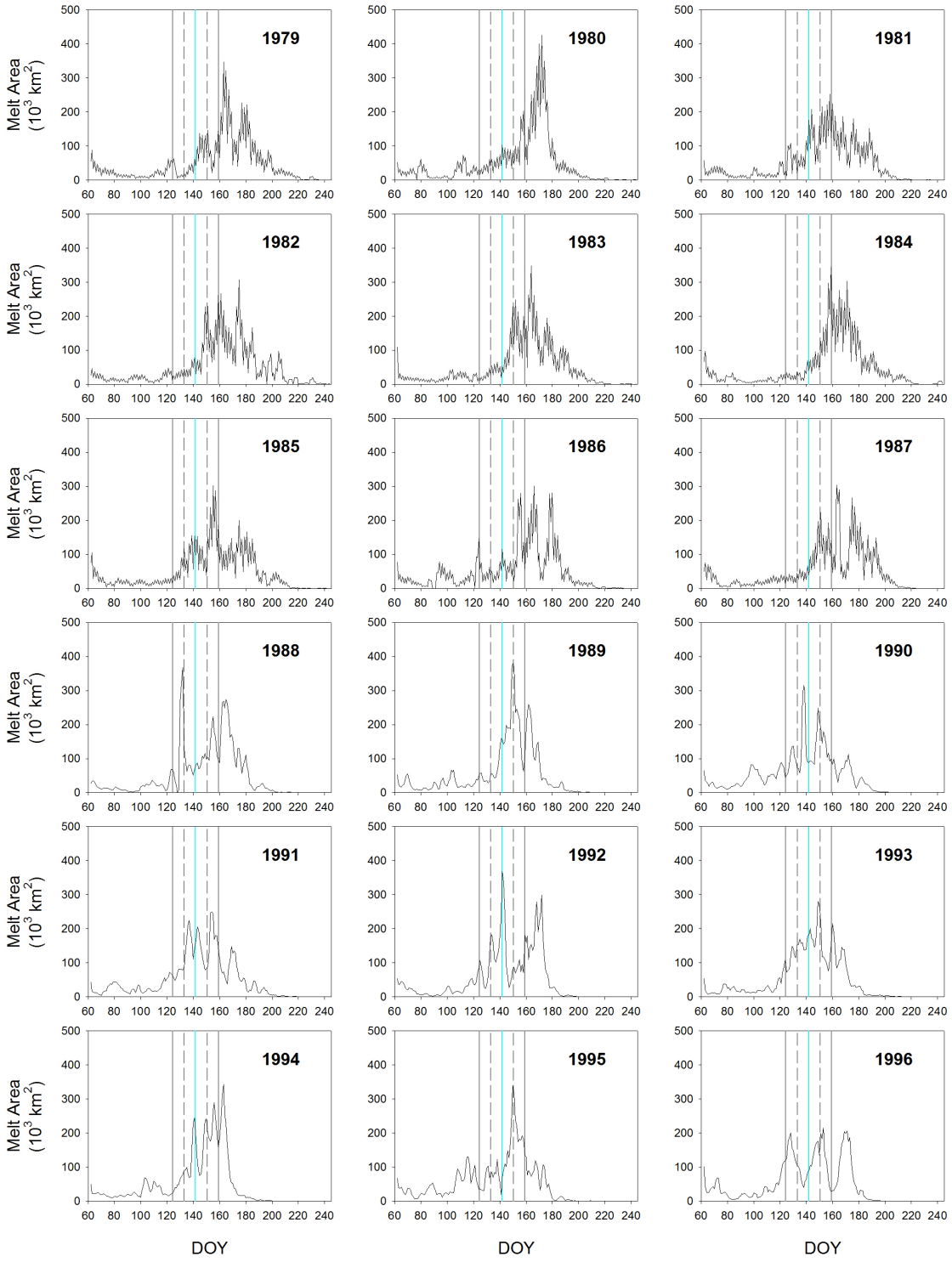

Figure 5.2 Arctic Ocean time series of daily MO area (1979 – 2012). The cyan line indicates the mean MO date, while the dashed and solid black lines indicate ± 1 and ± 2 standard deviations from the mean respectively.

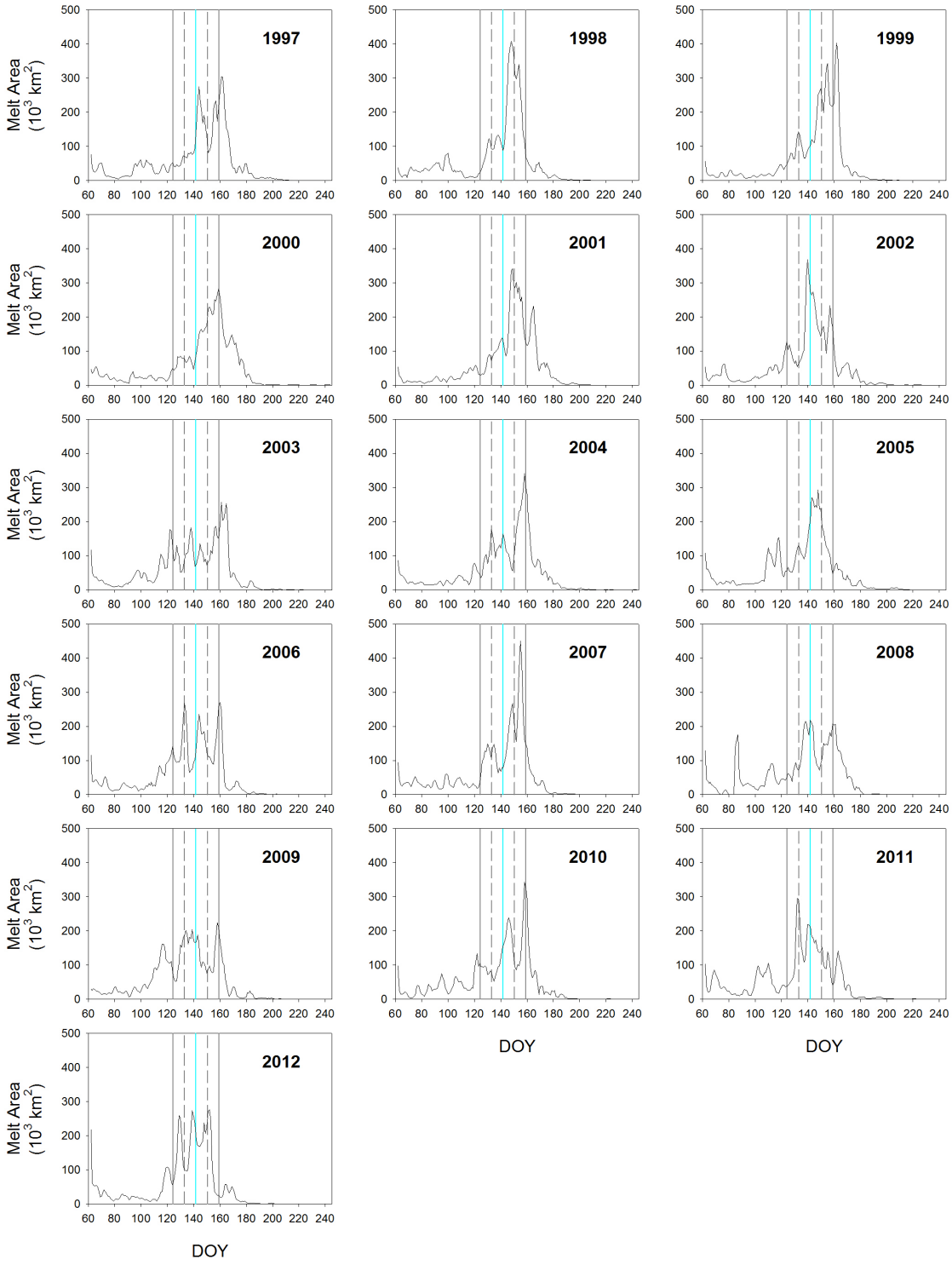

Figure 5.2 Arctic Ocean (Continued).

Since the Kara Sea and other Arctic Ocean sub-regions are highly variable in terms of MO timing from year to year, MO timing is attributed to the large-scale weather patterns, in particular, cyclonic activity present at the time of MO [*Anderson and Drobot*, 2001b]. The patterns of daily MO in these regions can ultimately point to the ideal atmospheric conditions necessary to initiate the onset of melting over large proportions of a region's area.

5.2 Melt onset events

The time series of daily MO area throughout a single melt season is used to determine the timing and magnitude of individual melting events within a defined region. Here, a "melting event" is defined as a period of time over which areas of MO occur for several consecutive days. Any peak in the time series of daily MO areas indicates that MO is occurring; however, a melting event as defined here is bounded by a daily MO area of 0 km^2 or near 0 km^2 per day. That is, a melting event begins with a period where nearly no MO is occurring in the region and ends when the accrual of new daily MO area stops. The duration of a melting event can vary from a few days to a period of a month or more. The end result of a typical, high-magnitude melting event is MO area covering the majority of a region's geographical area. Lower magnitude melting events do exist; however, they tend to occur anomalously early in the melting season, and only result in melting over a small portion of the region's area.

Since MO area can occur at each grid point location only once per year, there is a decreasing utility of daily MO area in identifying the magnitude or intensity of melting events that occur later in the melt season, simply because there are fewer grid points

remaining that can be considered new MO areas. Thus, melting events that occur earlier in the year and that cover the first 90% of a region are examined. Despite this limitation, valuable information can be gained by closely examining patterns in the daily MO areas, especially variations in the regional MO pattern from year to year.

The 3-day averaged daily MO area time series curves for the Arctic Region, the Arctic Ocean region, and Arctic Ocean sub-regions (Table 3.3) are shown for each year in the study period in Figures 5.1 – 5.12. The Arctic Region and the Arctic Ocean region represent the net daily MO area for all of the smaller sub-regions identified in Table 3.3. Given the spatial scale of synoptic weather events, it is most valuable to examine the daily MO area time series for the sub-regions of the Arctic Ocean (shown in Figures 5.3 – 5.12) where the regional variability in MO timing can be closely examined.

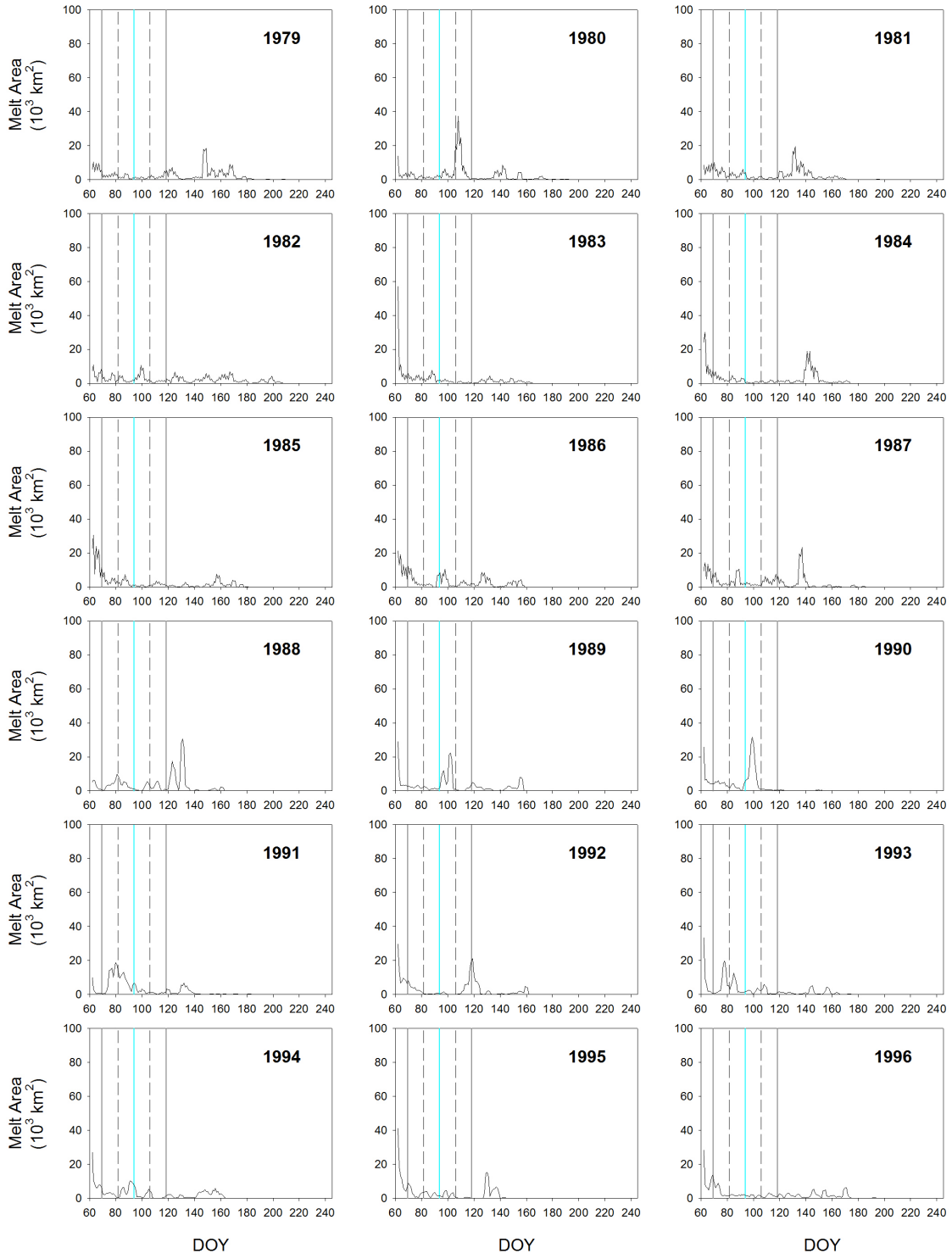

Figure 5.3 Barents Sea time series of daily MO area (1979 – 2012). The cyan line indicates the mean MO date, while the dashed and solid black lines indicate ± 1 and ± 2 standard deviations from the mean respectively.

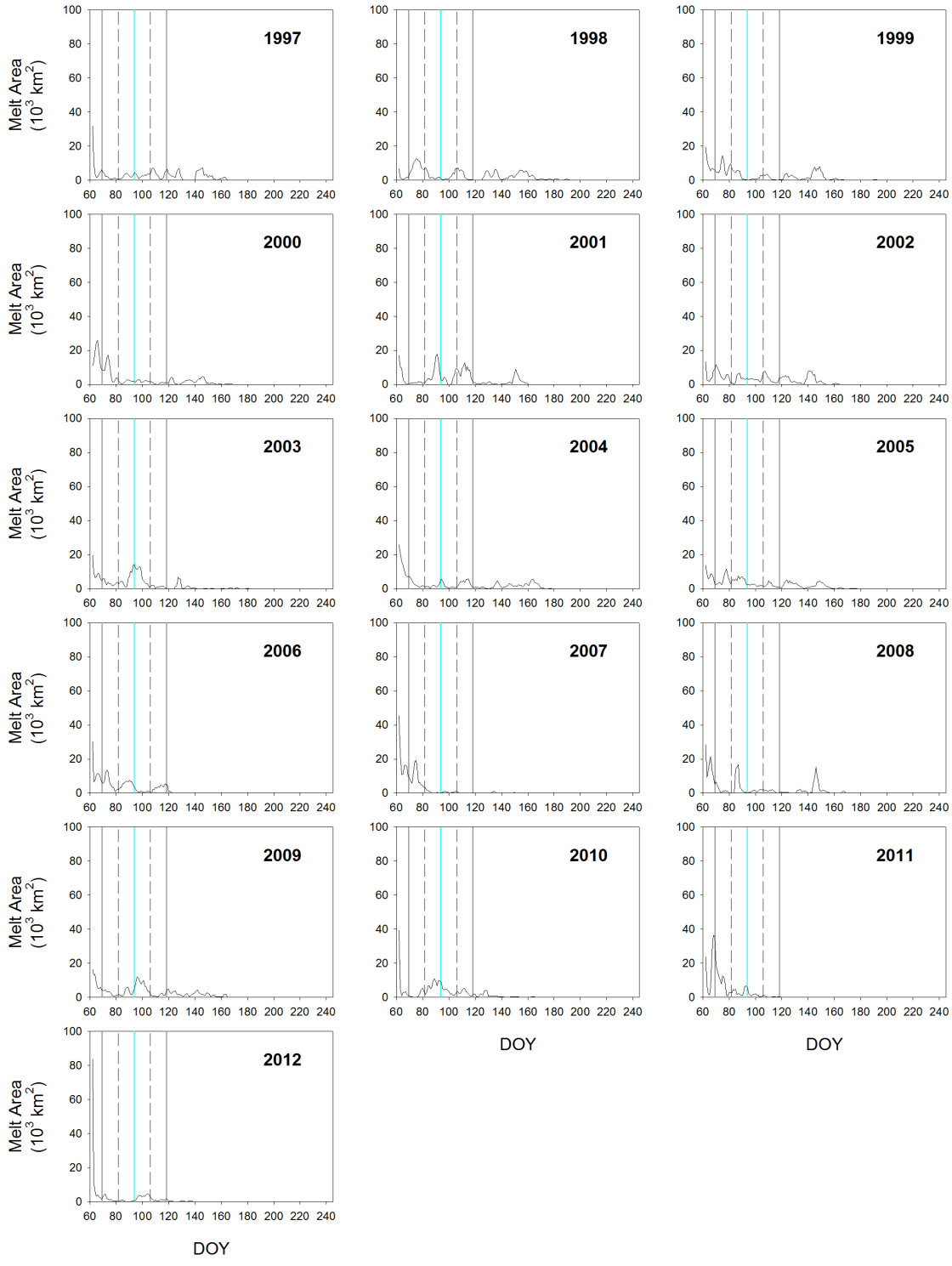

Figure 5.3 Barents Sea (Continued).

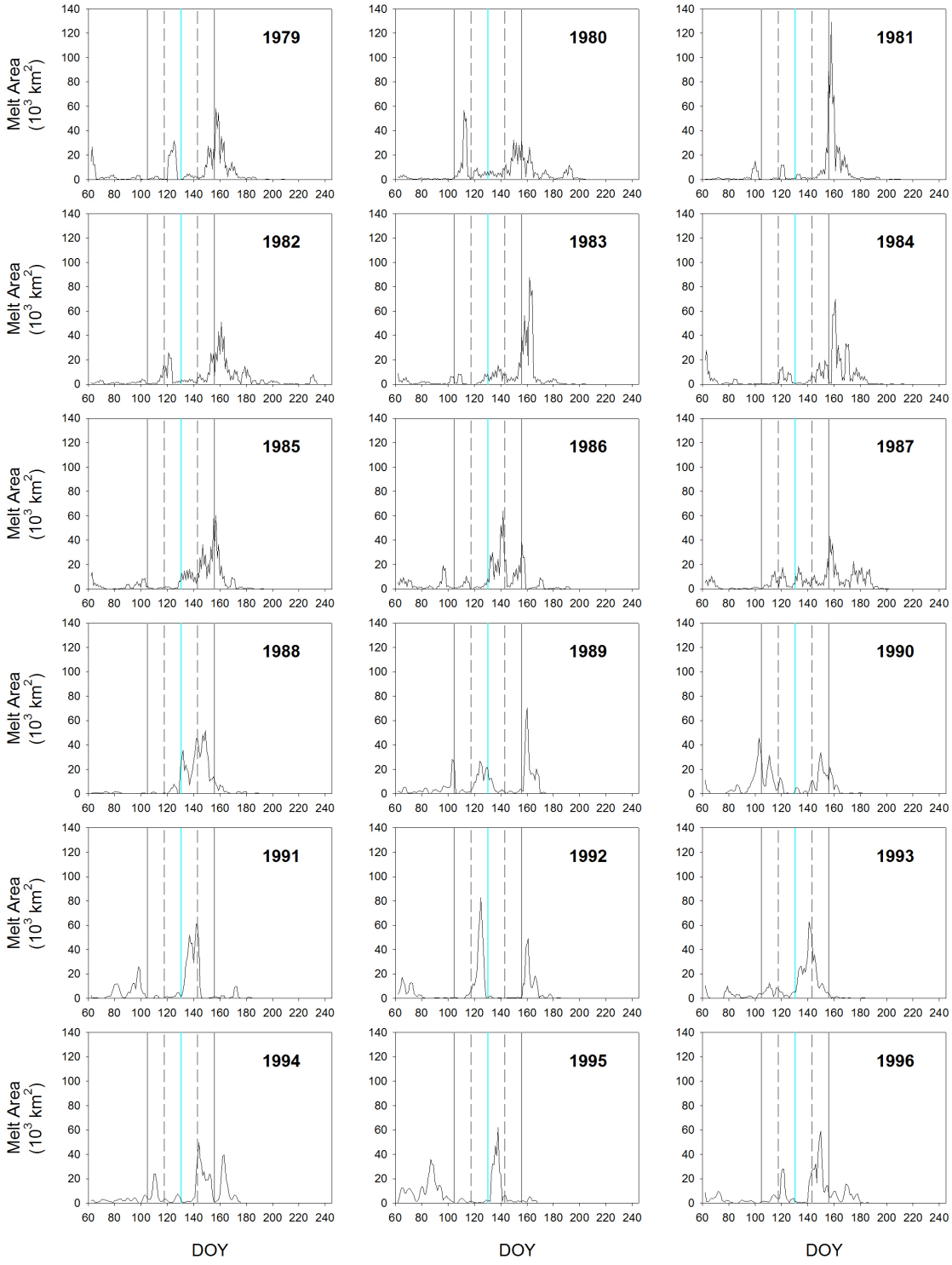

Figure 5.4 Kara Sea time series of daily MO area (1979 – 2012). The cyan line indicates the mean MO date, while the dashed and solid black lines indicate ± 1 and ± 2 standard deviations from the mean respectively. *Note that the 2008 peak on 27 March (DOY 87) is a result of a 7-day data outage, and is excluded from analysis.*

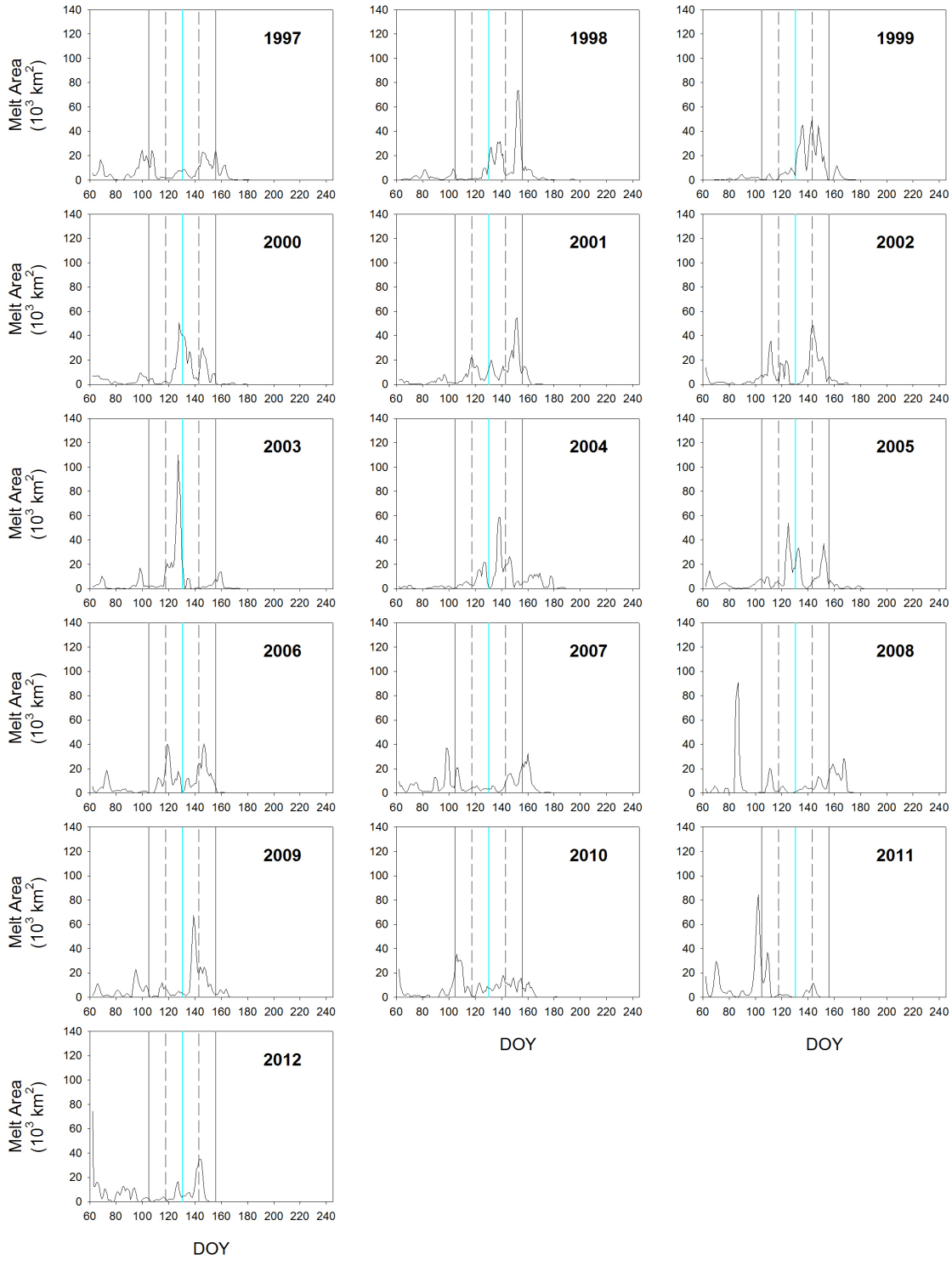

Figure 5.4 Kara Sea (Continued).

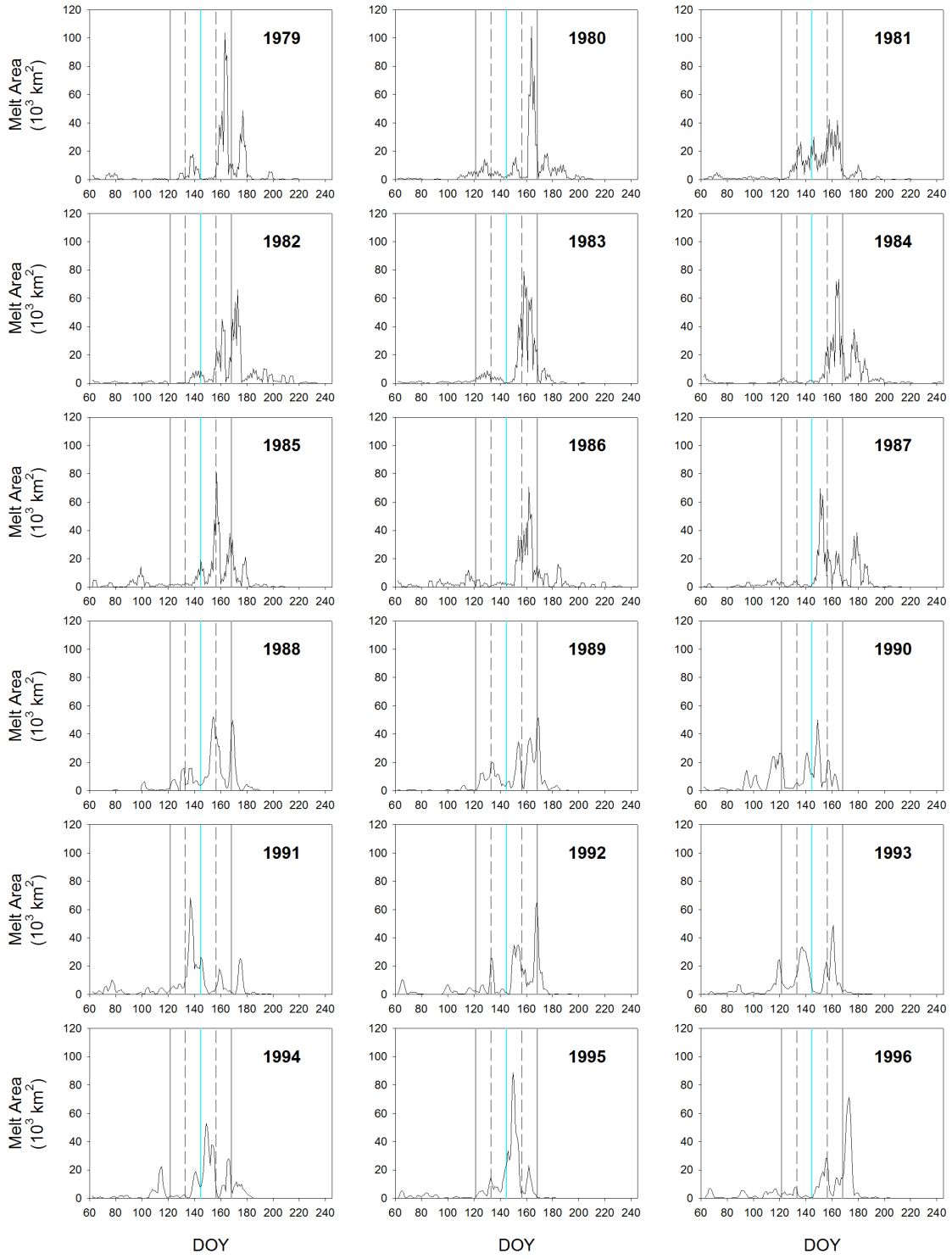

Figure 5.5 Laptev Sea time series of daily MO area (1979 – 2012). The cyan line indicates the mean MO date, while the dashed and solid black lines indicate ± 1 and ± 2 standard deviations from the mean respectively.

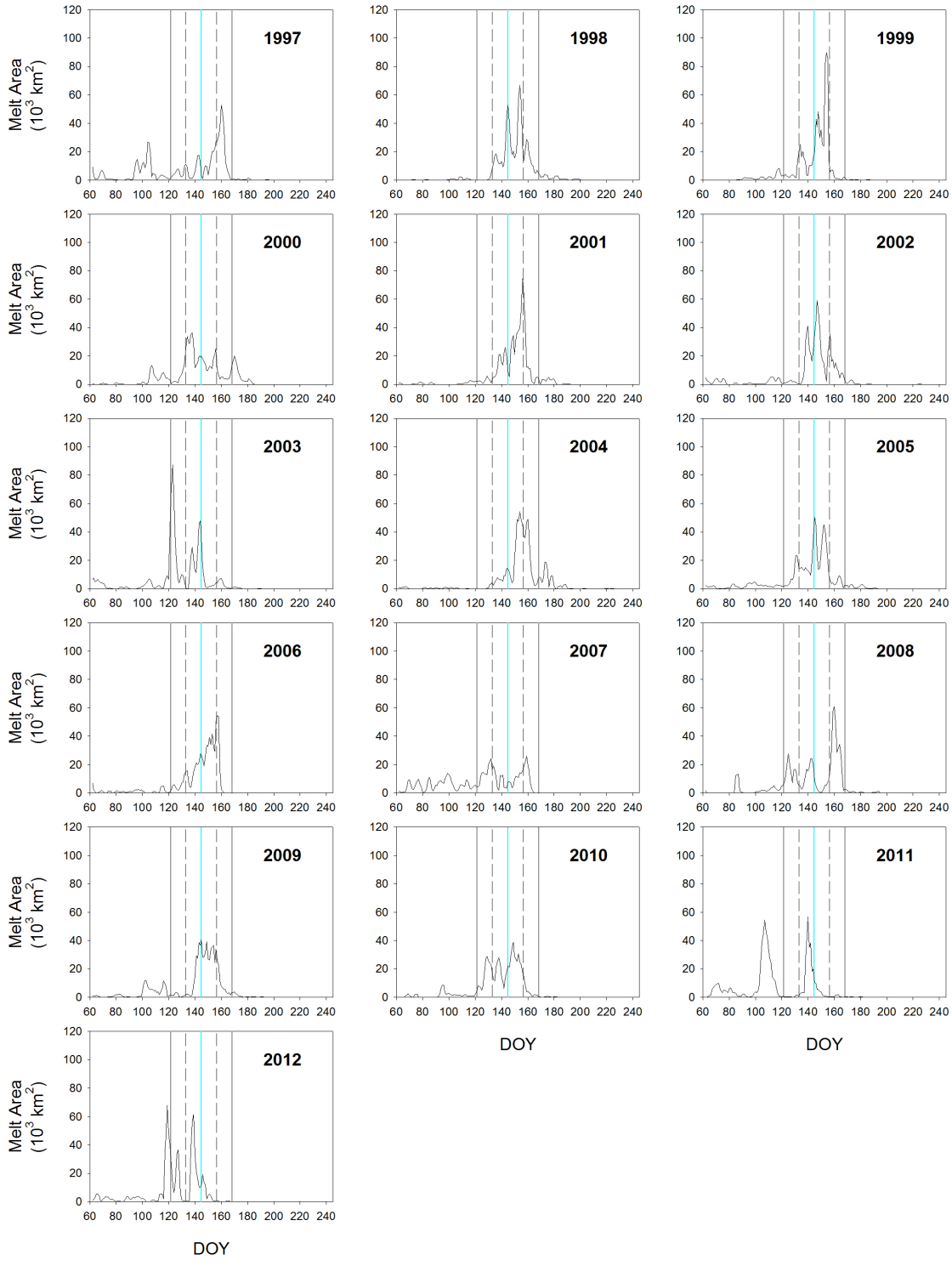

Figure 5.5 Laptev Sea (Continued).

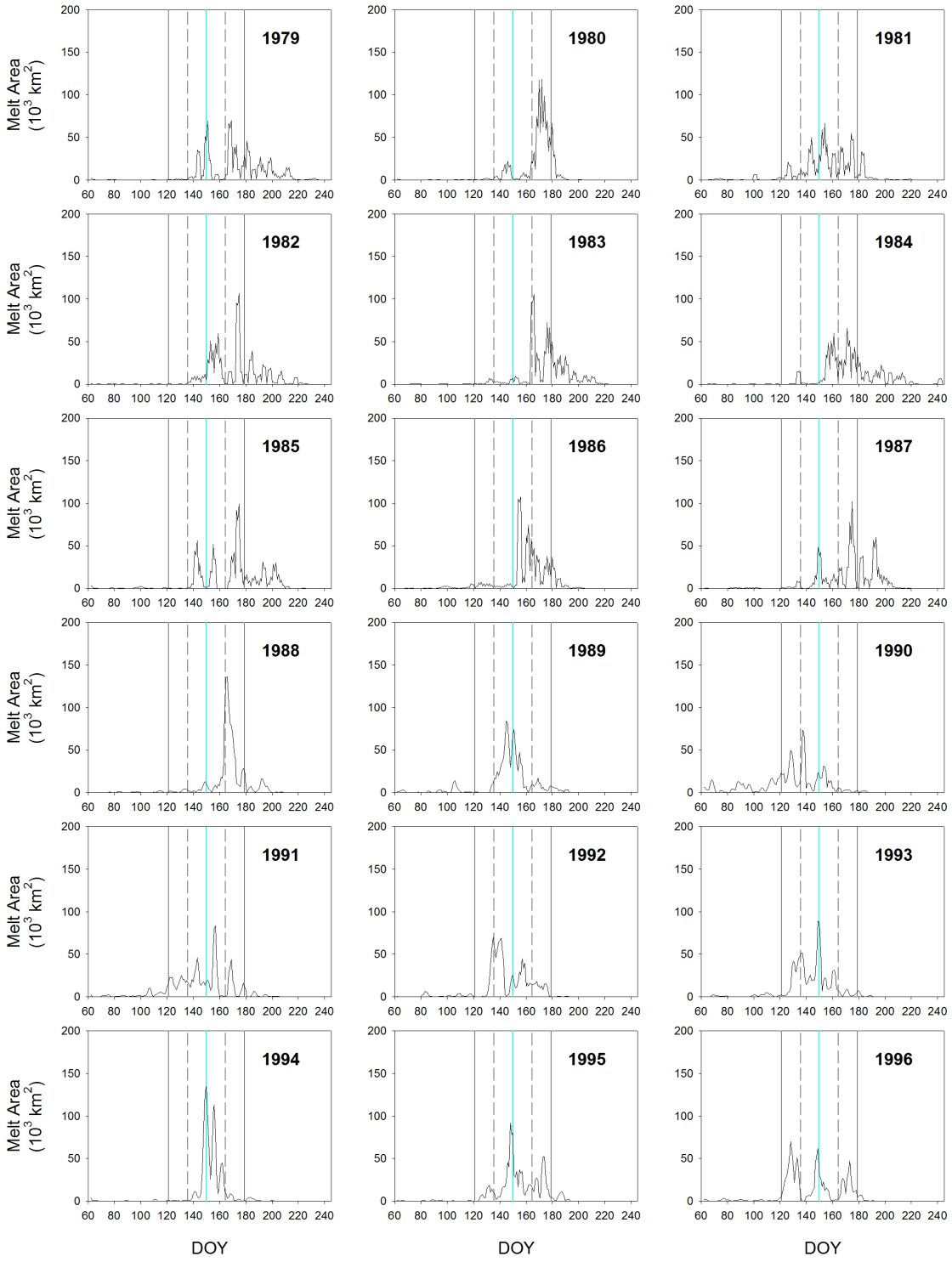

Figure 5.6 East Siberian Sea time series of daily MO area (1979 – 2012). The cyan line indicates the mean MO date, while the dashed and solid black lines indicate ± 1 and ± 2 standard deviations from the mean respectively.

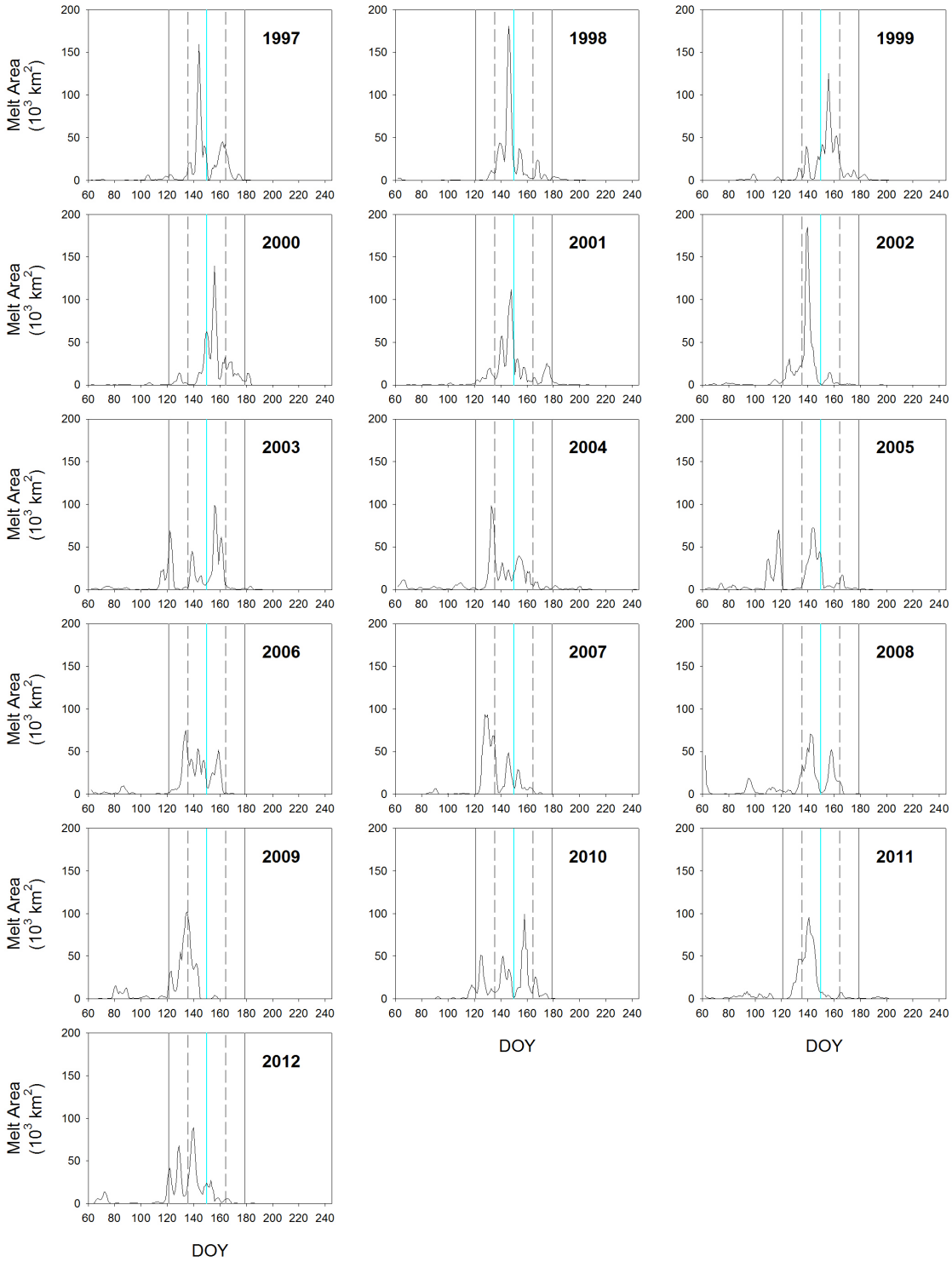

Figure 5.6 East Siberian Sea (Continued).

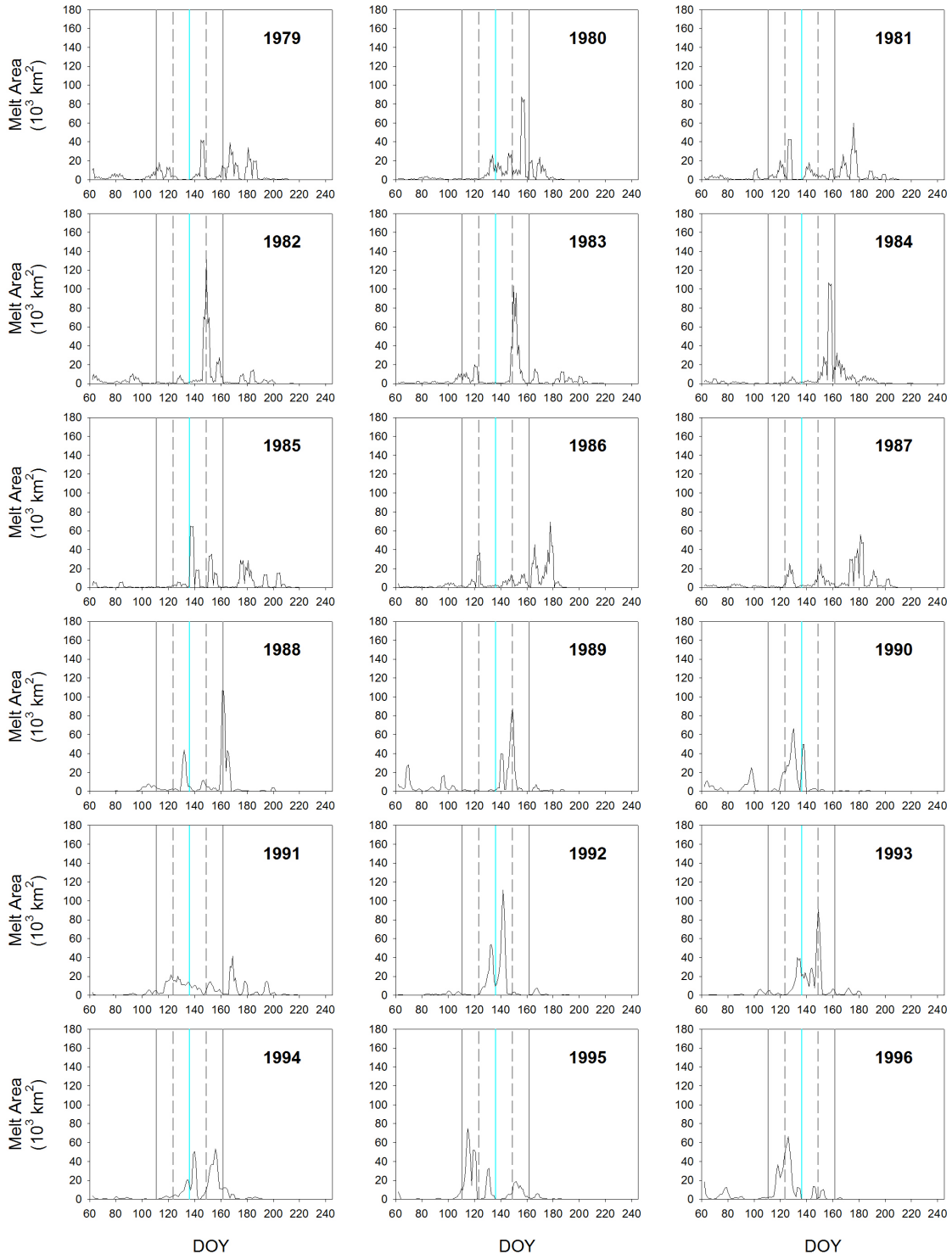

Figure 5.7 Chukchi Sea time series of daily MO area (1979 – 2012). The cyan line indicates the mean MO date, while the dashed and solid black lines indicate ± 1 and ± 2 standard deviations from the mean respectively.

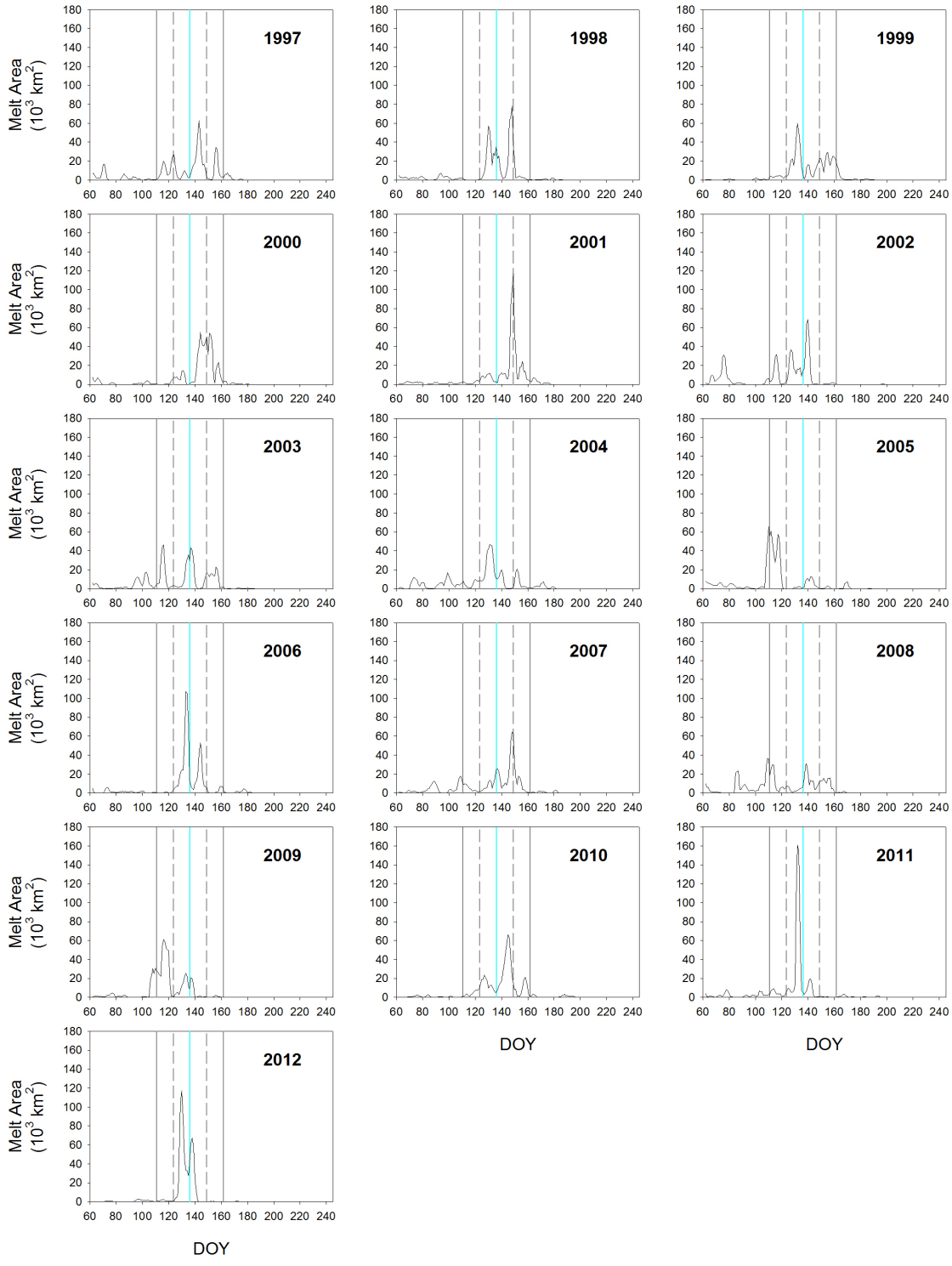

Figure 5.7 Chukchi Sea (Continued).

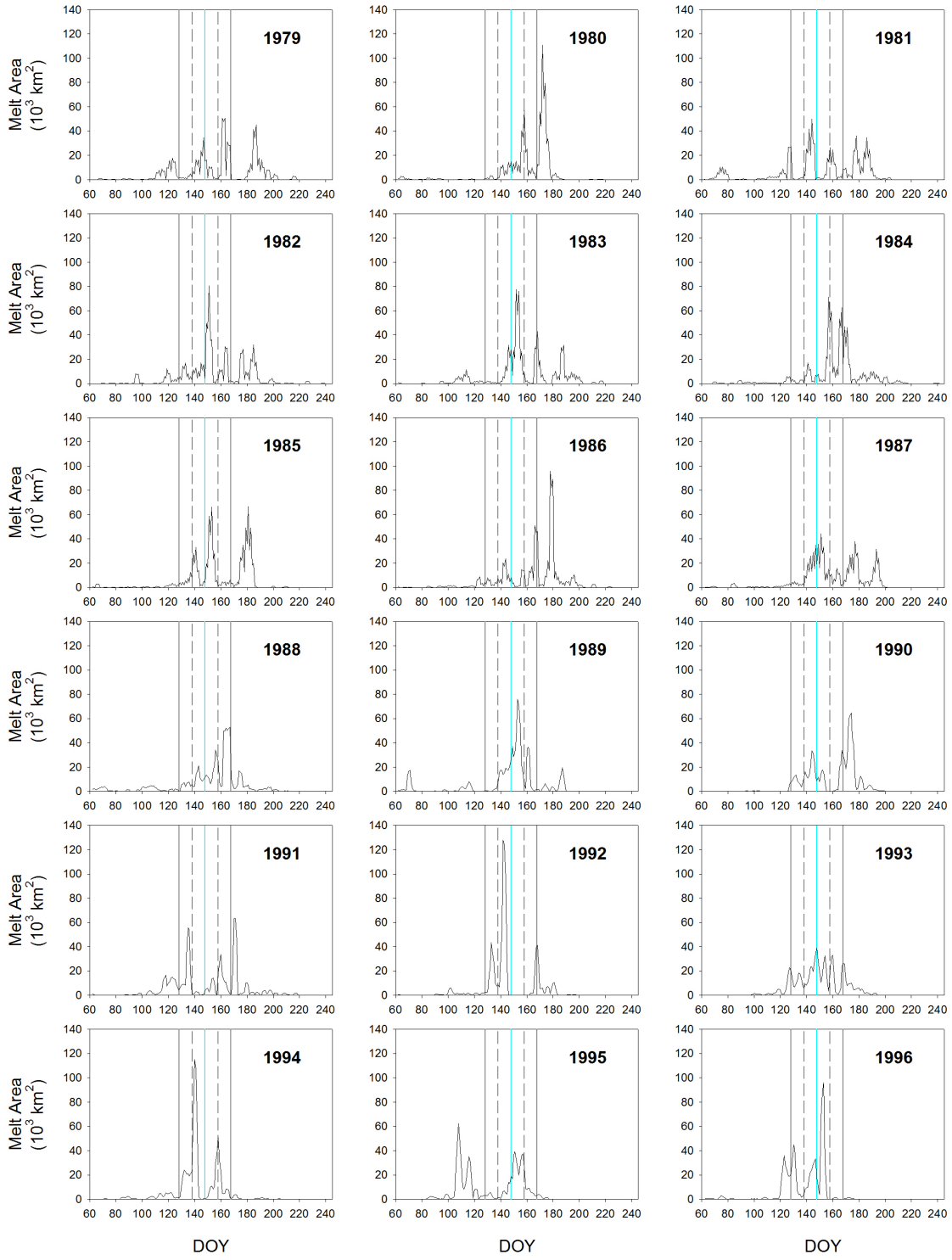

Figure 5.8 Beaufort Sea time series of daily MO area (1979 – 2012). The cyan line indicates the mean MO date, while the dashed and solid black lines indicate ± 1 and ± 2 standard deviations from the mean respectively.

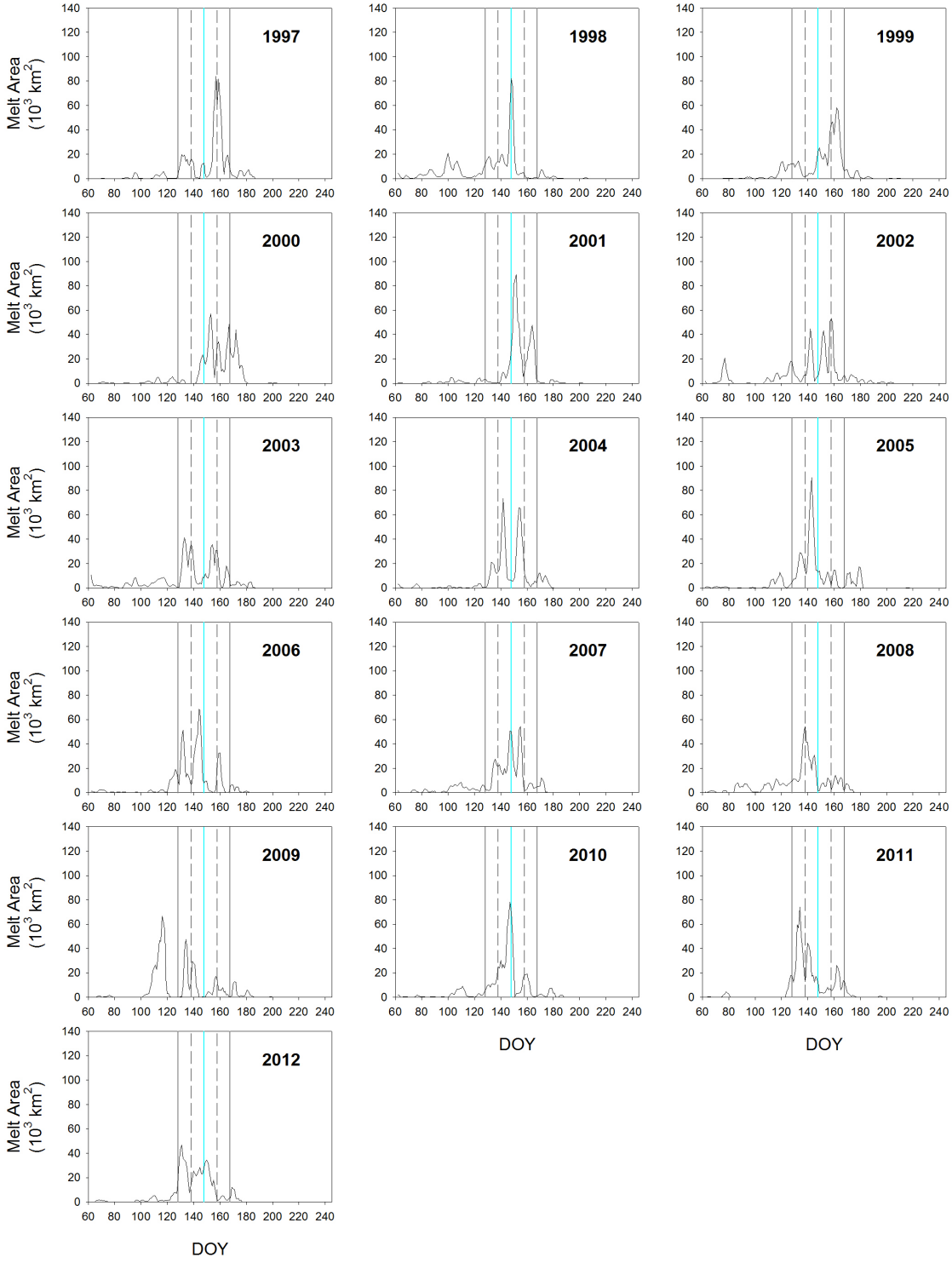

Figure 5.8 Beaufort Sea (Continued).

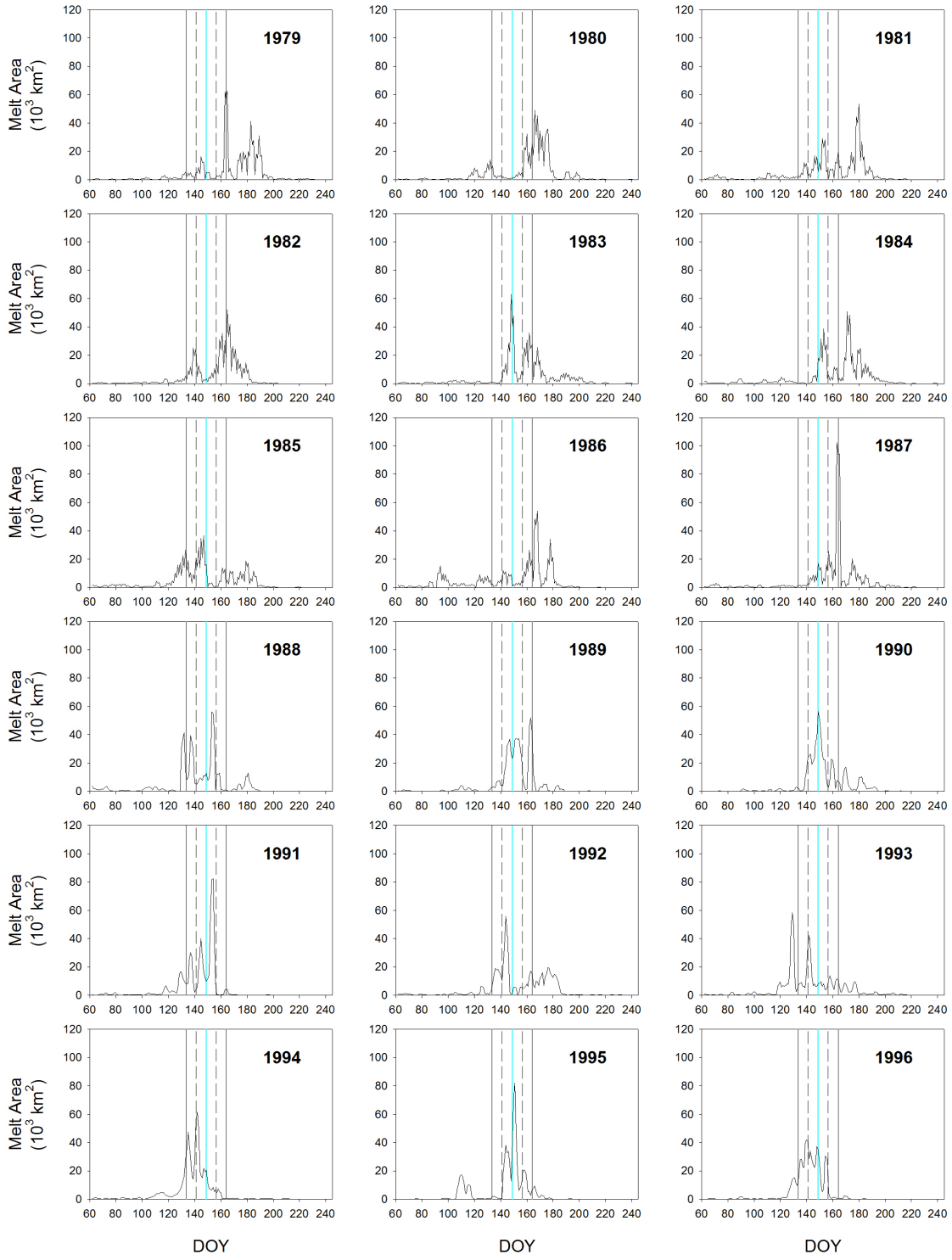

Figure 5.9 Canadian Arctic Archipelago time series of daily MO area (1979 – 2012). The cyan line indicates the mean MO date, while the dashed and solid black lines indicate ± 1 and ± 2 standard deviations from the mean respectively.

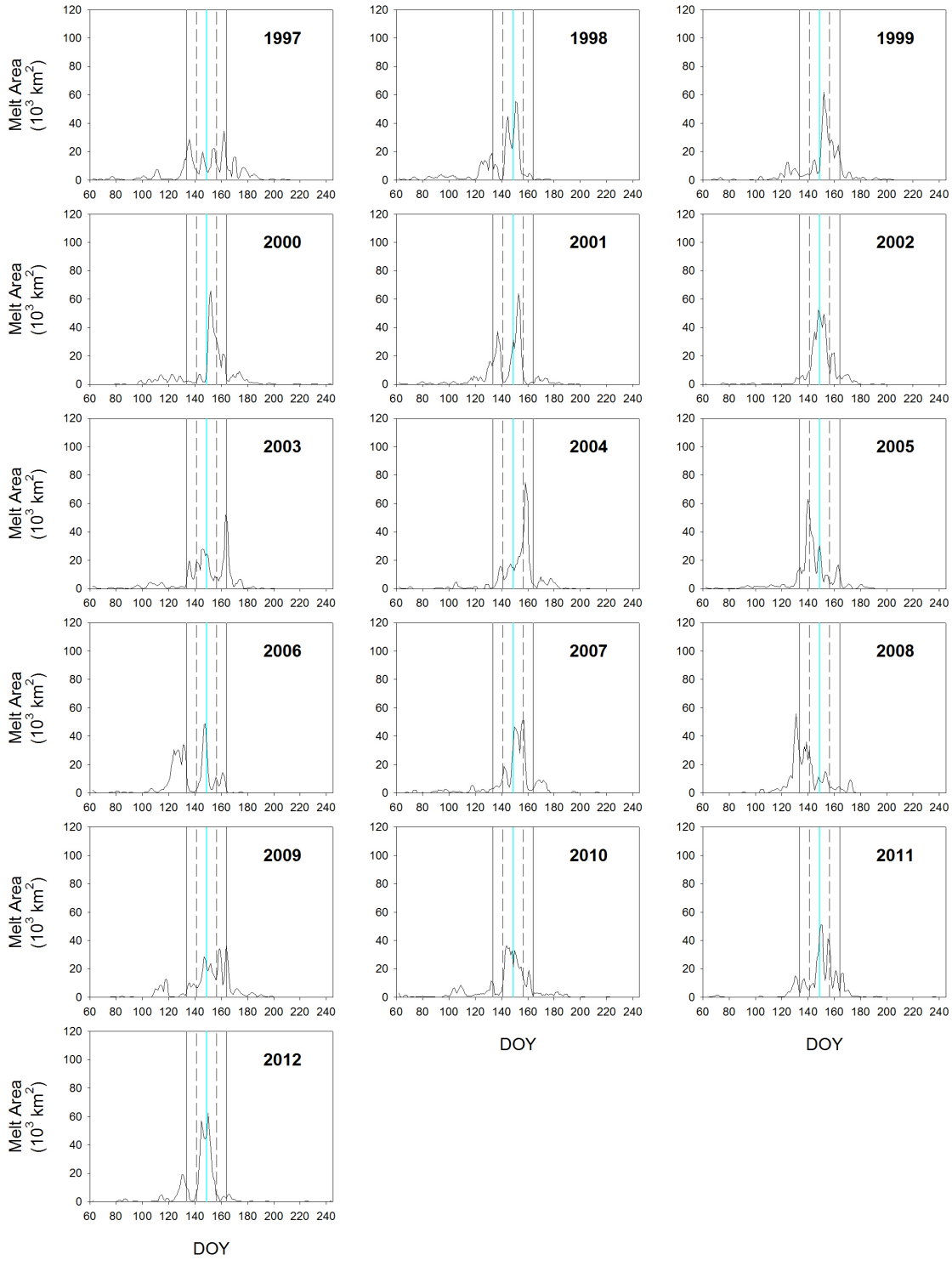

Figure 5.9 Canadian Arctic Archipelago (Continued).

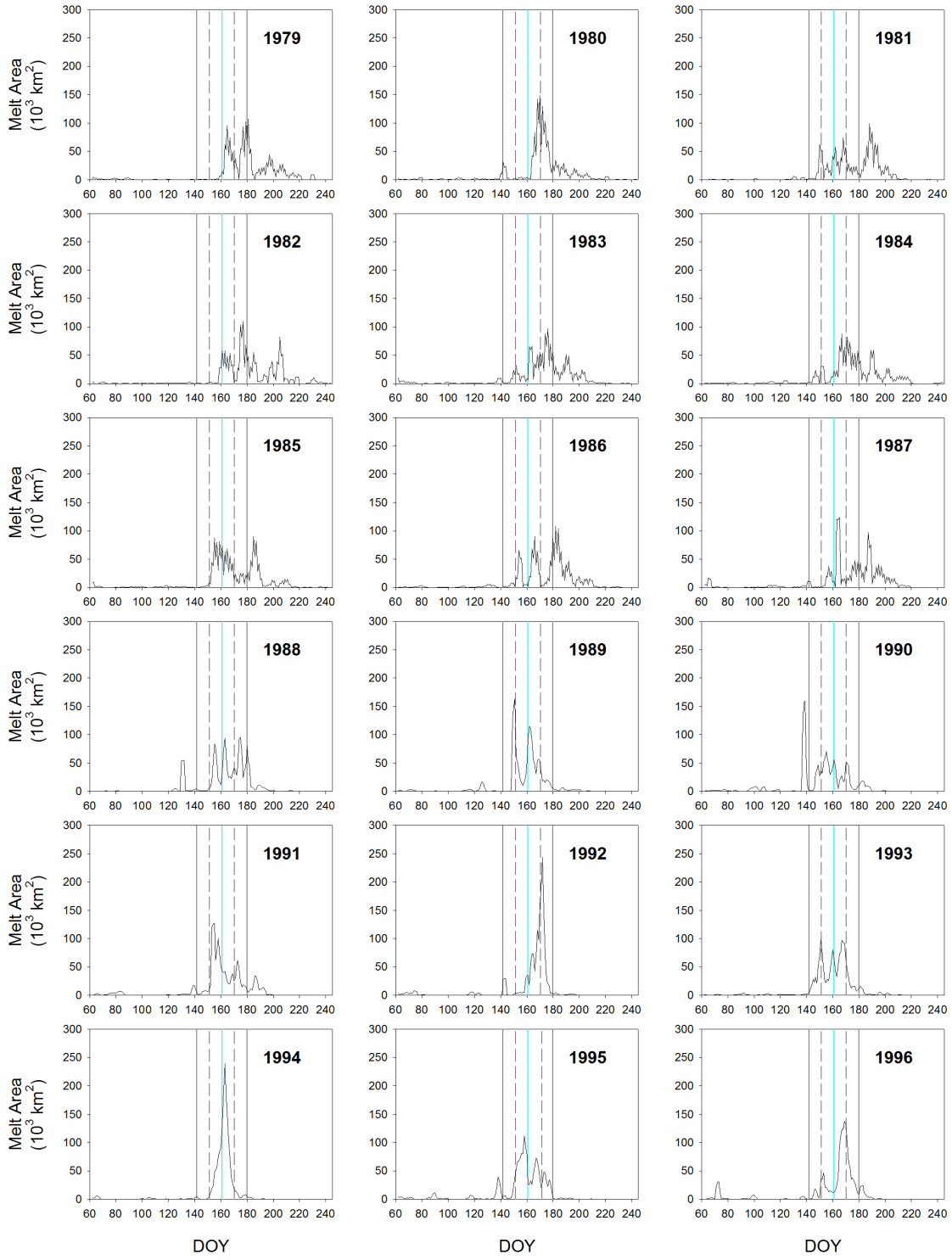

Figure 5.10 Central Arctic time series of daily MO area (1979 – 2012). The cyan line indicates the mean MO date, while the dashed and solid black lines indicate ± 1 and ± 2 standard deviations from the mean respectively.

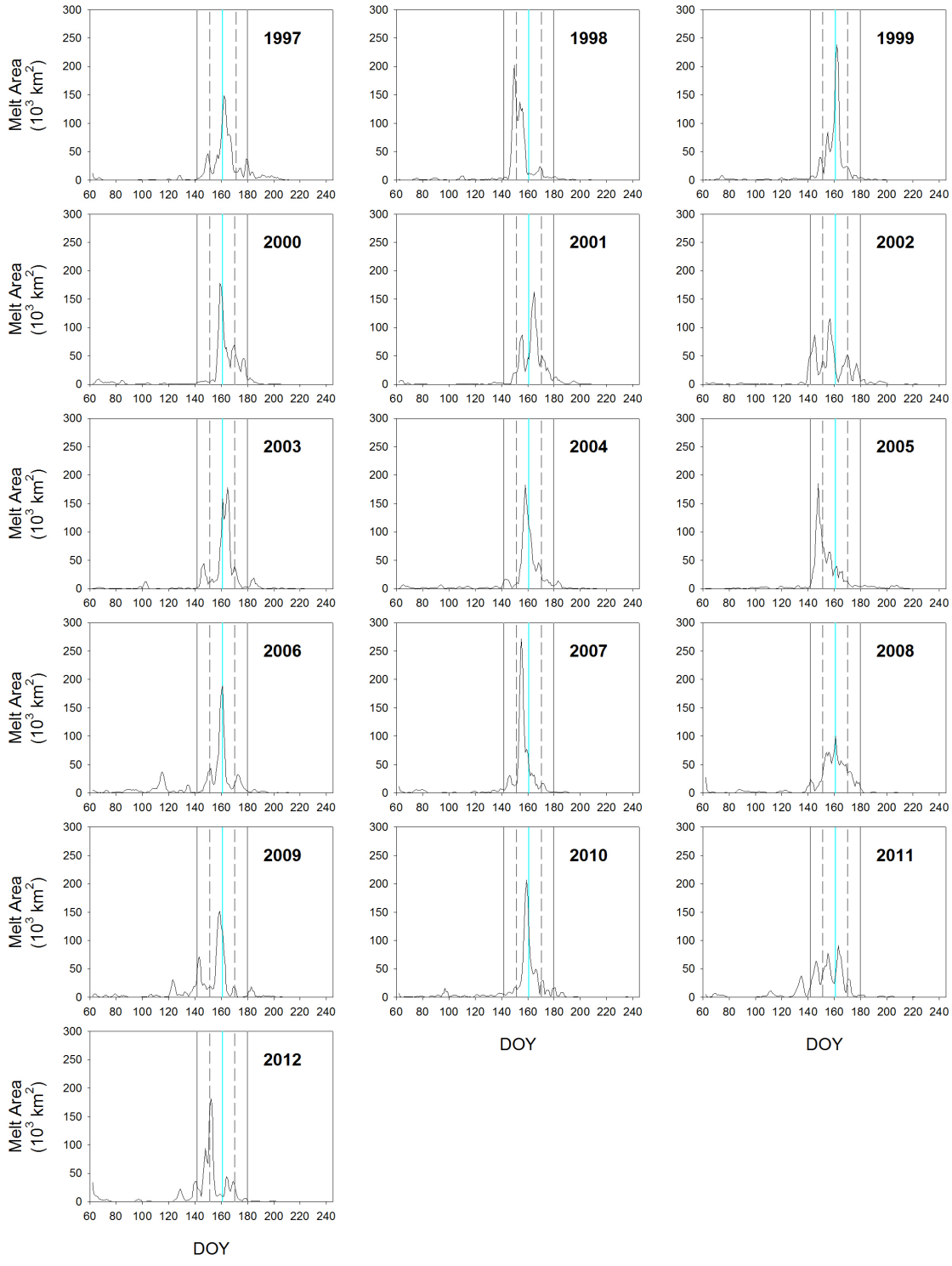

Figure 5.10 Central Arctic (Continued).

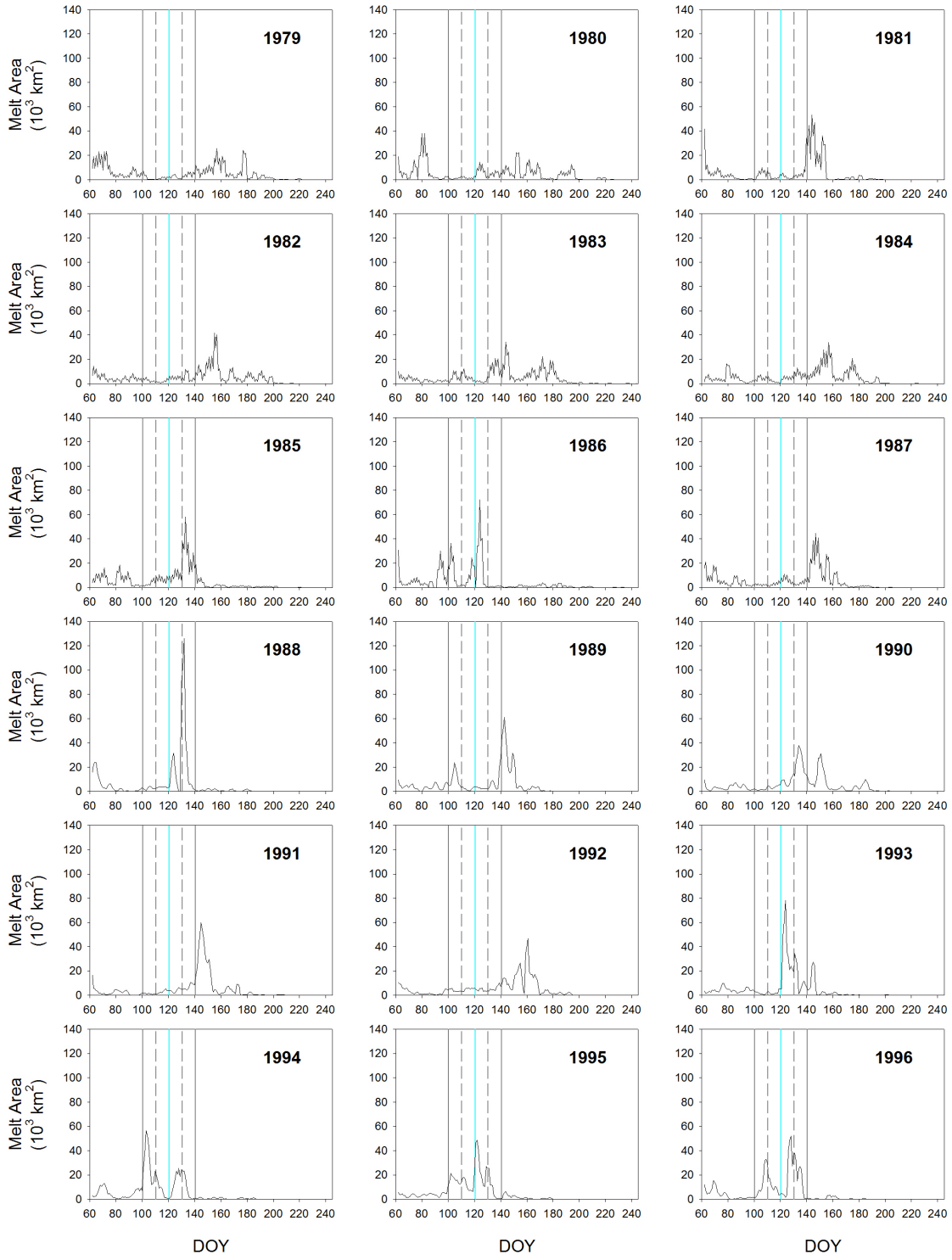

Figure 5.11 Baffin Bay time series of daily MO area (1979 – 2012). The cyan line indicates the mean MO date, while the dashed and solid black lines indicate ± 1 and ± 2 standard deviations from the mean respectively.

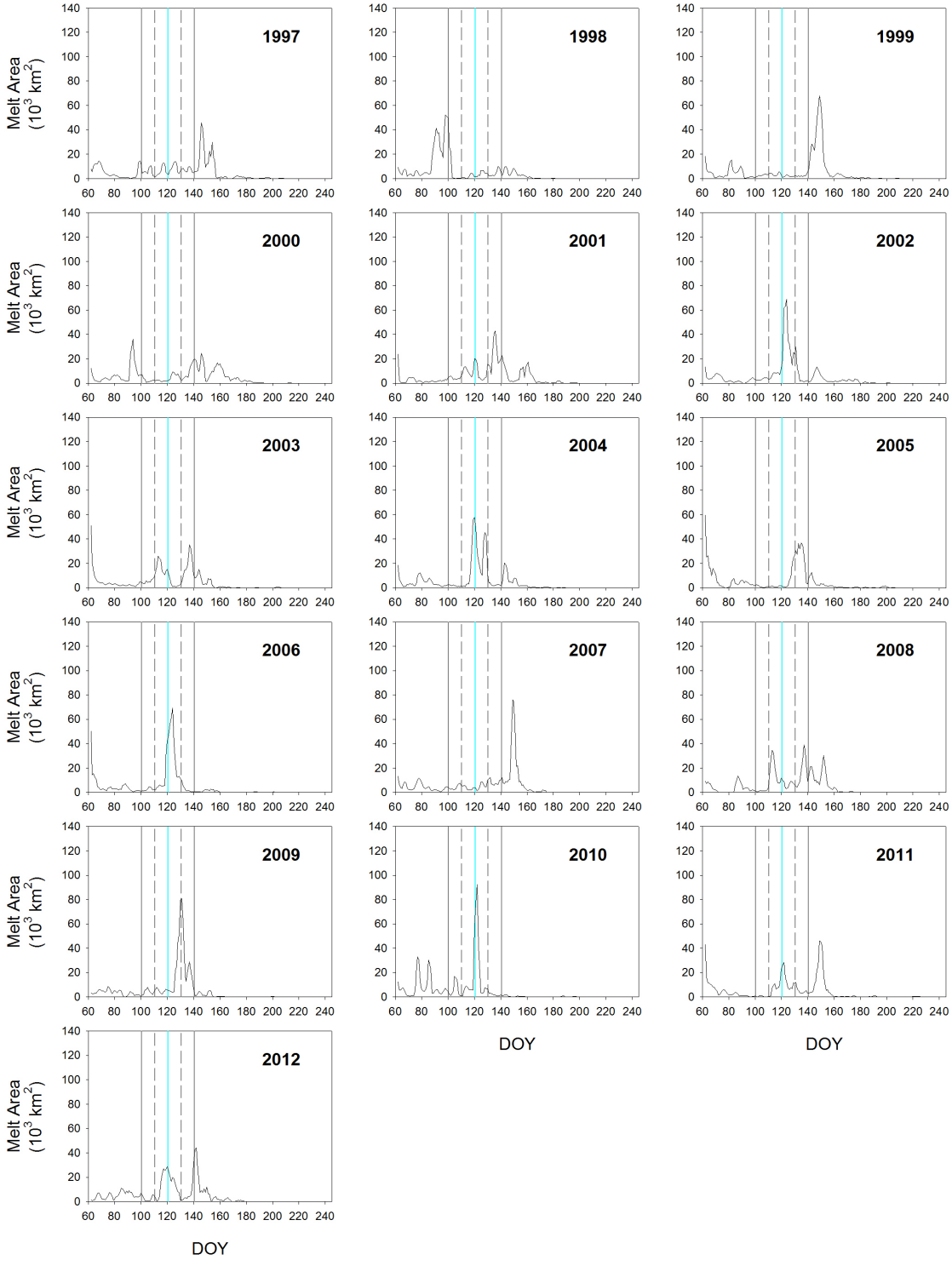

Figure 5.11 Baffin Bay (Continued).

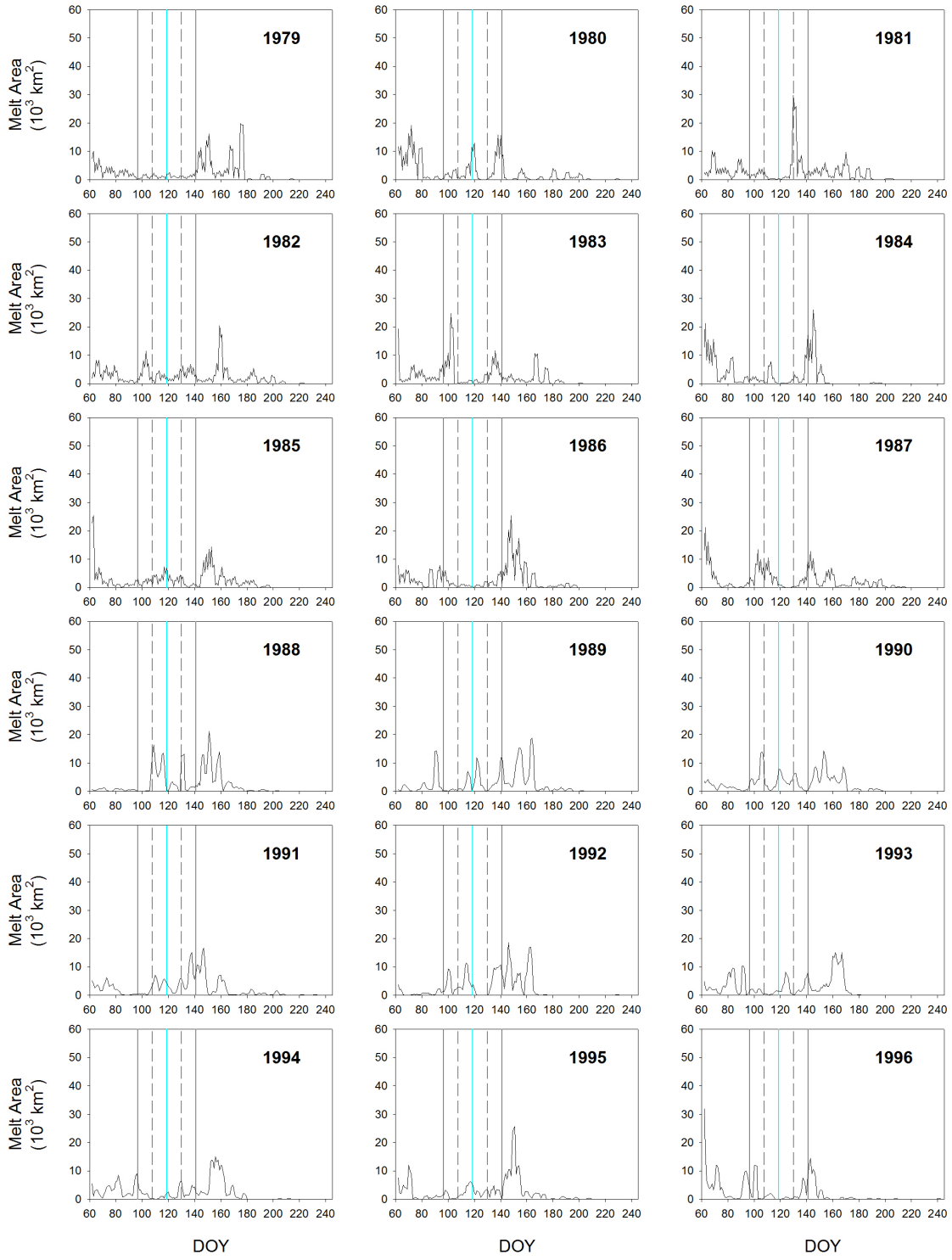

Figure 5.12 Greenland Sea time series of daily MO area (1979 – 2012). The cyan line indicates the mean MO date, while the dashed and solid black lines indicate ± 1 and ± 2 standard deviations from the mean respectively.

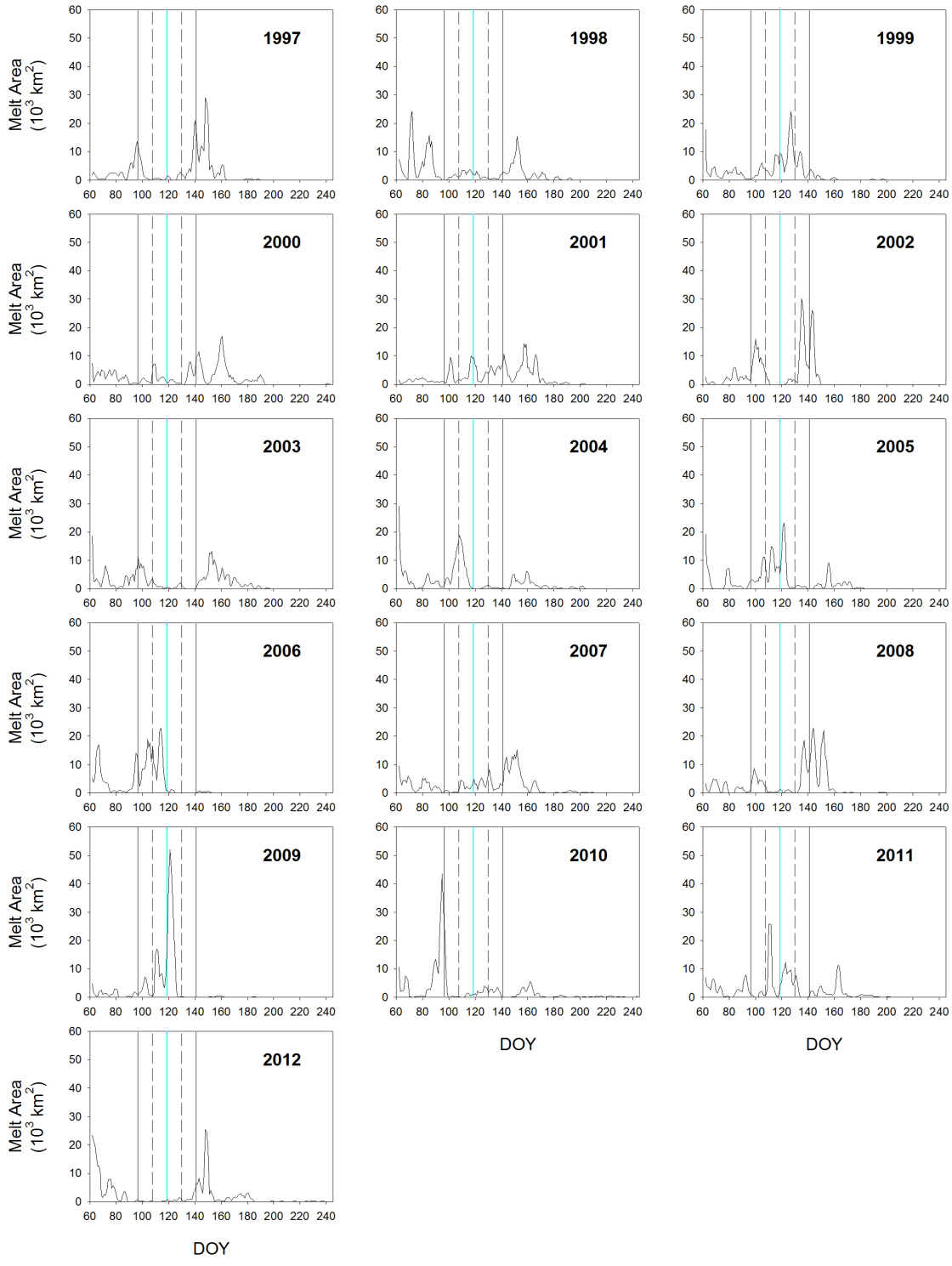

Figure 5.12 Greenland Sea (Continued).

Similar variations in the individual MO area curves exist in different regions and different patterns in the MO area time series can be identified in different years for the same region. Several patterns will be discussed for Arctic Ocean sub-regions (Figures 5.3 – 5.12). For example, there are large areas of melt which occur over very short periods of time, represented by high magnitude, short duration (tall, narrow) peaks in the 3-day averaged MO areas and smaller areas of melt that occur over short time periods, represented by low magnitude, short duration (short, narrow) peaks. Additionally, longer duration events of both higher and lower magnitudes can be identified. While the data for all Arctic Ocean sub-regions are presented in this work, not all melt events over the 34-year data record can be discussed here. Instead the primary focus is to describe common patterns in the magnitude and timing of peaks in the MO area time series and how the variability compares within a region and between regions. It should be noted that many similar patterns in the MO area time series can be identified in multiple regions and in different years although they cannot fully be addressed in this work.

5.3 Classification of melt event types

Peaks in the annual 3-day averaged MO area time series indicate the timing and magnitude of melting events for each sub-region; however, the timing of these peaks during the melt season also varies. Patterns in the daily MO area time series can be described in terms of magnitude (high or low), duration (long or short), and timing (ranging from early to late) of melting events. Figure 5.13 conceptually illustrates what the various combinations of magnitude and duration of melting events can look like. The

illustrations of melting events are shown at the climatological mean MO date (μ) for the region (Figure 5.13); however, actual melting events may occur anywhere along the range in time from early in the melt season, near the mean or middle of the melt season, and late in the melt season. Also note that several local peaks/maxima may occur during an event, especially in longer duration events. In cases where multiple local peaks/maxima occur during a single event, the magnitude of the maximum melting day is used to classify the magnitude of the whole event. MO area that occurs late in the season is not representative of the magnitude of actual melting area since there is less melt-free area available to melt at this point in the season. Thus, any peaks in the daily MO area curves that occur late in the melt season portion are ignored. The end of the season is shaded out in the conceptual diagram to de-emphasize any MO area that occurs during this period (Figure 5.13).

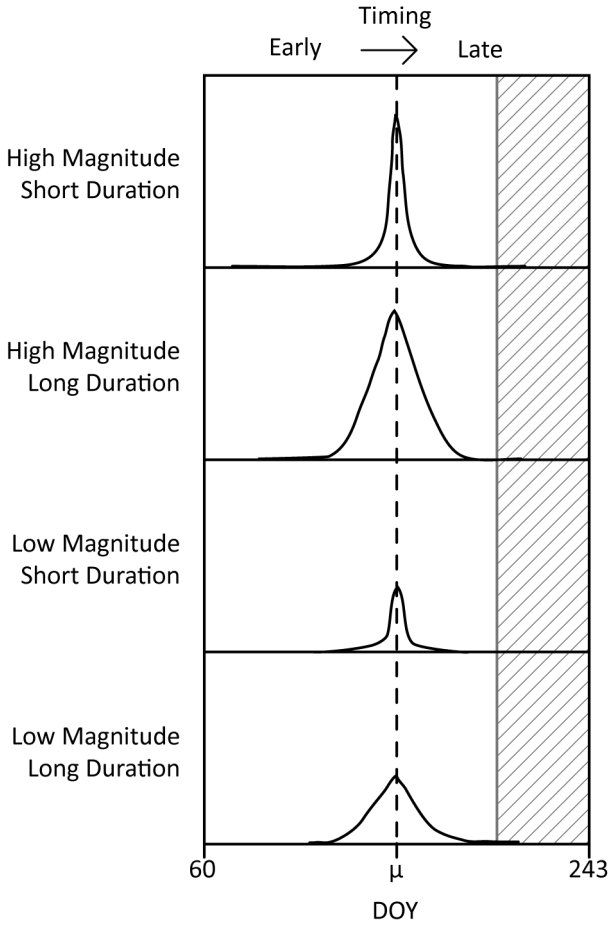

Figure 5.13 Conceptual organization of melt event types. The climatological mean melt onset date (μ) for a sub-region is represented as a dashed line. The hatched area identifies the end of the melt season and uncertainty surrounding late MO area.

A qualitative examination of the 3-day averaged daily MO area time series is used for Arctic Ocean sub-regions. For each sub-region, the magnitudes, duration, and timing of peaks in the daily MO area curves are compared to classify the melting event. For relative comparisons of the daily MO area curves in an individual region (Figures 5.1 – 5.12) note that the scales are the same from year to year and that the climatology mask has been applied before calculating the 3-day averaged time series. Thus, an

accumulation of the daily MO area for each year (1979 – 2012) will sum to the total region area (in km^2) shown in Table 3.2.

The magnitude of a melting event is determined by the relative height of the maximum melting day during the event. If the event contains the annual maximum melt day observed during the year (the tallest peak), the event is categorized as a high magnitude event. If the magnitude of the maximum melting day during the event is equal to or less than the magnitude of the annual maximum melting day, the event is categorized as a low magnitude event. The duration of a melting event is determined using an arbitrary threshold of ~ 10 days. If melting area occurs for fewer than 10 consecutive days, the event is categorized as a short duration event. If melting area occurs for more than 10 consecutive days, the event is considered a longer duration event. A melting event is considered complete on the DOY on which the MO area drops to 0 km^2. For the purposes of this work, "early" and "late" events are melting events that occur more than ±2 standard deviations from the mean MO date (outside of the solid lines on Figures 5.1 – 5.12) and "normal" events are those that occur within ±2 standard deviations from the mean MO date (inside of the solid lines on Figures 5.1 – 5.12).

5.3.1 High magnitude, short duration events

High magnitude, short duration events indicate intense melting where large areas of the sea ice within the region are experiencing MO over a relatively short period of time. In this type of event, the largest daily MO areas observed in the melt season typically occur over 3 – 5 consecutive days surrounded by a day or two where smaller daily MO areas occur. Some examples of this type of melting event are seen in the Barents Sea in

1980 (Figure 5.3); the Kara Sea in 1992 and 1980 (Figure 5.4); the Laptev Sea in 1979 and 1980 (Figure 5.5); the Chukchi Sea in 1982 (Figure 5.7); and the Greenland Sea in 1998 (Figure 5.12). These events are interesting because the melt forcing appears to be targeted over just a few days before ending and returning temperatures that are below freezing to the region. It is likely that these events are caused by transient cyclones that only impact the region for a few days, before moving out of the region and removing the melt forcing atmospheric conditions, shutting off the progression of melting until a later date when a new melting event occurs.

It should be noted that the 27 March (DOY 87) peak in the Kara Sea during 2008 (Figure 5.4) results from a 7-day data outage that occurred 19 – 25 March 2008. Immediately following this outage a melting event is recorded that would be classified as a high magnitude, short duration event responsible for melting over 3.06×10^5 km^2 (35%) of the Kara Sea area. However, due to the recovery of the 10-day window used to calculate MO in the AHRA following the data outage, the timing of this melted area cannot be fully resolved (Figure 5.4). Therefore, this melting event cannot be categorized and is excluded from further analysis.

5.3.2 High magnitude, longer duration events

The high magnitude, short duration melting events described above do not occur every year. It appears to be more common for longer duration melting events to occur where the MO area accumulates at a slower rate over a longer time period. The Kara Sea daily MO area in 1985 characterizes this high magnitude, longer duration melt event type (Figure 5.4). During this event, the MO area between 10 May (DOY 130) and 9 June

(DOY 160) accounts for melting over 74% (6.4 x 10^5 km^2) of the Kara Sea region (Figure 5.4). The MO area peaks on 5 June (DOY 156) in 1985 with 1.11 x 10^5 km^2 of new MO area (Figure 5.4). Since the MO area during this event accrues slowly over ~30 days it is likely that this type of slow-progressing MO event is the result of weaker atmospheric forcing than would occur in high magnitude, short duration cases.

Other examples of high magnitude, longer duration events include events that occur in the Kara Sea in 1981, 1983, 2000, 2003, and 2011 (Figure 5.4); in the East Siberian Sea in 1980, 1997, 1998, and 2002 (Figure 5.6); and in the Beaufort Sea in 1992, 1994, 1998, 2000, and 2009 (Figure 5.8). Although the accumulation of MO area occurs more slowly than short duration events, these melting events are generally responsible for MO over nearly all area in the sub-region. In cases such as these, it is likely that the weather conditions are different from conditions that occur high magnitude, short duration MO area peaks. The high magnitude, short duration events are likely the result of the influence of warm air advection associated with a cyclone where widespread warm temperature anomalies can exist, especially for events that occur early in the melt season. For years where high magnitude, longer duration events exist, it is likely that high pressure systems or northerly surface winds, lead to cooler temperatures and delayed accumulations of MO area.

5.3.3 Low magnitude, short duration events

Examples of low magnitude, short duration events occur in the Kara Sea in 2006 (Figure 5.4); the East Siberian Sea in 1989, 2009, and 2012 (Figure 5.6); and in the Beaufort Sea in 2002 (Figure 5.8). These events are primarily small melting events that

occur anomalously early in the melt season. In each of these cases, the peak in MO area occurs earlier in the melt season than −2 standard deviations from the mean MO date. Due to lower mean air temperatures near the beginning of the melt season, it is likely that the smaller magnitude melting during these events is a result of very limited warming from warm air advection or cloud cover from a transient cyclone. Once the transient system is no longer influencing the area, melting ceases and sub-freezing temperatures return to the region until later in the season when the next melting event occurs.

5.3.4 Low magnitude, longer duration events

Low magnitude, longer duration events are characterized by examples from the Kara Sea in 1997 (Figure 5.4), the East Siberian Sea in 2003 (Figure 5.6), and the Beaufort Sea in 1993 (Figure 5.8). In years where low magnitude, longer duration events are present, the daily MO area time series over the melt season lacks a large, high magnitude peak such as occurs when high magnitude, short or long duration events occur. In these years, there is an absence of any large, dominating melting event that is responsible for a majority of melted area in the sub-region. Rather, the melting area that occurs during the melt season develops gradually and in some cases such as 1997 in the Kara Sea, no single melting day is responsible for more than 2.5 x 10^4 km^2 of melted area (Figure 5.4).

5.4 Extreme melt onset events

The four types of MO events identified above can be distinguished in multiple sub-regions over the 34-year data record. The high magnitude, short duration peak events represent a fast occurring event that is responsible for the melting over a large

proportion of the sea ice cover in as little as 3 days. The high magnitude, longer duration events represent extended periods of melting areas that spread across the ice more slowly. The shape of the peak gives some insight into the type of atmospheric conditions that must be present during the melting periods as described above, however, the daily MO areas can also be described in terms of intensity based on how anomalous the timing of the melting events are. Peaks that occur earlier in the year than −2 standard deviations from the mean MO date are anomalous. While it is important to note that MO areas that occur later in the year do not carry the same weight as MO area that occurs earlier in the year due to the limitations of the MO data and the elimination of pixels melted earlier in the season, peaks in MO area that do not occur until +1 or +2 standard deviations from the mean later in the year are still interesting.

In cases where peaks in MO occur anomalously late in the year, it is not so much the presence of the peak late in the season that is surprising given that mean air temperatures reach the freezing point in the late spring and early summer months over much of the Arctic Ocean, rather the fact that the MO area did not occur earlier in the season indicates that melting was delayed in this region relative to the mean MO date. For example, the largest peak in daily MO area for the Kara Sea occurs in 1981 on 7 June (DOY 158, Figure 5.4). This peak is large in terms of intensity since the maximum melting day alone is responsible for melt over 16% of the Kara Sea region's area (Figure 5.4). However, take note that the largest single day of MO area during this year occurs more than +2 standard deviations from the mean MO date of 11 May (DOY 130.5, Table 4.1, Figure 5.4). Based on the shape of the peak and the amount of MO area that

accrues during this short time period, it may be assumed that a significant weather event occurred that induced the melting of this large area. However, the timing of this peak (one month later than normal) complicates this issue. During June, the sun angle approaches its highest point at the solstice, and average air temperatures warm. That is, the region is seasonally primed to melt at this time without the effects of strong forcing from a transient event. Rather, the important observation for this year in the Kara Sea is that the majority of sea ice extent in the region did not melt prior to this period, in the early summer, when melt onset should have typically occurred a month earlier.

Atmospheric conditions necessary to produce a melting pattern which would be expected to occur during a high magnitude, short duration MO peak that occurs early in the year, might not be observed during years where the peak occurs late in the season. The effects of seasonal air temperature increases as the season progresses in each Arctic sub-region, combined with the effects from previously melted pixels being unable to indicate areas of new melting, reduces the impact of single weather events on the observations of MO area late in the season. That is, due to the seasonal increases in air temperatures by latitude, less intense forcing from a cyclonic event would be needed to induce MO over the sea ice at a later date. Therefore, MO events that occur early in the year are more extreme or unexpected than those that occur late in the year.

5.5 Changes in MO event timing

Significant negative trends in the mean MO date over the last several decades exist for many of the Arctic Ocean sub-regions (Figure 4.7). Evidence of these trends also appears in the daily MO area time series even though interannual variability in

melting events is high. The greatest MO day in the Kara Sea over the 34-year data record occurs on 7 June (DOY 158) 1981 on which 1.34 x 10^5 km^2 of the region area experienced MO. The second greatest MO peak occurs on 7 May (DOY 127) 2003 on which 1.16 x 10^5 km^2 experienced MO and the third greatest MO peak occurs on 11 June (DOY 162) 1983 on which 0.92 x 10^5 km^2 of the region begins to melt. Given that the mean MO date for the Kara Sea occurs on 11 May (DOY 131, Table 4.1) it is interesting to note that the peak MO days in 1981 and 1983, occur approximately 30 days after the mean MO day 11 May (DOY 131), while the peak melting day in 2003 7 May (DOY 127) occurs near the mean MO day. An overall tendency towards earlier MO is apparent because of the early 2003 peak day relative to the peak days in 1981 and 1983; however, the magnitude of MO area in 2003 is not greater or dissimilar to the magnitude of large melting events in the 1980s. The melting event in 2003 does, however, occur earlier in the year than either of the 1980s peak events.

In the case of 1981 and 1983 in the Kara Sea, the magnitude of the melting event peaks appear significant, but when placed within the context of mean MO timing it becomes clear that the important feature during these years is that early springtime conditions suppressed earlier MO areas from occurring. Given the negative trend in Kara Sea MO timing (Figure 4.7), these events, while very large in terms of melted area, occur very late in the season. Being able to identify the exact point in time when these two melting events occur makes the magnitude of the peaks less relevant than the abnormally late timing of the events.

5.6 Discussion and summary: influence of melt onset and weather events on end of season sea ice loss

The changing timing of some extreme melting events and trends in MO dates is another signal of the rapidly changing Arctic cryosphere. However, the implications of these extreme events are still unclear. Given the effects of positive feedbacks that occur within the ice-albedo feedback mechanism [*Curry et al*., 1995], one would expect that anomalously early melting of the snow cover atop the sea ice in a melt season would precede anomalously low sea ice extents at the end of the melt season. However, *Wang et al.* [2011] have found that the timing of MO is largely independent from the subsequent end of season sea ice extent at the regional scale. That is, a region with anomalously early MO in the spring and early summer is not an indication that this same area will have observations of anomalously low sea ice extent at the end of the melt season. Despite this apparent incongruence between MO timing and the sea ice conditions at the end of the melt season, the significant trends towards increasingly early melt onset over the last 3 decades for much of the Arctic (Figure 4.7) align with the fact that sea ice is becoming more sensitive to changing atmospheric conditions.

The mechanisms leading to record-breaking low sea ice extents at the end of summer are complex. September 2012 currently holds the record for low sea ice extent [*Parkinson and Comiso*, 2013]. This coincides with the extremely early MO events observed in the East Siberian, Kara, and Barents Sea regions (Figures 5.6, 5.4, 5.3); however, *Simmonds and Rudeva* [2012] describe the "Great Arctic Cyclone of August 2012" over the Central Arctic, which drastically influenced the end of season sea ice extent. The cyclone had such a large impact on the sea ice extent in part due to the

timing and location of the cyclone. The cyclone occurred between 2 and 14 August when the ice concentrations were already low, and the thin, melting sea ice was more susceptible to transport by wind and ocean currents. The cyclone sheared off a large area of sea ice from the central sea ice pack and the separated area of sea ice was transported southward into the East Siberian Sea where it was more easily melted.

The year 2007 which had previously held the record for low sea ice extent experienced a different set of summertime conditions leading to the record low ice extent observed. In 2007, the end of season sea ice extent was largely impacted by preconditioning of the ice in prior months. Further, anomalous southerly winds were able to advect much of the thin, sea ice northward away from the Eurasian coastline in the Chukchi, East Siberian, and Laptev Seas [*Comiso et al.,* 2008]. Although preconditioning of the sea ice remains an important reason for the continued decline in sea ice in the Arctic, the specific factors contributing to the sea ice reaching record-breaking extents through the duration of the melt season for a single year are different. Due to continued volume loss of sea ice, there are several factors that can produce record lows in sea ice. The specific mix of these factors that present themselves during a record-breaking year can be different from the set of factors that lead to record low sea ice extents in another year.

A direct connection between early MO and end of season sea ice extents via the ice-albedo feedback loop remains hard to distinguish, but it is clear that melting and ablation of the sea ice can be greatly influenced by the passing of a single cyclone. Therefore, it is necessary to look in greater depth at the influence of the shorter-term

weather events on the sea ice cover. The timing of when large melting events occur during the melt season indicates an early or delayed MO signal for each region. The strength or track of the atmospheric weather system forcing the onset of melting over a region area can also affect the size of the peak of melting area where very intense melt conditions produce larger areas of MO. The regional and temporal variability of MO across the regions and the sensitivity of the timing of MO area accumulations are most likely due to the daily weather conditions during melt. Further analysis of the MO area patterns in each region and the direct relationship to the atmospheric conditions is necessary to thoroughly explain the causes of the variability in daily MO area at a larger scale.

CHAPTER 6 – RELATIONSHIP BETWEEN DAILY MELT ONSET PATTERNS AND ATMOSPHERIC CONDITIONS

6.1 Spatial patterns of melt onset area

To examine the spatial variation during melt onset (MO) events described in Chapter 5, the annual maps of MO dates (Figure 4.1) can be partitioned into daily maps which highlight those pixel locations on the sea ice that are experiencing MO. A daily map of MO pixel locations within a sub-region of the Arctic represents the spatial progression of MO area across an area of the sea ice for a period of time. Therefore, the daily spatial pattern in MO area is used to relate the melting events with the atmospheric conditions present at the time of melt.

To examine the spatial character of the accumulations of MO area in the melting event types described in Chapter 5, representative example cases were chosen from the Kara, East Siberian, and Beaufort Seas. The Kara, East Siberian, and Beaufort Sea regions were chosen to represent example cases because they are relatively large Arctic sub-regions and are distributed around the Arctic Ocean (Figure 3.2). These three regions represent the most highly variable in terms of MO timing (Table 4.1) and are representative of regions on both the Eurasian and North American sides of the Arctic. Since the boundaries drawn between Arctic sub-regions are largely arbitrary and the scale of individual transient, synoptic weather events has the potential to influence more than one region on a single day, the example regions have been chosen so that they are not adjacent to one another.

Identifying the timing of a MO event and further, identifying the day by day pattern in melting area provides a way to spatially track this progression across the surface of the sea ice cover. Given that the onset of melting is a result of atmospheric conditions producing surface air temperatures that reach the freezing point or slightly above, tracking the progression of melting area on the sea ice coincides with the presence of weather features that result in air temperatures near freezing. The hypothesis then becomes that distinct patterns in the daily MO area associated with melting events (described in Chapter 5) can be identified and are caused by differing sets of atmospheric conditions.

To illustrate the progression of melting area on the sea ice during a melting event, several maps are shown for each day of the event that highlight the pixel points that are flagged as melting on each day in the series. Hereafter, the pixels that are flagged as melting on a single date are referred to as "currently" melting (or "current MO"); that is, for the date in question all pixels flagged as melting on that DOY were *currently* experiencing MO on that date in time. Additionally, because each pixel can be flagged with a MO date only once per year, the status of all currently melting pixels changes to "previously" melted on the following day and remains flagged as previously melted (or "previous MO") for the remainder of the melt season.

For all maps showing the progression of MO area in the following sections, "current MO" locations are shown in red to highlight pixels that melted on the indicated DOY, while "previous MO" locations are shown in pink to highlight pixels that have melted prior to the currently mapped date. White pixels show sea ice locations that have

not yet melted or will melt at a later date. Due to the arbitrary boundaries between sub-regions, MO information for sea ice locations directly adjacent to the sub-region being examined are shown, however, shading is used to de-emphasize the MO locations occurring outside of the sub-region boundary.

Example events are shown for each type of MO event described in Chapter 5 including: (1) high magnitude, short duration events; (2) high magnitude, longer duration events; (3) low magnitude, short duration events; and (4) low magnitude, longer duration events. An example of the first type of MO event (a high magnitude, short duration peak) occurs in 1992 in the Kara Sea and is associated with the peak spanning 30 April – 6 May (DOY 121 – 127, Figure 5.4). The second MO event type (a high magnitude, longer duration peak) is represented by events in the Kara Sea during 10 May – 13 June (DOY 130 – 164) in 1985 (Figure 5.4) and in the Beaufort Sea during 10 May – 23 May (DOY 131 – 144) in 1992 and 19 – 28 April (DOY 109 – 118) in 2009 (Figure 5.8). The low magnitude, short duration events are represented by the East Siberian Sea peaks in the daily MO area time series over 14 – 20 April (DOY 104 – 110) in 1989 and over 5 – 15 March (DOY 65 – 75) in 2012 (Figure 5.6). The low magnitude, longer duration events are represented by the East Siberian Sea peak over 18 – 30 April (DOY 108 – 120) in 2005 (Figure 5.6). In addition to being distinct melt event peaks, the melt events presented for the Beaufort Sea in 2009 and all three East Siberian Sea events are anomalous because they occur more than two standard deviations from the mean MO date early in the year (Figures 5.6, 5.8).

For each of the example events, the daily maps of MO are shown and compared with atmospheric data from reanalysis products including mean sea level pressures (MSLP), air temperatures, and 10 m wind vector directions and magnitudes to characterize the synoptic scale weather events at the surface present during MO. The comparison of spatial patterns in MO area during melting events with atmospheric data gives insight into the type of atmospheric conditions necessary to induce varying types of melting events identified in Chapter 5.

6.2 High Magnitude, Short Duration Melting Event: Kara Sea 1992

The largest, intense peak in MO area for the Kara Sea in 1992 begins in May (Figure 6.1), with the greatest MO area day occurring on 3 May (DOY 124). Prior to this peak MO day, MO area accumulates slowly on 30 April – 1 May (DOY 121 – 122). MO is observed at only 14 pixel locations (0.09×10^5 km^2) on 30 April (DOY 121) and 41 pixel locations (0.3×10^5 km^2) on 1 May (DOY 122). On 2 May (DOY 123), however, the number of pixels, with MO begins to increase. 3 May (DOY 124) is the peak melting day with the majority of the Kara Sea (168 pixels, 1.05×10^5 km^2) being melted on this day. MO area continues to accumulate quickly through 4 – 5 May (DOY 125 – 126) before slowing on 6 May (DOY 127). During this melt event, the majority of the MO area accumulates between 2 May (DOY 123) and 6 May (DOY 127). Not only is the MO area accumulation for this event occurring over just a few days, but the melted area fills in locations adjacent to those that have previously melted and is primarily restricted to the southwestern portion of the region. In total, this 5-day melting event accounts for 3.37×10^5 km^2 of MO area or 39% of the Kara Sea's total area. The time frame and spatially

adjacent nature of MO area accumulations horizontally across the ice surface indicate that the melting across several days is the result of strong cyclonic forcing.

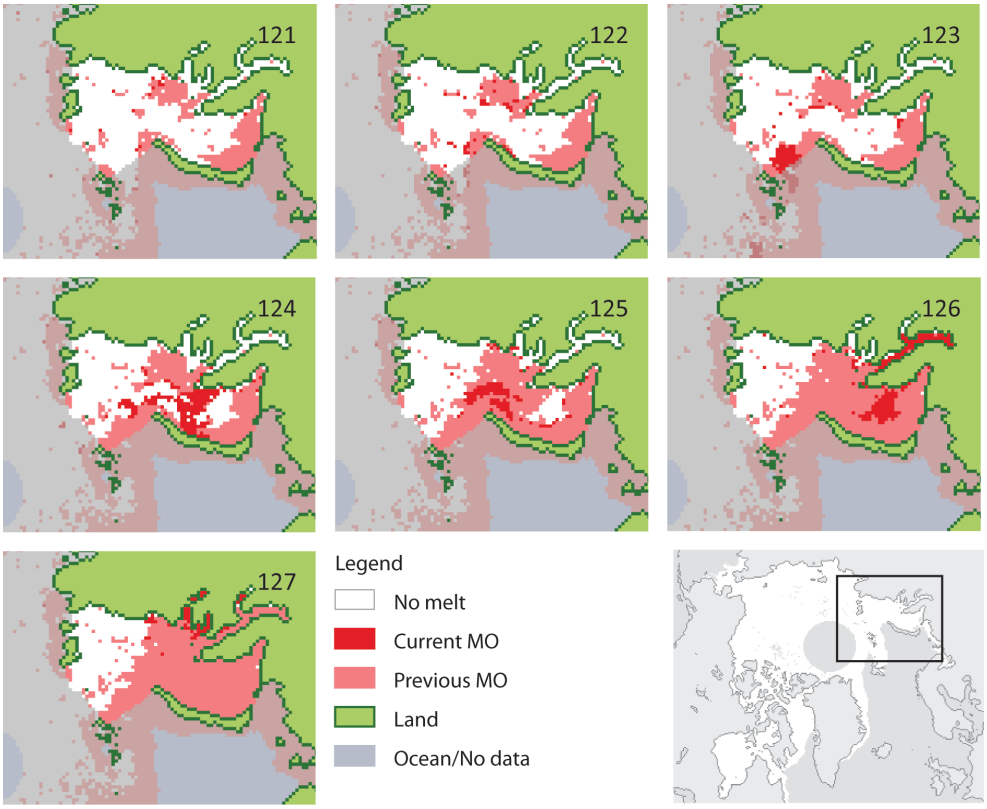

Figure 6.1 Progression of Kara Sea MO area for 30 April – 6 May (DOY 121 – 127) 1992. MO locations for the current DOY and where MO has already occurred on a previous day are highlighted. Pixels outside of the region (see Figure 3.1) are de-emphasized to indicate MO conditions adjacent to the Kara Sea.

During this event, the daily averaged MSLP, 925 hPa air temperatures, and wind vectors (Figures 6.2 – 6.4) indicate that a cyclone is present in the Kara Sea region during this melting event. On the peak melting day (3 May, DOY 124) an area of low pressure, located to the southwest of the Kara Sea and centered over northern Norway, develops (Figure 6.2) and during the next two days approaches and passes over the Kara Sea (Figure 6.2). The position of this cyclone results in a southerly wind direction within the

Kara Sea (Figure 6.3) on 3 – 4 May (DOY 124 – 125) and increasing air temperatures (Figures 6.4). During this three-day period, the 273 ºK isotherm advances over the Kara Sea region from the southwest (Figure 6.4) indicating the advection of warmer air temperatures from the south. The melting pattern seen over the southwestern Kara Sea during this period corresponds with the above freezing temperatures advancing over the sea ice (Figure 6.4). It is important to note that the 925 hPa air temperatures shown in Figure 6.4 are the averaged daily temperatures. The AHRA algorithm detects the metamorphosis of snow grains when air temperatures reach the freezing point and liquid water becomes present in the snow pack atop the sea ice from daily averaged brightness temperatures, however, diurnal temperature fluctuations above and below freezing can still occur after the MO date is detected [*Drobot and Anderson*, 2001a]. Thus, daily averaged 925 hPa temperatures above freezing are not necessary to trigger the onset of melting, but rather, the maximum daily air temperatures must reach the freezing point to initiate melt. In this case, however, the intense melting event over the Kara Sea is related to the presence of a cyclone tracking directly over the Kara Sea, which increased the daily average air temperatures above 273 ºK and induced MO over a large portion of the sea ice cover in this region.

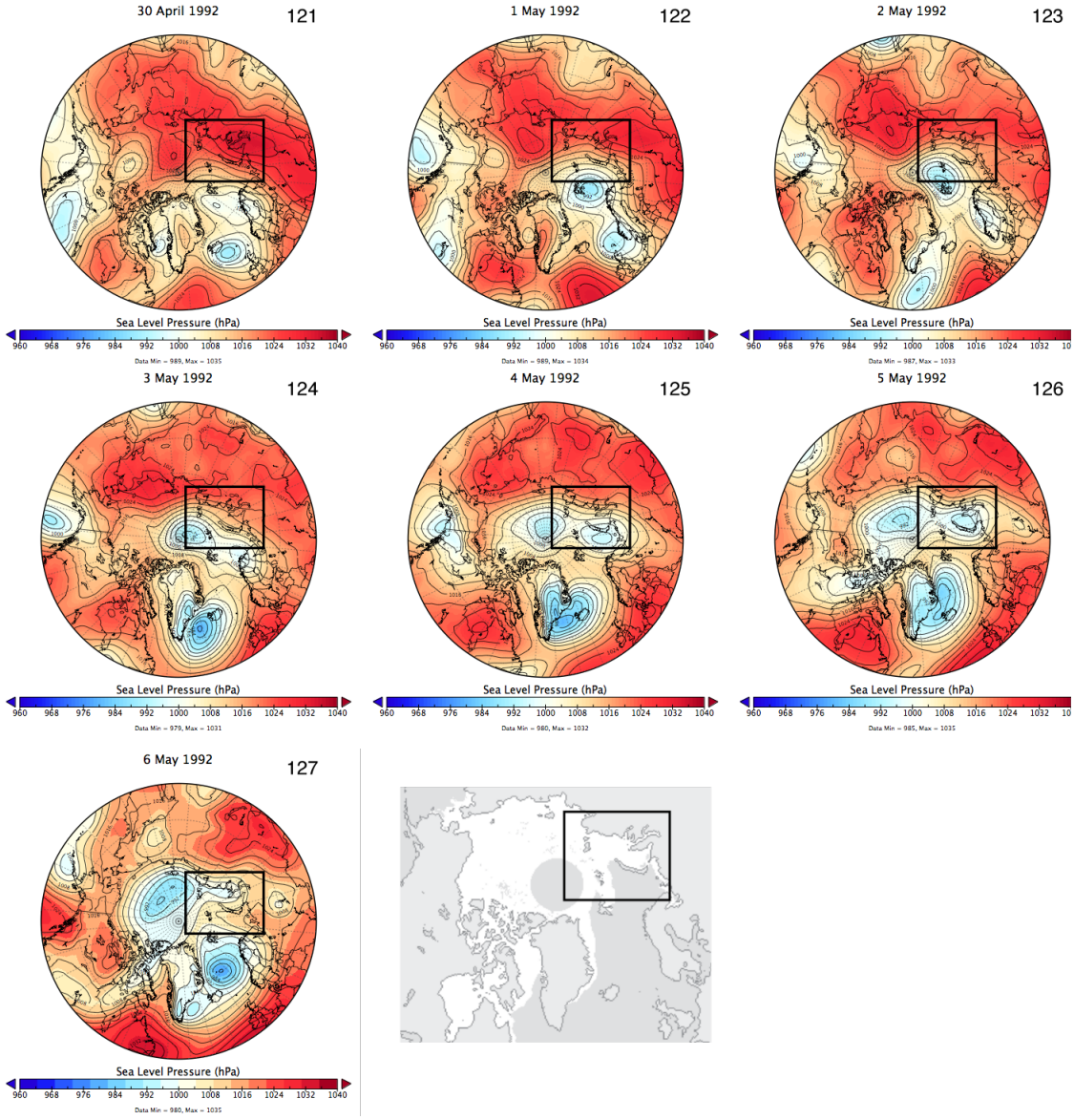

Figure 6.2 Daily mean sea level pressures (hPa) for 30 April – 6 May 1992.

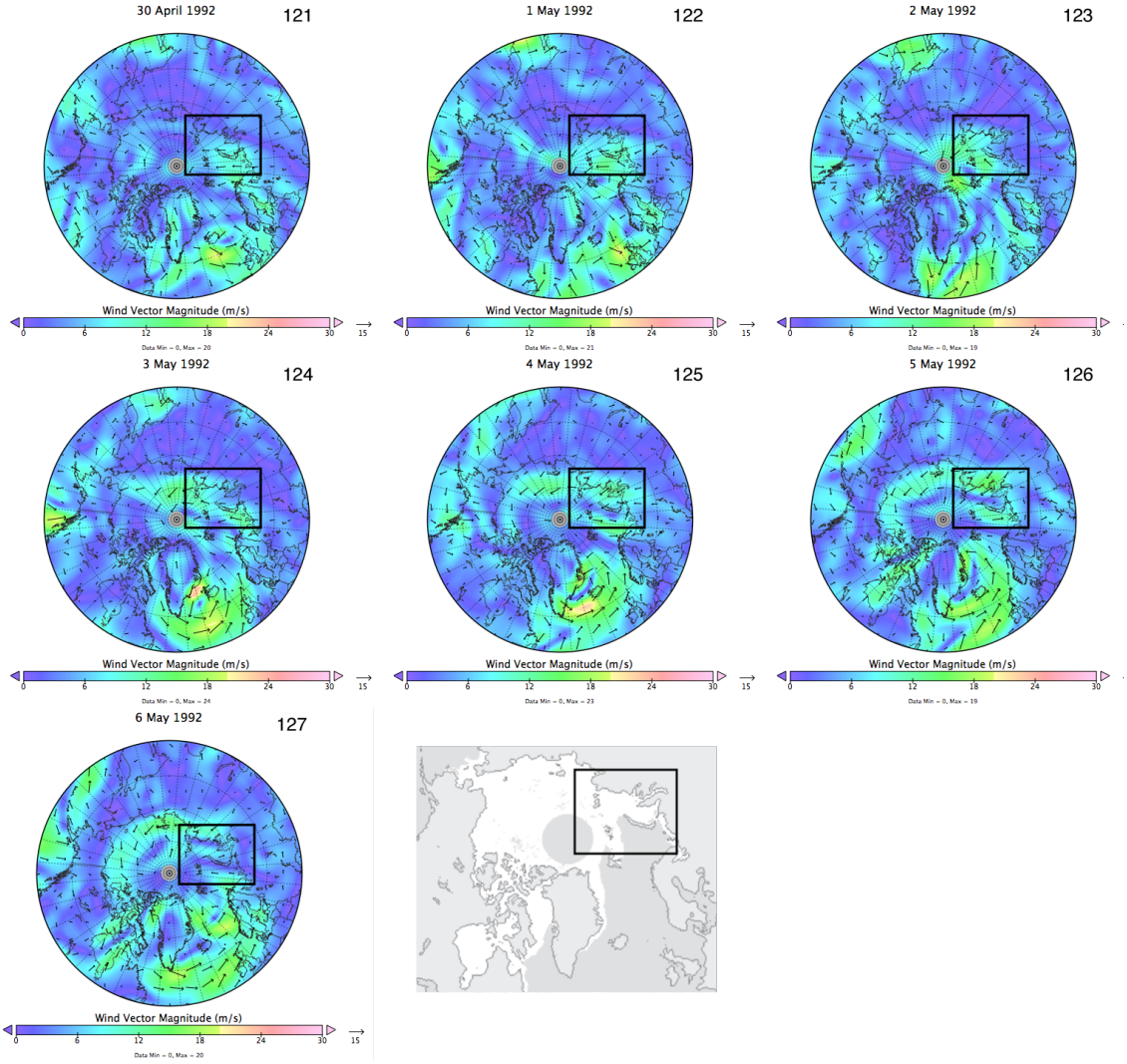

Figure 6.3 Daily mean vector wind directions and magnitudes (ms^{-1}) for 30 April – 6 May 1992.

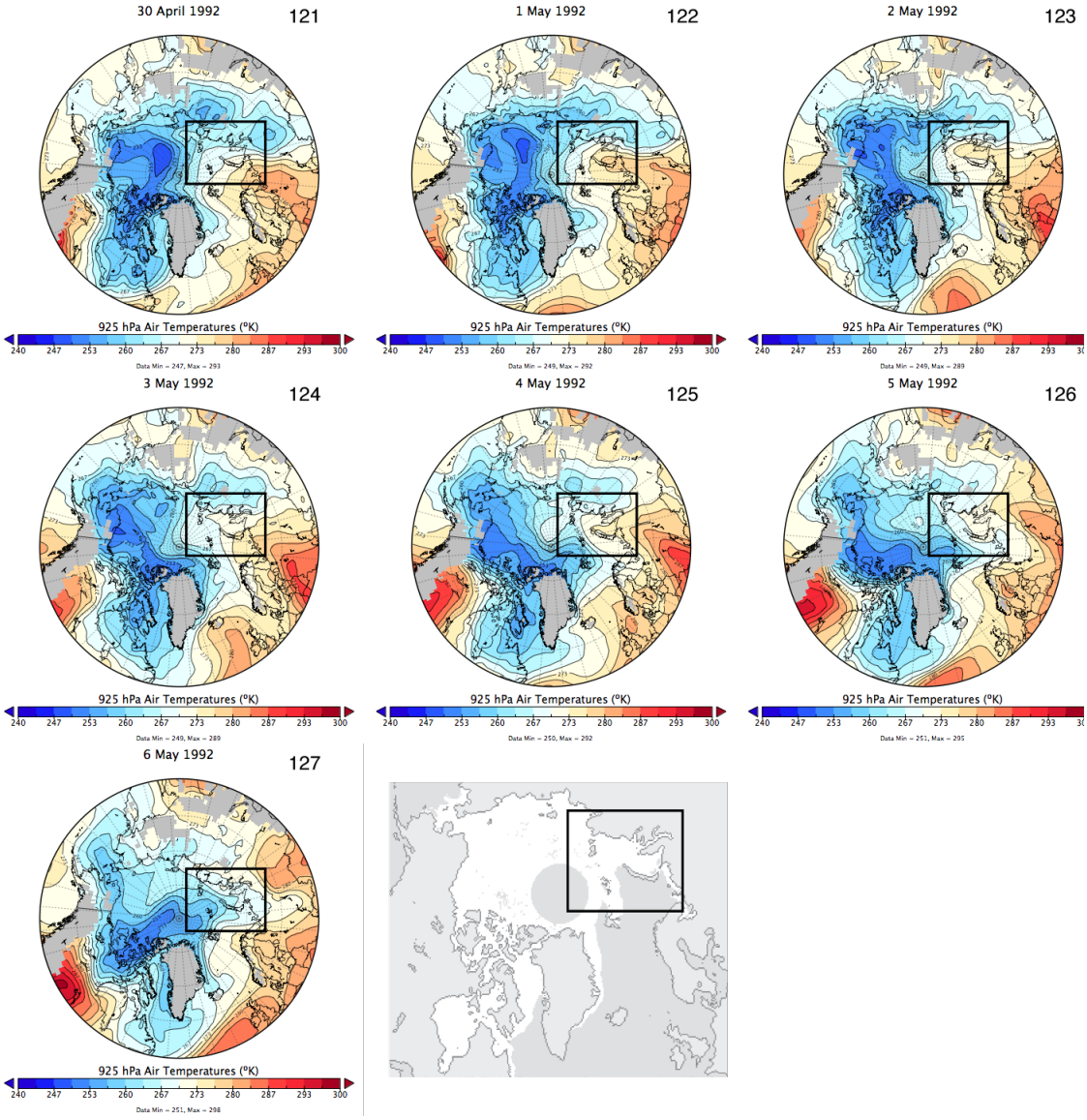

Figure 6.4 Daily mean 925 hPa air temperatures (ºK) for 30 April – 6 May 1992.

6.3 High Magnitude, Longer Duration Melting Events

6.3.1 Kara Sea 1985

A high magnitude, longer duration peak in the daily MO area curve, the second melting event type, can be characterized during 1985 for the Kara Sea (Figure 6.5). The

melt accumulation area from 10 May – 13 June (DOY 130 and 160) accounts for over 74% (6.4×10^5 km^2) of the Kara Sea region. It should be noted that MO data in 1985, a SMMR year, are collected every other day due to sensor limitations. The 1985 case occurs later in the year than the 1992 Kara Sea case although more total area begins melt during this event than for the 1992 case. Since the MO area accumulates more slowly over ~30 days this type of slow-accumulating MO event is the result of weaker atmospheric forcing. Similar to 1992, new MO area tends to accumulate at locations adjacent to MO locations from the previous day, showing the progression of MO. The MO area peaks on 5 June (DOY 156) in 1985 with 1.11×10^5 km^2 of new MO area.

Figure 6.5 Progression of Kara Sea MO area for 10 May – 13 June (DOY 130 – 164) 1985. MO locations for the current DOY and where MO has already occurred on a previous day are highlighted. Pixels outside of the region (see Figure 3.1) are de-emphasized to indicate MO conditions adjacent to the Kara Sea.

Composite mean atmospheric conditions for the 34 days from 10 May – 13 June (DOY 130 – 164) in 1985 including: MSLP, 2 m surface air temperatures, and wind vectors are shown in Figures 6.6a, 6.6c, and 6.6e. Composite anomalies of MSLP and 2 m air temperatures relative to the 1981 – 2010 climate averaging period for the same days in 1985 are shown in Figures 6.6b and 6.6d. The mean atmospheric conditions

during the 1985 Kara Sea melting event show near-normal MSLP over the northern portion of the Kara Sea and anomalously low MSLP over the southern Kara Sea and the Ural region of Russia on the continent (Figure 6.6b). Although low pressure systems are found adjacent to the Kara Sea during the melt event of 1985, the position of the low pressure area is different from the melting event of 1992 described above. In this case, several transient cyclones do occur during the 34-day period, however, they tend to track to the south of the Kara Sea. As a result of the mean pressure pattern, the mean wind direction over the Kara Sea tends to be northeasterly (Figure 6.6e) and 2 m air temperatures are anomalously cool (Figure 6.6d).

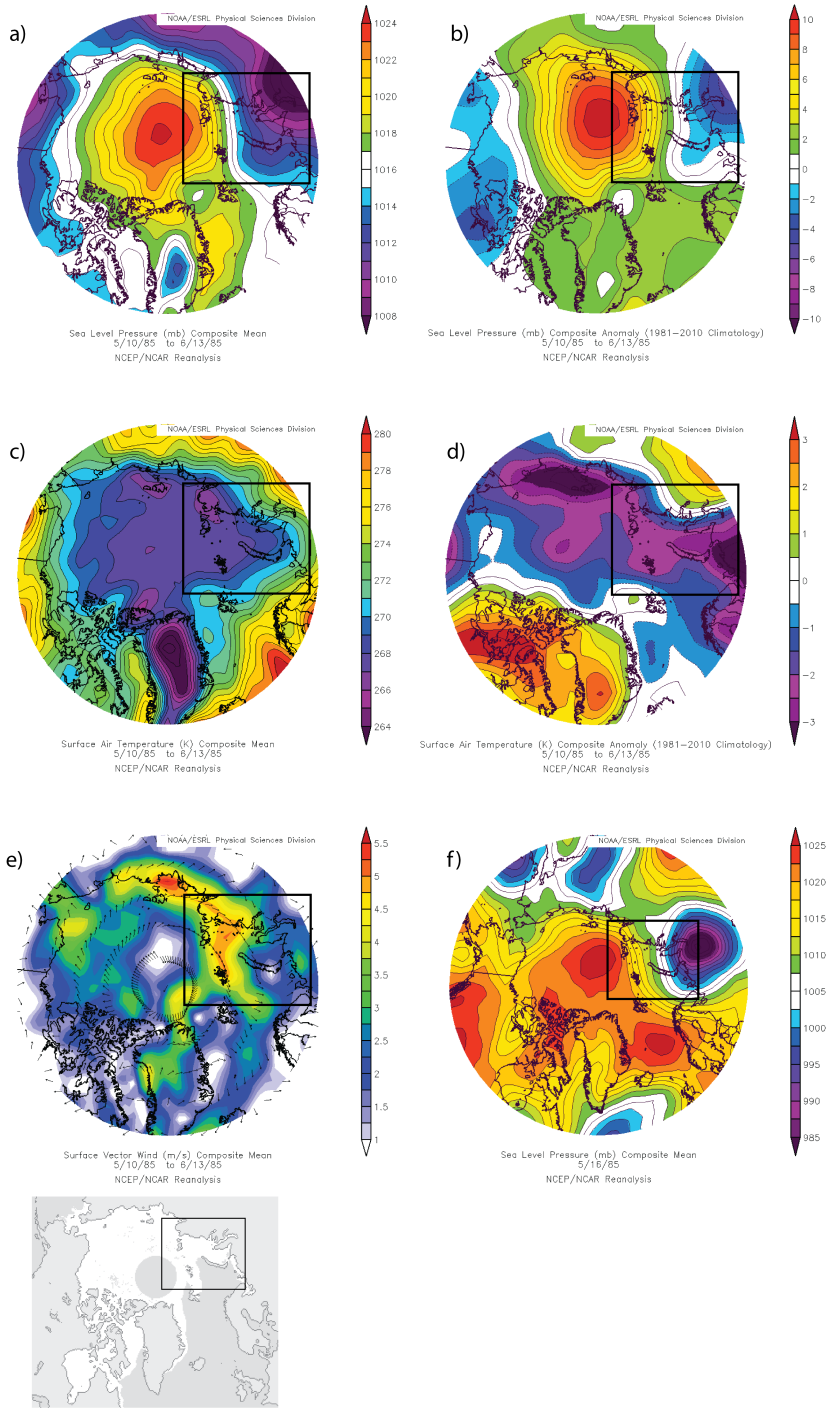

Figure 6.6 Composite mean atmospheric (a) mean sea level pressures; (b) sea level pressure anomalies; (c) surface temperatures; (d) surface temperature anomalies; (e) vector wind directions and magnitude for 10 May – 13 June (DOY 130 – 164) 1985. Daily (f) mean sea level pressures are shown for 16 May (DOY 136) 1985. Boxes define the region surrounding the Kara Sea as shown in Figure 3.1.

One example of a cyclone with a central pressure of less than 985 hPa (Figure 6.6f) occurs on 16 May (DOY 136). This cyclone tracks to the south of the Kara Sea, resulting in a northerly wind direction and cooler air temperatures over the region (not shown). Had the track of this cyclone passed over the Kara Sea, warm air advection via southerly cyclonic winds could have produced a more intense, 3 – 5 day melt onset pattern similar to that which occurred in 1992. The averaged MSLP pattern and resultant low temperature anomaly suppressed the melting during this period in 1985, leading to an extended period of slowly accumulating MO area in the Kara Sea. The spatial pattern in daily MO area shows that MO area in 1985 tends to begin near the coastline and spread towards the northeast towards the central Kara Sea (Figure 6.5) although temperatures in the region are 2 – 3 ºK below normal (Figure 6.6d). It is likely that in the absence of a strong cyclonic influence and advection of warmer temperatures like occurs in 1992, increasing latitudinal temperatures during May and early June contributed to the spatial patterns of MO area seen in the Kara Sea during the 1985 melting event.

6.3.2 Beaufort Sea 1992

The Beaufort Sea case during 1992, which occurs four days later than the end of the Kara Sea high magnitude, short duration event described above, is representative of a high magnitude, longer duration event. Two distinct peaks in the daily MO area time series in 1992 during 10 – 23 May (DOY 131 and 144) occur (Figure 5.8). During this time period, the first peak with the maximum on 13 May (DOY 134) is of a lower magnitude than the following peak with a maximum on 22 May (DOY 143). The definition of MO events based on the daily MO area time series alone (see Section 5.2),

would indicate that the period of time over which these two peaks occur is considered a single MO event since the daily MO area does not drop to 0 km^2 between the peaks in 1992. To further examine this event, the spatial patterns in daily MO area are shown for each day during this melting period (Figure 6.7).

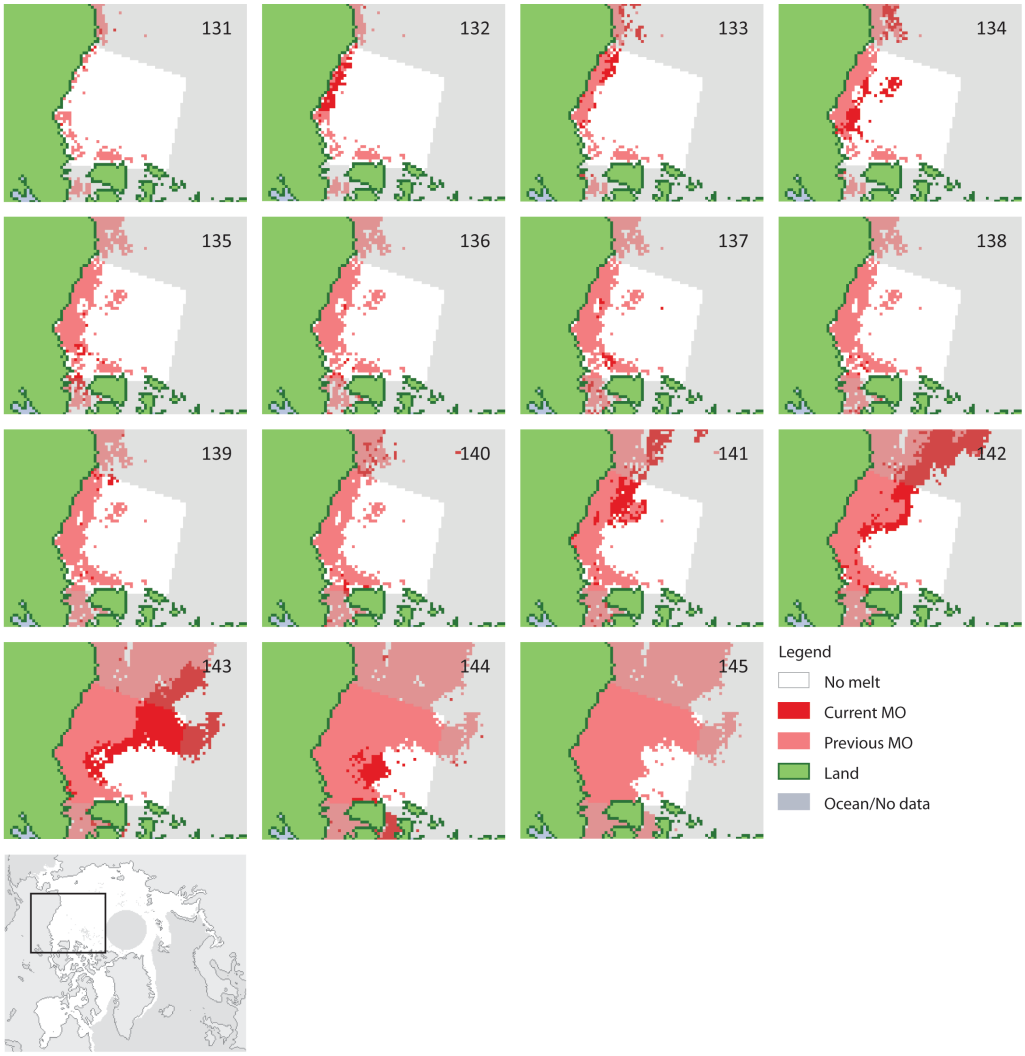

Figure 6.7 Progression of Beaufort Sea MO area for 10 May – 24 May (DOY 131 – 145) 1992. MO locations for the current DOY and where MO has already occurred on a previous day are highlighted. Pixels outside of the region (see Figure 3.1) are de-emphasized to indicate MO conditions adjacent to the Beaufort Sea.

A day-by-day analysis of the spatial patterns during the 1992 Beaufort Sea MO event show that the two peaks in MO area during this event represent melting in two separate regions of the Beaufort Sea. The first peak (maximum MO on 13 May, DOY 134) in the MO area time series is a result of melting occurring along the North American coastline (Figures 5.8, 6.7), over the southernmost portion of the Beaufort Sea region. The majority of MO area during this first peak in the daily MO area time series (Figure 5.8) accrues on 11 – 13 May (DOY 132 – 134, Figure 6.7). The spread of new MO area slows during 14 – 19 May (DOY 135 – 140) although the daily area never drops to 0 km^2 (Figures 6.7, 5.8). On 20 May (DOY 141), the addition of new melting area increases dramatically, reaching the maximum MO date for this melt event on 22 May (DOY 143). Melting for this second peak in the melt event largely occurs in the northwestern quadrant of the Beaufort Sea. Following the peak melting on 22 May (DOY 143), the majority of the Beaufort Sea Region has already melted and on 24 May (DOY 145) no new MO area occurs indicating the end of the MO event.

The locations of the melting area within the Beaufort Sea associated with each peak during this MO event are distinctly different. Since the spread of new MO area during each peak tends to occur adjacent to area melted in the few days previously and the peaks are separated by a short period of time where little MO area accumulation occurs, the spatial patterns in MO area confirms that the melting associated with these two separate peaks are associated with different atmospheric forcing.

The coastal melting from the first smaller peak (maximum 13 May, DOY 134) is associated with a weak low pressure system to the west of the Beaufort Sea (Figure 6.8)

and a westerly wind (Figure 6.9). On 13 May (DOY 134) the daily mean 270 ºK isotherm at the 925 hPa pressure level is located over the southern Beaufort Sea (Figure 6.10) where the MO area occurs along the coastline (Figure 6.7). Following the passing of the low pressure center, high pressure and light winds are present over the Beaufort Sea from 16 – 19 May (DOY 137 – 140, Figures 6.8 – 6.9). The new MO area accumulations during 16 – 19 May under the influence of high pressure are small and it is assumed that melting is ongoing at all pixels locations in the southern Beaufort Sea. The limited amount of new MO area during this period between peaks are attributed to the lack of clouds associated with high pressure systems and increasing sunlight intensity during mid-late May.

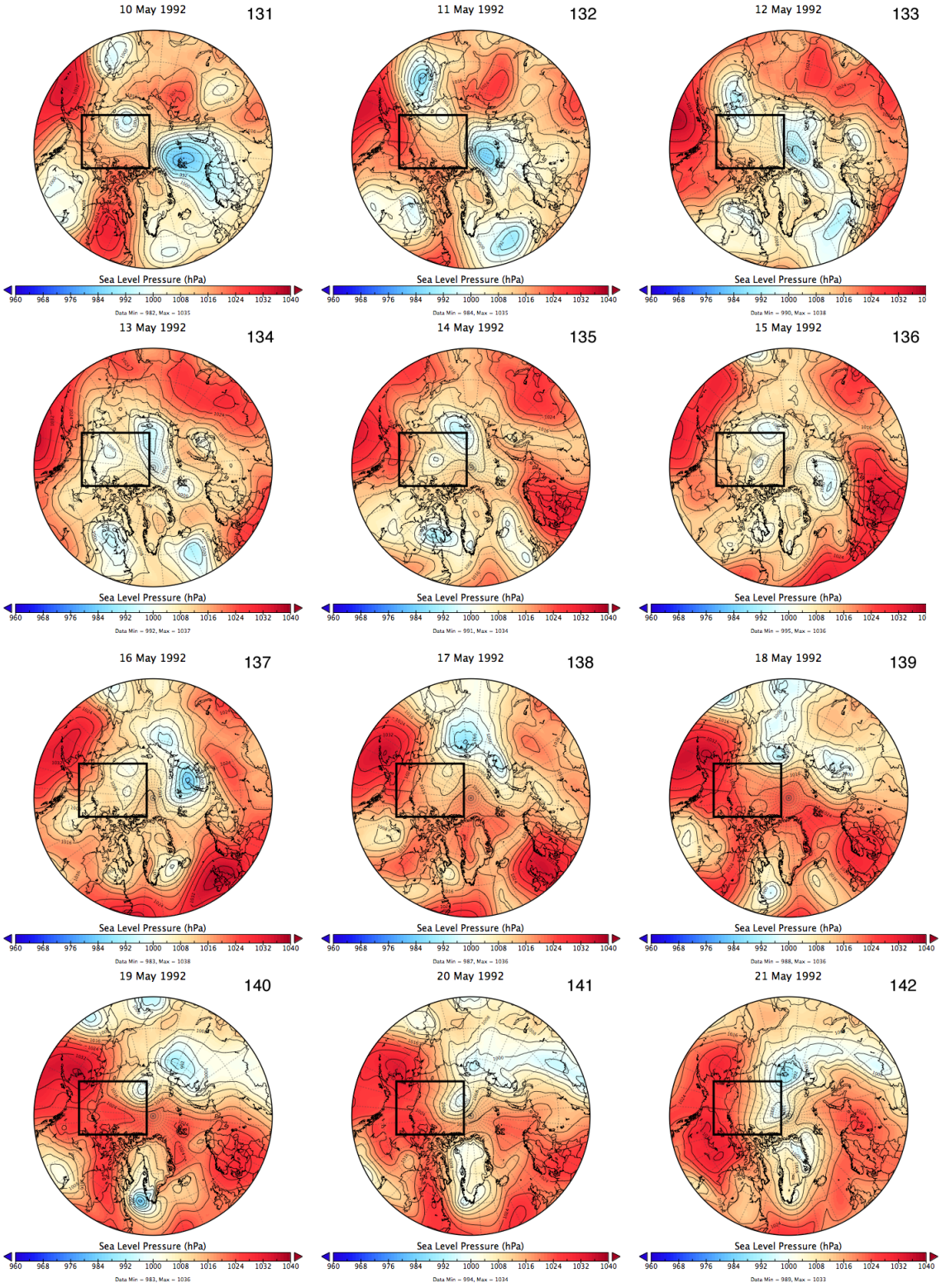

Figure 6.8 Daily mean sea level pressures (hPa) for 10 – 24 May 1992.

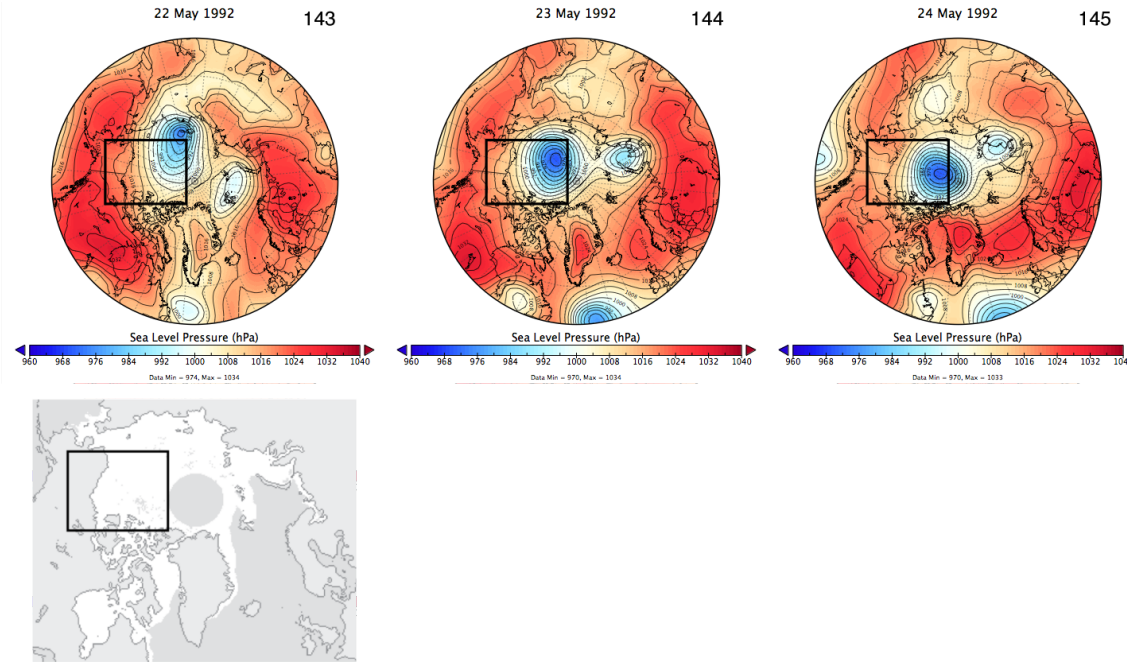

Figure 6.8 Continued.

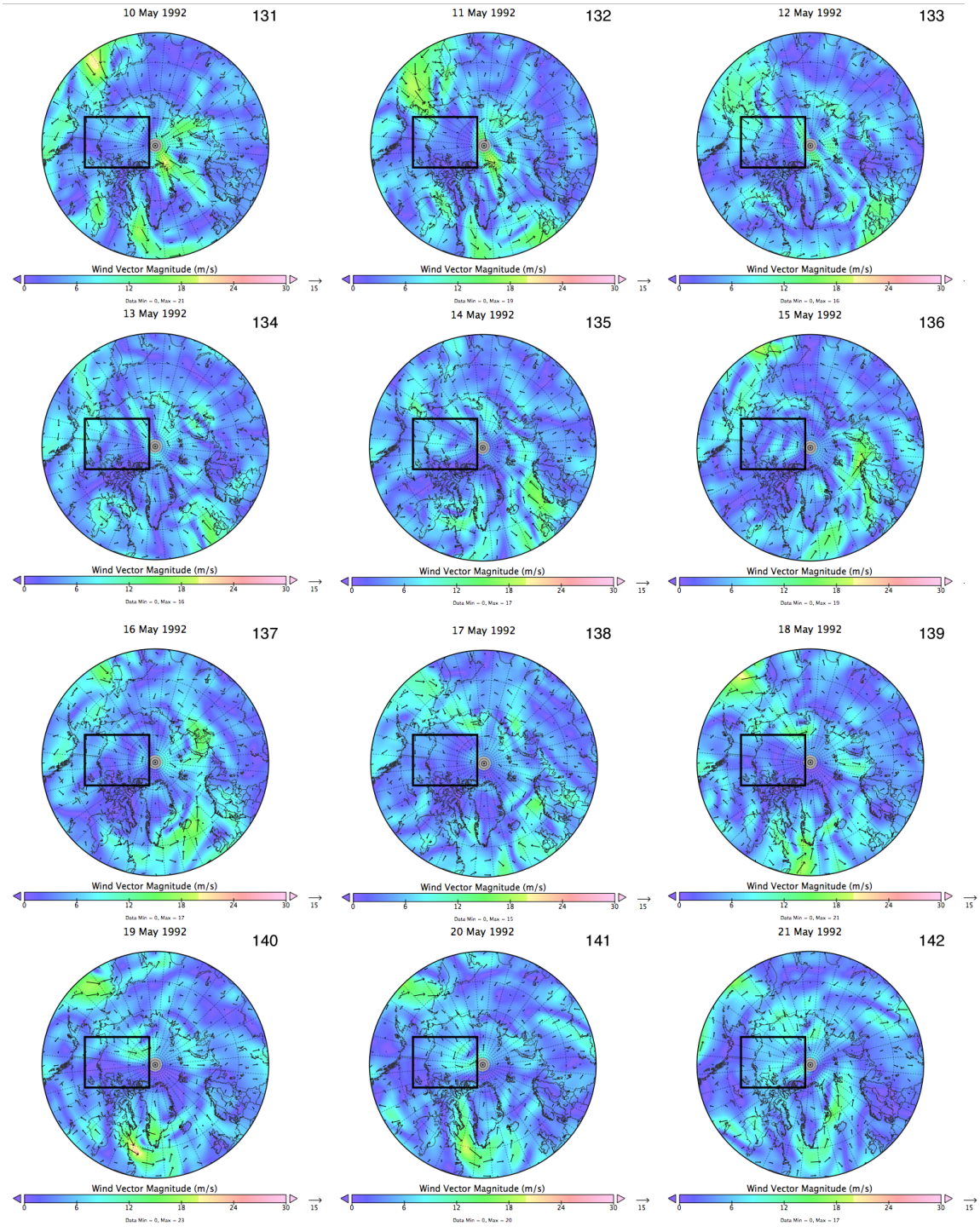

Figure 6.9 Daily mean 10 m vector wind direction and magnitude (ms^{-1}) for 10 – 24 May 1992.

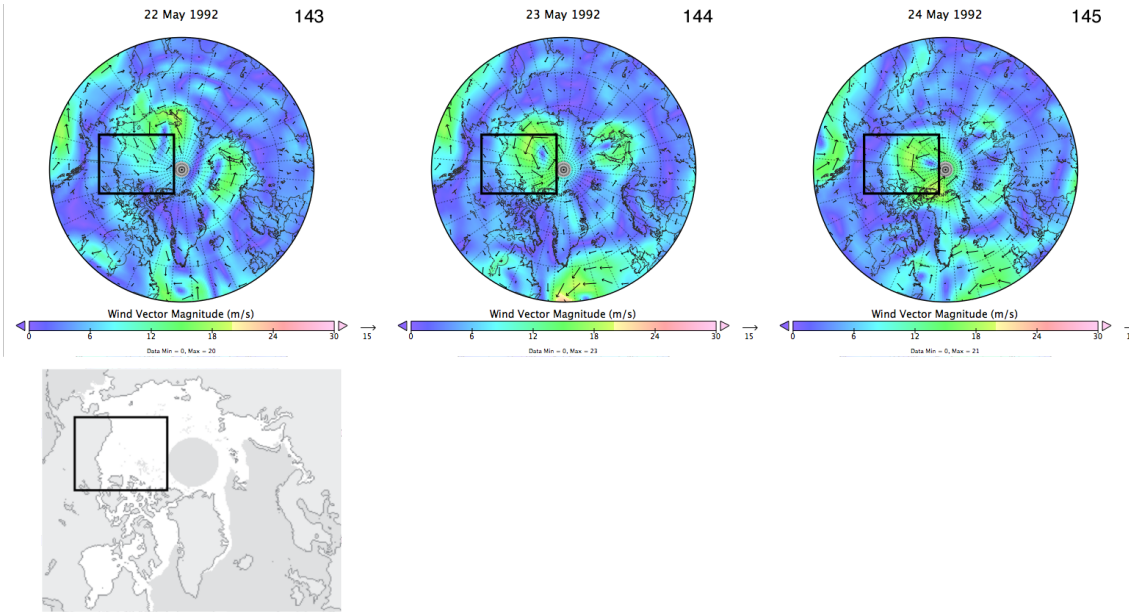

Figure 6.9 Continued.

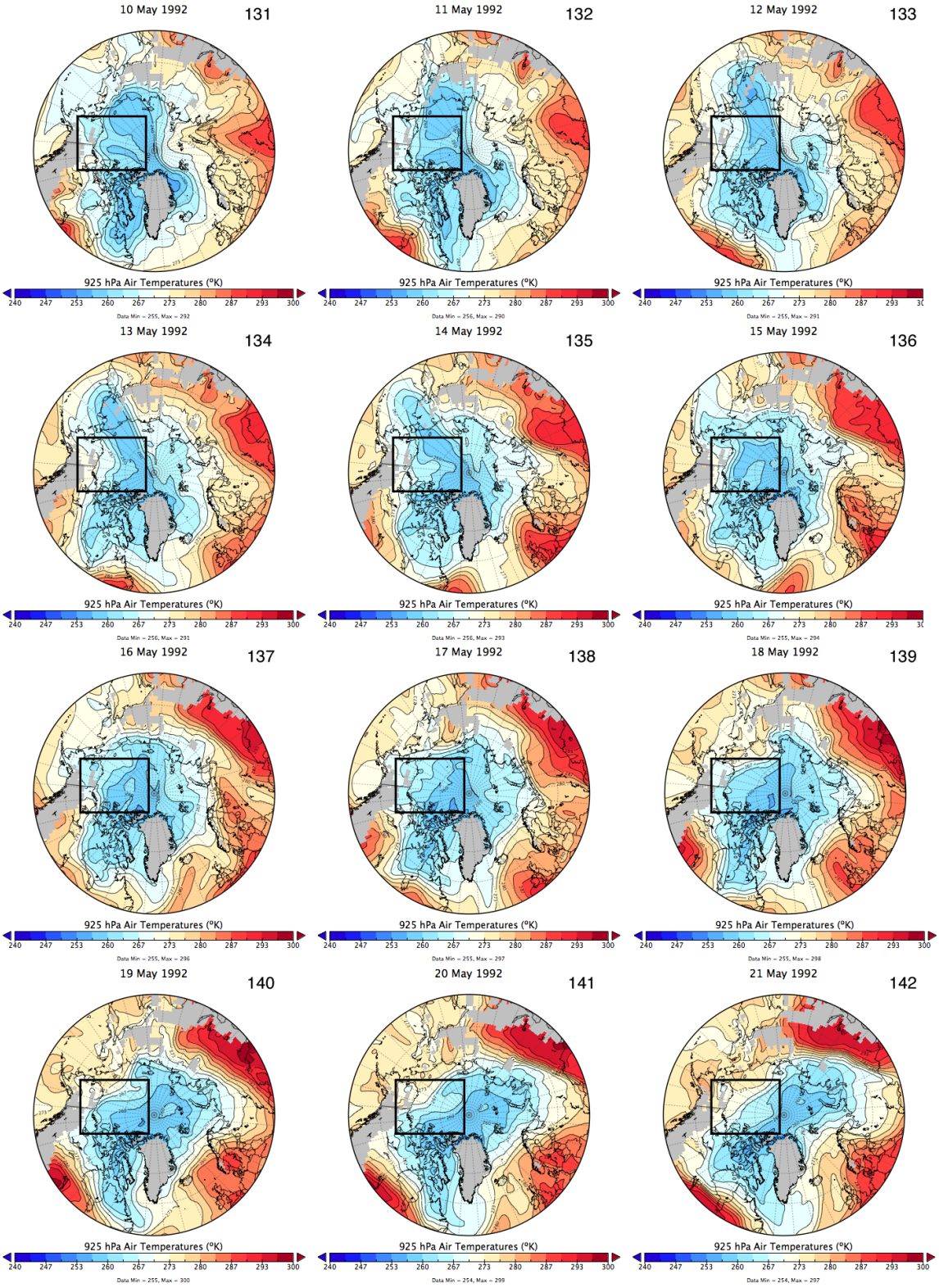

Figure 6.10 Daily mean 925 hPa air temperatures (°K) for 10 – 24 May 1992.

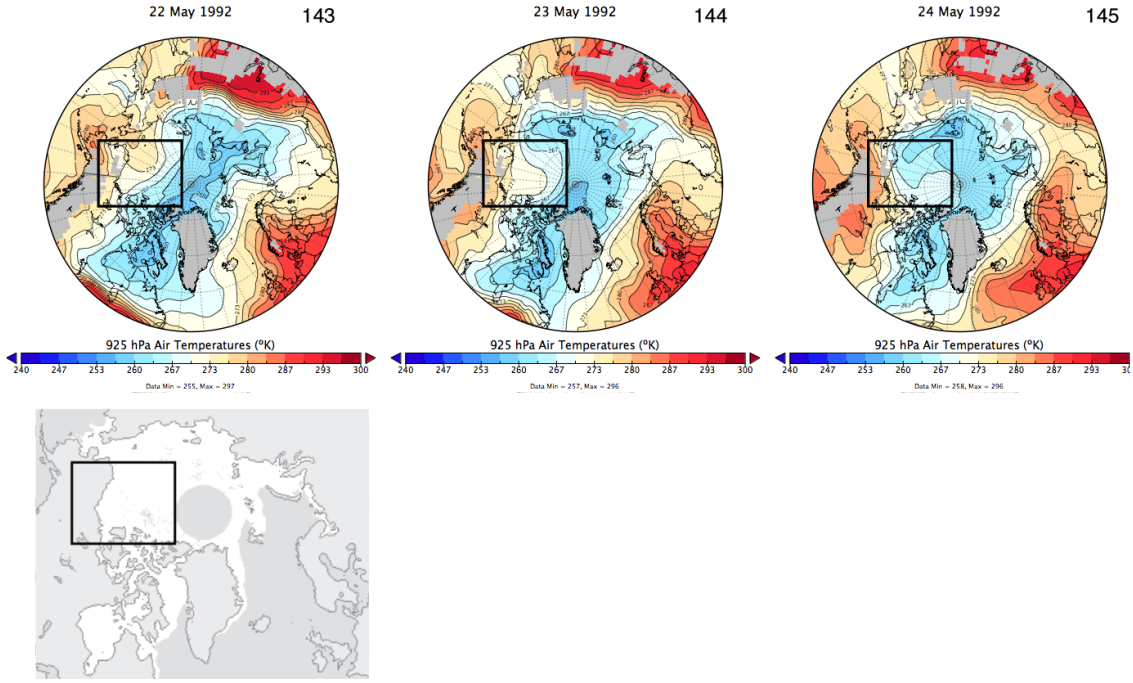

Figure 6.10 Continued.

The second peak in MO area during the 10 – 24 May 1992 MO event is associated with a low pressure system that begins to develop over the East Siberian Sea (Figure 6.8) on 18 May (DOY 139) and approaches the Beaufort Sea from the west on 19 – 20 May (DOY 140 – 141). The approaching cyclone shifts the wind direction to south-southwesterly and increases speeds (Figure 6.9) on 20 May (DOY 141), leading to the advancement of the 925 hPa 270 ºK isotherm (Figure 6.10) over the western Beaufort Sea on 20 – 21 May (DOY 141 – 142). By 22 May (DOY 143), the low pressure system over the East Siberian Sea deepens to 970 hPa and the southwesterly winds further increase in speed (Figures 6.8 – 6.9). Warm air is advected over the western Beaufort Sea and the 273 ºK isotherm approaches the western boundary of the region (Figure 6.10) on 22 May (DOY 143) leading to the maximum date of MO area (22 May) for 1992 in the Beaufort

Sea (Figure 6.7). On 23 May (DOY 144), a cold front begins to approach the Beaufort Sea from the west, however, the eastern half of the region remains within the warm sector of the cyclone (Figure 6.10) and MO occurs for portions of the east-central Beaufort Sea region (Figure 6.7). Note that on 23 May (DOY 144) the 925 hPa 273 ºK isotherm extends over the coastal Beaufort Sea (Figure 6.10), however, since this location in the region had melted previously (Figure 6.7), the full extent of melting area on 23 May (DOY 144) cannot be fully resolved, however, it is assumed that ongoing melting is occurring at previously melted areas where air temperatures are above freezing. On 24 May (DOY 145), the cold front has lowered the temperatures below freezing over the majority of the Beaufort Sea and all of the remaining melt-free sea ice locations (Figures 6.7, 6.10). The passage of the cold front over the region essentially shuts off the melt forcing from the cyclone and the daily MO area drops to 0 km^2 ending the MO event (Figures 5.8, 6.7).

Two distinct, melting periods take place during this Beaufort Sea melting event in 1992. The first peak in MO area, is associated with a weak cyclone, while the second peak and more extensive area of new MO area is associated with a second, stronger cyclone. Both of these low pressure systems, pass just to the northwest of the Beaufort Sea region, placing the ice areas within the region in the warm sector of the cyclones. The advection of warm air from the south, increases the mean daily 925 hPa air temperatures to near the freezing point (at least 270 ºK) and the accumulation of melting stops after the passage of a cold front, which reduces the mean daily 925 hPa air temperatures, well below freezing. In the case of the Beaufort Sea in 1992, the first,

lower magnitude peak in the daily MO area was associated with a relatively weaker low pressure system, but the second peak in MO area is associated with a stronger low. It is interesting to note that between these two cyclone events when the region is under the influence of a high pressure area, some MO area does occur. This melting, although not as extensive as the melting associated with the passage of low pressure systems, is attributed to cloud-free conditions and increasing daylight hours and stronger insolation during mid-late May.

Based on an analysis of the daily MO area time series only, the significance of any melting that occurs between the two larger peaks in MO area would likely be lost. Addressing where the MO areas in the daily time series are occurring provides much more insight into the atmospheric conditions necessary to produce varying patterns in the MO area. By identifying where MO area is occurring, the spatial analysis of the daily MO area highlights how sensitive the MO signal from passive microwave observations is to atmospheric conditions.

6.3.3 Beaufort Sea 2009

An anomalously early high magnitude, longer duration event occurs in the Beaufort Sea centered around the maximum MO day in 2009 on 27 April (DOY 117) where 1.2×10^5 km^2 of area experiences MO (Figure 5.8). The MO area spreads across the sea ice in the Beaufort Sea between 19 and 26 April (DOY 109 – 116) and is primarily found along the coast and in the northwestern quadrant of the Beaufort Sea. The peak melting day of this event (Figure 6.11) occurs on 27 April (DOY 117) and by 29 (DOY 119) and 30 April (DOY 120, not shown) new MO area drops to 0 km^2. At the

conclusion of this melting event, MO area has occurred over 50% of the Beaufort Sea Region.

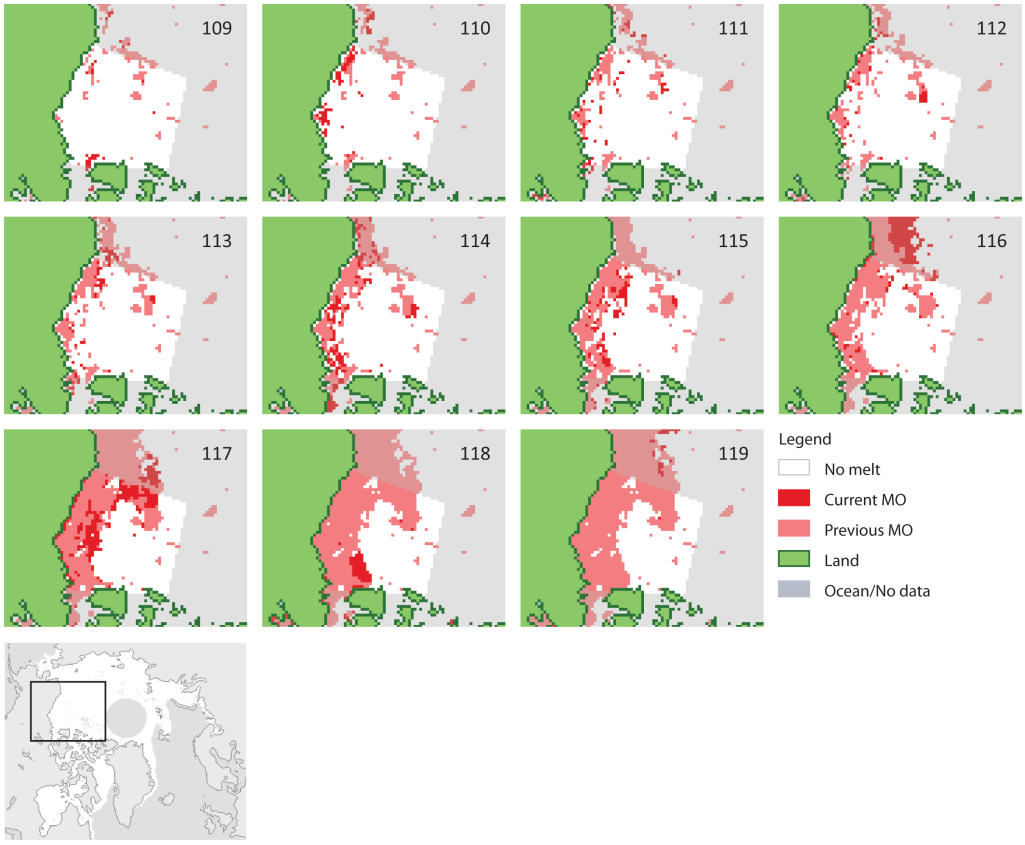

Figure 6.11 Progression of Beaufort Sea MO area for 19 – 29 April (DOY 109 – 119) 2009. MO locations for the current DOY and where MO has already occurred on a previous day are highlighted. Pixels outside of the region (see Figure 3.1) are de-emphasized to indicate MO conditions adjacent to the Beaufort Sea.

MO area accumulates relatively slow over the days leading up to the peak MO 27 April (DOY 117, Figure 6.11). During this time, a high pressure system is present directly over the Beaufort Sea (Figure 6.12). The high pressure system weakens through 23 April (DOY 113) and a weak area of low pressure begins to spread into the Beaufort Sea region from the west (Figure 6.12). The pressures recover and a ridge of higher

MSLP develops over the region by 26 April (DOY 116) ahead of a developing low pressure system in the Chukchi Sea (Figure 6.12). By 27 April (DOY 117) the low passes to the northwest of the Beaufort Sea (Figure 6.12), placing the region within the southwesterly flow at the surface and in the warm sector of the cyclone (Figure 6.13). The strongest advection of warm air at the surface occurs on 26 and 27 April (DOY 116 – 117) leading to the approach of the 273 ºK isotherm over the southern 1/3 of the region on 27 April (Figure 6.14).

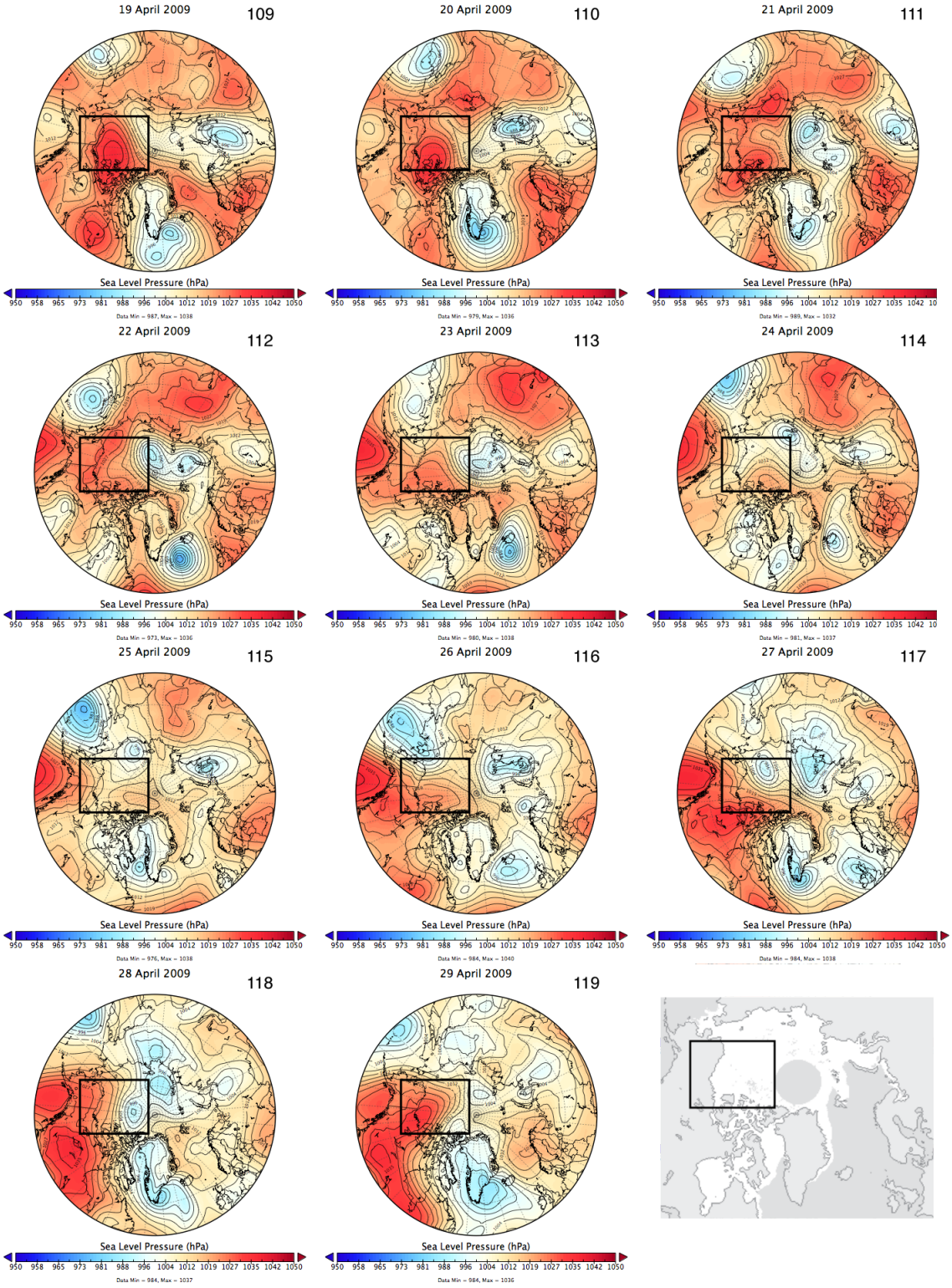

Figure 6.12 Daily mean sea level pressures (hPa) for 19 – 29 April 2009.

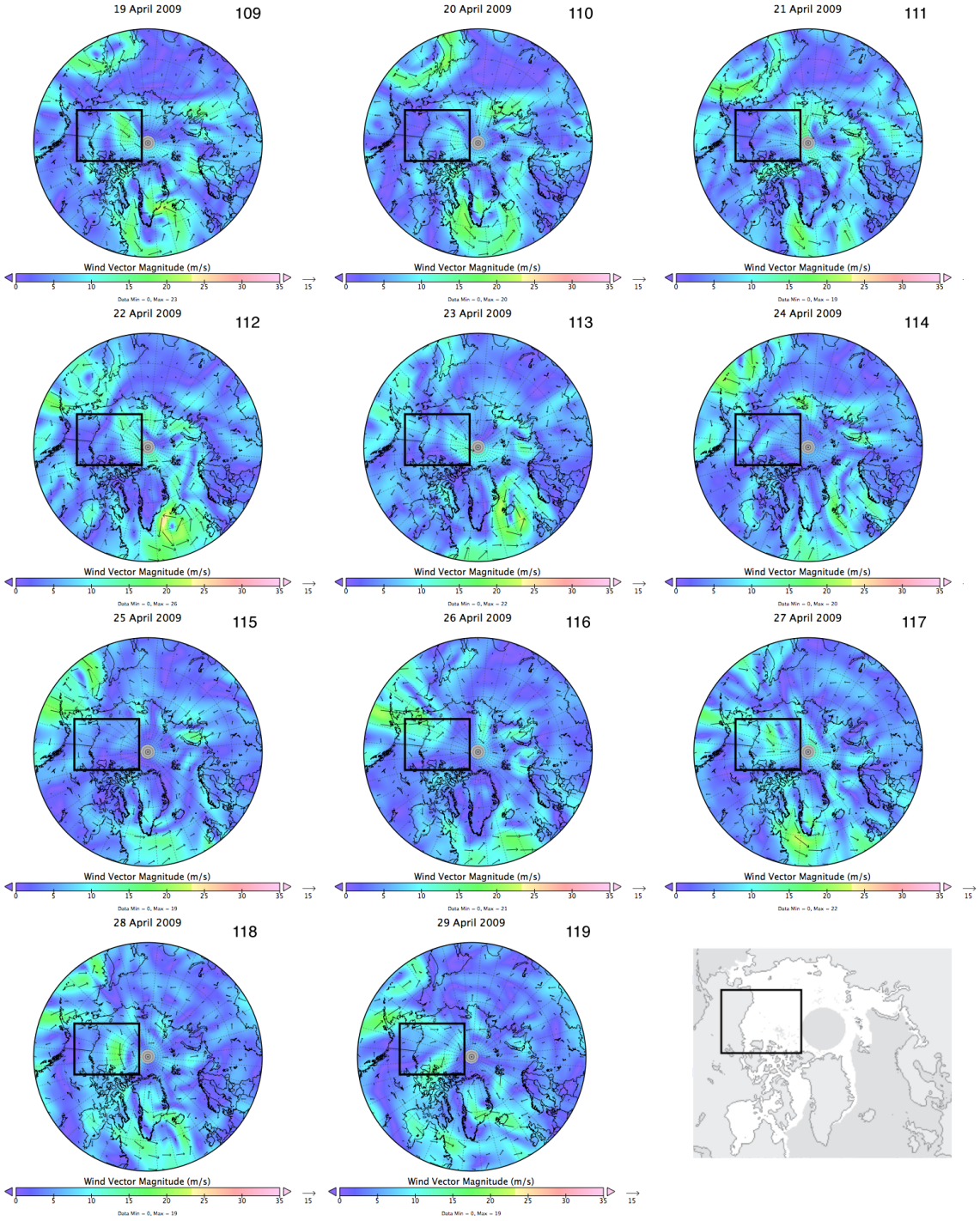

Figure 6.13 Daily mean 10 m vector wind direction and magnitude (ms^{-1}) for 19 – 29 April 2009.

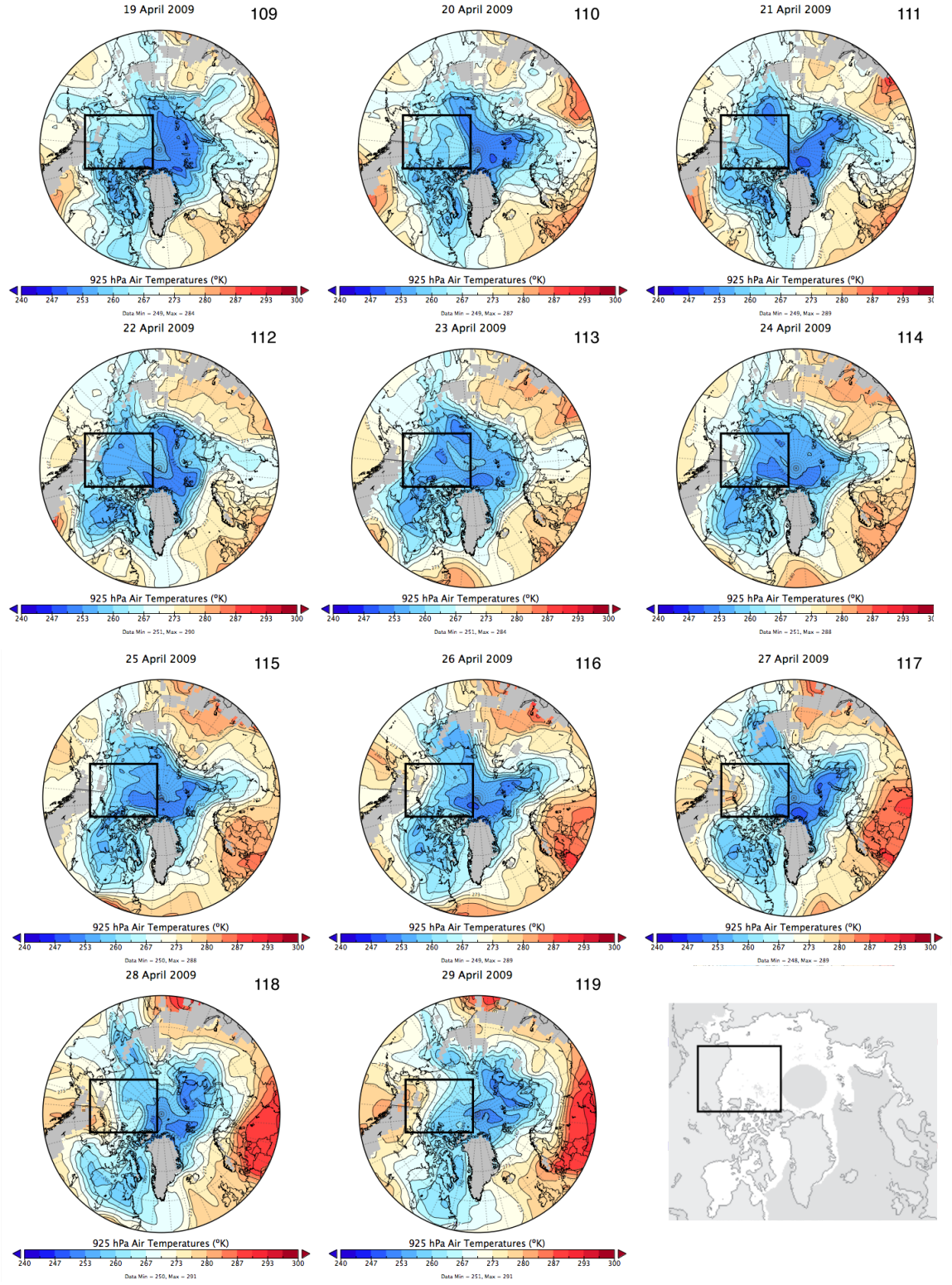

Figure 6.14 Daily mean 925 hPa air temperatures (ºK) for 19 – 29 April 2009.

The pattern in MO area prior to the occurrence of the low pressure system on 26 – 27 April (DOY 116 – 117) in 2009 is similar to that seen in the Beaufort Sea in the 1992 case, when the region was under the influence of high pressure in between two separate cyclone events described in the previous section. From 19 – 24 April (DOY 109 – 114) 2009 when the Beaufort Sea is under a high pressure system, the MO area that accumulates is sporadically distributed and the number of new MO pixel locations each day are relatively small when compared to days in which a cyclone track induces warm air advection from the south over the region (Figure 6.11). On 26 – 28 April (DOY 116 – 118), when the Beaufort Sea is located in the warm sector (Figure 6.14), the pixel locations that do melt are largely contiguous, in contrast to the scattered pattern in MO area seen under the high pressure system (Figure 6.11).

6.4 Low Magnitude Events

The low magnitude melting events in the East Siberian Sea in 1989, 2005, and 2012 are significant because they each occur more than 2 standard deviations from the mean MO date for the East Siberian Sea region early in the year (Figure 5.6). In contrast to the high magnitude events described previously, the relatively low magnitudes of peaks in the daily MO area time series in each of these cases is interesting due to the extremely early timing of the small areas of MO area that do occur.

6.4.1 Low Magnitude, Short Duration Events

6.4.1.1 East Siberian Sea 1989

A small peak in the daily MO area time series occurs between 14 and 20 April (DOY 104 – 110) in the East Siberian Sea in 1989 (Figure 5.6). This melting event is responsible for melting area over only a small area of sea ice extent, 0.5×10^5 km^2 or 4.2% of the East Siberian Sea region. The maximum melting day during this event occurs on 15 April (DOY 105), when MO occurs for 33 pixel point locations representing 0.2×10^5 km^2 of the region (Figure 6.15). The MO area that occurs during this event is primarily along the southern and western portions of the region, however, on the maximum melting day, 15 April (DOY 105), most of the melting locations are grouped near the coastline (Figure 6.15).

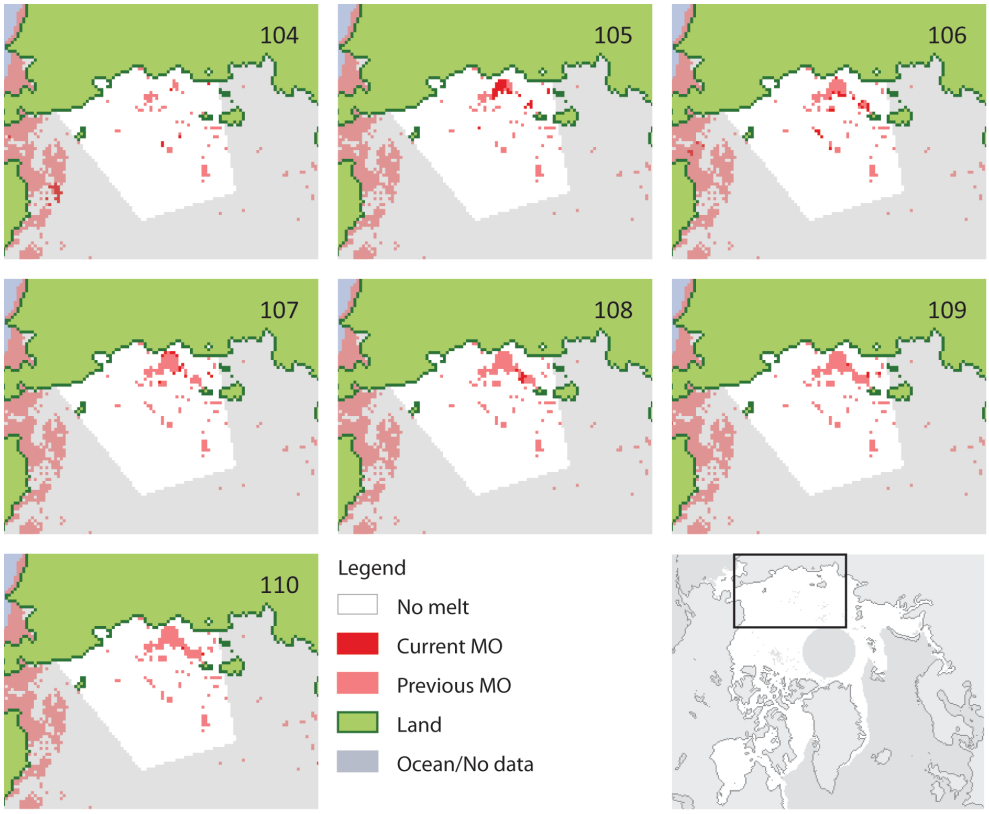

Figure 6.15 Progression of East Siberian Sea MO area for 14 – 20 April **(**DOY 104 – 110) 1989. MO locations for the current DOY and where MO has already occurred on a previous day are highlighted. Pixels outside of the region (see Figure 3.1) are de-emphasized to indicate MO conditions adjacent to the East Siberian Sea.

The atmospheric conditions at the time of the 1989 East Siberian Sea event are characterized by a low pressure system to the south of the region (Figure 6.16), resulting in primarily easterly and northeasterly wind directions (Figure 6.17). A strong area of low pressure exists over the Bering Sea from 14 – 18 April (DOY 104 – 108) and on the maximum melting day (15 April, DOY 105) a low pressure center with a central pressure of 996 hPa develops over the western East Siberian Sea (Figure 6.16). The low pressure system over the Bering Sea (Figure 6.16) deepens to its lowest central pressure (978 hPa) on 15 April (DOY 105), while the strongest daily mean winds in the East Siberian Sea

occur on 14 April (DOY 104) reaching 18 ms^{-1} (Figure 6.17). Under the easterly flow regime during 14 – 17 April (DOY 104 – 107), the 925 hPa air temperatures warm with advection from the east and the approach of the 267 ºK isotherm into the central East Siberian Sea (Figure 6.18).

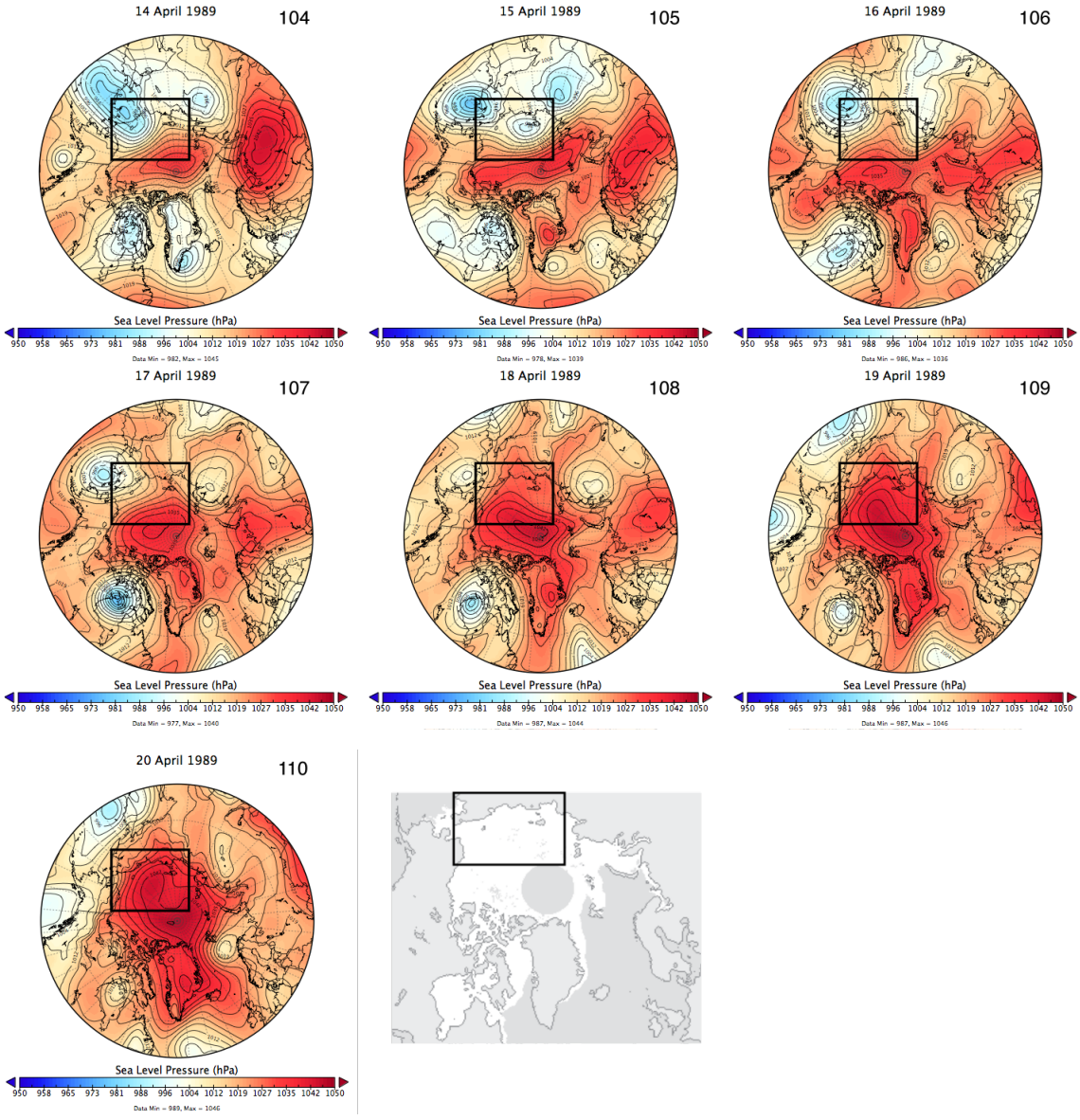

Figure 6.16 Daily mean sea level pressures (hPa) for 14 – 20 April 1989.

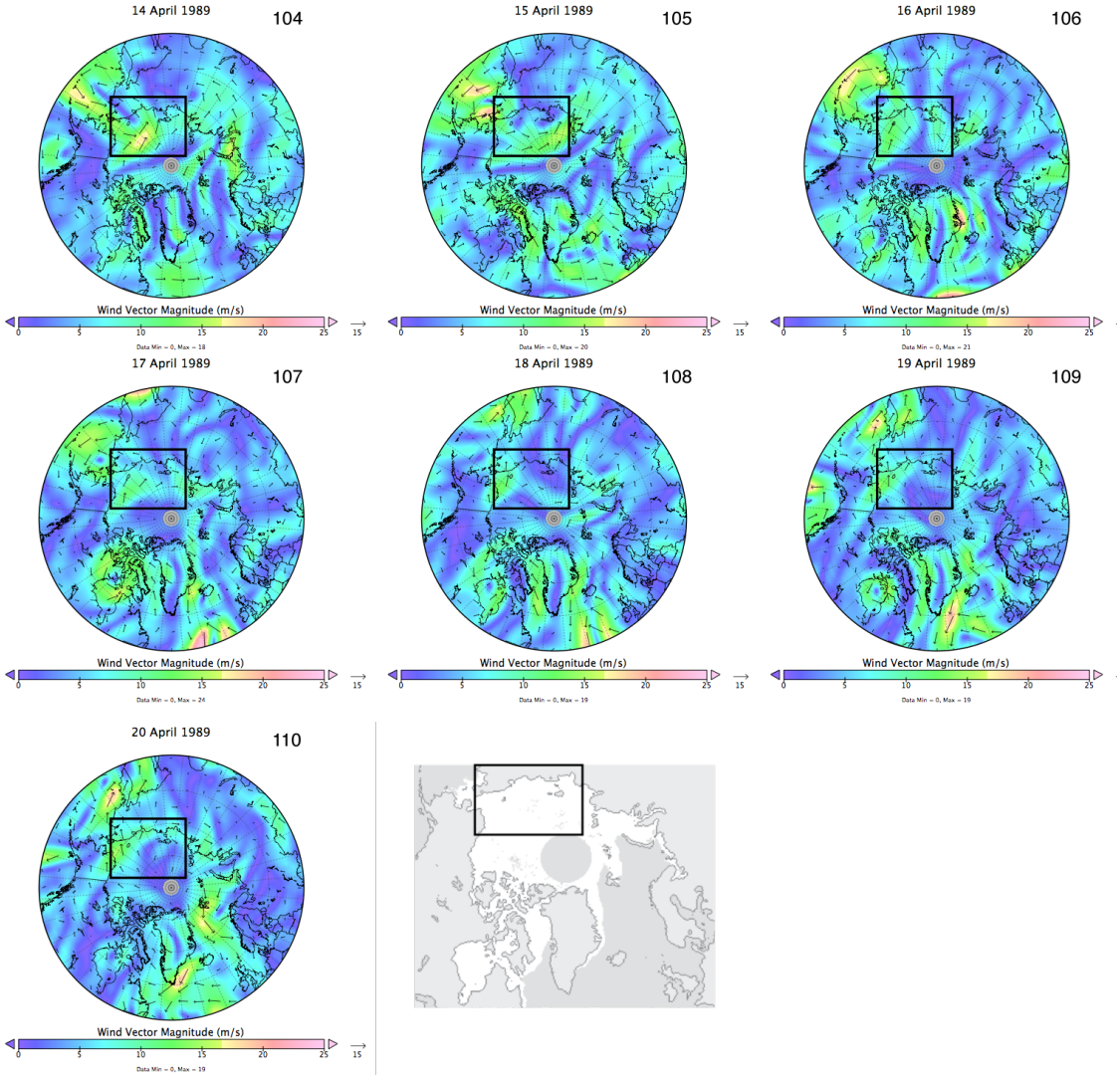

Figure 6.17 Daily mean 10 m vector wind direction and magnitude (ms^{-1}) for 14 – 20 April 1989.

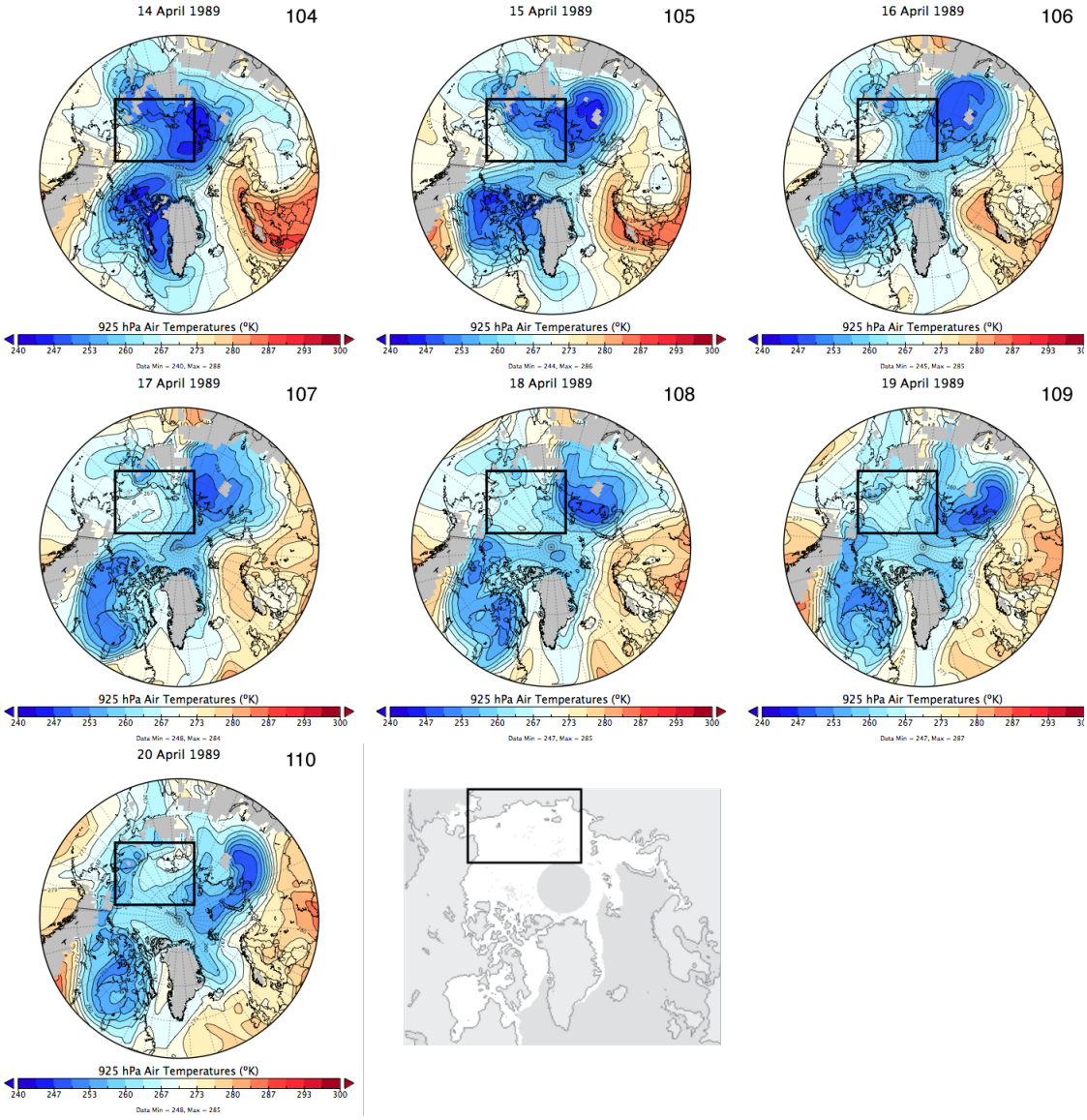

Figure 6.18 Daily mean 925 hPa air temperatures (ºK) for 14 – 20 April 1989.

The synoptic setting for this case is different from the peak melting days observed in high magnitude events described above. In 1989, the region is being influenced by a strong low pressure system; however, the low pressure system is located south of the region (Figure 6.16), rather than passing just to the northwest, placing the region within

the warm sector of the cyclone. The timing of this melting event places it very early in the melt season, mid-April, when typical air temperatures and available insolation are low. The 273 ºK isotherm never extends over the East Siberian Sea, but daily mean temperatures (Figure 8.18) above 267 ºK do occur on 16 – 17 April (DOY 106 – 107). It is expected that mean 925 hPa air temperatures are cooler in the earlier part of the melt season, thus it would be expected that if this event occurred later in the year when mean air temperatures are already warmer, much more MO area would have accumulated during the event.

6.4.1.2 East Siberian Sea 2012

The melt event spanning 5 – 15 March (DOY 65 – 75) in 2012 is another case in which a small amount of MO area occurs very early in the year (Figure 5.6). During this melt event, 121 pixel locations or 6% of the total area in the East Siberian Sea region experience MO (Figure 6.19). The locations of MO area that occur during this event are primarily scattered in the southern portion of the region and a grouping of melted pixels also occur in the far northwestern corner of the region. The maximum melting day is 13 March (DOY 73) when MO occurs at 34 pixels (Figure 6.19). Following this early melt event, peaks in the daily MO area time series occur until late in April (Figure 5.6).

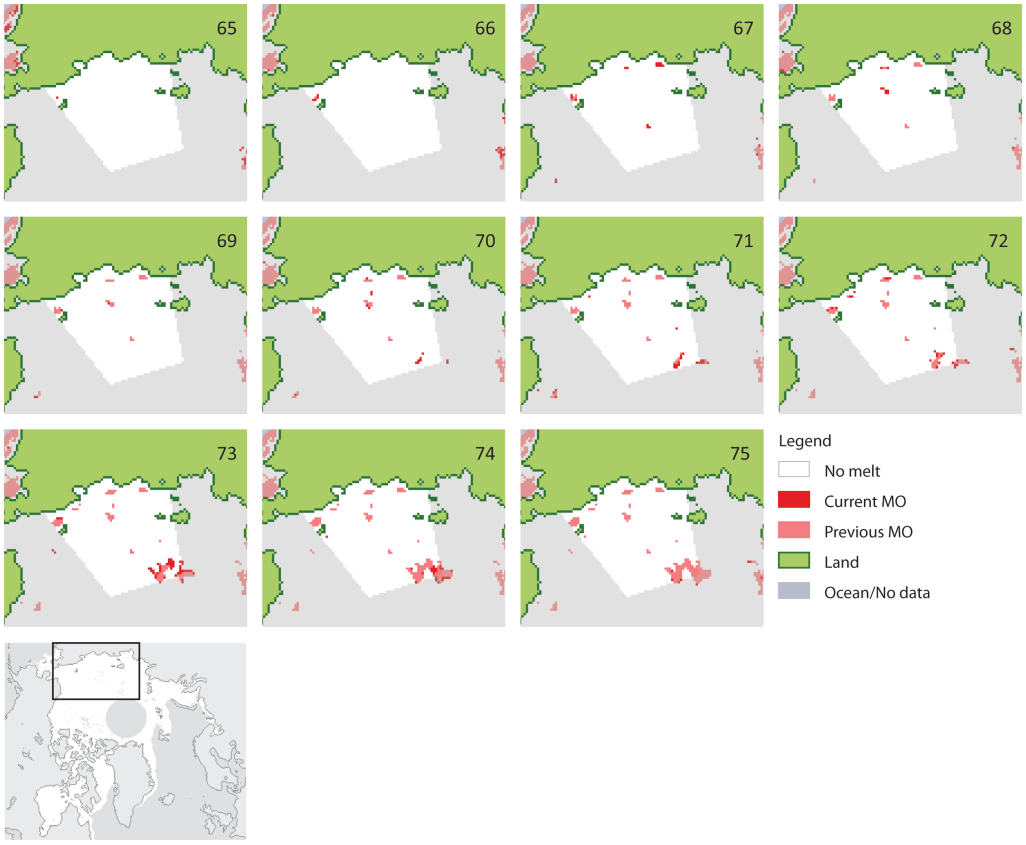

Figure 6.19 Progression of East Siberian Sea MO area for 5 – 15 March (DOY 65 – 75) 2012. MO locations for the current DOY and where MO has already occurred on a previous day are highlighted. Pixels outside of the region (see Figure 3.1) are de-emphasized to indicate MO conditions adjacent to the East Siberian Sea.

For the duration of the 2012 East Siberian Sea melt event, the MSLP over the region is high, except for a low pressure center to the north of the region on 6 – 7 March (DOY 66 – 67) which has a minimum central pressure below 981 hPa on 6 March (Figure 6.20). On 8 – 9 March (DOY 68 – 69) the low pressure system appears to weaken and drift to the southwest, placing the East Siberian Sea in the warm sector of the cyclone. Following the dissipation of the low pressure system on 10 March (DOY 70), high pressure builds over the East Siberian Sea and persists through 15 March (DOY 75), the end of the melt event (Figure 6.20). The cyclonic flow around the low pressure

system results in relatively strong west and southwesterly 10 m winds (Figure 6.21) over the East Siberian Sea from 5 – 8 March (DOY 65 – 68). The mean daily 925 hPa air temperatures over the region exceed 256 ºK on 5 – 6 March (DOY 65 – 66) when the low pressure system is located north of the region (Figure 6.22). As the low pressure system weakens and shifts to the southwest of the region, mean 925 hPa air temperatures initially fall back to less then 247 ºK over parts of the western East Siberian Sea. As the high pressure begins to build back over the region, winds calm to near 0 ms^{-1} and air temperatures increase back up above 256 ºK for the northern and eastern portions of the region under clear sky conditions (Figures 6.20 – 6.22) between 11 – 14 March (DOY 71 – 74).

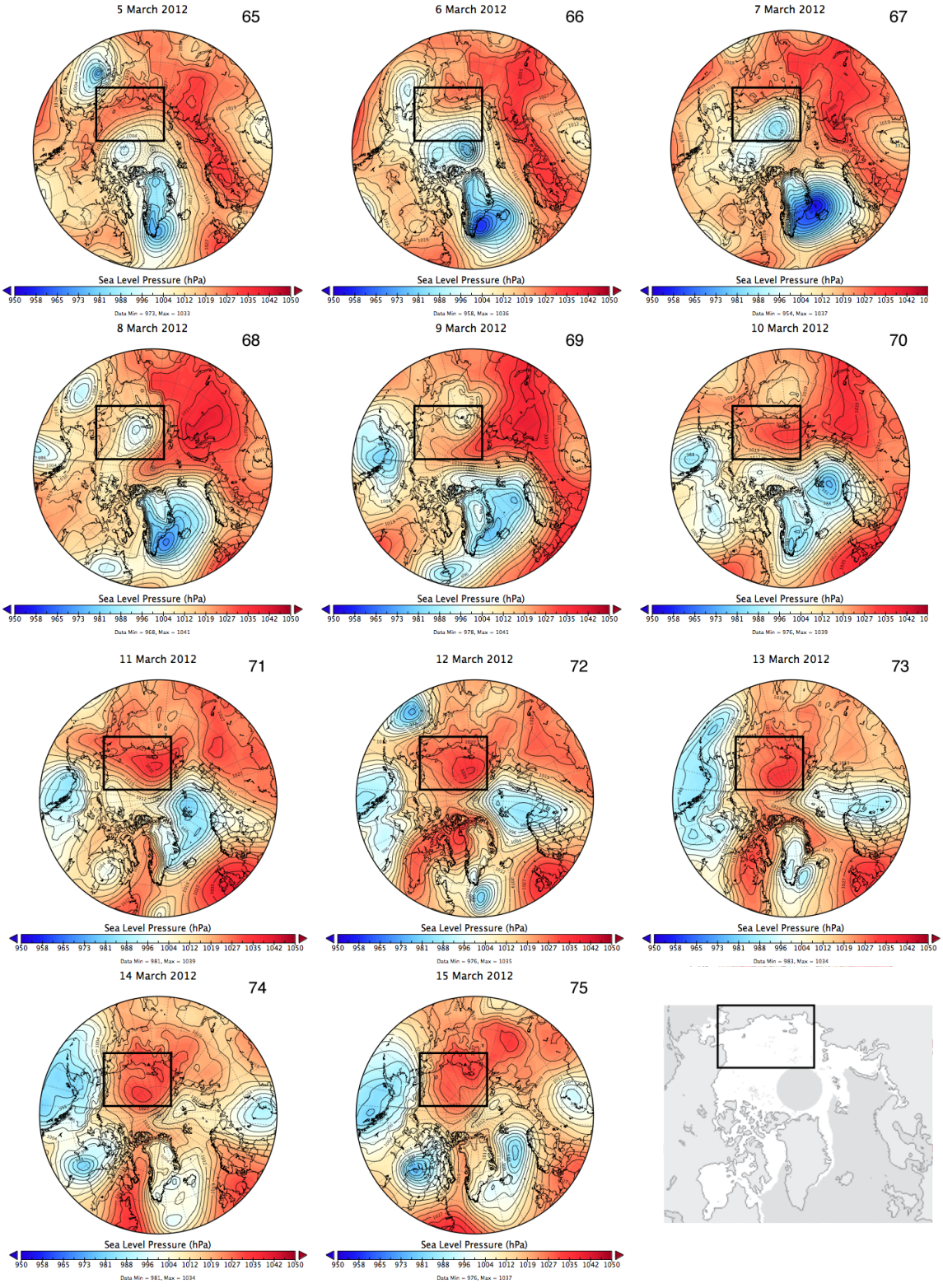

Figure 6.20 Daily mean sea level pressures (hPa) for 5 – 15 March 2012.

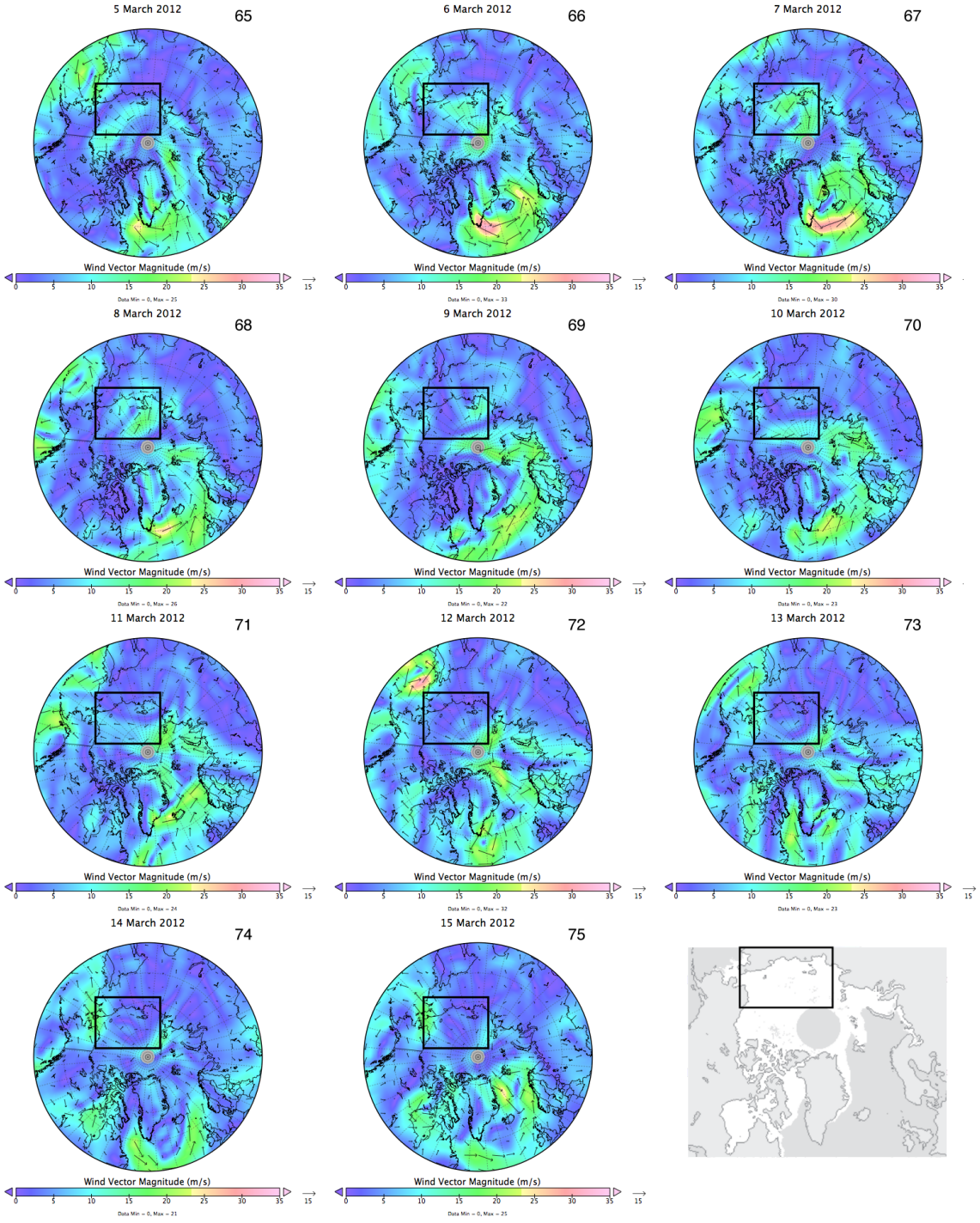

Figure 6.21 Daily mean 10 m vector wind direction and magnitude (ms^{-1}) for 5 – 15 March 2012.

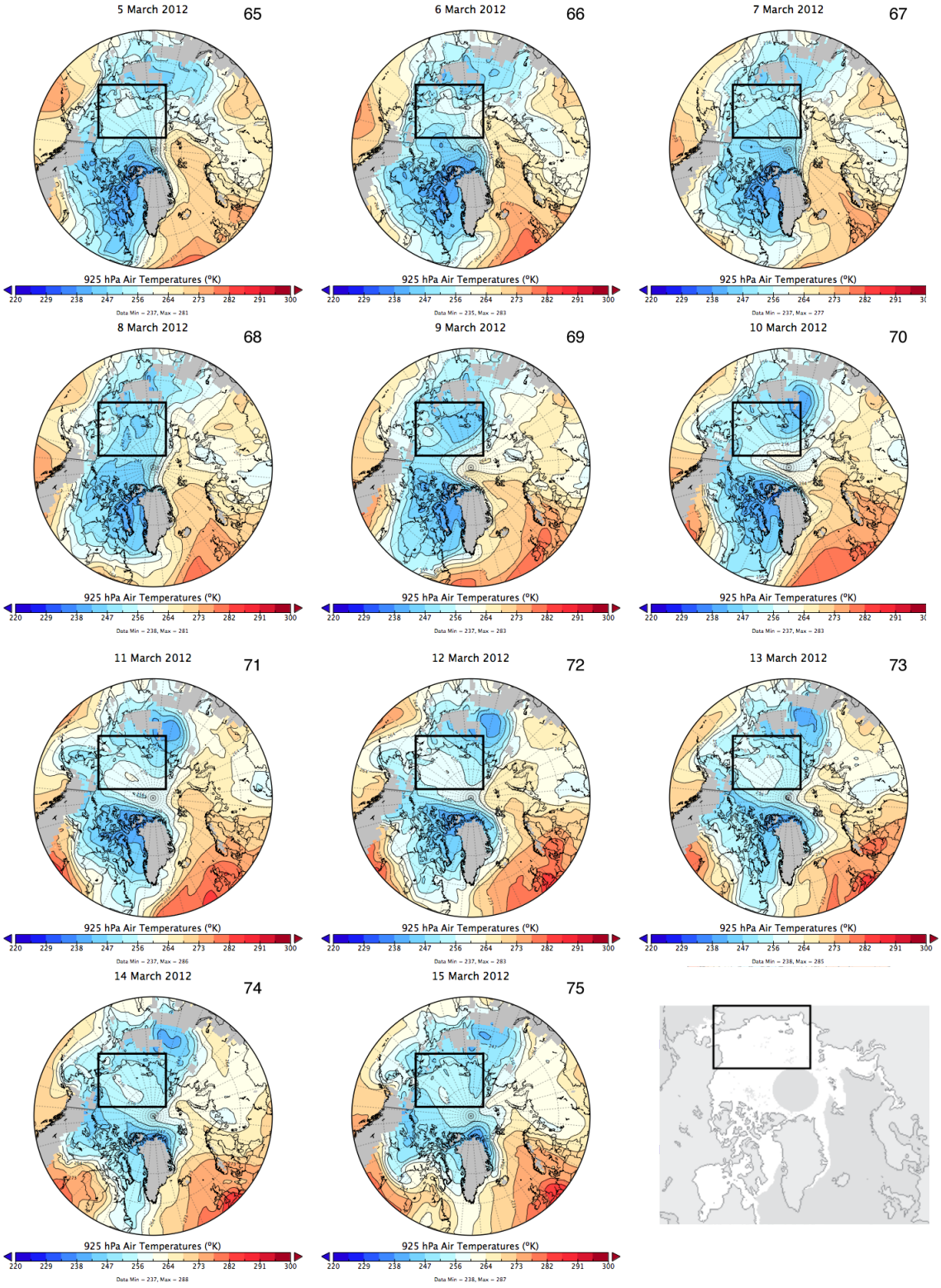

Figure 6.22 Daily mean 925 hPa air temperatures (ºK) for 5 – 15 March 2012.

The few pixel locations where MO is observed at the beginning of this melt event are primarily scattered over the southern half of the region (Figure 6.19) and are associated with the westerly winds and slight increase in mean 925 hPa air temperatures from the low pressure system. The MO area that occurs in the northwestern quadrant of the region and the MO which occurs on the maximum MO day (13 March, DOY 73) (Figure 6.19) appears to be associated with the high pressure system and moderate easterly winds resulting in westward advection of the 256 ºK isotherm over the region where maximum melting in the northwest of the region occurs (Figures 6.19 – 6.22). In the 2012 East Siberian Sea melt event, it appears that warm temperatures associated with the low pressure system is only responsible for a small amount of melting area at the beginning of the melt event near the coastline, while high pressures and warming air temperatures are responsible for the majority of MO area in the later half of the melting event.

6.4.2 Low Magnitude, Longer Duration Events: East Siberian Sea 2005

In 2005, a longer duration melting event in the East Siberian Sea occurs more than 2 standard deviations from the mean early (Figure 5.6) during 18 April – 29 April (DOY 108 – 119). This event is a larger melting event that is responsible for the MO area over 4.2×10^5 km^2 or 33% of the East Siberian Sea region (Figure 5.6). Similarly to the melting event in the Beaufort Sea during 1992 described in Section 6.3.2, the 2005 East Siberian Sea event has two peak melting days embedded within the melting event (Figure 5.6). The first, smaller peak melt day occurs on 20 April (DOY 110) when 105 pixel locations melt and the second, larger peak melt day occurs on 28 April (DOY 118)

when 142 pixel locations melt (Figures 5.6, 6.23). The melting that occurs with this event is primarily restricted to the eastern 1/3 of the region and is associated with a larger melting event that is occurring over the Chukchi Sea, directly adjacent to the East Siberian Sea (Figure 6.23).

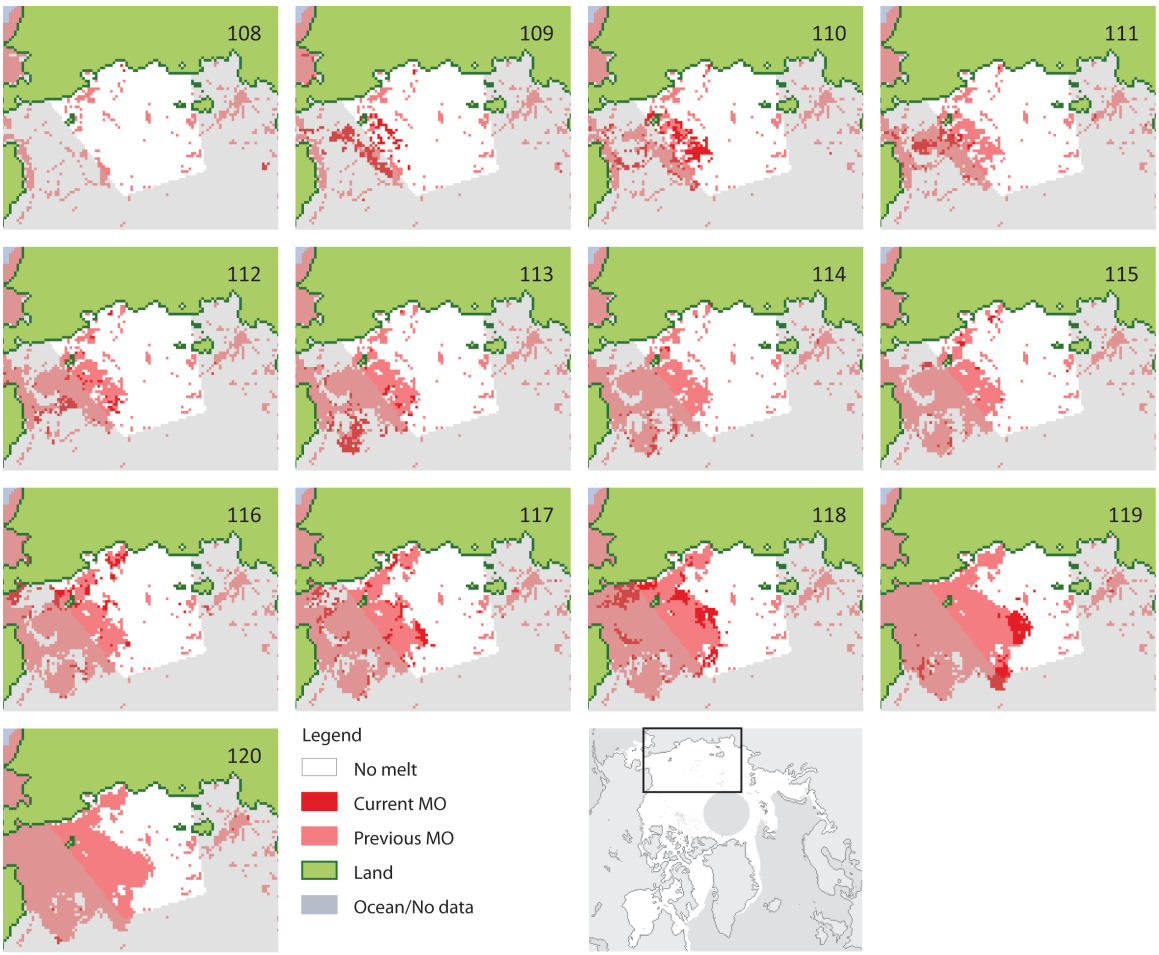

Figure 6.23 Progression of East Siberian Sea MO area for 18 – 30 April (DOY 108 – 120) 2005. MO locations for the current DOY and where MO has already occurred on a previous day are highlighted. Pixels outside of the region (see Figure 3.1) are de-emphasized to indicate MO conditions adjacent to the East Siberian Sea.

Like the Beaufort Sea event in 1992, two separate low pressure systems influence the East Siberian Sea, resulting in the two peak melting days observed during the melt

event. The first low pressure system is located to the north of the East Siberian Sea (Figure 6.24) from 18 – 21 April (DOY 108 – 111). The steep pressure gradient over the East Siberian Sea at this time results in strong westerly and southwesterly winds (Figure 6.25) from 18 – 20 April (DOY 108 – 110) and the advection of the 260 ºK isotherm over the southwestern half of the region (Figure 6.26). Through the remainder this melting event, the 925 hPa air temperatures remain warm with the 273 ºK isotherm approaching the eastern edge of the region (Figure 6.26) on 28 April (DOY 118). The advection of warmer temperatures during this melting event is enhanced by a weak low pressure center (Figure 6.24) that develops over the western East Siberian Sea during 21 – 23 April (DOY 111 – 113) which increases the air temperatures over the central portion of the region through 24 April (DOY 114). It is interesting that during this time period where warm air is being advected over the region, there is very little MO observed between 21 – 24 April (DOY 111 – 114) and the MO that does occur happens adjacent to previously melted area on the eastern side of the region (Figure 6.23). By 23 April (DOY 113), the 267 ºK isotherm advances northward through the central East Siberian Sea (Figure 6.26), however, no MO occurs in the central East Siberian Sea on this date (Figure 6.23). The mean 925 hPa air temperatures on 23 April (DOY 113) are warmer than those that induced the first peak melting day during this event on 19 April (DOY 109).

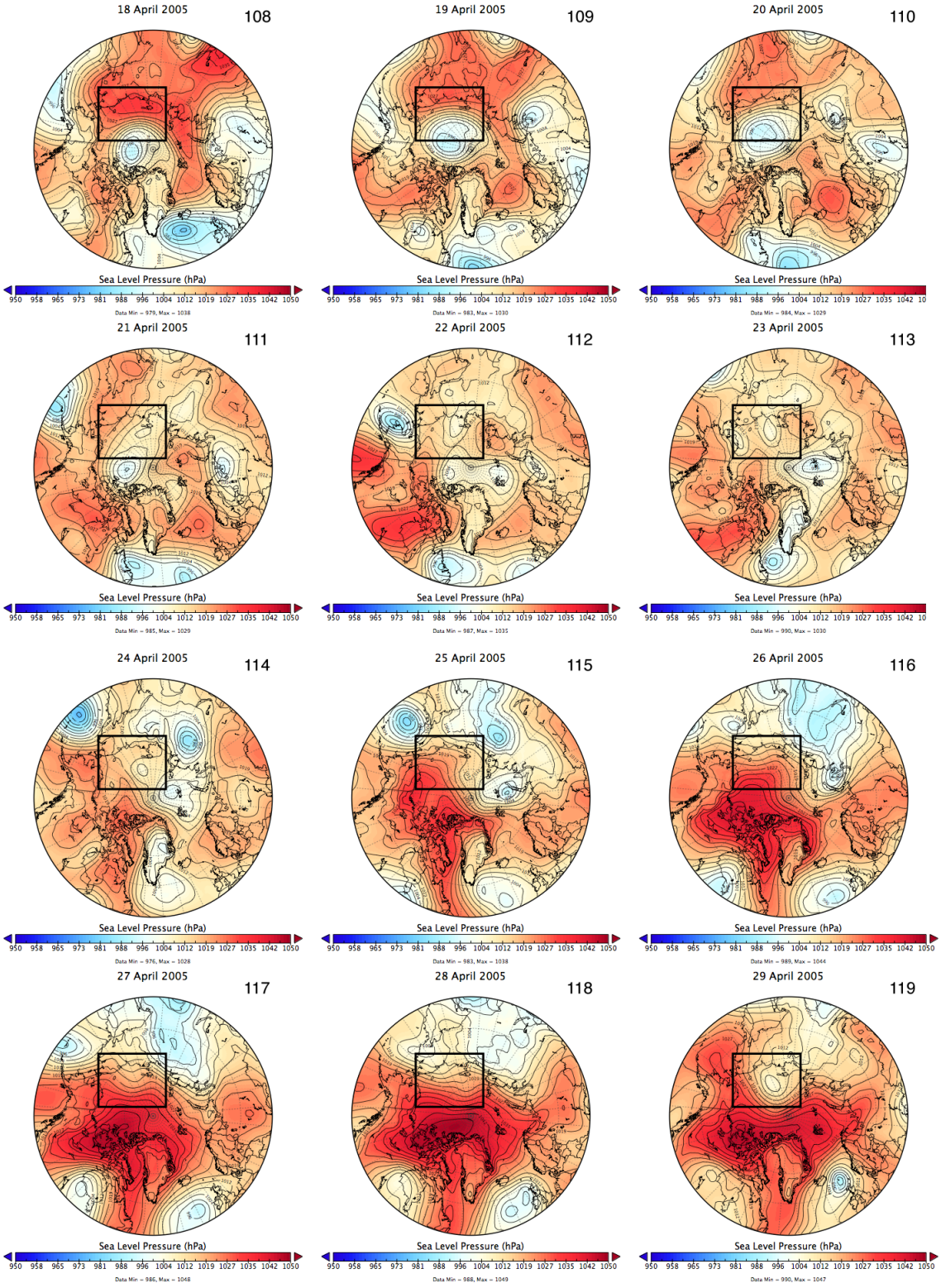

Figure 6.24 Daily mean sea level pressures (hPa) for 18 – 30 April 2005.

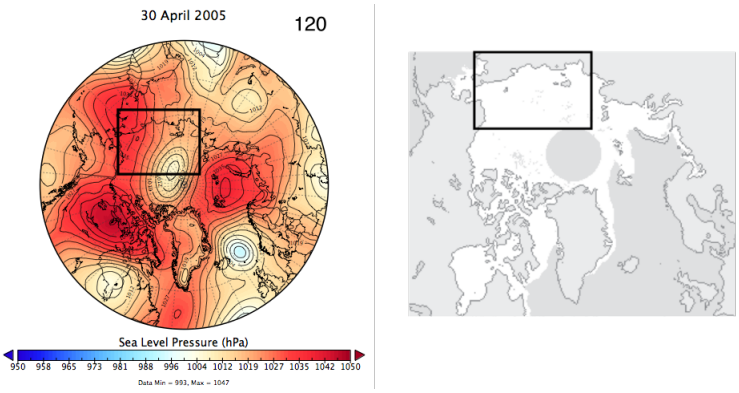

Figure 6.24 Continued.

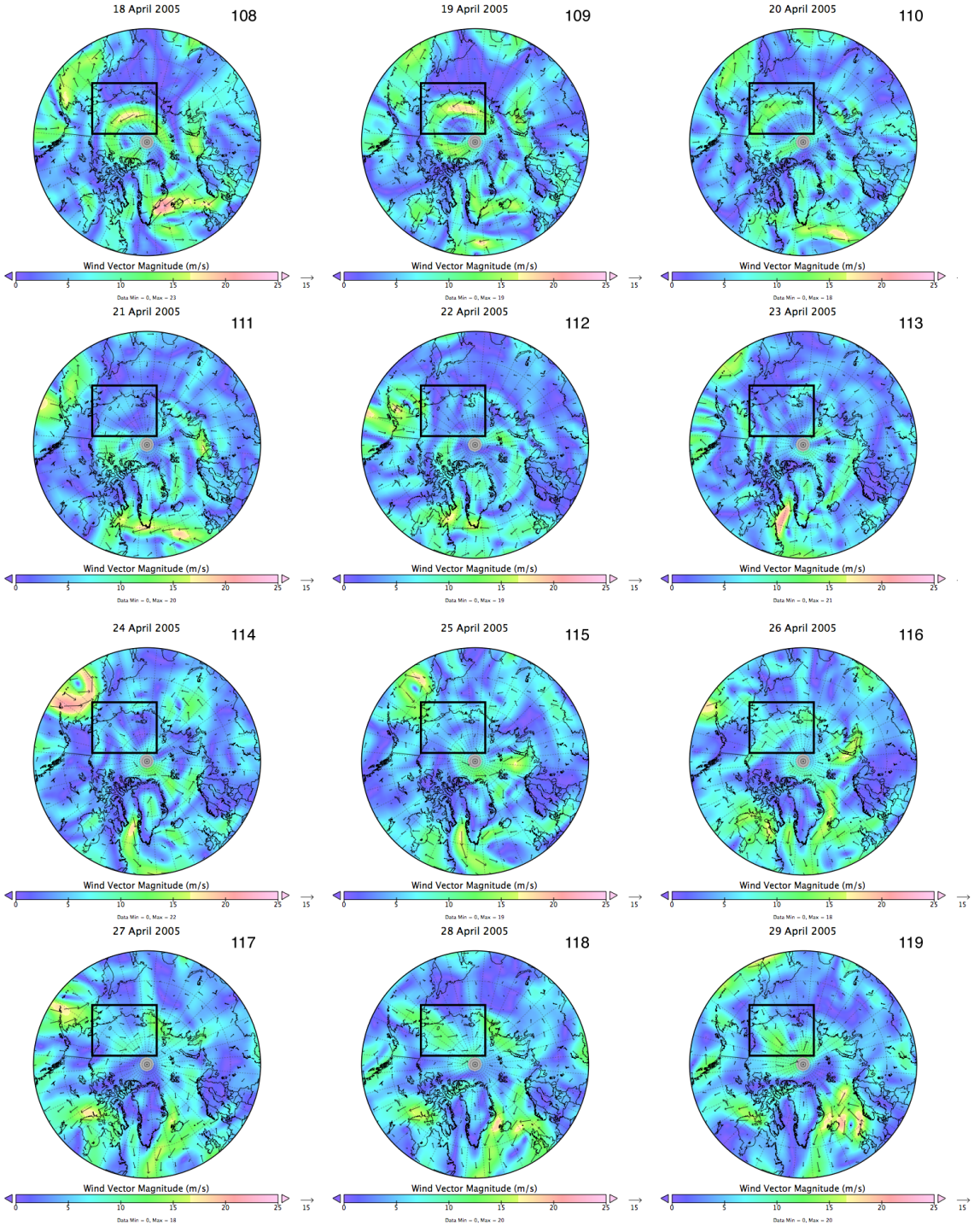

Figure 6.25 Daily mean 10 m vector wind direction and magnitude (ms^{-1}) for 18 – 30 April 2005.

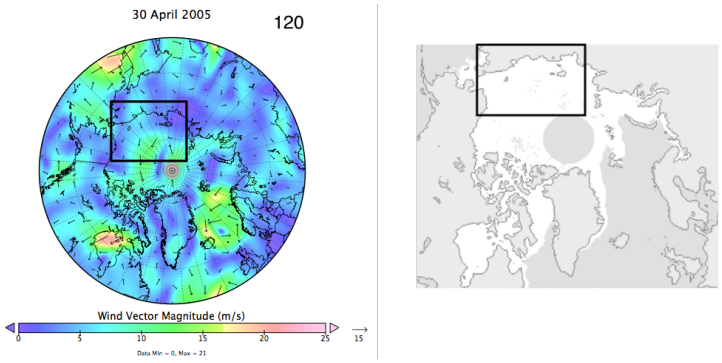

Figure 6.25 Continued.

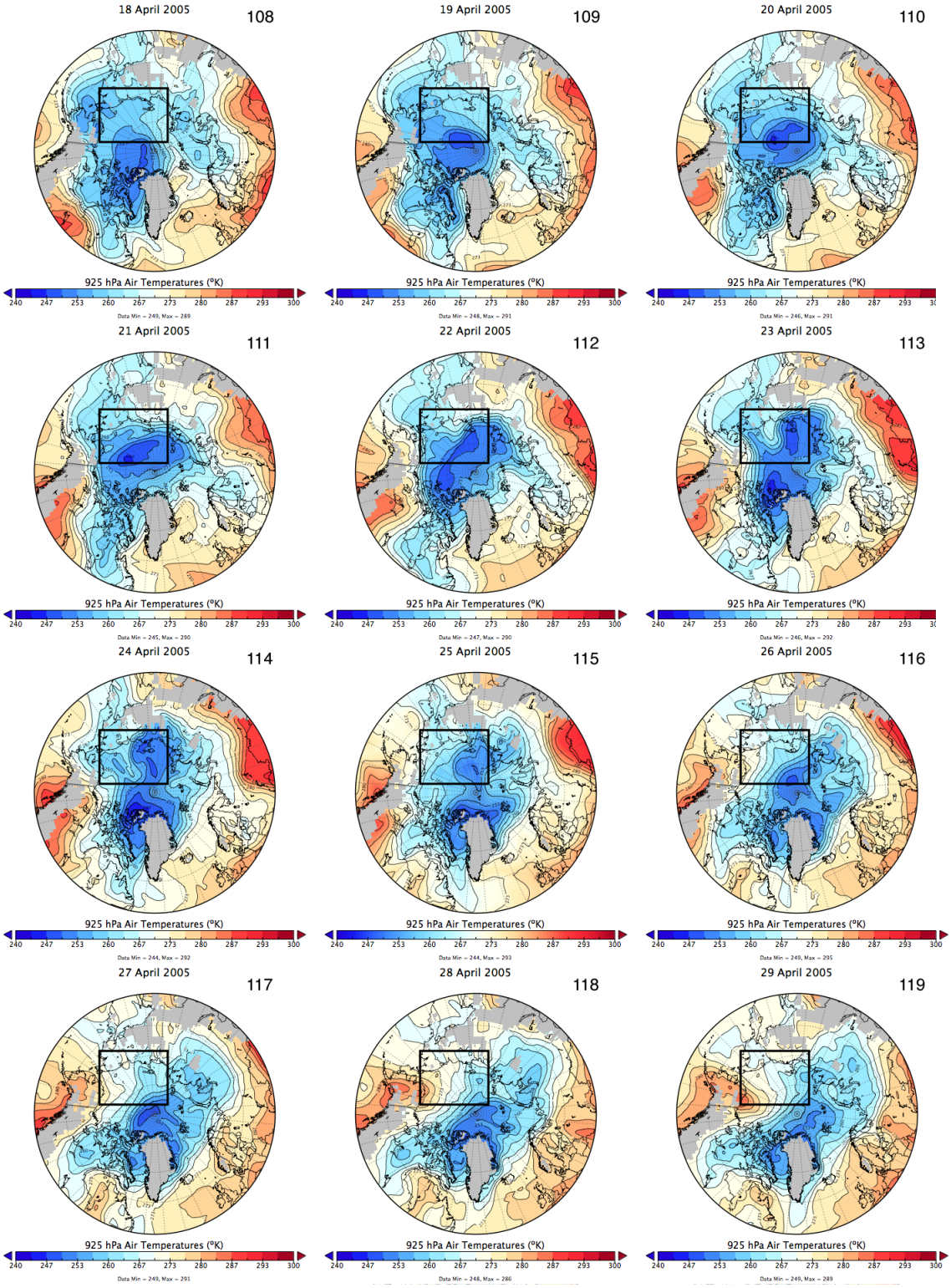

Figure 6.26 Daily mean 925 hPa air temperatures (ºK) for 18 – 30 April 2005.

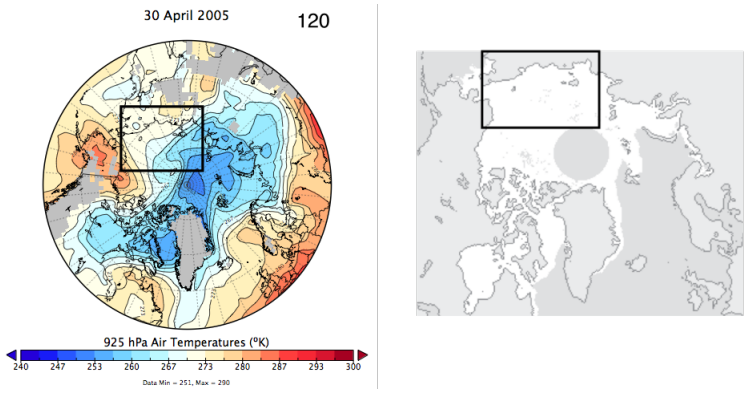

Figure 6.26 Continued.

The second peak MO day during this event on 28 April (DOY 118) is associated with strong southwesterly winds (Figure 6.25) and strong warm air advection over the eastern East Siberian Sea (Figure 6.26). On the maximum melting day of the 2005 East Siberian Sea melt event (28 April, DOY 118), an area of low pressure begins to develop south of the region (Figure 6.24) and tracks northward over the western side of the East Siberian Sea on 29 – 30 April (DOY 119 – 120). The cyclonic winds from this system, result in strong southwesterly and southerly winds (Figure 6.25), leading to the advection of warmer 925 hPa air temperatures (Figure 6.26) which induces MO over nearly the entire Chukchi Sea region and completes the melting over 33% of the East Siberian Sea region observed during this melting event.

6.5 Summary: MO area spatial patterns and associated atmospheric forcing

Due to the heavy reliance of the timing of MO on the local weather conditions at the time of melt shown for the Kara, East Siberian, and Beaufort Sea regions, it can be inferred that there may be similarities in the atmospheric forcing occurring at the time of

MO for other regions and in cases from other years not investigated here. Several case studies have been presented that show some remarkable similarities in spatial patterns of daily MO area despite intentional variation in geographic location of the sub-regions examined, varied timing of the MO events during the spring, and analysis during different years of the data record.

The analysis of spatial patterns in MO area has refined the interpretation of the MO area patterns observed in the daily time series of MO area discussed in Chapter 5. For example, in some cases, MO area accumulates gradually over a relatively longer period of time than occurs in high magnitude, short duration cases. In other cases, large areas of sea ice experience MO over a very short time period as occurs on the dates with the highest magnitude peaks in the daily MO area time series. For various melt event types the location and track of cyclonic activity can influence the degree to which MO area accumulates over a given short or long time period. The net effects of different types of melting events may produce similar total melt areas, but an intense melt event earlier in the year can have a greater impact on the total energy absorbed by the ice-ocean system [*Perovich et al.* 2007] in the region for the given season than a slower or delayed accumulation of MO area.

While the analysis presented in this work is in no way an exhaustive record of all possible atmospheric conditions that can lead to melting events on the sea ice, the type of spatial patterns observed during various MO events appear to be related to the atmospheric forcing that induces the MO. The influence of an approaching cyclone leads to MO area occurring over larger groupings of adjacent pixel points when the cyclone

tracks to the northwest of the region of interest, placing the region in the warm sector. High magnitude, short duration events may occur independent from other melting influences (e.g. Kara Sea 1992), or they may be embedded within other melt inducing conditions over a longer length of time (e.g. Beaufort Sea 2009, Kara Sea 1985).

The influence of a cyclone on a region of the sea ice pack via cyclonic winds increasing the air temperature by advection from the south and increased cloud cover trapping outgoing longwave radiation [*Bennartz et al.* 2013] is a primary mechanism leading to the high magnitude, short duration melting events such as occurs in the Kara Sea during 1992 and for periods of time during the 1992 and 2009 melt events in the Beaufort Sea. The warm air advection ahead of an approaching cyclone tracking to the west-northwest of the region of interest has been shown to raise daily mean 925 hPa air temperatures to near 273 ºK, resulting in the ideal pattern for producing a short-lived, widespread melting event similar to that in the Kara Sea during 1992. It has been shown that for melting events associated with the passage of a cyclone, the new MO area will tend to accumulate adjacent to locations that have experienced MO on the days immediately prior to the "current" MO date. Due to the strong melting response observed in cases where the cyclone track places the region of interest in the warm sector, the type of spatial pattern in MO area should be somewhat predictable for other high magnitude, short duration melting events.

It has been shown here that the longer duration melting events tend to be embedded with many shorter events that induce some larger areas of daily melt, interspersed with days where relatively smaller areas of daily melt occur. The high

magnitude, longer duration melting events such as occurs in the Kara Sea during 1985 are generally associated with relatively high MSLP and cooler temperatures, possibly delaying the rapid accumulation of large MO areas despite the seasonal warming of air temperatures into the late spring and summer. However, in some cases where high pressure exists over the region (e.g. Beaufort Sea 1992, East Siberian Sea 2012), clear skies and increasing insolation in the spring can also raise the maximum daily air temperature enough to induce melting on the sea ice with or without a mean daily 925 hPa temperature nearing 273 ºK. In these cases, the observed MO area occurs in a spatially dispersed, discontinuous pattern and in the time series of MO area, the daily MO area is greater than 0 km^2, but of a much lower magnitude than melting associated with a low pressure system. In longer duration events, the transient nature of passing cyclones tends to be masked in the MO area time series because warm, cloud-free high pressure conditions also induce some melting which appears in the daily time series of MO area.

Investigating the spatial patterns of MO area during these longer duration MO events has shown that the spatial pattern in MO area tends to differ under low pressure, cyclonic conditions versus high pressure, anticyclonic conditions. The Beaufort Sea 1992 case illustrates both situations. Initially, MO area tends to occur adjacent to MO area locations that melted on the previous day when the Beaufort Sea is under the influence of cyclonic conditions. Conversely, when the region is under anticylonic conditions, the pattern of new MO area shifts to a more scattered, discontinuous pattern in another location within the region. Although no two patterns in daily MO area are

exactly the same, forecasting the atmospheric conditions can help improve the predictability of the resultant spatial pattern in new MO area.

One of the biggest limitations with an analysis of MO area is that the pixels are flagged with a MO date only once per melt season. Due to this limitation, the daily MO area becomes less useful later in the melt season when a majority of the region's area has already had a MO date assigned and is classified as previous MO. Following a large melt event, inferring patterns in atmospheric circulation from the spatial patterns in MO becomes impossible since there are few melt-free pixel locations remaining. The analysis presented here is, therefore, primarily limited to the very first big peak in daily MO area for the season.

High magnitude peaks in the daily MO area time series are easy to identify and easy to analyze. Therefore, this analysis is necessarily biased toward the relatively large melting events that are easily identified in the data. Given the importance of the timing of MO and the effects it has on the surface energy balance of the ice-ocean system in the Arctic through the remainder of the year, the absence of anomalously early or very large melting events in a particular year can also have a significant impact on the surface energy budget. The methods employed in the present study are inherently biased toward an analysis of those early and extreme melting events, however, an analysis into the converse situation where MO is not occurring early in the season is equally justified as it also has important implications for sea ice change in the Arctic.

The overall trend towards increasingly early MO in the Arctic is related to warming temperatures in the Arctic; however, the high regional and inter-annual

variability and susceptibility of the sea ice to episodic events and sensitivity to individual cyclonic events described here warrants further analysis to determine how these smaller scale (spatial and temporal) events contribute to ongoing changes in sea ice volume loss. Daily MO areas provide details about the day to day progression of MO across Arctic sea ice within an individual year, however, accumulations of MO area throughout the melt season can better describe the inter-annual variability in these patterns of melt.

CHAPTER 7 – ANNUAL MELT ONSET AREA ACCUMULATIONS

7.1 Accumulations of melt onset area

The regional pattern of MO dates in a given melt season can be described by accumulating the daily MO area time series (described in Chapter 5) throughout the melt season on an annual basis. Summarizing the changes in daily MO area with annual accumulations clearly illustrates the significant changes in timing of MO area over the data record (described in Chapter 4) and makes the year-to-year variation in MO area easily comparable. Fluctuations in these accumulations of MO area during a single melt season show the temporal variation in the progression of melting area for the region. The MO area accumulations described here are calculated by summing the number of pixel point locations experiencing MO on each day of the melt season (March through August). The numbers of pixels are then scaled to represent the spatial area of MO by multiplying the number of pixels by the pixel ground resolution (25 km x 25 km). Progressing through the melt season, each day's new MO area is added to the running total, creating a curve that shows the annual accumulation of melting area (e.g. Figure 7.1).

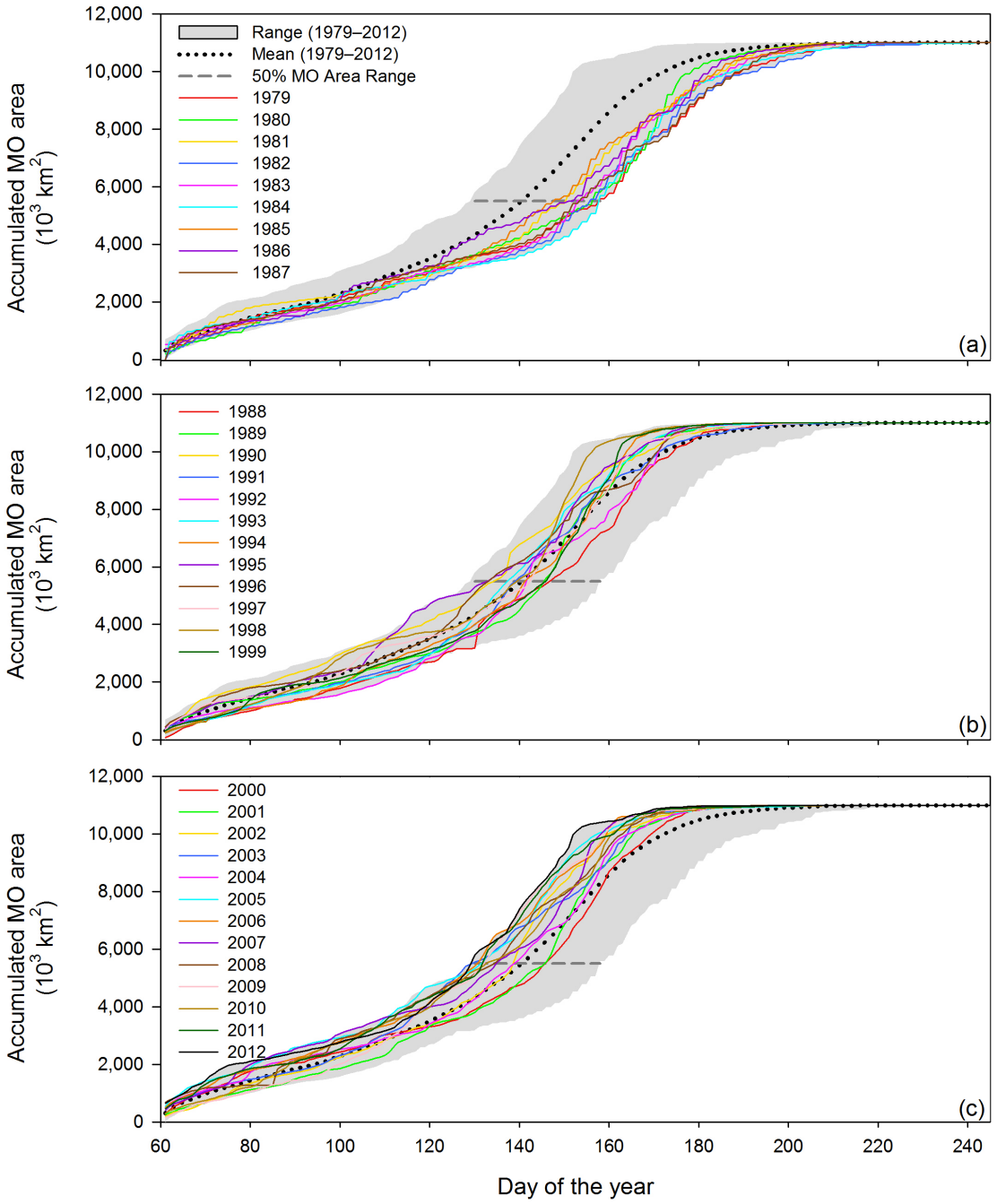

Figure 7.1 Arctic Region annual accumulated MO areas for (a) SMMR years, (b) early SSM/I years, and (c) late SSM/I and SSMIS years.

The slope of an accumulation curve corresponds to the amount of MO area occurring per unit time during the melt season (e.g. Figure 7.1). A steep slope indicates a relatively quick accumulation of melting area, while a lower slope indicates a slower accumulation of melting area. Therefore, a high magnitude, short duration melting event identified as a peak in the daily MO area time series curve (e.g. the Kara Sea 1992 MO event (Section 6.2, Figure 5.4)) would appear as a nearly vertical slope on the annual MO accumulation curve, while a high magnitude, longer duration melting event (e.g. the Kara Sea 1985 MO event (Section 6.3.1, Figure 5.4)) would be represented by a shorter, stair-stepped vertical change on the annual MO accumulation curve.

The annual MO accumulations are calculated for each year in the 1979 – 2012 study period for the Arctic Region as a whole (Figure 3.1), for sub regions within the Arctic Ocean (Figure 3.2), and the Bering Sea (Figure 3.1). For this analysis, the Bering Sea is shown because it is the only sub-region of the Arctic that has a statistically significant trend towards later MO (Figure 4.7). Inter-annual comparisons in the annual MO accumulation curves show the variability in timing of MO for the Arctic and sub-regions due to differences in springtime atmospheric conditions inducing MO described in Chapter 6. For consistency when comparing MO area accumulations for all years in the data record, the MO area accumulations for each melt season in the record is normalized by accumulating MO area only for pixel locations where a MO date exists for all 34 years in the study period. Therefore, the accumulation curves for every year in a given study region typically form an "S" shaped curve; beginning in March with 0 km^2 of melt area, accumulating MO area through the spring and summer, and finally, converging

to the total region area based on the climatology of existing MO dates near the end of the melt season (Table 3.2).

Since brightness temperature data from the SMMR sensor used to calculate the MO dates were only collected every second day, the accumulation curves for 1979 – 1987 are not smooth. Instead the curves for these early years of the record have a stair-step appearance; however, the general shape of these rough curves for SMMR years are comparable to annual MO accumulations for the other years in the record. Thus, SMMR data are grouped separately to avoid confusion regarding these data inconsistencies. Hereafter, the annual MO area accumulation curves for each region are divided into 3 time periods: (a) SMMR 1979 – 1987, (b) early SSM/I 1988 – 1999, and (c) late SSM/I and SMMIS 2000 – 2012 for better visualization (Table 3.1).

The MO area accumulation curves illustrate regional variability in addition to inter-annual variability. The patterns that appear in the accumulation curves in a single year represent the timing and magnitude of melting events as shown in Chapter 5. To summarize the MO area accumulation variability in each sub region, the day of the year on which 50% MO area occurs is used as a representation of the median of the time period over which MO area accumulates across all sea ice area within the region. The mean MO accumulation curve and range of accumulations for 1979 – 2012 are the same across the three sensor time periods defined above and are the same in all three plots (a – c) for each region. The annual accumulation curves are plotted against the mean MO area accumulation for all years (1979 – 2012) and the range of accumulation MO area is shown as grey shading.

7.2. Inter-annual variability in the Arctic Ocean

Inter-annual variability of MO area accumulation in the Arctic is evident by the spread of annual MO accumulation curves (Figure 7.1). The Arctic Region, represents MO data from all perpetually sea ice covered regions of the Arctic during early March and given that MO dates vary at a spatial scale that is smaller than the whole Arctic Region represented in Figure 7.1, the accumulation curves for the Arctic Region resemble a relatively smooth "S" shape. Some years have outlier periods where the accumulation curve indicates abnormally early accumulations of MO area such as occurs in 1995 surrounding 30 April, DOY 120 (Figure 7.1b); however, the net accumulations across all Arctic sea ice from year to year are not as highly variable as appear at the regional scale described below in Section 7.3. The absence of strong outliers in the Arctic Region accumulation curves illustrates the need for examination of MO area accumulations in smaller geographic regions where variability in MO is much greater.

Although smaller scale variability is largely absent from analyses of MO area for the Arctic Region as a whole, the trend toward increasingly early MO dates are clearly apparent in the annual MO area accumulations for the Arctic Region (Figure 7.1). In general, the comparison of SMMR years in the Arctic Region (Figure 7.1a) to the mean (1979 – 2012) and range in accumulation across all years shows that MO accumulation in the early part of the record is different from later years. Since the SMMR years (1979 – 1987) tend to fall below the mean, MO area accumulates later in the year than average indicating delayed MO relative to other years. The early SSM/I years (1988 – 1999) have an increased spread when compared to SMMR years and tend to fall both above and

below the mean accumulation curve (Figure 7.1b). Additionally, early SSM/I accumulations do not occupy the bottom of the range after approximately 10 May (DOY 130). The late SMM/I years (2000 – 2012) generally fall above the mean, indicating that MO area is accumulating sooner in the year than the mean (Figure 7.1c). The changes observed in the MO area accumulations for the Arctic Ocean with respect to the mean, describe the change in MO towards increasingly early melting over large regions of Arctic sea ice in terms of accumulated area.

7.3. Variability in Arctic Ocean sub-regions

There is considerable regional variability in the annual accumulations of MO area in addition to inter-annual variability for the entire Arctic Region. Here, we focus on the sub-regions in the Arctic Ocean shown in Figure 3.2. Compared to the relatively smooth "S" shaped accumulation curves for the Arctic Region (Figure 7.1), individual sub-regions of the Arctic Ocean show higher variability in the timing of MO area accumulations from year to year. The pattern of the range of MO area accumulation curves (i.e. the shape of the grey shaded regions of MO area accumulation plots) varies for each sub-region (Figures 7.2 – 7.11). For the purposes of this analysis, the period of time over which MO area accumulates over the total area of a region is referred to as the MO period. It is important to note that the MO period does not refer to the duration of melting at a point location or the local ablation of snow and ice cover, but the duration of time over which a region's total area experiences the onset of melt following the earliest occurrence of MO for the season.

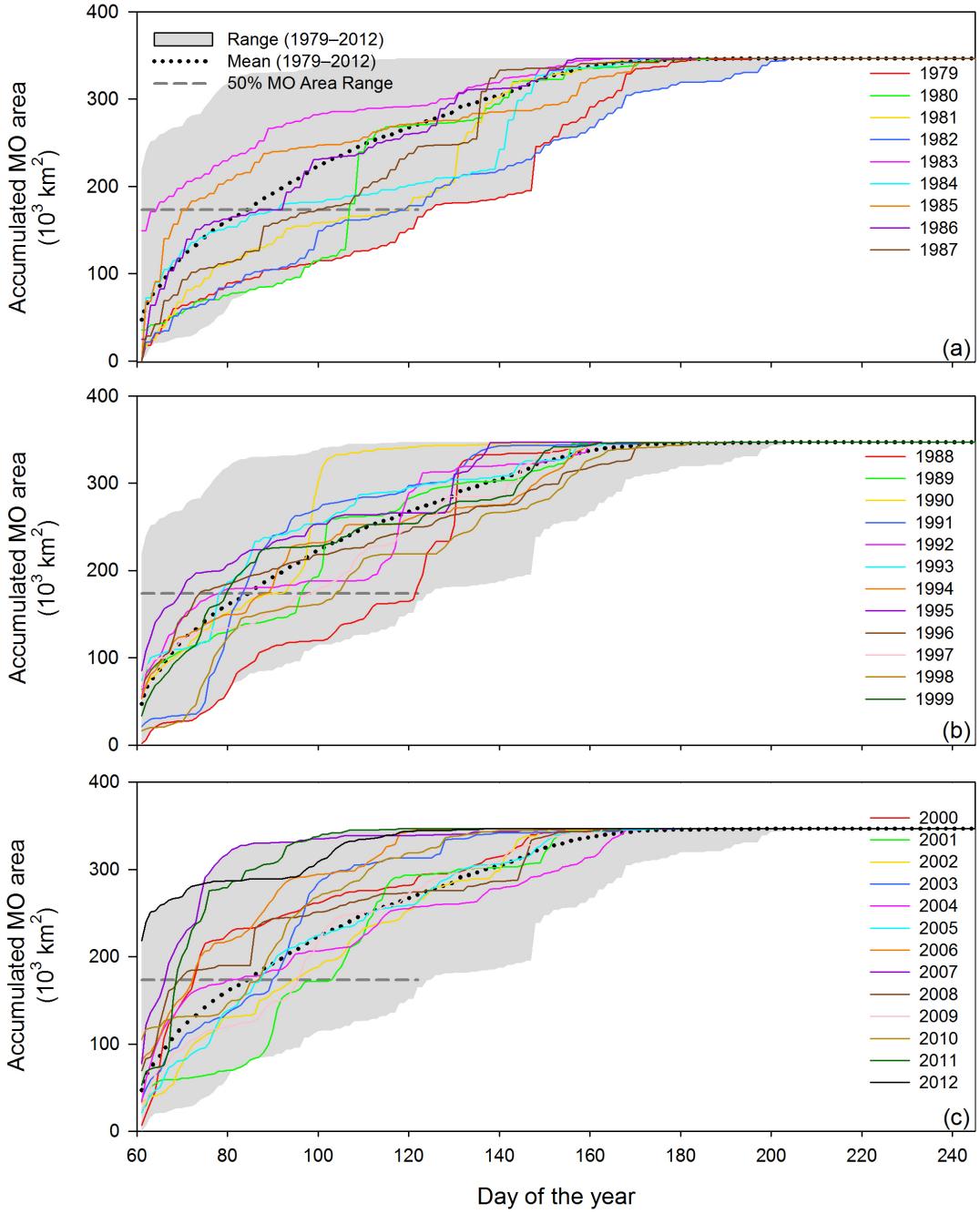

Figure 7.2 Barents Sea annual accumulated MO areas for (a) SMMR years, (b) early SSM/I years, and (c) late SSM/I and SSMIS years.

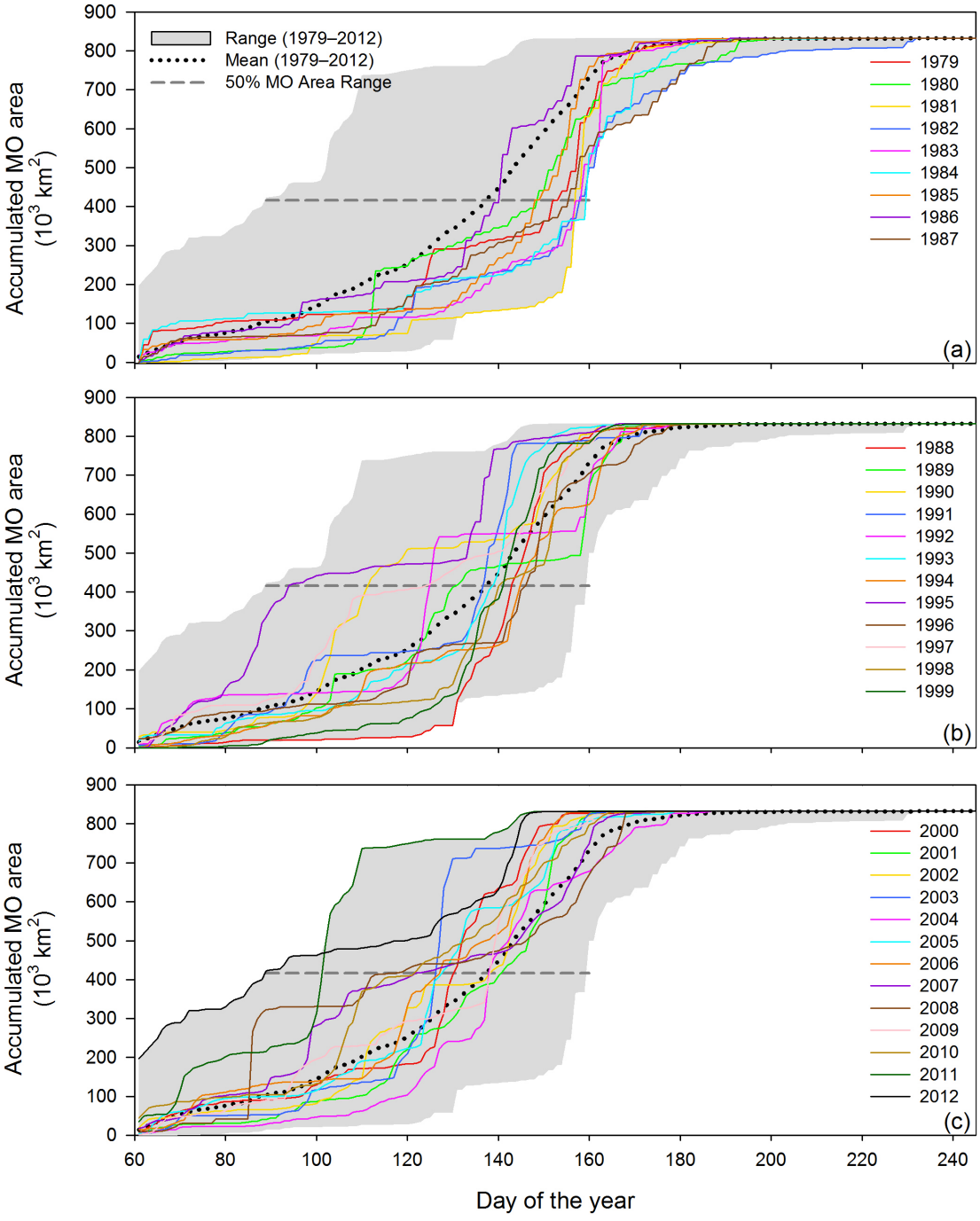

Figure 7.3 Kara Sea annual accumulated MO areas for (a) SMMR years, (b) early SSM/I years, and (c) late SSM/I and SSMIS years.

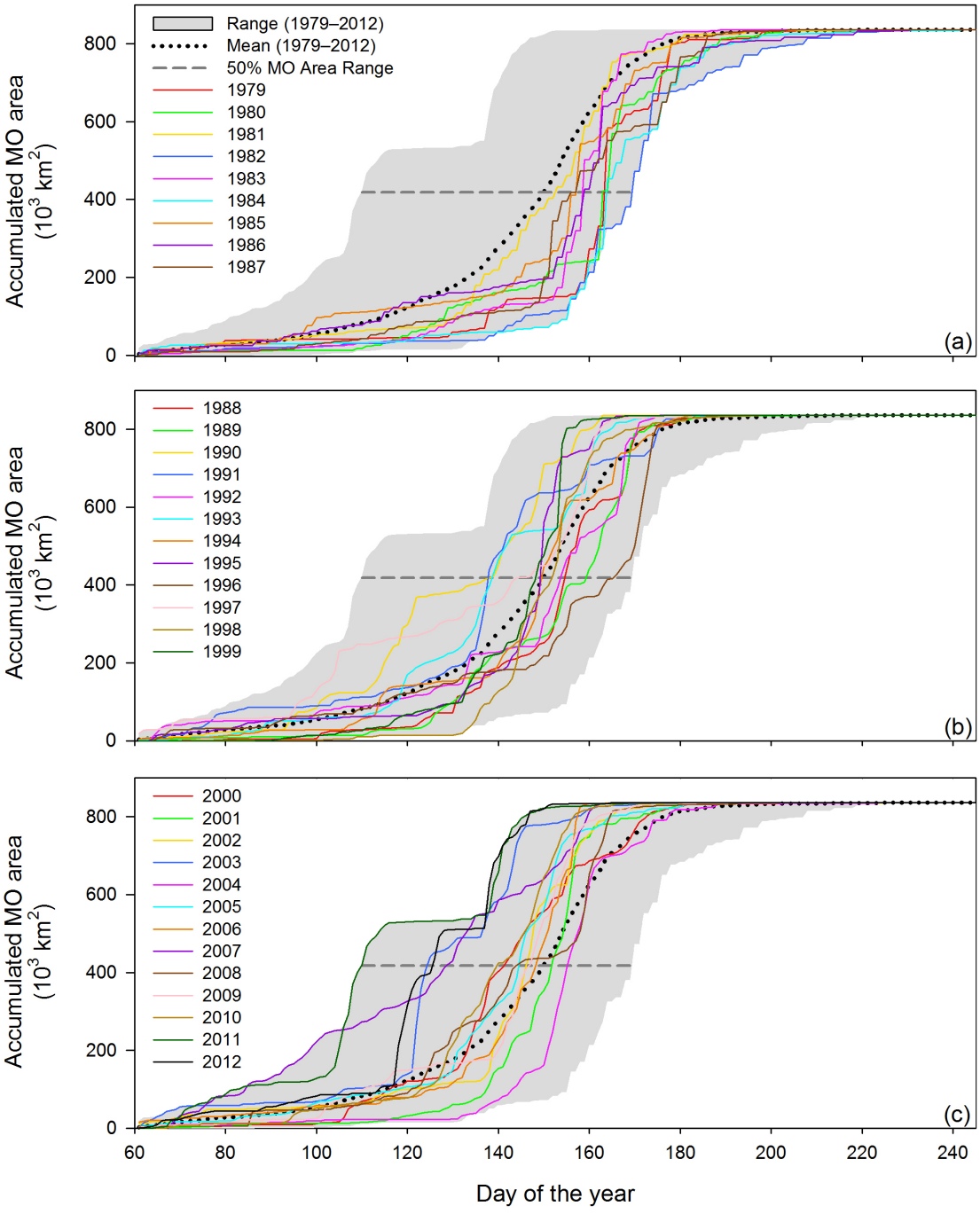

Figure 7.4 Laptev Sea annual accumulated MO areas for (a) SMMR years, (b) early SSM/I years, and (c) late SSM/I and SSMIS years.

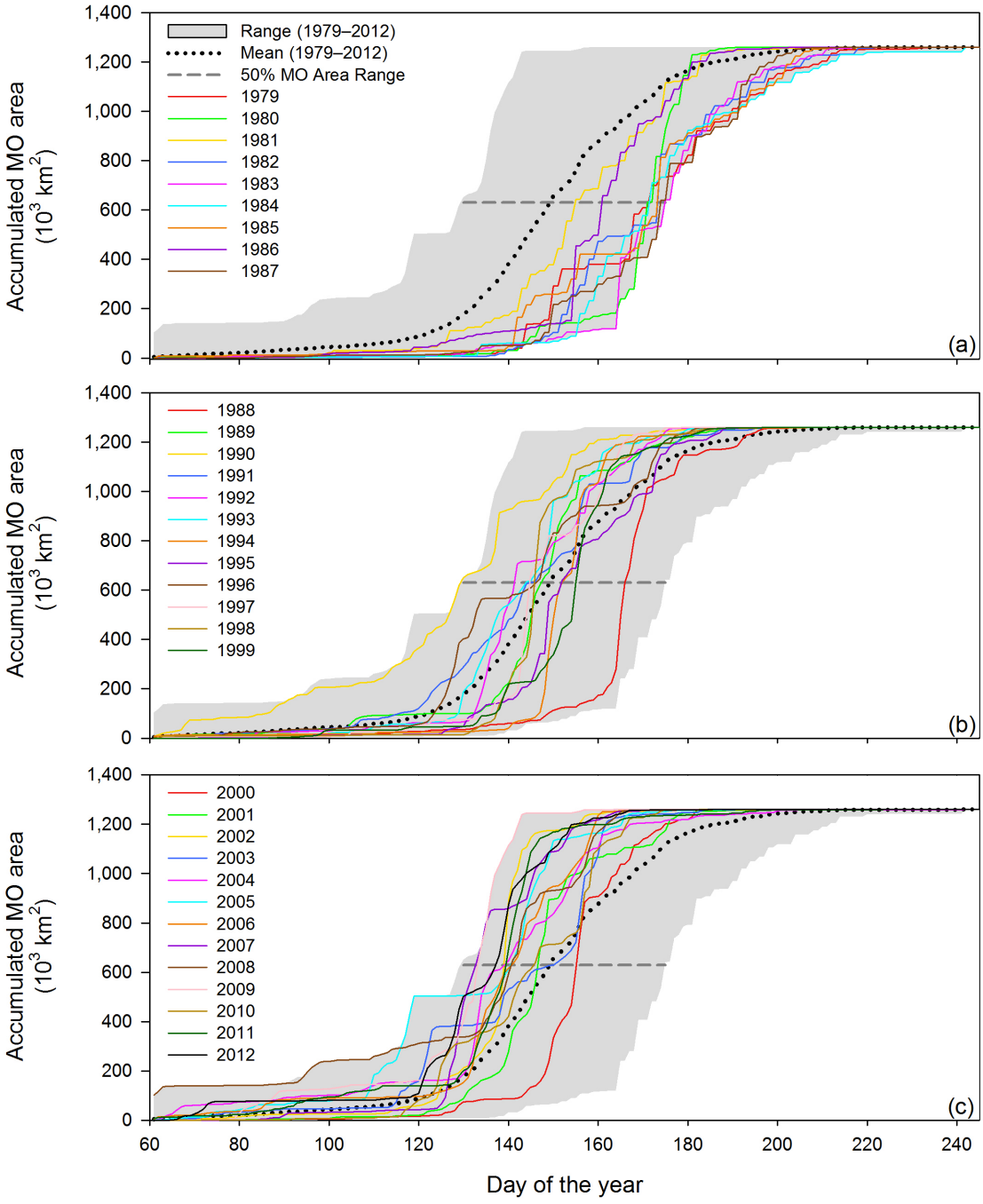

Figure 7.5 East Siberian Sea annual accumulated MO areas for (a) SMMR years, (b) early SSM/I years, and (c) late SSM/I and SSMIS years.

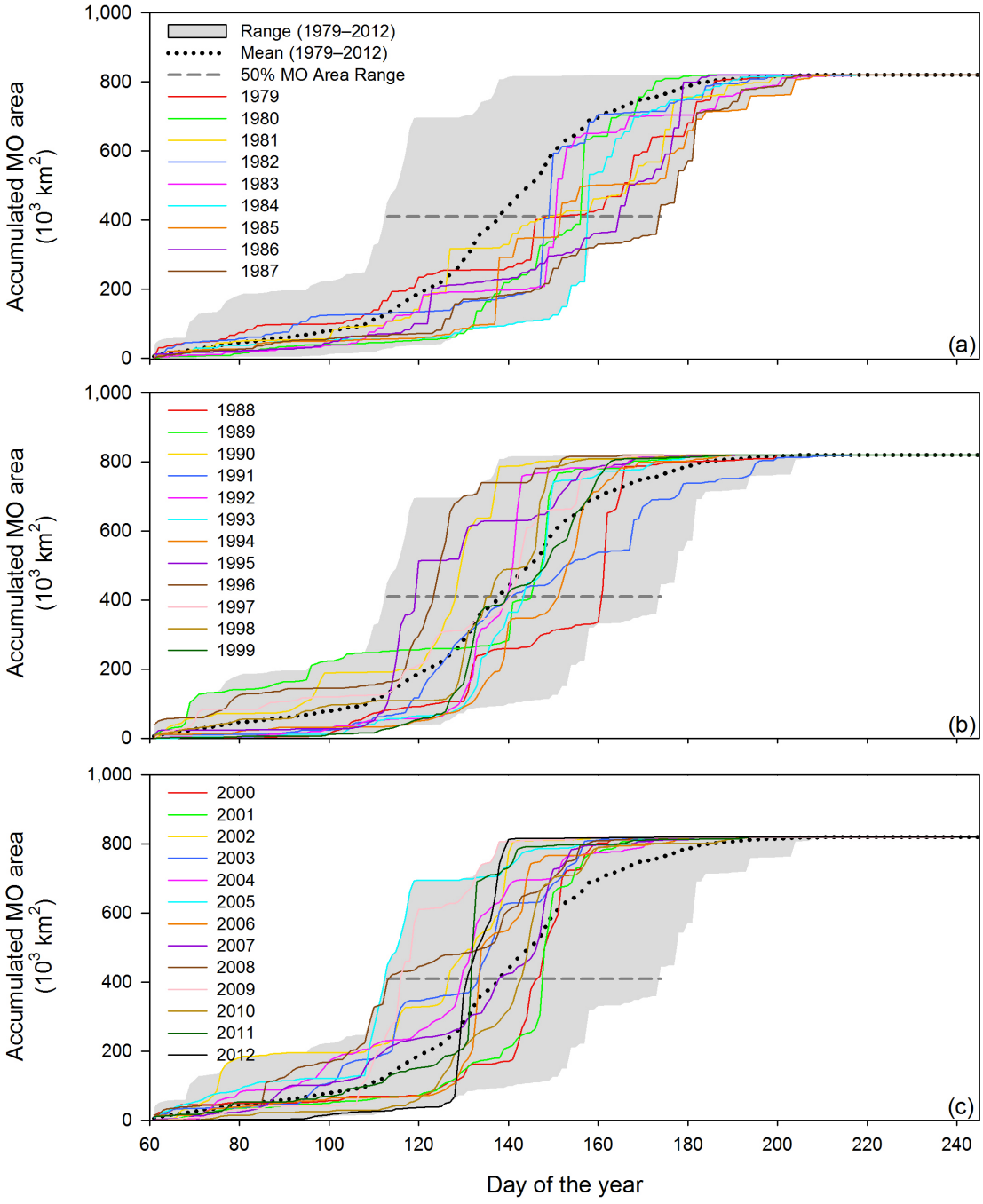

Figure 7.6 Chukchi Sea annual accumulated MO areas for (a) SMMR years, (b) early SSM/I years, and (c) late SSM/I and SSMIS years.

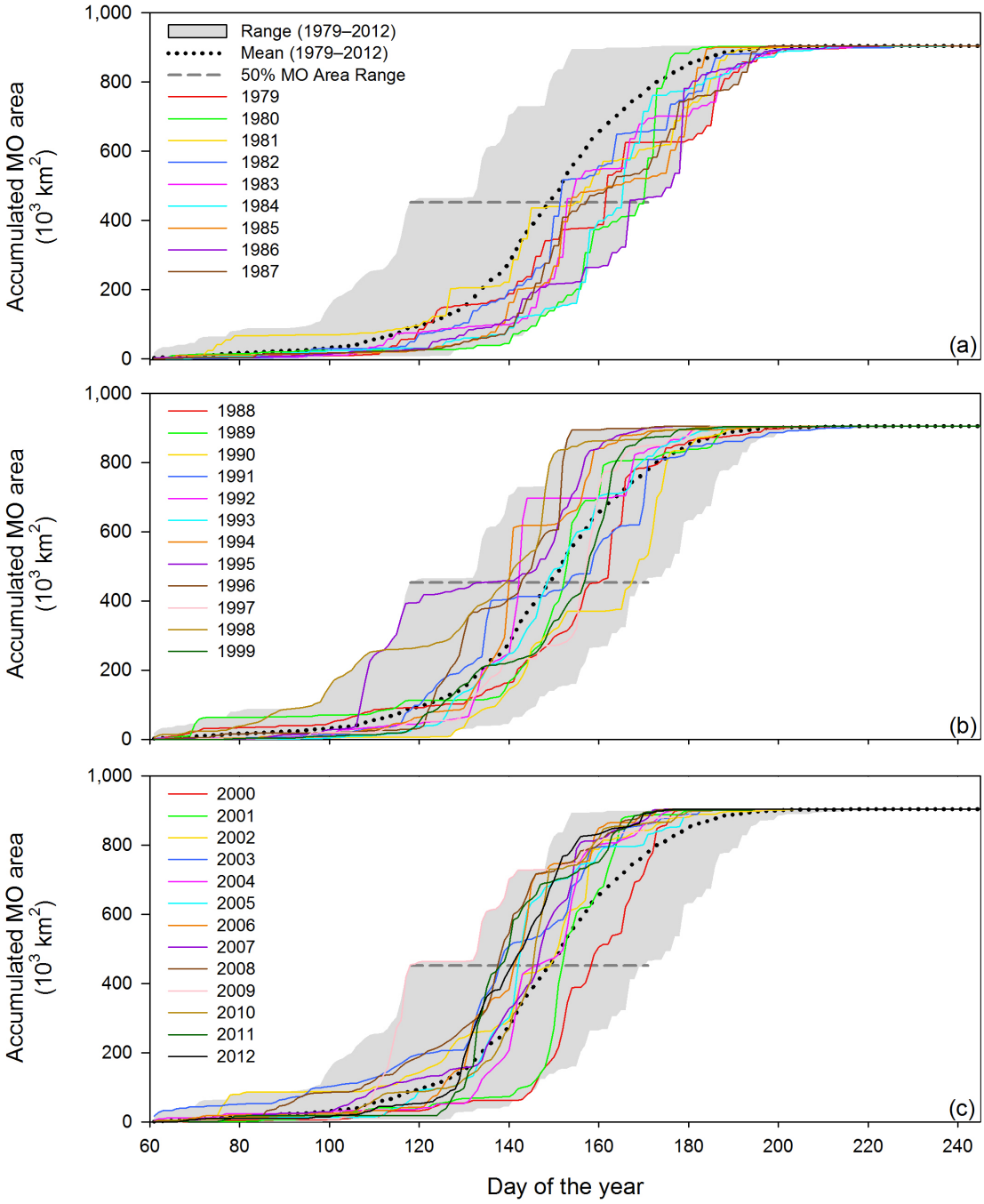

Figure 7.7 Beaufort Sea annual accumulated MO areas for (a) SMMR years, (b) early SSM/I years, and (c) late SSM/I and SSMIS years.

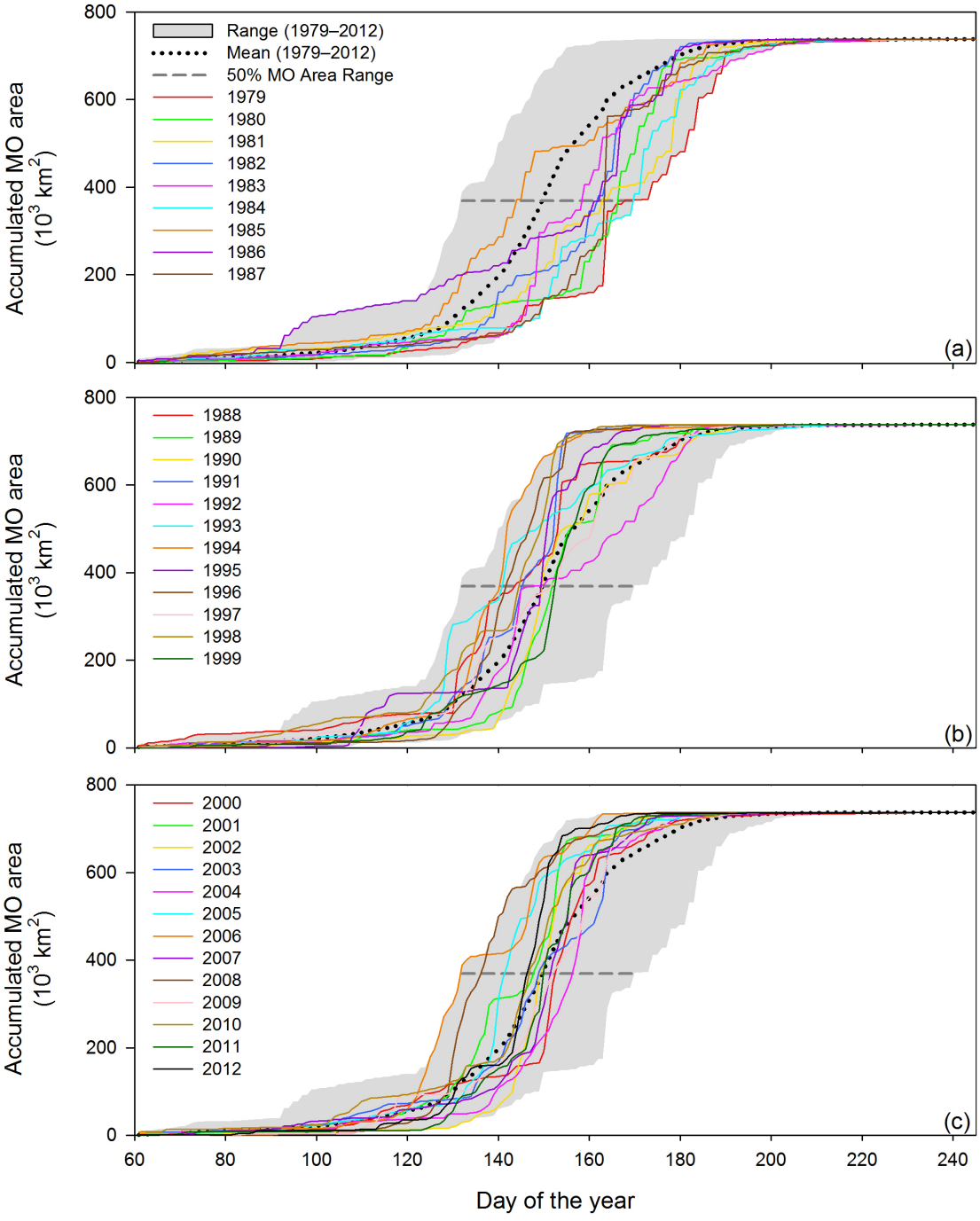

Figure 7.8 Canadian Arctic Archipelago annual accumulated MO areas for (a) SMMR years, (b) early SSM/I years, and (c) late SSM/I and SSMIS years.

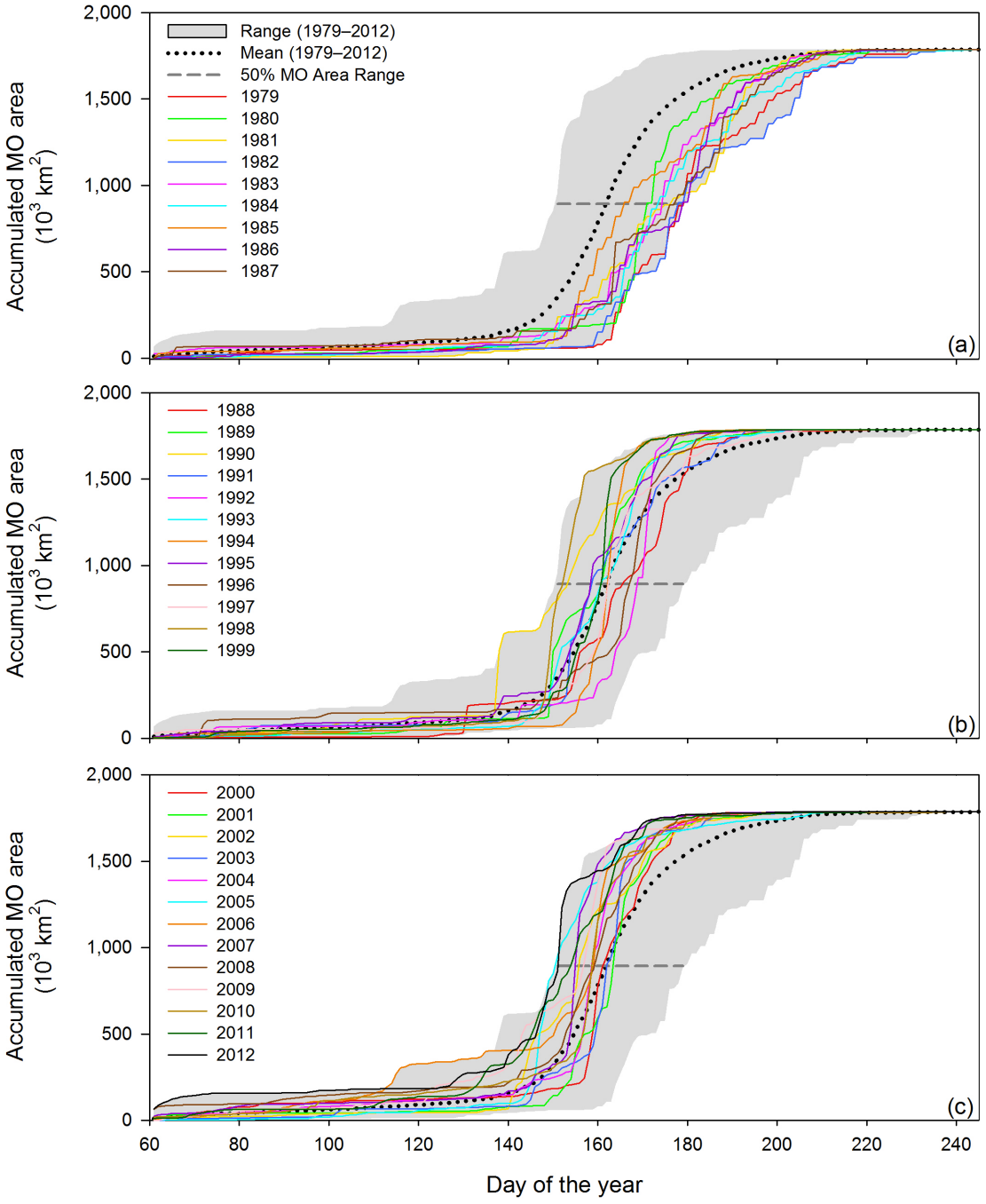

Figure 7.9 Central Arctic annual accumulated MO areas for (a) SMMR years, (b) early SSM/I years, and (c) late SSM/I and SSMIS years.

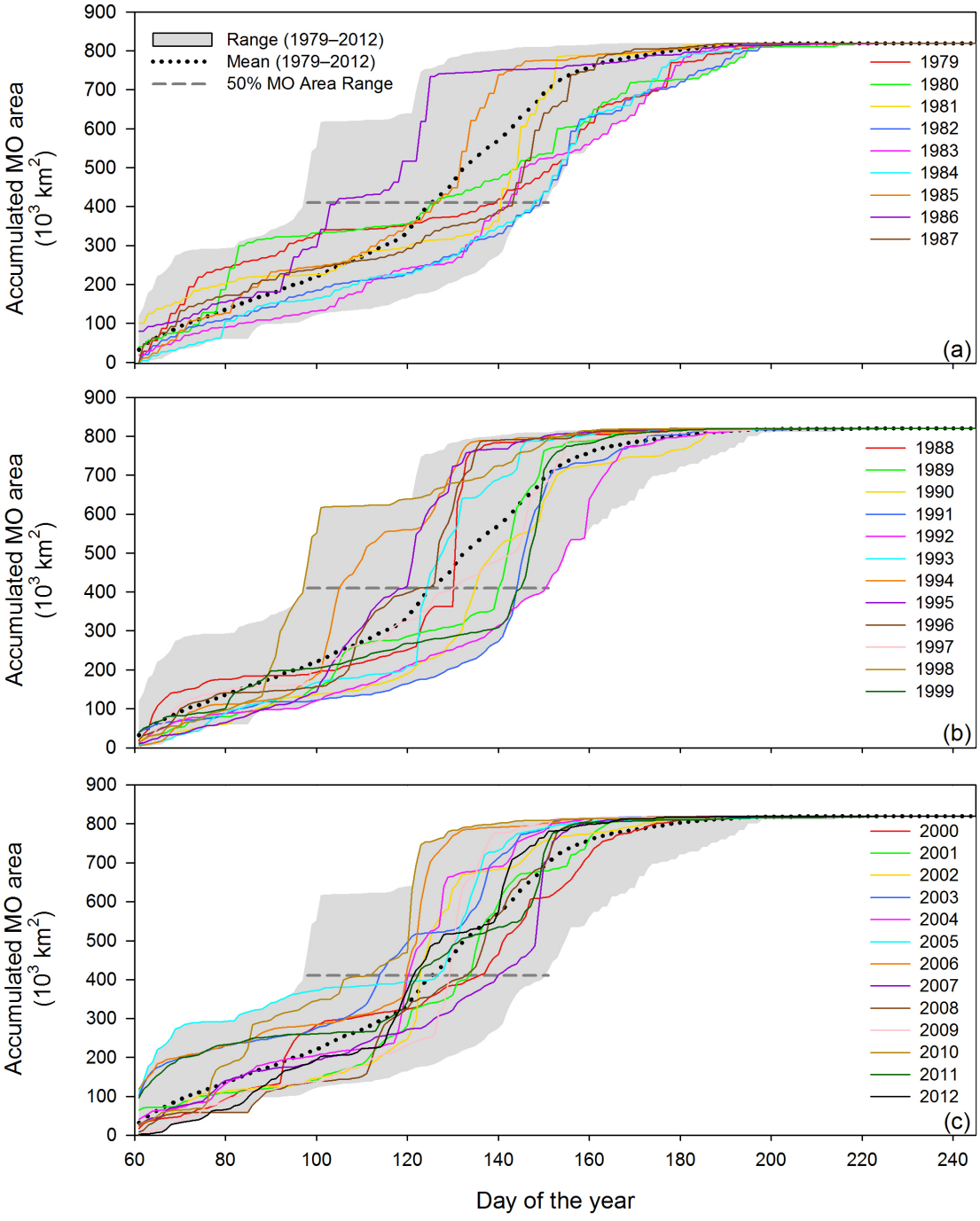

Figure 7.10 Baffin Bay annual accumulated MO areas for (a) SMMR years, (b) early SSM/I years, and (c) late SSM/I and SSMIS years.

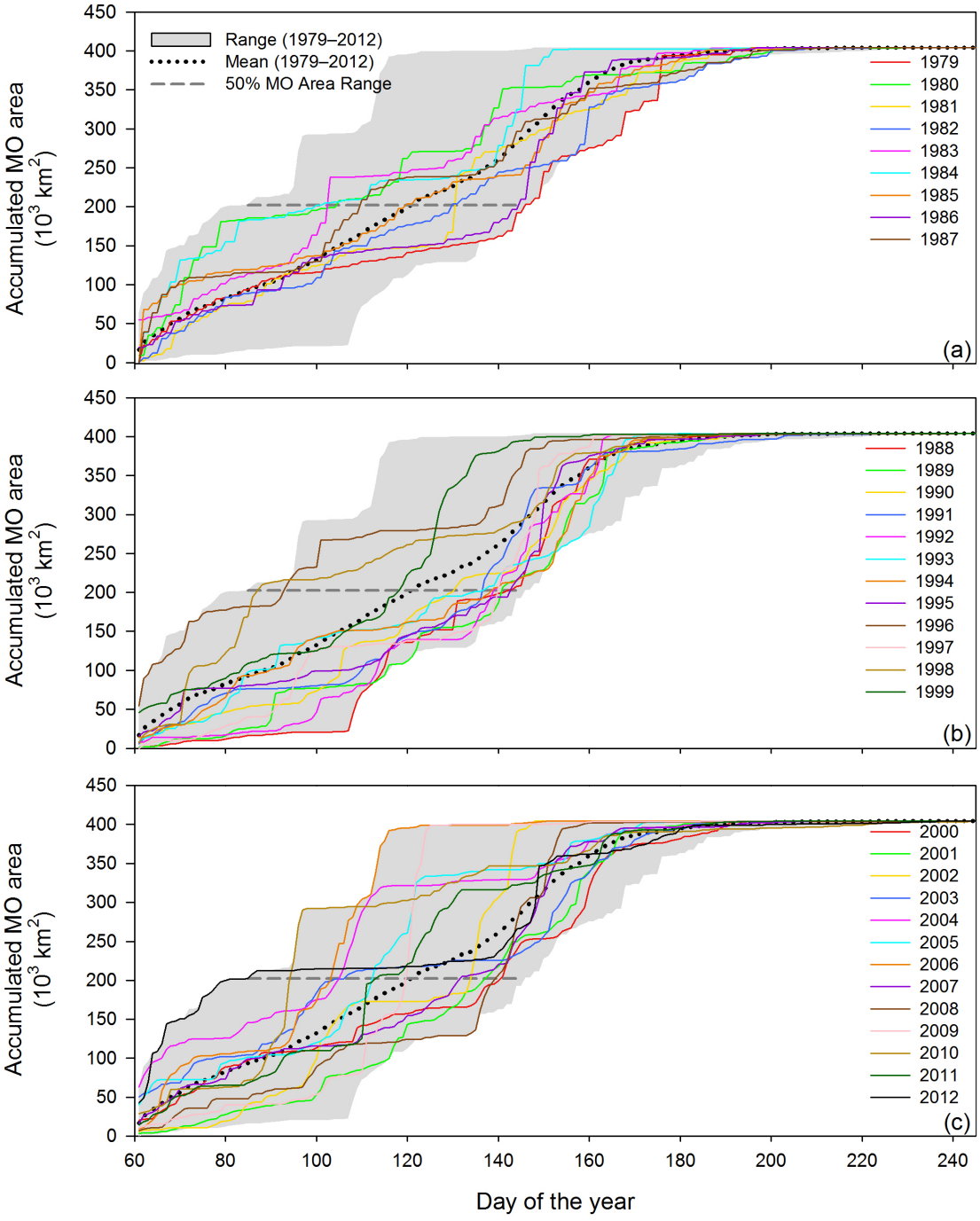

Figure 7.11 Greenland Sea annual accumulated MO areas for (a) SMMR years, (b) early SSM/I years, and (c) late SSM/I and SSMIS years.

The pattern in the range of MO area accumulations differs for each region. For example, the Central Arctic region surrounds the pole at the highest latitudes, excluding the "pole hole;" thus, the earliest MO area accumulations tend to begin later in the season than for regions at lower latitudes (Figure 7.9). However, MO area accumulates more rapidly here than for other regions; that is, the slope of the accumulation curve is much steeper over the length of the MO period than compared to other regions such as the Barents, Kara, Laptev, East Siberian, Chukchi, Beaufort, and Greenland Seas as well as Baffin Bay (Figures 7.2 – 7.7, 7.10 – 7.11). This result corresponds to the findings of *Wang et al.* [2011], which describe a fast progression of melting in the horizontal direction in the Central Arctic, upwards of 60 km day^{-1}, which is attributed to the influence of cyclonic weather activity.

In general, the shift towards earlier accumulations of MO area in the Arctic Region (Figure 7.1) over the satellite record also appears to a varying degree in all Arctic Ocean sub-regions (Figures 7.2 – 7.11). MO area accumulations for most regions generally fall below the region's mean MO accumulation during the early part of the record (SMMR years), while MO accumulations in the early and late SSM/I years shift earlier in the year. In addition to the shift towards earlier MO for the study years, inter-annual variability within single sub-regions of the Arctic can be large. There are cases where anomalously early or late MO area accumulation years appear clearly within each region. An example of very high inter-annual variability occurs in the East Siberian Sea in 1990 (an early MO area accumulation year) and 1988 (a late MO area accumulation year) which both occurred during the early SSM/I years (Figure 7.5b).

To compare the degree of variability from year to year in MO area accumulations for each region, the range of 50% MO area days is used (Table 7.1). This value is defined as the difference between the earliest date and latest date on which 50% of the region's total area had experienced MO for the 34 years in the record. The range (hereafter 50% MO area range) corresponds to the horizontal width of the grey shaded regions shown in Figures 7.1 – 7.11 at 50% of the region's total area (Table 3.2) and is marked on each plot with a horizontal dashed line. The day of year on which 50% of the area for a region has experienced MO is used as a measure of the central point of the MO period in terms of area.

Table 7.1 Range and Mean Date on which 50% MO Area Occurred 1979 – 2012

Region	50% MO area range (days)	Mean 50% MO Area Date (DOY)
Arctic Region	28	142.1
Barents Sea	61	88.6
Kara Sea	71	134.8
Laptev Sea	60	148.6
East Siberian Sea	45	151.4
Chukchi Sea	61	140.9
Beaufort Sea	53	149.9
Canadian Archipelago	38	151.2
Central Arctic	28	163.7
Baffin Bay	53	129.7
Greenland Sea	60	122.6
Bering Sea	39	74.7

The Kara Sea is the most highly variable region in MO area accumulation with a 71-day 50% MO area range (Table 7.1, Figure 7.3). By comparison, the Arctic Region

has a 28-day 50% MO area range. The large difference between the cumulative (whole Arctic) 50% MO area range and the 50% MO area range for a single sub-region of the Arctic again highlights the importance of regional analysis in MO area studies. Note that the most anomalously early melt years in the Kara Sea are 2012, 2011, and 1995 (Figure 7.3) and the 71-day 50% MO area range (Table 7.1) is largely influenced by the extremely early MO observed in the early part of 2012 (Figure 7.3), before 30 March (DOY 90) and in 2011 following 10 April (DOY 100).

Following the Kara Sea, the Barents (Figure 7.2), Laptev (Figure 7.4), Chukchi (Figure 7.6), and Greenland Seas (Figure 7.11) have the next largest 50% MO area range (Table 7.1) which spans about two months (60 – 61 days in each region). Although the range is similar for these four regions, the 50% MO area range in the Laptev Sea seems to be heavily influenced by two extremely early MO area accumulation years: 2007 and 2011 (Figure 7.4). In the Chukchi and Greenland Seas (Figures 7.6, 7.11), however, the variability of MO area accumulation curves is larger, and highly anomalous years such as in the Laptev Sea do not stand out as clearly against the other years. This might indicate that, with the exception of extreme years, the Laptev Sea MO area accumulations are in general not as highly variable as the MO accumulations in the Chukchi Sea as the similar 50% MO area ranges might suggest.

7.4 Variability in the Bering Sea

The Bering Sea is unique in terms of MO area accumulations because it is the only sub-region of the Arctic that has shown a positive decadal trend in the timing of MO over the 34-year data record (Figure 4.7). The statistically significant trend towards later

MO timing (Figure 4.7) and the observed increase in sea ice extent at the beginning of the melt season (Figure 4.1) indicates that the sea ice response to climate change is different in this region of the Arctic than for the rest of the sea ice extent. The trend towards later MO in the Bering Sea also appears in the MO area accumulations (Figure 7.12).

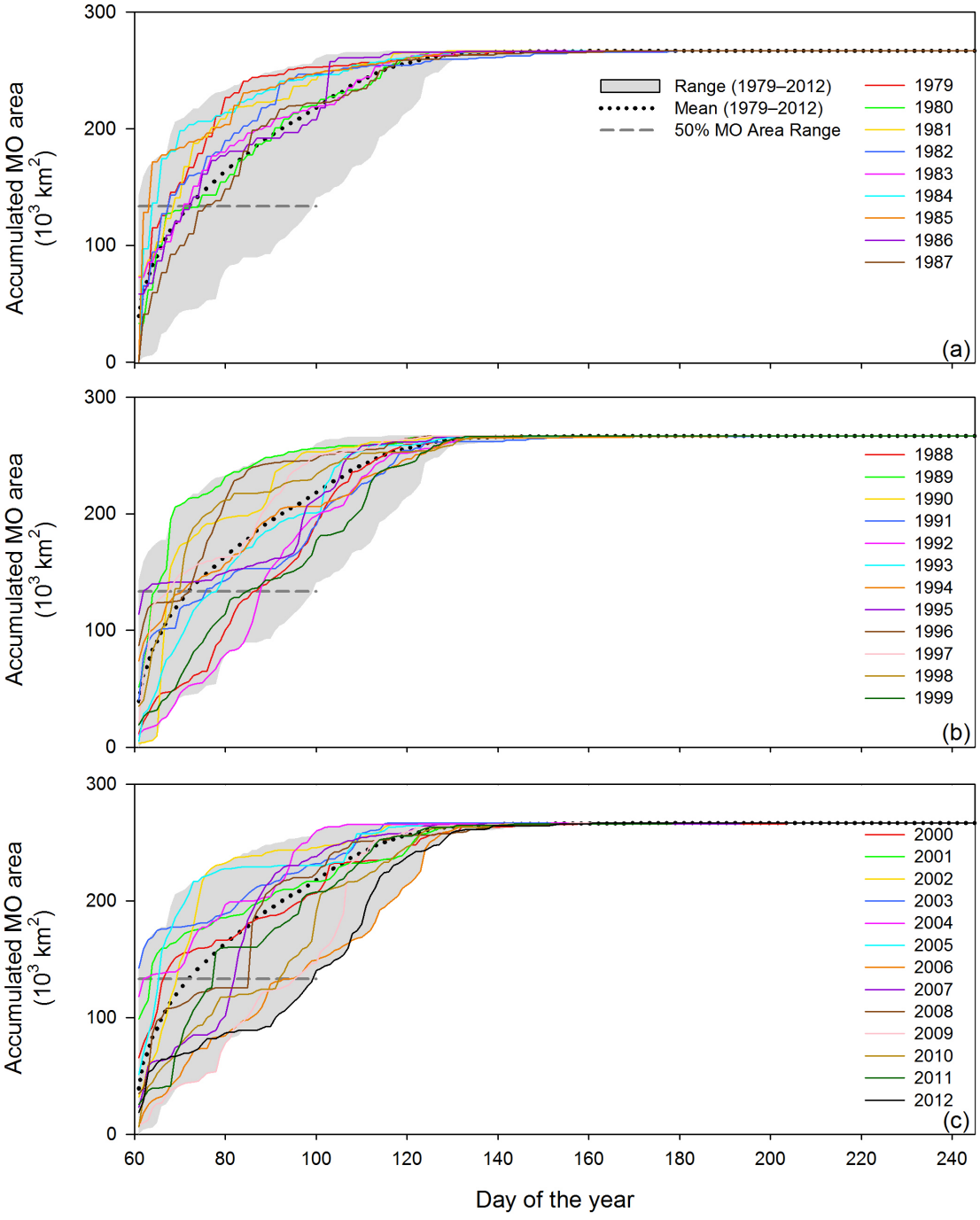

Figure 7.12 Bering Sea annual accumulated MO areas for (a) SMMR years, (b) early SSM/I years, and (c) late SSM/I and SSMIS years.

Contrary to every other Arctic Ocean sub-region, the earliest MO area accumulations generally occur in the Bering Sea (Figure 7.12) during the SMMR years (1979 – 1987) while the SMM/I years (1988 – 2012) have an increased spread around the mean MO area accumulation and more years occupy the bottom or later MO portion of the range. The latest MO area accumulations in the Bering Sea occur in 2009, 2012, and 2006 (Figure 7.12c).

The Bering Sea is located at lower latitudes than most of the Arctic Ocean sub-regions, so it is expected that the MO area accumulations will tend to occur earlier in the year than regions closer to the pole and this is the case. The mean 50% MO area date for the Bering Sea is 16 March (DOY 74.7), the earliest of the sub-regions discussed here (Table 7.1). However, the range of 50% MO area accumulations in the Bering Sea (39 days) is very similar to that of the Canadian Arctic Archipelago (38 days). This example illustrates that the 50% MO area range for different regions may be similar, however, given the geographic differences between individual regions of the Arctic, the ranges are similar for different reasons. In this case, the mean 50% MO area date captures the distinct difference between MO accumulation patterns in these two regions. The mean date on which 50% MO area is reached in the Bering Sea is 16 March (DOY 74.7), while the same for the Canadian Arctic Archipelago is 31 May (DOY 151.2). The variability in MO area accumulations between these two regions from year to year is similar, however, it is very clear that the patterns in MO area accumulations between these two regions are very different. The majority of MO area in the Canadian Arctic Archipelago (Figure 7.8) does not occur until after ~ 30 April (DOY 120), while nearly all MO area in the Bering

Sea (Figure 7.12) has accumulated by 30 April (DOY 120) for nearly all years. Utilizing both the 50% MO area range and mean date of 50% MO area together can provide a more accurate description of the record of MO accumulations in Arctic sub-regions.

7.5 Summary and discussion: interannual variability in MO area accumulations

The characteristics in the timing of MO area accumulations from year to year in various sub-regions are influenced by many factors, including geography, mean air temperatures, and whether the region is land or ice locked (i.e. the fetch of the region in question may influence the response of melting due to weather conditions) [*Drobot and Anderson*, 2001b]. For example, the Canadian Arctic Archipelago is a largely land-locked region that is largely dominated by the presence of thick, multiyear sea ice which makes the sea ice less susceptible to early MO (Figure 2.2). Conversely, the Bering Sea's latitude and its position adjacent to the North Pacific Ocean allows for greater heat transport into the region at an earlier date in the year. Thus it is expected that MO would occur relatively earlier in the melt season in the Bering Sea and other peripheral sea ice regions than for regions within the Arctic Ocean.

Although there is an overall shift towards earlier MO for much of the Arctic sea ice cover (Chapter 4), the high variability from year to year in individual sub-regions, gives further evidence that the timing and magnitude of MO area accumulations are highly dependent on the atmospheric conditions present at the time of MO in a particular region (Chapter 5). *Anderson and Drobot* [2001] have shown that the MO dates in one region of the Arctic are largely independent of the MO dates in other regions. This is

most likely due to the regional nature of cyclonic activity and the associated warm air anomalies [*Drobot and Anderson*, 2001b; *Belchansky et al*., 2004] and increased longwave radiation flux at the surface due to enhanced cloud cover (e.g. *Crane and Anderson*, 1994; *Bennartz et al*., 2013). Therefore, an extreme MO area accumulation (one that is at either the early or late ends of the 50% MO area range) in a region one year may not appear to be an abnormal year for other regions. For example, the MO area accumulation is extremely early for 1990 in the East Siberian Sea (Figure 7.5b) and also shows up as an early MO accumulation year for the Kara, Laptev, Chukchi, and for at least a portion of the Central Arctic region (Figures 7.3b, 7.4b, 7.6b, and 7.9b). However, 1990 MO area accumulation occurs later in the year than the mean for the Beaufort Sea and the Canadian Arctic Archipelago (Figures 7.7b and 7.8b). 1990 is an anomalous year in terms of MO area because this year is associated with a strongly positive AO Index in the winter and the early spring [*Drobot and Anderson*, 2001b]. The positive AO Index was found to be associated with earlier MO in the Laptev, East Siberian, and Chukchi Sea regions.

Since MO is so closely tied to the cyclonic-scale weather conditions, variations in the MO area accumulations from year to year reflect the variability of spring weather. The significant trends in MO dates reported in Chapter 4, the close relationship between weather conditions and spatial patterns in MO area shown in Chapter 5, and changes observed changes in MO area accumulations over the data record reported here indicate that the weather conditions influencing the timing of MO have changed over the last several decades.

The onset of melting causes a reduction in surface albedo of the snow cover atop the sea ice [*Curry et al.,* 1995; *Perovich and Polashenski*, 2012]. Earlier reductions in surface albedo increase the amount of solar radiation that can be absorbed by the ice-ocean system throughout the remainder of the melt season. The fact that larger areas of the ice cover are beginning to melt earlier in the season, gives evidence that the surface energy balance in the Arctic is changing. Thus, more solar energy can be absorbed into the region until freeze-up occurs during the autumn. Overall warming air temperatures in the Arctic (e.g. *Serreze and Francis*, 2006; *Serreze et al*., 2009; *Screen and Simmonds*, 2010) may provide a mechanism for the shift towards earlier MO area accumulations. However, variability in MO area from year to year is also related to the atmospheric circulation patterns and the frequency of cyclonic activity [*Drobot and Anderson,* 2001b]. Due to the size and time scale of cyclonic disturbances, it is necessary to complete further investigations into daily Arctic weather conditions at the time of MO and also when MO is delayed to fully understand the changes in regional MO area.

CHAPTER 8 – CONCLUSIONS AND FUTURE WORK

This research documents the trends in melt onset (MO) for an updated record of passive microwave-derived snowmelt onset dates on Arctic sea ice and explores the utility of identifying temporal and spatial patterns in daily MO area for the 1979 – 2012 data record. Further, this research examines the relationship between the patterns of MO area and the atmospheric conditions present at the time of MO that induce melting over large portions of Arctic sub-regions.

For the majority of the Arctic, mean MO dates are occurring increasingly early. Statistically significant decadal trends (99% confidence) exist for the Arctic Region (-6.6 days decade^{-1}) and many Arctic Ocean sub-regions including: the East Siberian Sea (-11.8 days decade^{-1}), the Kara Sea (-9.2 days decade^{-1}), the Chukchi Sea and Central Arctic (both having a -8.3 days decade^{-1} trend), the Laptev Sea (-8.2 days decade^{-1}), the Barents Sea (-7.6 days decade^{-1}), and the Canadian Arctic Archipelago (-4.6 days decade^{-1}). Interestingly, the only sub-region of the Arctic to have a positive trend in mean MO date is the Bering Sea, where a ($+3.1$ days decade^{-1}) trend exists (95% confidence) indicating that MO in the Bering Sea is occurring later in the year than at the beginning of the data record. This finding coincides with a larger extent of sea ice at the beginning of the melt season in later years of the record found in the re-processed MO date dataset.

The highest variability in mean MO dates occur in the large sub-regions of the Arctic Ocean where mean standard deviations of MO dates from 14.5 days in the East Siberian Sea to 7.7 days in the Canadian Arctic Archipelago, while the greatest range in

mean MO dates occur in the Kara Sea (54 days). This variability in MO timing in sub-regions of the Arctic Ocean is attributed to variability in spring weather conditions while the southernmost, peripheral sea ice regions outside of the Arctic Ocean are typically less variable from year to year where MO occurs earlier in the year.

Temporal variability in MO area is shown by the identification of four types of melting events. Peaks in the daily time series of MO area defined as melting events for each year are characterized by the magnitude of melting (high or low) and the duration of the event (short or long). Melting events can occur anytime during the melt season, however, the low magnitude, short duration events tend to only occur anomalously early in the melt season (less than −2 standard deviations from the mean MO date). The high magnitude, short duration events are indicative of a cyclone tracking to the northwest, placing the region in the warm sector of the cyclone where warm air advection produces extensive melting over a short time period, about 3-5 days. High magnitude, long duration events tend to be composites of multiple, larger melting events interspersed with low melting days.

Spatial patterns in MO area are examined by mapping the spatial patterns during four types of melting events. The spatial analysis reveals that the spatial pattern in melted pixel point locations differs depending on the type of weather system impacting the area. Low pressure systems tracking to the northwest of the region tend to produce large continuous patches of melting, while the effects of high pressure, cloud free conditions tends to produce melting area that is sparsely distributed. In longer duration melting event types, multiple cyclone events can be distinguished by the day-by-day spatial pattern in MO area, which produce local peaks in the daily MO area time series.

Annual accumulations of daily MO area effectively describe the interannual variability in melting area. For most of the Arctic and sub-regions, MO area accumulations in the early part of the data record (SMMR) years occur later in the season, while greater spread about the mean and earlier accumulations begin to occur in the SSM/I and SSMIS years. The negative trends in mean MO date are apparent in the annual accumulations of MO area, but regional variability is high and anomalous melting events can have a large influence on the range of annual MO area accumulations at a regional scale.

This work primarily focused on the large melting events in terms of area melted, however, the results of this study have indicated that the timing of melting events may be more important than overall magnitude for describing the influence of MO on Arctic sea ice loss. High magnitude melting events can occur at any time during the melt season, but it is the anomalously late, high magnitude melting events that are primarily due to seasonal warming that are most interesting. Given that a MO date can only be determined at each pixel point location once per year, the lack of melting area earlier in the season when late season, very high magnitude melting events occur could have important implications for the end of season sea ice conditions.

While this work raises the issue of seasonality in the MO data, further work is needed to determine when the effects of seasonality become more significant than the effects of transient weather events in producing higher magnitude MO events. It is likely that seasonality has a large influence on the MO area observed during late season events, however, at this time, it is unknown when that transition may occur. Future work is needed to investigate these types of events in order to complete a more thorough analysis

of the springtime weather conditions forcing various types of MO area patterns. A better understanding of the atmospheric conditions leading to these late season, seasonal melting events in addition to the anomalously early melting events described here are necessary to improve predictability of the Arctic sea ice response to changing climate conditions. Further investigation into the atmospheric conditions during more complex, long duration MO events and across regional boundaries could help pinpoint specific changes in mean synoptic conditions throughout the MO record.

Additionally, further study of the duration of melting that occurs following the initial onset of melting could help to fully address the complicated nature of MO and annual sea ice extent minima. Although the onset of melting signals the beginning of the melt season for Arctic sea ice, an investigation of the continuation of sea ice melt during the remainder of the melt season could better characterize the springtime weather patterns and improve predictability of summer sea ice conditions

REFERENCES

Abdalati, W., K. Steffen, C. Otto, and K. C. Jezek (1995), Comparison of brightness temperatures from SSMI instruments on the DMSP F8 and F11 satellites for Antarctica and the Greenland ice sheet, *Int. J. Remote Sens.*, 16, 7, 1223-1229, doi:10.1080/01431169508954473.

Anderson, M. R. (1987), Snow melt on sea ice surfaces as determined from passive microwave satellite data, *Large Scale Effects of Seasonal Snow Cover*, Proceedings of the Vancouver Symposium, August 1987, International Association of Hydrological Sciences, *166*, 329–342.

Anderson, M. R., A. C. Bliss, and S. D. Drobot (2014), Snow melt onset over Arctic sea ice from SMMR and SSM/I brightness temperatures, version 3, [1979 – 2012], http://nsidc.org/data/nsidc-0105.html, NASA DAAC at the National Snow and Ice Data Center, Boulder, Colorado, USA.

Anderson, M. R. and S. D. Drobot (2001), Spatial and temporal variability in snowmelt onset over Arctic sea ice, *Ann. Glaciol*., 33, 74-78.

Belchansky, G. I., D. C. Douglas, and N. G. Platonov (2004), Duration of the Arctic sea ice melt season: regional and interannual variability 1979-2001, *J. Climate*, 17, 67-80, doi:10.1175/1520-0442(2004)017<0067:DOTASI>2.0.CO;2.

Bennartz, R., M. D. Shupe, D. D. Turner, V. P. Walden, K. Steffen, C. J. Cox, M. S. Kulie, N. B. Miller, and C. Pettersen (2013), July 2012 Greenland melt extent enhanced by low-level liquid clouds, *Nature*, 496, 83–86, doi:10.1038/nature12002.

Bliss, A. C. and M. R. Anderson (2014), Snowmelt onset over Arctic sea ice from passive microwave satellite data: 1979–2012, *The Cryosphere*, 8, 2089-2100, doi:10.5194/tc-8-2089-2014.

Cavalieri, D. J. and C. L. Parkinson (2012), Arctic sea ice variability and trends, 1979–2010, *The Cryosphere*, 6, 881-889, doi:10.5194/tc-6-881-2012.

Cavalieri, D., C. Parkinson, P. Gloersen, J. Comiso, and H. J. Zwally (1999), Deriving long-term time series of sea ice cover from satellite passive-microwave multisensor data sets, *J. Geophys. Res.*, 104, C7, 15,803-15,814, doi:10.1029/1999JC900081.

Comiso, J. C., C. L. Parkinson, R. Gersten, L. Stock (2008), Accelerated decline in the Arctic sea ice cover, *Geophys. Res. Lett.*, *35*, L01703, doi:10.1029/2007GL031972.

Comiso, J. C. (2012), Large decadal decline of the arctic multiyear ice cover, *J. Climate*, 25, 1176–1193, doi: http://dx.doi.org/10.1175/JCLI-D-11-00113.1.

Crane, R. G. and M. R. Anderson (1994), Springtime microwave emissivity changes in the southern Kara Sea, *J. Geophys. Res.,* 99, C7, 14,303-14,309, doi:10.1029/94JC00381.

Cullather, R. I. and M. G. Bosilovich (2012), The energy budget of the polar atmosphere in MERRA, *J. Climate*, 25, 5–24, doi:10.1175/2011JCLI4138.1.

Curry, J. A., J. L. Schramm, and E. E. Ebert (1995), Sea ice-albedo climate feedback mechanism, *J. Climate*, 8, 240-247, doi:10.1175/1520-0442(1995)008<0240:SIACFM>2.0.CO;2.

Deser, C. and H. Teng (2008), Evolution of Arctic sea ice concentration trends and the role of atmospheric circulation forcing, 1979 – 2007, *Geophys. Res. Lett*., 35, L02504, doi:10.1029/2007GL032023.

Drobot, S. D. (2000), Spatial and temporal variability in snow melt onset over Arctic sea ice and associated atmospheric conditions, Doctoral Dissertation, Dept. of Geosci., University of Nebraska, Lincoln, Nebraska, USA.

Drobot, S. D., and M. R. Anderson (2001a), An improved method for determining snowmelt onset dates over Arctic sea ice using Scanning Multichannel Microwave Radiometer and Special Sensor Microwave/Imager data." *J. Geophys. Res.*, 106, D20, 24,033-24,049, doi:10.1029/2000JD000171.

Drobot, S. D., and M. R. Anderson (2001b), Comparison of interannual snowmelt-onset dates with atmospheric conditions, *Ann. Glaciol*., 33, 79-84.

ESR-PSD (2015), NCEP-DOE Reanalysis 2: pressure level data, NOAA/ESRL Physical Sciences Division, http://www.esrl.noaa.gov/psd/, Boulder, Colorado, USA, accessed on 8 March 2015.

ESR-PSD (2014), The NCEP/NCAR Reanalysis Project, NOAA/ESRL Physical Sciences Division, http://www.esrl.noaa.gov/psd/, Boulder, Colorado, USA, accessed on 3 October 2014.

Forster, R. R., D. G. Long, K. C. Jezek, S. D. Drobot, and M. R. Anderson (2001), The onset of Arctic sea-ice snowmelt as detected with passive- and active-microwave remote sensing, *Ann. Glaciol*., 33, 85–93, doi:10.3189/172756401781818428.

GES DISC (2015), NASA MERRA IAU 3d assimilated state on pressure, [10 May 1985 – 15 March 2012], http://disc.sci.gsfc.nasa.gov/daac-bin/DataHoldings.pl, Goddard Earth Sciences Data and Information Services Center, Greenbelt, Maryland, USA, accessed 8 March 2015.

Howell, S. E. L., C. R. Duguay, and T. Markus (2009), Sea ice conditions and melt season duration variability within the Canadian Arctic Archipelago: 1979 – 2008, *Geophys. Res. Lett.,* 36, L10502, doi:10.1029/2009GL037681.

Jezek, K. C., C. Merry, D. Cavalieri, S. Grace, J. Bedner, D. Wilson, and D. Lampkin (1991), Comparison between SMMR and SSM/I passive microwave data collected over the Antarctic ice sheet, *Byrd Polar Research Center Technical Report,* no. 91-03. The Ohio State University, Columbus, Ohio USA.

Kalnay, E., M. Kanamitsu, R. Kistler, W. Collins, D. Deaven, L. Gandin, M. Iredell, S. Saha, G. White, J. Woollen, Y. Zhu, A. Leetmaa, R. Reynolds, M. Chelliah, W. Ebisuzaki, W. Higgins, J. Janowiak, K. C. Mo, C. Ropelewski, J. Wang, R. Jenne, and D. Joseph (1996), The NCEP/NCAR 40-Year Reanalysis Project, *Bull. Amer. Meteor. Soc.*, 77, 437–471, doi:10.1175/1520-0477(1996)077<0437:TNYRP>2.0.CO;2.

Kanamitsu, M., W. Ebisuzaki, J. Woollen, S.-K. Yang, J. J. Hnilo, M. Fiorino, and G. L. Potter (2002), NCEP–DOE AMIP-II reanalysis (R-2), *Bull. Amer. Meteor. Soc*., 83, 1631–1643, doi:10.1175/BAMS-83-11-1631.

Kunzi, K. F., S. Patil, and H. Rott (1982), Snow-cover parameters derived from Nimbus-7 scanning multichannel microwave radiometer (SMMR) data, *IEEE Trans. Geosci. Remote Sens.*, GE-20, 4, 452 - 467, doi:10.1109/TGRS.1982.350411.

Kwok, R., G. F. Cunningham, and S. V. Nghiem (2003), A study of melt onset in RADARSAT SAR imagery, *J. Geophys. Res*., 108, C11, 3363, doi:10.1029/2002JC001363.

Kwok, R., G. F. Cunningham, M. Wensnahan, I. Rigor, H. J. Zwally, and D. Yi (2009), Thinning and volume loss of the Arctic Ocean sea ice cover: 2003 – 2008, *J. Geophys. Res.,* 114, C07005, doi:10.1029/2009JC005312.

Lindsay, R. W., J. Zhang, A. Schweiger, M. Steele, and H. Stern (2009), Arctic sea ice retreat in 2007 follows thinning trend, *J. Climate,* 22, 165–176, doi:10.1175/2008JCLI2521.1.

Livingstone, C. E., K. P. Singh, and L. Gray (1987), Seasonal and regional variations of active/passive microwave signatures of sea ice, *IEEE Trans. Geosci. Remote Sens.*, GE-25, 2, 159-172.

Markus, T., J. C. Stroeve, and J. Miller (2009), Recent changes in Arctic sea ice melt onset, freezeup, and melt season length, *J. Geophys. Res*., 114, C12024, doi:10.1029/2009JC005436.

Maslanik, J., S. Drobot, C. Fowler, W. Emery, and R. Barry (2007), On the Arctic climate paradox and the continuing role of atmospheric circulation in affecting sea ice conditions, *Geophys. Res. Lett.,* 34, L03711, doi:10.1029/2006GL028269.

Maslanik, J., J. Stroeve, C. Fowler, and W. Emery (2011), Distribution and trends in Arctic sea ice age through spring 2011, *Geophys. Res. Lett.,* 38, L13502, doi:10.1029/2011GL047735.

Meier, W., F. Fetterer, M. Savoie, S. Mallory, R. Duerr, and J. Stroeve (2013), NOAA/NSIDC Climate Data Record of Passive Microwave Sea Ice Concentration, Version 2, National Snow and Ice Data Center, Boulder, Colorado USA, doi:10.7265/N55M63M1.

Meier, W. N., J. Stroeve, and F. Fetterer (2007), Wither Arctic sea ice? A clear signal of decline regionally, seasonally and extending beyond the satellite record, Ann. Glaciol., 46, 428-434, doi:10.3189/172756407782871170.

Nghiem, S. V., I. G. Rigor, D. K. Perovich, P. Clemente-Colón, J. W. Weatherly, and G. Neumann (2007), Rapid reduction of Arctic perennial sea ice, *Geophys. Res. Lett.,* 34, L19504, doi:10.1029/2007GL031138.

NSIDC (2014), Documentation: polar stereographic projection and grid, https://nsidc.org/data/polar_stereo/ps_grids.html, National Snow and Ice Data Center, Boulder, Colorado, USA, accessed on 28 March 2014.

NSIDC (2012), Open water means a warm Arctic, *Arctic Sea Ice News and Analysis,* Monthly Archives 15 October 2012, http://nsidc.org/arcticseaicenews/2012/10/, National Snow and Ice Data Center, Boulder, Colorado, USA, accessed on 24 March 2015.

Ogi, M., I. G. Rigor, M. G. McPhee, and J. M. Wallace (2008), Summer retreat of Arctic sea ice: role of summer winds, *Geophys. Res. Lett*., 35, L24701, doi:10.1029/2008GL035672.

Ogi, M., and J. M. Wallace (2007) Summer minimum Arctic sea ice extent and the associated summer atmospheric circulation, *Geophys. Res. Lett*., 34, L12705, doi:10.1029/2007GL029897.

Parkinson, C. L., and J. C. Comiso (2013), On the 2012 record low Arctic sea ice cover: combined impact of preconditioning and an August storm, Geophys. Res. Lett., 40, 1356-1361, doi:10.1002/grl.50349.

Parkinson, C.L., D.J. Cavalieri, P. Gloersen, H.J. Zwally and J.C. Comiso (1999), Arctic sea ice extents, areas, and trends, 1978–1996, J. Geophys. Res., 104, C9, 20,837–20,856, doi:10.1029/1999JC900082.

Perovich, D. K., S. V. Nghiem, T. Markus, and A. Schweiger (2007), Seasonal evolution and interannual variability of the local solar energy absorbed by the Arctic sea ice–ocean system, *J. Geophys. Res*., 112, C03005, doi:10.1029/2006JC003558.

Perovich, D. K. and C. Polashenski (2012), Albedo evolution of seasonal Arctic sea ice, *Geophys. Res. Lett.*, *39*, L08501, doi:10.1029/2012GL051432.

Rienecker, M. M., M. J. Suarez, R. Gelaro, R. Todling, J. Bacmeister, E. Liu, M. G. Bosilovich, S. D. Schubert, L. Takacs, G.-K. Kim, S. Bloom, J. Chen, D. Collins, A. Conaty, A. da Silva, W. Gu, J. Joiner, R. D. Koster, R. Lucchesi, A. Molod, T. Owens, S. Pawson, P. Pegion, C. R. Redder, R. Reichle, F. R. Robertson, A. G. Ruddick, M. Sienkiewicz, and J. Woollen (2011) MERRA: NASA's modern-era retrospective analysis for research and applications, *J. Climate*, 24, 3624–3648, doi:10.1175/JCLI-D-11-00015.1.

Rigor, I. G. and J. M. Wallace (2004), Variations in the age of Arctic sea-ice and summer sea-ice extent, *Geophys. Res. Lett*., 31, L09401, doi:10.1029/2004GL019492.

Rigor, I. G., J. M. Wallace, and R. L. Colony (2002), Response of sea ice to the Arctic Oscillation, *J. Climate*, 15, 2648–2663, doi:10.1175/1520-0442(2002)015<2648:ROSITT>2.0.CO;2.

Screen, J. A. and I. Simmonds (2010), The central role of diminishing sea ice in recent Arctic temperature amplification, *Nature,* 464, 1334-1337, doi:10.1038/nature09051.

Serreze, M. C. and A. P. Barrett (2008), The summer cyclone maximum over the central Arctic Ocean, *J. Climate*, 21, 1048–1065, doi:10.1175/2007JCLI1810.1.

Serreze, M. C., A. P. Barrett, J. C. Stroeve, D. N. Kindig, and M. M. Holland (2009), The emergence of surface-based Arctic amplification, *The Cryosphere*, 3, 11-19, www.the-cryosphere.net/3/11/2009/.

Serreze, M. C. and J. A. Francis (2006) The Arctic amplification debate, *Climatic Change,* 76, 241-264, doi:10.1007/s10584-005-9017-y.

Serreze, M. C., J. A. Maslanik, T. A. Scambos, F. Fetterer, J. Stroeve, K. Knowles, C. Fowler, S. Drobot, R. G. Barry, and T. M. Haran (2003), A record minimum arctic sea ice extent and area in 2002, *Geophys. Res. Lett.,* 30, 3, 1110, doi:10.1029/2002GL016406.

Simmonds, I. and I. Rudeva (2012), The great Arctic cyclone of August 2012, *Geophys. Res. Lett.*, *39*, L23709, doi:10.1029/2012GL054259.

Smith, D. M. (1998), Observation of perennial Arctic sea ice melt and freeze-up using passive microwave data, *J. Geophys. Res.,* 103, C12, 27,753-27,769, doi:10.1029/98JC02416.

Stroeve, J. C., T. Markus, L. Boisvert, J. Miller, and A. Barrett (2014), Changes in Arctic melt season and implications for sea ice loss, *Geophys. Res. Lett.,* 41, 1216–1225, doi:10.1002/2013GL058951.

Stroeve, J., T. Markus, W. Meier, and J. Miller (2006), Recent changes in the Arctic melt season, *Ann. Glaciol*., 44, 367-374, doi:10.3189/172756406781811583.

Stroeve, J., J. Maslanik, and L. Xiaoming (1998), An intercomparison of DMSP F11- and F13-derived sea ice products, *Remote Sens. Environ.*, 64, 132-152, doi:10.1016/S0034-4257(97)00174-0.

Stroeve, J. C., M. C. Serreze, M. M. Holland, J. E. Kay, J. Maslanik, and A. P. Barrett (2011), The Arctic's rapidly shrinking sea ice cover: A research synthesis, *Climatic Change*, doi:10.1007/s10584-011-0101-1.

Tietsche, S., D. Notz, J. H. Jungclaus, and J. Marotzke (2011), Recovery mechanisms of Arctic summer sea ice, *Geophys. Res. Lett*., 38, L02707, doi:10.1029/2010GL045698.

Wang, L., G. J. Wolken, M. J. Sharp, S. E. L. Howell, C. Derksen, R. D. Brown, T. Markus, and J. Cole (2011), Integrated pan-Arctic melt onset detection from satellite active and passive microwave measurements, 2000 – 2009, *J. Geophys. Res.,* 116, D22103, doi:10.1029/2011JD016256.

Winebrenner, D. P., E. D. Nelson, R. Colony, and R. D. West (1994), Observation of melt onset on multiyear Arctic sea ice using the ERS-1 synthetic aperture radar, *J. Geophys. Res.,* 99, 22,425–22,441, doi:10.1029/94JC01268.

Zhang, J., D. Rothrock, and M. Steele (2000), Recent changes in Arctic sea ice: the interplay between ice dynamics and thermodynamics, *J. Climate*, 13, 3099-3114, doi:10.1175/1520-0442(2000)013<3099:RCIASI>2.0.CO;2.